UNIVERSITY OF SOUTHAMPTON

FACULTY OF ENGINEERING, SCIENCE AND MATHEMATICS

School of Engineering Sciences

Development of a Fabrication Process for a MEMS Component from Ultra Fine Grained Alloys

by

Xiao Guang Qiao

Thesis for the degree of Doctor of Philosophy

February 2010

UNIVERSITY OF SOUTHAMPTON
ABSTRACT
FACULTY OF ENGINEERING, SCIENCE & MATHEMATICS
SCHOOL OF ENGINEERING SCIENCES

Doctor of Philosophy

DEVELOPMENT OF A FABRICATION PROCESS FOR A MEMS COMPONENT FROM ULTRA FINE GRAINED ALLOYS

By Xiao Guang Qiao

This thesis presents a study on the feasibility of fabricating a MEMS component by embossing using ultra-fine grained (UFG) aluminium alloys. The main elements of the work involved designing the equipment, production of UFG aluminium alloys through equal channel angular pressing (ECAP), embossing of the UFG alloys and the construction of models that improve the understanding of the main elements of the processing.

ECAP was performed on Al-1050, AlZr and AlZrSiFe alloys to produce UFG Al alloys. Microstructure and texture evolution were analyzed by electron backscattered diffraction (EBSD) and transmission electron microscopy (TEM). A new predictive model of grain refinement allows the understanding of the grain refinement process. Microhardness inhomogeneity of UFG Al-1050 processed by one pass of ECAP was studied through measuring the distribution of Vickers hardness and microstructure on the cross section before and after annealing at different temperature. Microhardness of UFG Al alloys processed by various passes of ECAP was measured after annealing at various temperatures. The relation between microhardness and microstructure was studied with the aid of a dislocation model. The model suggests that most of the strengthening in the severely plastically deformed alloys is due to enhanced dislocation density. Nanoindentation hardness of UFG Al-1050 was also measured. A modified model of indentation size effect was derived. The model was justified through comparison with our own data and data in literature.

The UFG Al alloys were embossed using a micro silicon die with a pattern of microchannels at both room temperature and high temperature. The topography of embossed sample was observed by scanning electron microscopy (SEM), optical microscopy (OM) and confocal laser system. Nanoindentation hardness was measured on cross section of the embossed sample to detect the hardness distribution. Focus ion beam (FIB) and EBSD were used to characterize the microstructure on the cross section. A model employing concept of geometrically necessary dislocations (GND) was present to predict embossing force and hardness distribution on the cross section.

This study shows a good potential for fabrication of microdevices by embossing UFG alloys processed by ECAP. An optimized process was obtained through analysis of microstructure and properties of the UFG alloys before and after embossing. The understanding of the processing was enhanced through construction of models.

List of Contents

ABSTRACT I
List of Contents II
List of Figures VI
List of Tables XI
Declaration of Authorship XII
Acknowledgements XIV
Definitions and Abbreviations XV
1 Introduction 1
2 Literature Review 4
2.1 Introduction of aluminium alloys 4
2.2 Al-Zr alloys 6
2.2.1 Microstructure of Al-Zr alloys 6
2.2.2 Property of Al-Zr alloys 10
2.3 MEMS technologies 13
2.3.1 Developments of MEMS technology 13
2.3.2 Applications of MEMS 14
2.3.2.1 Communications 14
2.3.2.2 Automobile 14
2.3.2.3 Biotechnology 15
2.3.3 Microfabrication technologies 15
2.3.3.1 Anisotropic wet etching 16
2.3.3.2 Dry etching 17
2.3.3.3 LIGA 20
2.3.4 Embossing 21
2.3.4.1 Embossing equipment 22
2.3.4.2 Embossing Process 24
2.3.4.3 Embossing on metals 24
2.3.4.4 Nanoindentation as a method for characterising embossed metals 27
2.4 Micro-heat exchangers 30
2.4.1 Classification of micro heat exchangers 30
2.4.2 Materials and forming methodology for micro heat exchangers 32

2.5 Severe plastic deformation 36
2.5.1 High pressure torsion 38
2.5.2 Multi-directional forging 38
2.5.3 Accumulative roll bonding 39
2.5.4 Cyclic extrusion and compression 40
2.5.5 Repetitive corrugation and straightening 41
2.5.6 Twist extrusion 42
2.6 Equal channel angular pressing 42
2.6.1 Principle of ECAP 43
2.6.2 Mechanisms of grain refinement in ECAP 45
2.6.3 Application of ECAP in aluminium alloys 49
2.6.3.1 Microstructure of aluminium alloys after ECAP 49
2.6.3.2 Thermal stability of UFG aluminium alloys 51
2.6.3.3 Properties of aluminium alloys after ECAP 54
2.7 Summary 58
3 Design of Equipment 60
3.1 ECAP facilities 60
3.2 ECAP processing procedures 63
3.3 Embossing Facilities 63
3.4 Embossing process and procedures 73
4 Material, Testing and Microstructural Analysis 75
4.1 Materials 75
4.2 Heat treatment 76
4.3 Microhardness testing 76
4.4 Electron backscattered diffraction 77
4.5 Transmission electron microscopy 79
4.6 Confocal laser system 79
4.7 Optical microscopy 79
4.8 Scanning electron microscopy 79
4.9 Focussed ion beam microscopy 80
4.10 Nanoindentation 80
5 Analyzing Ultra Fine Grained Al Alloys 81
5.1 Results 81
5.1.1 Electron backscattered diffraction analysis 81
5.1.1.1 Grain sizes and grain boundaries in Al-1050 81

5.1.1.2 Texture in Al-1050 84
5.1.1.3 EBSD on AlZr alloy 87
5.1.1.4 EBSD on AlZrSiFe alloy 90
5.1.2 Transmission electron microscopy 94
5.2 A model of grain refinement 96
5.2.1 The model 96
5.2.2 The modelling results 98
5.3 Summary 99
6 Strength/Microhardness of UFG Al Alloys Processed by ECAP 100
6.1 Results 100
6.1.1 Thermal stability of UFG structure 100
6.1.1.1 Microhardness of Al-1050 annealed at various temperatures 100
6.1.1.2 Microhardness of AlZrSiFe after annealing at various temperatures 101
6.1.1.3 Microhardness of AlZr alloy after annealing at various temperatures 102
6.1.1.4 Discussion on annealling behaviour of UFG Al alloys 103
6.1.2 Local microstructure and microhardness of Al-050 processed by ECAP 104
6.1.2.1 Microhardness of the ECAP-processed billet 104
6.1.2.2 Microstructure of the ECAP-processed billet by EBSD 105
6.1.2.3 Microstructure of the heat treated billet 108
6.1.2.4 Microhardness of the heat treated billet 109
6.2 Discussion of strengthening mechanism of the ECAP-processed aluminum 109
6.3 A model for microhardness/strength of the alloys after ECAP 110
6.3.1 Modelling of strengthening of Al alloys after various passes of ECAP 112
6.3.2 Modelling on microhardness inhomogeniety of Al-1050 after one pass of ECAP 117
6.4 Summary 121
7 Nanoindentation of UFG Aluminium Alloys 122
7.1 Results 122
7.2 A model of indentation size effect for blunted tip. 123
7.2.1 Aims of the model 124
7.2.2 Generation of GNDs. 124
7.2.3 Strength model 128
7.2.4 Model predictions 129
7.2.5 Modelling Results and Model verification 132
7.2.5.1 Determining the blunted tip radius. 132

7.2.5.2 Predicting nanoindentation hardness of UFG Al-1050. 133
7.2.5.3 Predicting dislocation densities 136
7.2.5.4 ISE of several FCC metals 138
7.2.6 Discussion of the model 143
7.3 Summary 144
8 Embossing of UFG Aluminium 146
8.1 Results 146
8.1.1 Micro silicon die 146
8.1.2 Cold embossing 149
8.1.2.1 Embossing force 149
8.1.2.2 Microscale topography of cold embossed foils 150
8.1.2.3 Microstructure and nanoindentation hardness on cross section of the embossed UFG Al 155
8.1.3 Hot embossing 159
8.2 Summary on embossing 162
8.3 A model of micro embossing of UFG Al alloys 163
8.3.1 The model 163
8.3.2 Modeling results 165
8.3.3 Discussion of the model 166
8.3.3.1 Indentation size effect in UFG alloys and coarse grained (CG) alloys 166
8.3.3.2 Influence of embossing force on the embossing quality 168
8.3.3.3 Evaluating hardness homogeneity over the cross section of embossed UFG Aluminium using nanoindentation 168
8.4 Summary 169
9 General Discussion 171
9.1 Materials selection 171
9.2 SPD process 173
9.3 Potential of mass fabrication of MEMS components using UFG Al via embossing process 174
9.4 Model development 175
10 Conclusions 177
11 Future Work 180
Appendix A Drawings of Embossing Rig Components 182
Appendix B Topography of Micro Silicon Dies Measured by Confocal Laser System 187
References 189

List of Figures

Fig. 2.1 Al-Zr alloys equilibrium phase diagram 7

Fig. 2.2 The unit cell of Al_3Zr, (a) cubic, $L1_2$, (b) tetragonal, DO_{23} 9

Fig. 2.3 Microhardness as function of (a) Zr-content in the as-quenched (A) and peak aged (B) conditions and (b) of temperature T during isochronal (1h) ageing for Al-2.3, 3.9, 4.9, 6.2 and 8.6wt% Zr (A to E respectively) 11

Fig. 2.4 Variation of elongation with initial strain rate for: (a) as-rolled and (b) post-extrusion aged and subsequently rolled conditions 12

Fig. 2.5 A wet bulk micromachining process 15

Fig. 2.6 Schematic of the principle of the Bosch process 19

Fig. 2.7 The hot embossing process: heating, moulding and demoulding 24

Fig. 2.8 Schematic illustration of the difficulty associated with forming of features that are smaller than the grain size in polycrystalline materials. 26

Fig. 2.9 Flow arrangement classifications: (a) concurrent-flow; (b) counter-flow; (c) cross-flow, both fluids unmixed; (d) cross-flow, fluid 1 mixed and fluid 2 unmixed 31

Fig. 2.10 SEM of microchannels etched in <110> silicon using KOH 32

Fig. 2.11 A copper cross-flow micro heat exchanger fabricated by diamond machining 33

Fig. 2.12 Micro cross-flow heat exchangers made of (a) PMMA [89] and (b) Ni [92] 34

Fig. 2.13 (a) Passage of fluids in the extruded structure and (b) Serpentine heat transfer structure 34

Fig. 2.14 Optical micrograph of a stainless steel cross-flow micro heat exchanger [63] 35

Fig. 2.15 Principle of a counter-flow micro heat exchanger with (a) two plates per passage and (b) guided mass flows [95] 36

Fig. 2.16 The principle of HPT [98] 38

Fig. 2.17 The principle of MDF: (a), (b), (c) forging along the first axis; (d), (e), (f)-forging along the second axis; (g),(h), (i) forging along the third axis [100] 39

Fig. 2.18 The principle of ARB [101] 40

Fig. 2.19 The principle of CEC [102] 41

Fig. 2.20 The principle of RCS: (a) die set up for discontinuous RCS process and (b) set up for continuous RCS process [103] 41

Fig. 2.21 The principle of TE [104] 42

Fig. 2.22 The schematic of ECAP 43

Fig. 2.23 The four processing routes in ECAP 45

Fig. 2.24 Schematic model of dislocation structure evolution at different stages during severe plastic deformation [120]. 46

Fig. 2.25 TEM microstructure of the A1-4%Cu-0.5%Zr alloy: (a) HPT processed, (b) HPT and then annealed at 106˚C for 1 h..... 46

Fig. 2.26 Grain boundary structure of a nanostructured A1-3%Mg alloy observed by HREM. Edge dislocations are marked by the symbol ⊥..... 47

Fig. 2.27 A slip model for grain refinement in ECAP [125]..... 48

Fig. 2.28 The microstructures on the Y plane after four passes using route A, B_C and C [125] 49

Fig. 2.29 Comparison of tensile properties of cold rolling and ECAP for AA3004 [140] 55

Fig. 3.1 A plunger for ECAP process 60

Fig. 3.2 The drawing of the ECAP die for room temperature processing 61

Fig. 3.3 The drawing of the ECAP die for elevated temperature processing..... 62

Fig. 3.4 ECAP process system 63

Fig. 3.5 The embossing setup showing different components used in the experiments; the inset photo in a red box shows the sample and the silicon mould. 64

Fig. 3.6 Schematic drawing of embossing rig equipped with guide rods. 65

Fig. 3.7 DRIE process with different channel width in a wafer..... 67

Fig. 3.8 Mask design 68

Fig. 4.1 Schematic illustration of cross section of the ECAP-processed Al-1050 billet for microhardness measurement. 77

Fig. 5.1 Microstructure of Al-1050 alloys from EBSD (a) in the as-received conditions and processed by ECAP for (b) 1, (c) 2, (d) 4, (e) 8 and (f) 12 passes. 82

Fig. 5.2 Grain boundary misorientation distribution for Al-1050 alloys (a) in the as-received conditions and processed by ECAP for (b) 1, (c) 2, (d) 4, (e) 8 and (f) 12 passes. 83

Fig. 5.3 (a) Illustration of ECAP process and (b) (111) pole figure projected on y plane showing the main ideal slip system in simple shear [156]. 85

Fig. 5.4 (100) and (111) Pole figures of Al-1050 alloys in the as-received conditions projected on x plane 86

Fig. 5.5 (111) Pole figure projected on y plane of Al-1050 alloys processed by ECAP for (a) 1 (c) 2 , (d) 4, (e) 8 and (f) 12 passes; (b) the ideal slip systems in the Simple Shear Model..... 86

Fig. 5.6 Microstructure of AlZr alloys processed by ECAP for (a) 1, (b) 2, (c) 4 and (d) 8 passes..... 88

Fig. 5.7 Misorientation distribution of AlZr alloys processed by ECAP for (a) 1, (b) 2, (c) 4 and (d) 8 passes..... 89

Fig. 5.8 (111) Pole figures of AlZr alloys processed by ECAP for (a) 1, (b) 2, (c) 4 and (d) 8 passes. 90

Fig. 5.9 Microstructure of AlZrSiFe alloys processed by ECAP for (a) 1, (b) 2, (c) 4 and (d) 8 passes. 91

Fig. 5.10 Misorientation distributions of AlZrSiFe alloys processed by ECAP for (a) 1, (b) 2, (c) 4 and (d) 8 passes. The curves in the figures represent the theoretical misorientation distribution of randomly oriented grains [153] 92

Fig. 5.11 (111) Pole figures of AlZrSiFe alloys processed by ECAP for (a) 1, (b) 2, (c) 4 and (d) 8 passes..... 93

Fig. 5.12 TEM micrographs showing the structural evolution of AlZr alloy after (a), (b) 1; (c), (d) 4 and (e), (f),(g), (h) 8 passes of ECAP. 95

Fig. 5.13 Measured and predicted grain size of UFG Al alloys processed by two or more passes of ECAP..... 98

Fig. 6.1 Microhardness of UFG Al-1050 at elevated temperature..... 101

Fig. 6.2 Microhardness of UFG AlZrSiFe at elevated temperature..... 102

Fig. 6.3 Microhardness of UFG AlZr at elevated temperature. 103

Fig. 6.4 The average microhardness distribution over the cross section from the top edge to the bottom edge of the ECAP-processed billet and the heat treated billet. 105

Fig. 6.5 The microstructure of the billet cross section at (a), (b) the top edge, (c), (d) the centre and (e), (f) the bottom edge. (a), (c) and (e) are from the ECAP-processed billet; (b), (d) and (f) are from the 350 ˚C heat treated billet. 106

Fig. 6.6 Misorientation distribution of (a), (c), (e) the ECAP-processed billet, and (b), (d), (f)350 ˚C heat treated billet at (a), (b)the top edge, (c), (d)the centre and (e), (f)the bottom edge. 107

Fig. 6.7 Predicted and measured microhardness of Al-1050, AlZr and AlZrSiFe alloys after different passes of ECAP. 116

Fig. 6.8 The relationship between microhardness and yield strength of Al-1050. .. 119

Fig. 7.1 The influence of indentation depth on nanoindentation hardness of UFG Al-1050 processed by two passes of ECAP. 122

Fig. 7.2 Schematic sketch of distribution of GNDs underneath the rounded conical tip [78]..... 125

Fig. 7.3 Comparison of GND density predicted by various models 130

Fig. 7.4 Illustration of contacted area, residual area, assumed residual area and projected area during nanoindentation 131

Fig. 7.5 Influence of rounded tip on the GND density created under different indentation depth. 132

Fig. 7.6 Fitting of h_b. The blue cubes are the area function measured by experiments; the dash line is ideal function for the sharp tip; the red line is fitting curve using Eq. 7.15. 133

Fig. 7.7 Measured and predicted nanoindentation value against the indentation depth. The error bars are defined by standard deviations. 134

Fig. 7.8 Measured and predicted nanoindentation value of UFG Al-1050. The indentation depth ranges from 100 nm to 800 nm. 135

Fig. 7.9 Evolution of measured and predicted GND density of (111) copper single crystal with the indentation depth. 136

Fig. 7.10 Comparison of the prediction of the nanoindentation hardness of annealed Ir-0.3wt%W by Huang et al model [206], Abu Al-Rub model [84] and current model. 139

Fig. 7.11 The measured nanoindentation hardness of annealed Ir-0.3wt%W and predicted nanoindentation by the current model. 140

Fig. 7.12 Comparison of the prediction of the nanoindentation hardness of single crystal MgO by Huang et al model [206], Abu Al-Rub model [84] and the current model. 141

Fig. 7.13 The measured nanoindentation hardness of single crystal MgO and predicted nanoindentation by the current model. The experimental data were taken from [81]. 142

Fig. 8.1 SEM image of micro silicon die with the channel depth of 10 μm and width of (a) 3 μm, (b) 5 μm, (c) 10 μm and (d) 25 μm. 148

Fig. 8.2 Embossed topography of the UFG Al-1050 foil after two passes of ECAP, embossing force: 5 kN. (a) optical micrograph; (b) SEM image. 151

Fig. 8.3 The cross section of the embossed UFG Al-1050 foil, (a) two passes of ECAP, SEM image; (b) eight passes of ECAP, OM image. 152

Fig. 8.4 SEM SEI image showing the topography of a transition zone from the embossed area to unembossed area on the surface of the Al-1050 foil embossed by 5kN force. 152

Fig. 8.5 The optical microscopy topography of the Al-1050 foil embossed by (a) 8kN force, (b) 9kN force. 154

Fig. 8.6 The optical microscopy image for the uniform pattern on the surface of the Al-1050 foil embossed by 9kN force. 154

Fig. 8.7 Indentation mapping on the cross-section of embossed UFG Al-1050 foil 156

Fig. 8.8 Nanoindentation hardness distribution over the cross-section of the embossed UFG Al-1050 foil produced by two passes of ECAP. 156

Fig. 8.9 Microstructure on the cross-section of cold embossed UFG Al-1050 produced by two passes of ECAP, (a) FIB image, (b) OIM image by EBSD . 157

Fig. 8.10 300 ˚C embossed UFG Al-1050 produced by eight passes of ECAP, (a) Secondary electron SEM image of the top surface; (b) Secondary electron FIB image of the cross-section. 160

Fig. 8.11 Optical image of 300 ˚C embossed coarse-grained Al-1050 with the channel size of (a) 25 μm wide and (b) 5 μm wide. 161

Fig. 8.12 Schematic sketch of GND distribution underneath the embossed surface, *D* is the channel depth and *W* is channel width. 164

Fig. 8.13 Predicted embossing force against the embossing width 166

Fig. 8.14 Comparison of ISE in UFG Aluminium and CG Aluminium 167

Fig. 8.15 Predicted nanoindentation difference between edge and centre on the cross-section of the UFG Al-1050 at various indentation depths..... 169

Fig. 9.1 Effect of Mg contents on grain refinement and thermal conductivity of Al-Mg alloys after eight passes of ECAP. 172

Fig. 9.2 The principle of the DCAP process for use in continuous production [235] 174

Fig. 0.1 Drawing of a connector for connecting rigs to Instron..... 182

Fig. 0.2Drawing of a water chamber for cooling. 183

Fig. 0.3 Drawing of a shaft 184

Fig. 0.4 Drawing of a platen with holes for guiding rods, heat elements. 185

Fig. 0.5 Assembling drawing 186

Fig. 0.1 Data from the confocal laser system showing the topography of the micro silicon die with different channel size: (a) 5 μm deep, 10 μm wide, (b) 10 μm deep, 10 μm wide, (c) 15 μm deep, 10 μm wide, (d) 15 μm deep, 25 μm deep. 187

List of Tables

Table 2.1 Microstructure and properties of aluminium alloys after ECAP 50

Table 4.1 Composition of aluminium alloys used in this study 75

Table 4.2 Taicaan Xyris 4000 Confocal Laser System specifications 79

Table 5.1 The comparison of grain size, fraction of HAGBs and LAGBs and average misorientation of Al-1050 alloy processed by ECAP for different passes 84

Table 5.2 Main ideal slip system in simple shear 85

Table 6.1 Measured dislocation density for several Al alloys subjected to cold deformation (incl ECAP) and the total amount of dislocations generated per volume. 113

Table 6.2 Average free path of Al-1050, AlZr and AlZrSiFe alloys after various passes of ECAP 114

Table 6.3 Microhardness predictions of AlZr alloy after different passes of ECAP and values of parameters for microhardness calculation 115

Table 6.4 Microhardness predictions of AlZrSiFe alloy after different passes of ECAP and values of parameters for microhardness calculation 115

Table 6.5 Microhardness predictions of Al-1050 alloy after different passes of ECAP and values of parameters for microhardness calculation 116

Table 6.6 Strength predictions for the ECAP-processed billet and the heat treated billet. 118

Table 6.7 Hardness and yield strength of Al-1050 at various states of heat treatments [171] 120

Table 7.1 RMSE of nanoindentation hardness predictions by there models for two Alloys. 144

Table 8.1 Dimensions of channels measured by confocal laser system 149

Table 8.2 Predicted nanoindentation difference between edge and centre on the cross-section of the UFG Al-1050 at various indentation depths. 166

Declaration of Authorship

I, Xiaoguang Qiao

declare that the thesis entitled

Development of a Fabrication Process for a MEMS Component from Ultra Fine Grained Alloys

and the work presented in the thesis are both my own, and have been generated by me as the result of my own original research. I confirm that:

- this work was done wholly or mainly while in candidature for a research degree at this University;
- where any part of this thesis has previously been submitted for a degree or any other qualification at this University or any other institution, this has been clearly stated;
- where I have consulted the published work of others, this is always clearly attributed;
- where I have quoted from the work of others, the source is always given. With the exception of such quotations, this thesis is entirely my own work;
- I have acknowledged all main sources of help;
- where the thesis is based on work done by myself jointly with others, I have made clear exactly what was done by others and what I have contributed myself;
- parts of this work have been published as:

1. **X.G. Qiao**, M.J. Starink and N. Gao, The influence of indenter tip rounding and multiple strengthening mechanisms on the indentation size effect, *Acta Mater,* 58 (2010) 3690-3700.
2. **X.G. Qiao**, N. Gao, Z. Moktadir, M. Kraft and M. J. Starink, Fabrication of MEMS components using ultra fine grained aluminium alloys, *J. Micromech. Microeng.* 20(2010) 045029.
3. M.J. Starink, **X.G. Qiao**, J. Zhang, and N. Gao, Predicting grain refinement by cold severe plastic deformation in alloys using volume averaged dislocation generation, *Acta Mater*. 57, (2009), 5796-5811.

4. **X.G. Qiao**, M.J. Starink and N. Gao, Hardness inhomogeneity and local strengthening mechanisms of an Al1050 aluminium alloy after one pass of equal channel angular pressing, *Mater. Sci. Eng. A* 513–514 (2009) 52–58.
5. S.C. Wang, M.J. Starink, N. Gao, **X.G. Qiao**, C. Xu, T.G. Langdon, Texture evolution by shear on two planes during ECAP of a high-strength aluminium alloy, *Acta Mater*.56, (2008) 3800-3809.
6. M.J. Starink, S.C. Wang, **X.G. Qiao**, N. Gao, H.J. Roven, T. G. Langdon, Shear deformation and texture evolution in Al alloys processed for one pass by ECAP, *Mater. Sci. Forum* 584-586, (2008) 679-684.
7. **X.G. Qiao**, N. Gao, Z. Moktadir, M. Kraft and M. J. Starink, Development of a fabrication process for micro channels from ultrafine grained aluminium alloy, The 12 International Conference on Aluminium Alloys (ICAA-12), 5-9 Sep. 2010, Yokohama, Japan, Submitted
8. M.J. Starink, **X.G. Qiao** and N. Gao, A predictive model for grain refinement by cold severe plastic deformation, 2nd international symposium on Bulk Nanostructure materials, Ufa, Russia (BNM-2009), 22-26 Sep, 2009.

Signed: …… ……..

Date:……10/02/2010…….

Acknowledgements

This work would not have been possible without the guidance of my supervisors, Dr Nong Gao and Prof. Marco Starink. It was an honour to be your student. I am most appreciative of your stimulation and encouragement. I am very grateful to Prof Terence Langdon for valuable discussions and help on ECAP. I thank also Prof. Michael Kraft and Dr Zakaria Moktadir for DRIE fabrications.

I am most appreciative of Prof. S.M. Spearing and Dr. Liudi Jiang for valuable discussions on this project. Foremost, I acknowledge Dr Shuncai Wang for stimulating conversations and training on electropolishing, SEM, EBSD and TEM. I especially thank Prof. John McBride for confocal laser system testing and Prof. Hans Roven (Norwegian University of Science & Technology) for providing AlZr and AlZrSiFe alloys. Dr. Dan Sun and Dr. Jurgita Zekonyte are gratefully acknowledged for training and assisting on nanoindentation. Dr. Georgi Lalev (University of Cardiff) is gratefully acknowledged for FIB work. I especially thank Dr. Jing Cao (School of Civil Engineering), Dr Wenjing Wang (Ship Science) and Alex Dickinson for training on hydropress and Instron press.

I especially thank Dave Beckett, Robert Barnes, Erik Roszkowiak, Steve Pilcher Chris Willims and Clive Stafford for sample cutting, machining and rig establishment. I thank also support of Gwyneth Skiller. I am very grateful to all colleagues in Bioengineering, Engineering Materials and Surface Engineering Groups for informal discussion and comments in seminars.

This work was partly funded by the Engineering Physics Science Research Council under Grant No. EP/D00313X/1. The FIB work was funded under grant No. EP/F056745/1. I also thank studentship from ORSAS and School of Engineering Sciences of University of Southampton.

This thesis is dedicated to my wife, Jia, my parents and sisters. It would not have been possible without their love and support.

Definitions and Abbreviations

AFM	atomic force microscope
ARB	accumulative roll bonding
CEC	cyclic extrusion and compression
CMSG	mechanism-based stain gradient plasticity
CND	chemically necessary dislocation
CRSS	critical resolved shear stress
DCAP	dissimilar channel angular pressing
DRIE	deep reactive ion etching
EBSD	electron backscattered diffraction
ECAP	equal-channel angular pressing
ECAR	equal channel angular rolling
EDM	electrical discharge machining
FCC	face-centred cubic
FE	finite element
FIB	Focussed ion beam
GND	geometrically necessary dislocations
HAGB	high angle grain boundary
HPT	high pressure torsion
ISE	indentation size effect
KME	Kocks-Mecking-Estrin
LAGB	low angle grain boundary
LIGA	lithography electroforming and moulding (German acronym: Lithographie Galvanoformung Abformung)
MDF	multi-directional forging
MEMS	microelectro mechanical systems
MSP	main shear plane
OIM	orientation imaging microscopy
OM	optical microscopy
PMMA	polymethylmethacrylate
RCS	repetitive corrugation and straightening
RIE	reactive ion etching

RMSE	root mean square error
SEM	scanning electron microscopy
SPD	severe plastic deformation
SSD	statistically stored dislocation
SSP	secondary shear plane
TE	twist extrusion
TEM	transmission electron microscopy
UFG	ultra-fine grained
VLSI	very-large-scale integrated
A	Dimensionless constant
a_c	Radius of the contact area
A_c	Contact area
A_E	Embossed area
a_{pz}	Radius of the plastic zone
B_i	Constant
C	Ratio of yield strength and hardness
C_1	Constant
C_2	Constant
d	Grain size
D	Channel depth
D_{gb}	Coefficient for grain boundary diffusion
f	Ratio of radius of the plastic zone and radius of the contact area
F	Embossing load
f_p	Volume fraction of particles
f_{sub}	Fraction of LAGB
G	Shear modulus
h	Indentation depth
h^*	Constant
h_2	height of the spherical cap
h_b	Blunting distance
h_c	Contact depth
H	Indentation hardness
H_0	Constant

H_y	Hardness contribution by the intrinsic stress
Hn	Nanoindentation hardness
Hv	Vickers hardness
HV_{cal}	Vickers hardness calculated using the model
HV_{exp}	Measured Vickers' hardness
H_n^E	Nanoindentation hardness
k	Boltzmann's constant
K	Thermal conductivity
K_A	Constant
l_{ch}	Mean free path caused by dissolved elements
l_D	Mean free path caused by forest dislocations
l_{gb}	Mean free path caused by cell walls/grain boundaries
l_p	Mean free path caused by hard, non shearable particles
$\overline{l}$	Mean free path
$\overline{L}$	Mean lineal intercept length
M	Taylor factor
N	Pass number of ECAP
N_{GND}	Number of GNDs
R	Tip radius
R_E	Diameter of the embossed sample
r_0	Radius of the bottom surface of the spherical cap
r_p	Mean radius of particles
$\overline{r}$	Nye factor
S	Contact area
S_v	Boundary area per unit volume
T	Absolute temperature
W	Channel width
x_i	Concentrations of dissolved alloying elements i
α_1	Constant
α_2	Constant
β	Constant
δ	Subgrain size
ε_N	Accumulated shear strain after N passes of ECAP

ε_p	Plastic strain
$\dot{\varepsilon}_{sp}$	Steady state strain rate
η	Strain gradient
θ	Misorientation angle between cells/grains
θ_0	Angle of conical indent surface to the sample planar surface
$\bar{\theta}$	Average misorientation angle between cells/grains
λ	Ratio of subgrain boundary strengthening contribution to grain boundary strengthening contribution
λ^{E}	Electrical conductivity
$\lambda(h)$	Total length of GND
$\lambda_1(h_1)$	Length of GND underneath the conical frustum
$\lambda_2(h_2)$	Length of GND underneath the spherical cap
ρ	Dislocation density
ρ_1	Dislocation density in the unrecrystallized grains
ρ_2	Dislocation density in the recrystallized grains
ρ_{GB}	Dislocation density at cell walls/grain boundaries
ρ_{GND}	Dislocation density of GND
$\rho_{\mathrm{GND}}^{\mathrm{E}}$	GND density underneath the embossed surface
$\rho^{N-G}{}_{GNB}$	Average density of GNDs predicted by the Nix-Gao model
$\rho^{Huang}{}_{GND}$	Average density of GNDs predicted by the Huang et al model
ρ_{SSD}	Density of SSD
σ_0	Intrinsic strength
σ_{y}	Yield strength
$\Delta\sigma$	Increase in strength due to dislocation density
$\Delta\sigma_{\mathrm{gb}}$	Strengthening due to the presence of grain or subgrain boundaries
τ_{d}	Strengthening by dislocations inside the grains
τ_{tot}	Total critical resolved shear stress
Ψ	Outer angle
Φ	Inner angle

1 Introduction

Equal channel angular pressing (ECAP) is the most well known processing method among the group of severe plastic deformation (SPD) methods [1], and is different from the common deformation methods such as extrusion, rolling and forging. ECAP can be performed on a single specimen repeatedly because the specimen's cross section shape does not change after ECAP processing. In the ECAP process, conventional microstructures materials are changed to nanostructured ones [2]. Materials with submicron- or nano-scaled grains produced by ECAP processing are low cost, low porosity, low oxide content and safe compared with the counterparts by gas condensation and mechanical alloying [1,3]. The feasibility of ECAP has already been demonstrated at the lab scale, but so far its industrial application is still under consideration. A promising, but as yet unexplored application is for microelectromechanical systems (MEMS), which are batch fabricated miniature systems with both electrical and non-electrical (e.g. mechanical) functionalities [4]. These micromachines provide the advantages of small size and high-functionality to integrated microelectromechanical systems. MEMS technology captured the imagination of the world in the 1980s with the first demonstration of a functioning silicon motor that had been manufactured entirely with standard integrated circuit (IC) manufacturing techniques [5]. The past decade has seen a rapid growth of microelectromechanical systems (MEMS) as an important area of technology, growth that is expected to continue well into this century [6]. The success of MEMS offers the opportunity to exploit materials which are too small to be available for large scale devices as well as taking advantage of scale dependent properties, particularly yield and fracture strength [7].

Nano-structured aluminium is attractive for MEMS as it can offer improved mechanical properties compared to competing materials (Si, SiO_2, Si_3N_4, Ni) combined with greatly superior electrical and thermal conductivity. In addition, the use of the proposed SPD processing coupled with sub-micron dimensional tolerances has the potential for low cost mass production. Another attractive advantage of making MEMS components by using ECAP processed materials is that only small volumes of materials are required.

Micro heat exchangers are important components of a range of MEMS devices. Micro heat exchangers were first investigated to apply to very-large-scale integrated (VLSI) circuits in 1981 [8] because the advent of systems employing high-speed, high-density VLSI circuits implies the requirement for effective and compact heat removal. Actually, micro heat exchangers can be applied in many important fields [9]: micro-electronics, aviation and aerospace, medical treatment, biological engineering, materials sciences, cooling of high temperature superconductors, thermal control of film deposition, cooling of powerful laser mirrors and other applications where lightweight, small heat-exchangers are required.

This project is aimed at the design and fabrication of components with microchannels by embossing using ultra-fine grained (UFG) aluminium alloys produced by ECAP, which may be applied in MEMS devices, for instance, micro heat exchanger. The work is multifaceted, involving several stages of process design, equipment design, materials processing, evaluation and materials testing. Several elements of the work involved were untried and untested methodologies, introducing elements of trial and error in the work. To improve understanding of the process, several new models were developed and some existing models were modified. A starting point in the work was the design, construction and commissioning of a cost-effective lab-scale ECAP facility for the production of ultra-fine grain materials. A series of micro silicon dies for MEMS components embossing has been designed and created by deep reactive ion etching (DRIE). An instrumented embossing rig, together with electron microscopy and mechanics modelling of the process has been investigated to understand the microstructures and properties of the UFG alloys and the MEMS components produced from it.

The structure of this thesis is as follows. Following this introduction, Chapter 2 contains a literature review which summarises the relevant work reported by various investigators regarding Al alloys, micro fabrication technologies, SPD processing and properties of UFG materials. The work on design of equipment is described in Chapter 3. In Chapter 4, the materials and analysis methods involved in the current work are described. Microstructure of the UFG Al alloys processed by ECAP and a model on grain refinement are presented and discussed in Chapter 5. In Chapter 6, microhardness of UFG Al alloys after different passes of ECAP and a model on

strength/microhardness of UFG Al alloys are reported. Nanoindentation analysis of UFG Al alloys and a modified model on indentation size effect were presented in Chapter 7. The embossing of UFG Al alloys at both room temperature and high temperature is described in Chapter 8. Topographies, microstructure and nanoindentation hardness of embossed Al alloys and the embossing process optimization are also analyzed in this chapter. Furthermore, Chapter 8 develops a model employing concept of geometrically necessary dislocations to interpret the embossing force and nanoindentation hardness distribution on the cross section of embossed Al alloys. Chapter 9 discusses the material and processing issues as well as the potential of mass production of MEMS components using UFG Al via embossing process. Conclusions are drawn in Chapter 10. Chapter 11 presents the future work.

2 Literature Review

This literature review contains four sections. Section 2.1 introduces the classification of aluminium alloys. Section 2.2 presents the microstructure and properties of Al-Zr alloys which are planned to be used in manufacture of MEMS components. Section 2.3 describes developments, application and several microfabrication technologies of MEMS. Among those microfabrication technologies, deep reactive ion etching (DRIE) and embossing have been used in the present project. Section 2.4 contains an overview of the classification, materials and forming methodologies for micro heat exchangers which are the objective of MEMS components in this project. Section 2.5 describes several major severe plastic deformation (SPD) techniques. Section 2.6 introduces the principle of ECAP and applications of ECAP for aluminium alloys.

2.1 Introduction of aluminium alloys

Aluminium and it alloys have been extensively used as structural material and functional material in many fields such as building, automobile, aircraft, electrical engineering and packaging due to their unique properties. These advantageous properties are low density, high thermal conductivity, high electrical conductivity, suitability for surface treatments, corrosion resistance, diversity of aluminium alloys and semi-products, specific strength, functional advantages of extruded and cast semi-products, weldability, easy formability and ease of recycling. Several of these, and other, properties are influenced by alloying.

Aluminium alloys can be classified to casting alloys and wrought alloys. The major alloy systems of casting alloys include Al-Cu alloys, Al-Mg alloys, Al-Si alloys and Al-Zn alloys [10]. Most of the casting alloys produced are consumed in the automotive industry for engine components. These cast alloys are mostly Al-Si based alloys and most of which also contain at least 3% copper. Apart from the automotive industry, the cast alloys are also extensively used in mechanical construction, electrical engineering, transport, household electrical appliances and ironmongery. Due to a long history of widespread use of casting alloys, four groups of casting techniques have been developed and each of which can be further divided into

several subgroups. In sand casting, alloys are cast by gravity in a sand mould. It is a basic casting technique and can easily achieve a large cast part. Investment casting and permanent mould casting use a ceramic mould and a permanent metal mould, respectively. Both techniques are realized by gravity. Pressure die-casting also uses a permanent metal mould but uses a pressure. The advantage of the last technique is that it leads to a compact cast component.

Aluminium wrought alloys can be further split into two subcategories: heat treatable and non-heat treatable alloys [11]. Non-heat treatable alloys include all the pure aluminium in various grades and all other alloys that are strengthened largely by solid solution hardening and by strain hardening from the annealed temper. The variety of properties of the non-heat treatable alloys results from elements that are present as major impurities for some alloys. For other alloys, the elements are additions. Such elements include chromium, iron, magnesium, manganese, silicon, and zinc. In addition, minor amounts of other elements such as copper may be added. Apart from strengthening, strain hardening also involves a modification of the microstructure and the texture due to plastic deformation. It occurs not only during the manufacturing of semi-products in the course of rolling, extruding, drawing, etc., but also during subsequent manufacturing steps such as forming, bending or fabricating operations. The non-heat treatable alloys are primarily in the 1XXX (pure aluminium), 3XXX (Al-Mn-(Mg)), 4XXX (Al-Si), 5XXX (Al-Mg) series.

Heat treatable alloys include the wrought aluminium alloys that contain one or more of the elements copper, magnesium, silicon, and zinc. The alloying elements dissolve in considerable amounts in aluminium at elevated temperatures but dissolve in a much smaller degree at room temperature. This characteristic makes it possible strengthen these alloys through heat treatments. To achieve a maximum mechanical property, these alloys can be processed through three steps [10]. Firstly, solution heat treatment, in which the alloys are heated to a high temperature in order to put into solution the alloying element contained in the aluminium. Secondly, quenching, in which the alloys are rapidly cooled to room temperature. It is usually achieved by immersion in water at room temperature. The effect of this quenching heat treatment is to keep the alloying elements and additives in a supersaturated solid solution within the aluminium matrix. Finally, ageing, which includes natural ageing and

artificial ageing. Ageing at room temperature, i.e. around 20˚C is called natural ageing, while ageing at elevated temperature, between 100 and 200˚C is called artificial ageing. Ageing heat treatment leads to the formation of hardening precipitates from the supersaturated solid solution. The nature, size and volume fractions of these hardening precipitates, which can be controlled by ageing temperature and time, determine the level of mechanical properties. The heat treatable alloys generally are found in the 2XXX (Al-Cu-(Mg)), 6XXX (Al-Mg-Si), and 7XXX (Al-Zn-(Mg)) series, although a few such alloys occur in the 4XXX (Al-Si) and 5XXX (Al-Mg) series [11]. Manganese, chromium, or zirconium may be added to retard or prevent recrystallization during heat treatments.

2.2 Al-Zr alloys

Pure or near-pure aluminium has good ductility, high electrical conductivity, high thermal conductivity but poor thermal stability of deformed or fine grained structures which is very important when it is used to components fabricated by superplastic forming. Addition of alloy elements such as Ti, V, Cr and Mn to aluminium can improve the thermal stability but reduce the thermal conductivity. However, Zr addition can improve thermal stability with a minimal loss of thermal and electrical conductivity. This is discussed in detail as follows.

2.2.1 Microstructure of Al-Zr alloys

Small additions of zirconium are employed as a grain refiner in several aluminium alloys [12]. As shown in the Al-Zr alloys phase equilibrium diagram (Fig. 2.1), a peritectic reaction, Liquid + Al_3Zr → Al (solid solution), takes place at 660.5˚C, 0.28 percent Zr. It is believed that the peritectic reaction is responsible for the grain refining because Al_3Zr, solidifying at high temperature, acts as a crystallization nucleus and an inhibitor for grain growth.

Small additions of Zr have the potential promise to improve the properties of wrought high strength Al alloys by forming metastable, coherent Al_3Zr dispersoids. Apart from precipitation strengthening, the Al_3Zr phase can also inhibit recrystallization of the deformed aluminium alloys at high temperature, so that the improved strength can be maintained to the relative higher temperature. The coherent

metastable Al_3Zr phase has a structure of cubic $L1_2$ (Fig.2-2 (a)) which has a very low lattice mismatch to Al-matrix (about 0.7% [13]). Although the $L1_2$ Al_3Zr is a metastable phase, the transformation of $L1_2$ Al_3Zr particles is so slow that they can be effectively stable for realistic processing times at the recrystallization temperature. The reason for this stability may be twofold: one is the low diffusivity of zirconium in Al [14] which slows down the diffusion controlled coarsening; the other is low driving force for coarsening which is due to the low interfacial energy of the cubic $L1_2$ phase with Al matrix.

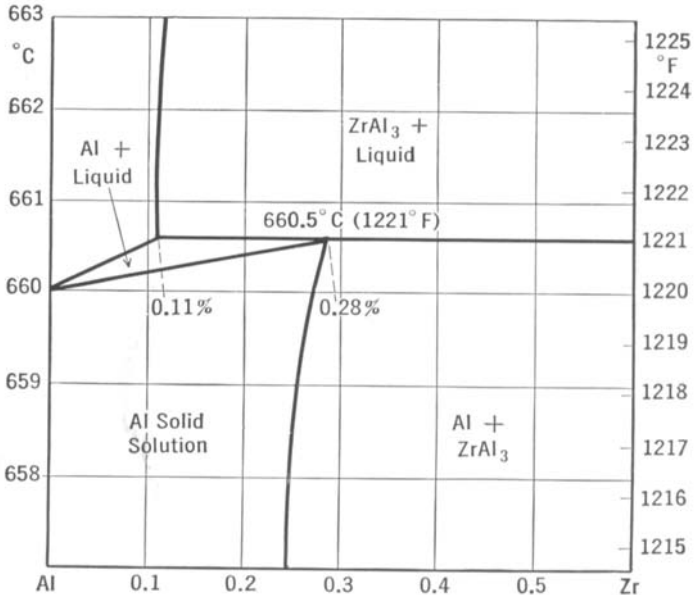

Fig. 2.1 Al-Zr alloys equilibrium phase diagram [12]

Zirconium can also be added to aluminium alloys to improve the superplasticity by forming the metastable $L1_2$ Al_3Zr particles. It is generally accepted that the main mechanism of superplasticity is grain boundary sliding and rotation on the condition of small grain size and high angle grain boundary. The superplasticity of aluminium alloys can normally only be achieved at high temperature (>350˚C). However, the fine-grained structure is generally not stable at the superplastic deformation temperature and must be stabilized by stable, fine and dispersed second phase particles. The metastable $L1_2$ Al_3Zr phase particles can inhibit the grain growing at superplastic temperature. As shown in Fig. 2.1, the solid solubility limit of Zr in aluminium is very low with a weak temperature dependence, which makes metastable $L1_2$ Al_3Zr phase easy to precipitate out from the supersaturation. In

addition, as described before, the prospective coarsening of the metastable Al_3Zr particles which is believed to be diffusion controlled at the temperatures of superplastic deformation is very slow as the diffusion rate of Zr in Al is the slowest one among all of transition metals [14] and the lattice mismatch between the metastable Al_3Zr phase and the Al matrix is very low [13].

The metastable $L1_2$ Al_3Zr precipitates are essential to improve the microstructure and properties of the Zr-contained aluminium alloys. The effectiveness of the metastable $L1_2$ Al_3Zr precipitates will depend on its size, spacing and distribution. The metastable $L1_2$ Al_3Zr particles are normally achieved by being precipitated from a supersaturated solid solution during post solidification ageing or homogenization annealing.

The sequence of reactions during casting of Al-Zr can be derived from the phase diagram (Fig. 2.1). During conventional casting of dilute Al-Zr alloys, which is close to equilibrium solidification, the Zr-rich properitectic, or primary Al_3Zr phase, is the first solid to form. The Zr composition in the remaining liquid is lower than the solubility in solid solution. During the peritectic reaction, the Zr atoms would need to diffuse from the primary phase to the Al-rich liquid, but as this diffusion is relatively slow, the Zr composition in the Al solid solution will be lower than the equilibrium composition. In this case, the potential for the precipitating the $L1_2$ Al_3Zr phase is limited because the supersaturation is significantly reduced.

In the 1960s, rapid solidification of Al-Zr alloys attracted attention [15] because the solid solubility limit of Zirconium in Al (0.28wt% at 660˚C for equilibrium solidification) can be extended up to 4.9wt% [16] and the precipitation of tetragonal DO_{23} Al_3Zr equilibrium phase can be avoided. A very fine and stable dispersion of particles will be precipitated out from a supersaturated solid solution obtained after rapid solidification by annealing at 500˚C [17]. The particles are identified by TEM analysis as a coherent metastable Al_3Zr phase with a structure of cubic $L1_2$ (Fig. 2.2 (a)) which has a very low lattice mismatch to Al-matrix (about 0.7% [13]). According to Ryum [17], the metastable Al_3Zr appears in a lengthened fanshaped arrangement. The rod-shaped particles form the arms of the fan and spherical particles are distributed between the arms.

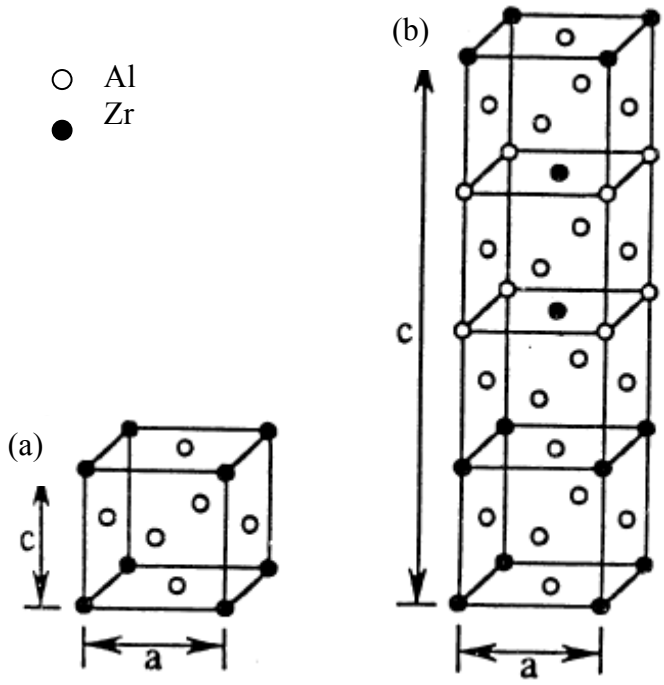

Fig. 2.2 The unit cell of Al_3Zr, (a) cubic, $L1_2$, (b) tetragonal, DO_{23} [18]

A coarse plate-like equilibrium tetragonal DO_{23} Al_3Zr phase appears when the annealing temperature is elevated. The structure of tetragonal DO_{23} Al_3Zr is shown as Fig. 2.2 (b). The lattice mismatch to Al-matrix is about 2.9% [19], which is a little bigger than that of cubic $L1_2$ Al_3Zr. The DO_{23} Al_3Zr phase obtained after rapid solidification by annealing is different to the primary DO_{23} Al_3Zr formed in equilibrium solidification, which is coarse and is detrimental to the mechanical properties.

Al-Zr alloys were also studied to be used as creep resistant alloys at temperatures exceeding 400˚C [20,21,22]. Rapid solidification processing followed by ageing is a good method to make fine grained Al-Zr alloys with metastable $L1_2$ Al_3Zr precipitation but the refined grain size is undesirable for creep resistant applications. Knipling et al. [20] developed a series of castable and heat-treatable precipitation-strengthened Al-Zr-(Ti) alloys exhibiting grain coarsening (with a grain size increasing up to 1 mm) and creep resistance at temperatures exceeding 400°C by conventional casting followed by ageing. Those Al-Zr alloys exhibited a coarse grain size suitable for creep resistant applications at high temperature. The primary

precipitation of Al_3Zr did not occur during the casting due to the dilute Zirconium composition in combination with controlled cooling rate. After ageing at 425°C for 25 hours, the Al-Zr alloys achieved peak strength due to precipitation of dispersed small coherent metastable $L1_2$ Al_3Zr particles.

Another application of Al-Zr alloys is to transport electrical energy because of their low density and good electrical conductivity. In addition, Al-Zr alloys have enhanced strength and creep resistance but nearly the same high electrical conductivity as the pure aluminium, which is attributed to the small addition of zirconium. As shown in the phase diagram (Fig. 2.1), the largest solubility of zirconium in aluminium is 0.28% at 660 °C. When temperature is decreased to 500°C, the solubility of zirconium is only 0.05% so that the Zr can precipitate as metastable Al_3Zr particles during post solidification ageing. Compared with Zr dissolved in aluminium solid solutions, Zr atoms in Al_3Zr phases are much less detrimental to the electrical conductivity. Furthermore, controlling the particle size, shape and distribution by adjusting the ageing temperature and time will increase the strength and creep resistance of Al-Zr alloys. Some studies on ageing and creep of Al-Zr alloys with the aims to electrical transmission application have been reported [23].

2.2.2 Property of Al-Zr alloys

High amounts of Zr can be dissolved in the Al-rich phase after rapid solidification, and precipitate in form of fine metastable $L1_2$ Al_3Zr particles during subsequent processing operations, such as hot rolling and solution heat treatment. These fine dispersoids will not only improve the mechanical properties at room temperature, but control the evolution of grain and subgrain structure, increase the microstructure stability and raise the recrystallization temperature.

Sahin et al. [24] studied the effect of addition of zirconium and isochronal ageing on the microhardness of Al-Zr alloys. The results are shown in Fig. 2.3. In as-quenched and peak aged condition the hardness is increased with increase of Zr-content (Fig. 2.3 (a)). The temperature to reach peak hardness is decreased with the increasing Zr-content (Fig. 2.3 (b)).

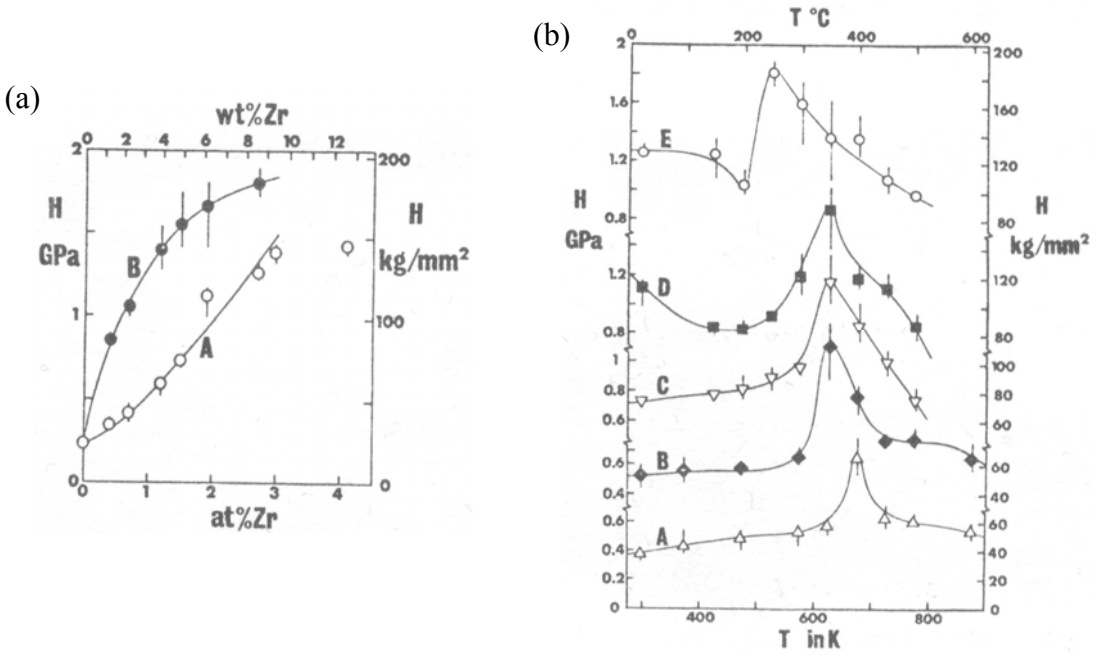

Fig. 2.3 Microhardness as function of (a) Zr-content in the as-quenched (A) and peak aged (B) conditions and (b) of temperature T during isochronal (1h) ageing for Al-2.3, 3.9, 4.9, 6.2 and 8.6wt% Zr (A to E respectively) [24]

Katsas et al. [25] studied dynamic recrystallization and superplasticity in Al-1wt%Zr alloys fabricated by impulse atomization (IA) (a rapid solidification technique). The superplastic performance of the Al-1wt%Zr was rather poor (<100%) both in the as-extruded and extruded and aged condition for a range of temperature (550-600˚C) and strain rates (10^{-2} to 10^{-1} s^{-1}) because no grain refinement mechanisms were activated. In the as-rolled condition and extruded, aged and rolled condition, the performances of the Al-1wt%Zr alloy were significantly better, which is shown in Fig. 2.4. In the latter condition, the ductility reached a maximum of 475% at the strain rates of 10^{-1} s^{-1}.

Compared with microstructure and mechanical properties of Al-Zr alloys, there have been very few studies on the physical properties. Effects of deformation on electric conductivity in Al-Zr alloys were studied with the aims to application in power line [26]. As a conductor material for power line, especially for large power and long distance electrical transmission, Al-Zr alloys are heat resistant due to the low diffusivity of Zr in the Al-rich phase. Furthermore, small additions of Zr to Al can

increase the strength and creep resistance, but has little impact on the electrical conductivity because of the low solubility of Zr in the Al-rich phase.

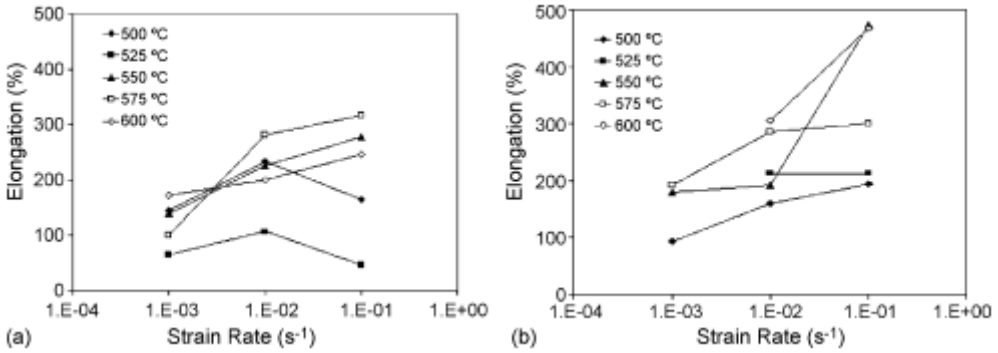

Fig. 2.4 Variation of elongation with initial strain rate for: (a) as-rolled and (b) post-extrusion aged and subsequently rolled conditions [25]

It is well known that metallic additions to aluminium reduce its electrical conductivity. Metals in solid solution depress the conductivity to a greater extent than when out of solution. The average increase in resistivity per 1wt% zirconium element in solution and out of solution is 1.74μΩ·cm and 0.044μΩ·cm respectively [11]. For example, if the alloy contains 1.0wt% zirconium and the maximum amount of it (0.28wt% at 660˚C) is in solid solution, the increase in resistivity of high-purity aluminium (2.65μΩ·cm at 20 ˚C) is 0.28×1.74+0.72×0.044=0.512μΩ·cm. Therefore effect of the zirconium on the electrical conductivity of aluminium is very low.

Although no research about thermal conductivity of Al-Zr alloy has been reported, Al-Zr alloys are expected to have a good thermal conductivity because the mechanisms of thermal conductivity and electrical conductivity in metals are similar, both being mainly due to movement of free (conduction) electrons. Generally, alloys with good electrical conductive properties will also have a good thermal conductivity because all the factors that are favourable for electrical conductivity such as low solid solubility, small residual stress and texture, will also favour the thermal conductivity.

The thermal conductivity of aluminium alloys can be estimated from electrical conductivity using the relationship between thermal and electrical conductivities for

annealed aluminium alloys between 0 and 400˚C. This relationship is expressed by the Eq. 2.1:

$$K = 5.02\lambda^{E}T \times 10^{-9} + 0.03 \qquad \text{Eq. 2.1}$$

where K is thermal conductivity, λ^{E} the electrical conductivity, and T the absolute temperature [11].

2.3 MEMS technologies

Microelectromechanical systems (MEMS) refer to devices that have characteristic length of less than 1 mm but more than 1 μm, that combine electrical and mechanical components [27]. The acronym MEMS originated in the United States and originally applied exclusively to silicon based mechanical applications. The MEMS field was dominated by mechanical applications in the early stage; MEMS in present days refers to all subminiaturized systems including silicon based mechanical devices, chemical and biological sensors and actuators, and miniature non-silicon structure (e.g., devices made from plastics or ceramics) [28].

2.3.1 Developments of MEMS technology

MEMS technology development has been driven by commercialization and miniaturization and is developing with the microelectronic and micromechanical revolution. The development of MEMS technology used to a large extent the materials and fabrication methods developed for microelectronics [29].

MEMS technology started with machine and machining development through the advent of microelectronics. The investigation of the piezoresistive properties of the semiconductor materials used to develop the transistor in the 1950s [30] linked the electronic materials with mechanical sensing together. This link was exploited early in the time of MEMS development to produce strain gages and pressure sensors. The technical advances in the planar silicon transistor [31] and fabrication process (lithography, etching, diffusion, and implantation) [32] provided a path that enabled the integration of large numbers of transistors to create many different electronic devices and a continual reduction in size of the transistor. This development of fabrication tools enables MEMS technology for increasingly smaller dimensions.

Nathanson et al. [33] developed the resonant gate transistor, which showed the possibilities of an integrated mechanical–electrical device and silicon micromachining. In 1982, Petersen [34] wrote a seminal paper, "Silicon as a Mechanical Material." Thus, silicon was considered and utilized to an even greater extent to produce sensors that needed a mechanical element and a transduction mechanism (mechanical–electrical) to produce a sensor. Development of bulk micromachining, surface micromachining and LIGA (Lithographie Galvanoformung Abformung) process enabled to produce complex mechanical elements of MEMS [29] using silicon, metals and ceramics as structural material and polymers as sacrificial material.

2.3.2 Applications of MEMS

There are numerous possible applications for MEMS. As a recently developed and continuously innovating technology, many new MEMS applications are emerging, expanding beyond that is currently identified or known. Several typical applications will be introduced in following subsections.

2.3.2.1 Communications

The performance of high frequency circuits will significantly improve compared to integrated components if electrical components such as inductors and tunable capacitors are made using MEMS. In the meanwhile, the total circuit area, power consumption and cost will be decreased [35]. Moreover, RF (radio frequency)-MEMS devices can also be applied in microswitches to reduce the number of components. They can also be applied in integrated voltage-controlled oscillators (VCOs) in global positioning systems (GPSs) [36].

2.3.2.2 Automobile

MEMS technology can be applied in an automobile in many locations such as pressure sensors, gyroscopes, accelerometers used for air bag deployment, the oil condition sensor and the wheel speed sensor. The automotive market is a mass market in which MEMS is playing an ever increasing role. For example, MEMS accelerometers tend to replace conventional accelerometers for crash air-bag deployment systems in automobiles because the conventional counterparts are too large and contain many discrete components mounted in the front of the car with

separate electronics near the air-bag. However, MEMS accelerometers are integrated, which are much smaller, more functional, lighter and more reliable [29].

2.3.2.3 Biotechnology

Another mass market in which MEMS has an increasing impact is the biological medical market. Using MEMS technology, a number of biological or medical devices have been developed such as the Polymerase Chain Reaction (PCR) microsystems for DNA amplification and identification, Scanning Tunnelling Microscopes (STMs), biochips for detection of hazardous chemical and biological agents, and microsystems for high-throughput drug screening and selection [35].

2.3.3 Microfabrication technologies

Microfabrication technologies originate from the microelectronics industry. Initially, the devices were usually made on silicon wafers. Later, the substrates were extended to glass, plastics and many other materials.

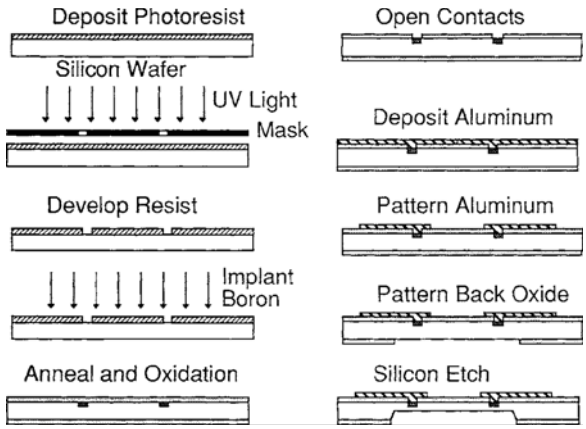

Fig. 2.5 A wet bulk micromachining process [27].

Microfabrication involves a group of technologies which are used to make microdevices. During microfabrication, many processes must be performed alternately and repeatedly. For instance, during fabrication of meomery chips around 30 lithography steps, 10 oxidation steps, 20 etching steps and 10 doping steps are involved. Typical microfabrication processes include: micromachining, photolithography, etching, thin film deposition, thermal oxidation, doping or ion implantation, wire bonding, chemical-mechanical planarization (CMP) and wafer

cleaning. A typical structure fashioned in a bulk micro machining process is shown in Fig. 2.5 [27].

The idea of microfabrication has been expended to precision machining especially in the field of MEMS because traditional machining techniques such as electro-discharge machining, spark erosion machining, precision milling, diamond machining and laser drilling have been scaled from the millimeter size range to micrometer range. And the materials are not limited to silicon: both metallic materials and ceramic can be micro machined to MEMS components.

Several typical microfabrication technologies relevant to the present project will be introduced in the following sections.

2.3.3.1 Anisotropic wet etching

Anisotropic wet etching was the first process that successfully realized mass fabrication of micromechanical components through etching single crystal silicon. Etch velocities in different crystalline directions are significantly different for a number of etchants. For example, the etch rate of Si using KOH as an etchant in (100) direction at 85˚C is 1.4μm/min and is 400 times higher than that in (111) direction [27]. The anisotropic wet etching relies on this etch velocity difference to achieve desirable structure on single crystal silicon. Therefore, anisotropic etching results in geometric shapes bounded by perfectly defined crystallographic planes.

The etch rate in anisotropic etching is related to the rate of reactants transporting to the sample surface, reaction rate and the rate of reaction product transporting away from the sample surface. Generally, the etch rate is controlled by reaction rate and thus temperature dependent. The etch rate in all crystal directions increases with increasing temperature while the surface roughness decreases with increasing temperature, so etching at the higher temperatures provides the best results. In practice, etch temperatures are usually set as 80 to 85°C to avoid solvent evaporation and temperature gradients in the solution [37].

A large range of etchants are available for anisotropic etching of silicon, such as alkaline aqueous solutions of KOH, NaOH, LiOH, CsOH, NH_4OH, and quaternary ammonium hydroxides in which alcohol is possibly added. Alkaline organics are

employed as well such as ethylene diamine, choline or hydrazine with additives such as pyrocathechol and pyrazine. The most popular used are KOH and ethylene diamine/ pyrocathechol +water (EDP) [38].

Automation of anisotropic wet etching makes this technology attractive for many components with small/micro features. By means of batch processing, many structures are achievable in parallel on one wafer. A number of simple geometric structures such as grooves, channels, filters, cantilevers or membranes, can be realized by means of patterned etch stop layers. An example for this is that micro channels etched on a wafer were employed for a number of micro heat exchangers [8]. A drawback is that the anisotropic wet etching can only be performed on a single crystal material on a specific crystal direction, taking also into account the limited ratio of etching depth/width achievable.

2.3.3.2 Dry etching

Isotropic wet etching provides a reliable process with a high etch selectivity for the semiconductor industry if the smallest structures are larger than 6μm. With the increasing packing density and wafer sizes, the conventional wet etching techniques were not reliable enough especially for the applications in fabricating a component with a microfeature in a large aspect ratio. This was true especially in the critical processing needed for making components of poly-crystalline silicon and the silicon nitride oxidation [39].

Dry etching refers to the process using plasmas or ions to etch the target surface to achieve a desired feature. As a result, application of dry etching is not limited to single crystal silicon. Plasma etching in barrel reactors offered better process control, which has originally been developed to replace the inadequate wet etching techniques [40]. However, the plasma etching was still isotropic and the smallest structure sizes achieved was larger than 1μm in the first stage. To pursue a further miniaturization of components with smoother surface and more accurate size, Anisotropic dry etching was developed, which is so called reactive ion etching (RIE) [39]. RIE in low-pressure plasmas resolved the above problems by using the characteristic of the positive ions towards the substrate on the powered electrode. A high degree of anisotropy is obtained due to ion-induced etching perpendicular to the substrate. As a result, a smooth sidewall can be achieved. In addition, the feature size

is also highly accurate because the etch rate can be accurately controlled. Compared with wet chemical etching, a number of advantages can be observed such as reduced environmental impact, fewer geometrical restrictions concerning the microstructures, to a further improved structural resolution and an extension of material choice [37].

Using fluorinated and chlorinated gases, anisotropic RIE processes have been developed for a wide range of materials [41]. Typical materials are silicon, aluminium, tungsten, molybdenum, silicon nitride, silicon oxide and disilicides of tungsten, molybdenum, titanium and tantalum. The boiling point of their fluorides and chlorides is relatively low, so that the reaction products can easily be pumped away.

In the RIE process, the etch rate is sufficiently high for application with etch depths up to a few microns. However, both high etch rates and anisotropic profiles are required by advanced applications such as MEMS for which the etch depths are often more than 100μm. One way to get a large etch depth in a high etch rate is to use a more powerful plasma generator. This process is often called high density plasma (HDP) etch system [42]. In HDP etching, the etch rate significantly increases and is orders of magnitude higher than in RIE systems due to the high density of radicals and ions. However, the anisotropy of this etching process is lost because the powerful plasma generator also increases the lateral etch rate.

Typical methods to obtain anisotropic profiles in RIE system are in two categories [42]. One is to suppress the lateral etch rate by reducing the reaction of radicals such as lowering the substrate temperature, reducing the plasma pressure, diluting the plasma with an inert gas. The other is passivation of sidewall such as the addition of oxygen at very low temperatures for creating a thin layer of oxide on the sidewall or addition of a fluorocarbon gas to high density SF_6 plasma for creating a layer of polymer on the sidewall. Obviously, it is impossible to prevent lateral etching and simultaneously to keep high etch rate by above methods because these methods will inevitably lead to a lower vertical etching rate.

The invention of a new method of anisotropic silicon etching at room temperature by Robert Bosch GmbH resolved these problems [43]. This process is often referred as deep reactive ion etching (DRIE). In the Bosch DRIE process, etching and

passivation steps alternate. SF_6 is used for etching and C_4F_8 is used for passivation, so that the etching and passivation can be optimized separately in two consecutive plasma pulses. A high etch rate and anisotropic profiles are obtained in combination with a high selectivity and relatively smooth sidewall surfaces. The main idea of DRIE is very simple but it opened the way to a new generation of silicon-MEMS that was free from the restrictions of classical wet etching, plasma etching and RIE technology.

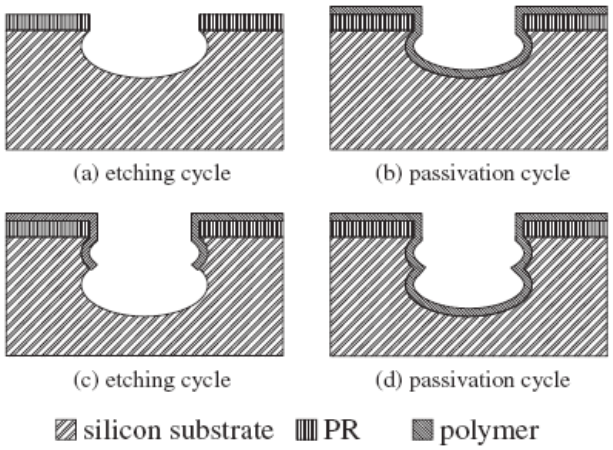

Fig. 2.6 Schematic of the principle of the Bosch process [44]

Fig. 2.6 shows the operating principle of the DRIE process [44]. Firstly, fluorine-containing plasma is used for a single short-time isotropic etching on a patterned silicon substrate (see Fig. 2.6 (a)). Secondly, a Teflon-like polymer is deposited on the etched trench as a protective layer to passivate the sidewall, as shown in Fig. 2.6 (b). Thirdly, ion bombardment occurs during the etching step to remove the polymer layer on the bottom, so that the radicals continues to react with the exposed silicon, as shown in Fig. 2.6 (c). Meanwhile, the polymer layer on the sidewall still remains after the ion bombardment due to its directionality so that the lateral etching is avoided. After that, another passivation step follows the etching step, as shown in Fig. 2.6 (d). The Bosch DRIE process is in fact a segregation of etching and passivation steps that enable deep etching, and can be used to fabricate MEMS structures with high aspect ratio. It is worth noting that etching in the Bosch DRIE process is isotropic in nature, but it eventually obtains anisotropy because etching steps and

passivation steps alternate and both the etching and deposition times are very short, usually less than 10s.

Ideally, the sidewall should be extremely smooth and vertical, and the bottom of the groove is also smooth and flat. However, the real profile of the groove is as shown in Fig. 2.6 (d): the sidewall is not vertical, it is scalloped, and the bottom of the groove is bowl-shaped due to the cyclic nature of the Bosch process. The scallop effect can be decreased by modifying the etching recipe, for instance, reducing the etching cycle time. Several methods have been developed to decrease the scallop [45] or control it to realize the sophisticated sidewall profiles [46].

2.3.3.3 LIGA

LIGA and related techniques are based on a sequence of process steps combining (deep) lithography, electroforming and moulding (German acronym: Lithographie, Galvanoformung, Abformung). This technique was first reported by Becker et al. [47] at the Karlsruhe Nuclear Research Center (the Kernforschungszentrum Karlsruhe, or KfK), in 1982. The LIGA technique showed a potential to be a new means of low-cost micromanufacture even at this very first stage. Using this technique, a wide variety of micro parts can be fabricated in batch with unprecedented accuracies from various materials previously.

The LIGA process is depicted in detail as follows [27,48,49].

In a first step, a microfeature is generated in a thick resist layer by means of a lithographic process. This can be achieved by utilizing a laser, a high-energy electron or ion beam as well as standard UV- or X-ray lithography with synchrotron radiation, which is similar as the counterpart process in DRIE. X-ray synchrotron radiation used as a lithographic light source is taken as an example to explain this process in LIGA. High energy x-rays from the synchrotron are highly collimated to filter through a patterned mask and approach an x-ray-sensitive photoresist, typically polymethylmethacrylate (PMMA). In most cases, the PMMA is attached to a substrate that is used later as an electroplating base. The regions of PMMA exposed to the x-rays experience bond scission, and these areas are selectively dissolved in a chemical developer. Thus, an ultraprecise microstructure with large aspect ratios is produced to be a mould for the later step.

In a second step, once the PMMA is developed, the desired metal will fill the nonconductive mould from a conductive base by electrodeposition. As a result, a complementary metal structure is generated from the resist master.

In a third step, after electrodeposition and dissolution of the PMMA, the electroplated structures can be removed from the substrate and used as individual metal microparts, or the metal pattern can be used as a mould insert or embossing tool allowing replication processes to be performed such as injection moulding or embossing, respectively. Moulded plastic parts may in turn be final products or lost moulds. The plastic mould retains the same shape, size, and form as the original resist structure but is produced quickly and inexpensively as part of an infinite loop. The plastic lost mould may generate metal parts in a second electroforming process or generate ceramic parts in a slip casting process. Thereby, microstructures preferably made of plastics are mass manufactured.

Fabrication of microparts using the LIGA process is characterized by high precision, high surface quality and high aspect ratios. Unlike many other processes, which are monolithically based on one material or one class of materials, this process can be applied on many materials ranging from metals, metal alloys and ceramics to polymers [50].

Given the cost of the LIGA equipment, various low cost LIGA-like processes were developed. These pseudo-LIGA methods involve the replication of masters created by alternate means such as deep reactive ion etching (DRIE) and novel ultraviolet thick photoresists. These techniques use other methods to create a mould in a nonconductive polymer or a semiconducting material, which can then be electroplated and processed in a manner similar to x-ray synchrotron patterned wafers. Likewise, techniques other than polymeric replication have been developed to allow microstructures to be replicated from LIGA masters in other materials [51].

2.3.4 Embossing

Embossing is a technique of the creation of an impression of some kind of design, decoration, lettering or pattern on another surface like paper, cloth, metal and even leather, to make a relief. It has been introduced to polymer microfabrication and called hot embossing because it is often performed at high temperature.

Hot embossing is an efficient method for the parallel replication of precision micro-features of polymers such as PMMA at low cost. It is a single step process for net-shape forming of components that might otherwise require multiple processing steps using conventional lithographic processes on glass or semiconductor substrates. With a single master or stamp, identical structures can be reproduced onto substrates. This technique is widely applied in microstructure fabrication in optical-sensor, micro-fluidic devices and bio-chip applications can achieve sub-10 nm imprint resolution on large areas [52].

2.3.4.1 Embossing equipment

Many commercial hot embossing machines are available, such as Jenoptik Hex-02 [53] and EVG750 [54]. Most of them are designed primarily for polymer embossing. Considering the cost and special requirement, some institutes developed their own embossing machines. The embossing facilities normally consist of loading system, aligning system, heating system, cooling system, control system, vacuum chamber and the mould.

The loading system is required to supply a sufficient load and an accurate position control to emboss the mould to the substrate. Generally, the substrate is polymer and embossed after heating, so a normal universal material testing machine with accurate position control can match the load and accuracy requirements. University of Texas at Arlington (UTA) [55] and Massachusetts Institute of Technology (MIT) [56] developed a hot embossing machine on an Instron hydraulic loading system, respectively.

Alignment is very important part of embossing especially when the mould is embossed into the substrate for only hundreds of micrometer or even nanometer deep. UTA [55] used 4 steel guide rods to assure the top embossing unit along with the mould slides move to the substrate in vertical direction. Otto et al. [57] reported a cold embossing machine for fabricating aluminium micro optical components, which used two guide rods for alignment, similar to the UTA design. MIT design [56] did not emphasise the alignment of embossing mould and substrate. However, they designed a work piece holder to fix the substrate. This work piece holder actually assured the alignment of the embossing mould and substrate, although it was not

design to that effect because this holder had a 0.9mm deep recess to hold the 1 mm thick PMMA chip.

The heating system is required to provide enough power to heat the substrate to the embossing temperature. In addition, a high power allowing a high heating speed is also important to reduce processing time and achieve high throughput. Basically, there are two designs for the heating system. One design employs heating cartridges to both top and bottom platens, and the other is to put the whole rig into a furnace. Obviously, the heat efficiency of the cartridge design is limited, so it is generally used for polymer embossing machine because the embossing temperature is low, normally under 200˚C. Both the UTA [55] and MIT [56] designs used the heating cartridge. The second design employs a furnace. This is efficient and powerful, so it is generally used for metal embossing machine because relative higher temperatures are required for embossing. Chen et al. [58] introduced an embossing rig with a furnace for press forging of AZ31 magnesium alloy sheets. The highest embossing temperature in this experiment was 400˚C. For heating systems using a heating cartridge, a suitable heat insulation should surround the whole rig in order to increase the heating efficiency [55,56]. The system can further contain a cooling system using water [56] or air [59].

Controlling system aims to control the embossing force, embossing and cycle time, platen displacement and embossing temperature. Generally, controlling the embossing force, time and platen displacement are realized by the controlling system of the material testing machine [55, 56]. For more accurate controlling the force and displacement, an extra quartz force sensor and a displacement gauge have been employed [60]. Cycle time and embossing temperature are controlled by heating and cooling control system [55, 56].

Embossing moulds are normally made of silicon patterned by DRIE [55, 56, 57, 59]. Some embossing machines had a vacuum chamber to hold the mould and substrate in order to provide clean and moisture environment during the embossing process [55, 56, 59].

2.3.4.2 Embossing Process

The process of hot embossing of thermoplastic polymers involves the plastic flow of material around a tool that has a shape inverse of the desired part shape. There are three basic steps in hot embossing [61]: Firstly, a polymer substrate is heated to a certain temperature between the glass transition temperature (T_g) and the melting temperature (T_l). Secondly, a mould (stamp or master) fabricated by either CNC-machining or LIGA-type methods is pressed against the substrate, allowing the pattern to be fully transferred onto the substrate (embossing). Finally, after a suitable amount of contact time between the mould and substrate to allow for the visco-elastic material to flow into the tool, where this hold time is a function of both material temperature and forming force, the system is cooled down below T_g, followed by separating the mould from the substrate (de-embossing). Fig. 2.7 shows schematically the apparatus for a typical hot embossing process.

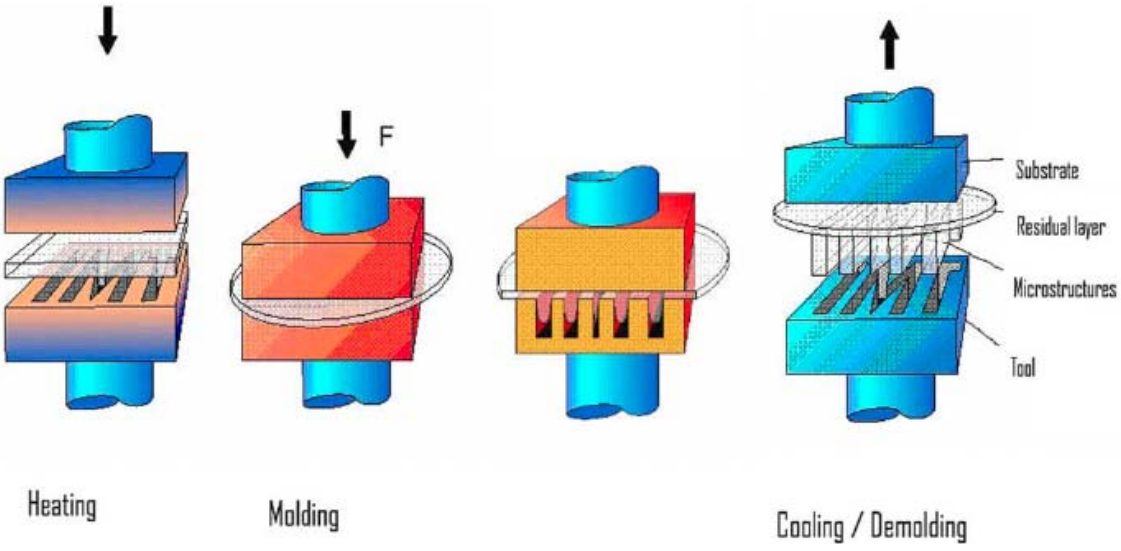

Fig. 2.7 The hot embossing process: heating, moulding and demoulding [61]

2.3.4.3 Embossing on metals

Embossing on polymer makes it easier to automatise production. However, polymers are generally not an ideal material for a micro heat exchanger because of low thermal conductivity. With the widening of material variety in MEMS technology the use of

metals became more interesting. High thermal conductive metals with low costs such as aluminium and copper have been used extensively to fabricate traditional heat exchangers. Micro heat exchangers with channel size in a scale of hundreds of micrometers fabricated of steel, copper and titanium by diamond machining have been reported [62,63,64,65]. However, only very few studies on fabrication of metallic micro channels at micrometer scale using embossing method are reported.

An embossing technology for forming metallic microstructures has been developed. The idea of this technology is to form metallic microstructure for instance, microchannels by micro silicon mould fabricated by deep reactive ion etching (DRIE). (See an example of this in [45].)

Otto et al. [57] attempted to fabricate optical components with micro channels in size of a few micrometers by cold embossing using conventional coarse grained aluminium. Embossed gratings made of aluminium have been manufactured with various groove depths (5.0, 2.5 and 1.0 μm) and a grating period of 10μm. Groove shape was always rectangular. The ratio of groove widths and plank widths should be 1:1. The embossed surface showed uneven and rounded planks with ridges. Jiang et al [66] did a further attempt to emboss a coarse grained pure aluminium with a small area (2 mm × 2 mm) at ambient temperature using silicon mould with parallel channels with a width of 11.7 μm. A very high mould failure rate was observed due to misalignment. Böhm et al. [67] studied straight channels and complex structures fabricated by cold and superplastic embossing using a silicon die in various relatively fine materials (grain size > 3μm) including pure aluminium, stainless steel, pure copper and brass CuZn37. The minimum structure width was 10 μm. The cold embossed surface showed a better quality than their previous attempts [57], which is due to the finer grain, although the channel edges were still rounded. In order to achieve complete moulding of the structure a compressive stress much higher than the yield stress proved necessary.

A significant lower loading force was observed during complex structure embossing of the Zn78Al22 alloys at elevated temperature, but the channel edges were still rounded which is due to superplastic deformation by grain boundary sliding and grain rotation[67,68]. A similar lower embossing force was reported in [69], where superplastic micro-forming with a fine grained Zn–22Al eutectoid alloy was studied

using hot embossing technology. Experimental results indicated that neither fibre-flow lines nor internal cracks could be observed when the fine-grained Zn–22Al eutectoid alloy was forged at a temperature range from 150 to 200˚C under a compressive strain rate range from 0.6 to 0.006 s^{-1}. A good dimensional accuracy for a mini compound spur gear was obtained by using hot embossing technology. Finally, a 5:1 mini reduction gear train was assembled. Its rotational motion was very continuous and smooth, indicating that the micro-forming method is a suitable technology for manufacturing micro metal components for MEMS.

The problems reported in above literature, such as large embossing force and rounded edges, are thought to be related, amongst others, to the difficulty in reliably embossing metals with conventional microstructures. A solution to those problems is to use amorphous alloys or ultra fine-grained metals. Saotome et al. [70] introduced imprinting forming to $Pd_{40}Cd_{30}Ni_{10}P_{20}$ amorphous alloys. Two kinds of V-type groove with the width of 1.5 μm and 2.0 μm respectively were formed under a compressive mean stress of 10 MPa for 1 ks in worktime. However, high cost, complicated melting process and limited properties of amorphous alloys restrict their applications.

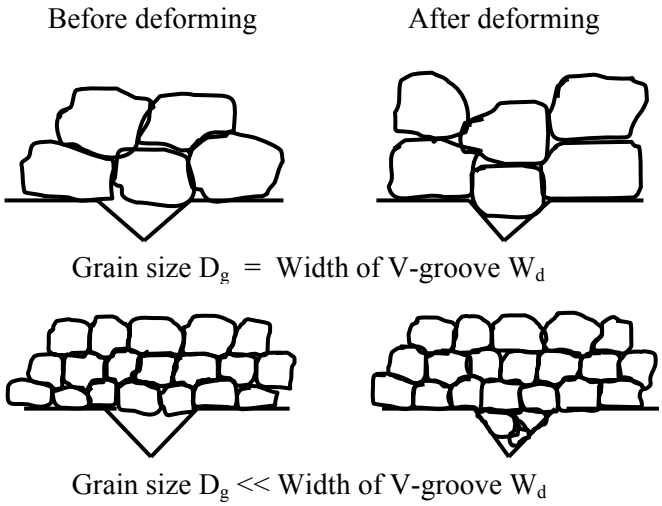

Fig. 2.8 Schematic illustration of the difficulty associated with forming of features that are smaller than the grain size in polycrystalline materials. [19]

Conventional aluminium alloys have a grain size of > 50 μm, which is larger than the microchannel size produced by embossing, leading to large local deviations of forming force and channel size [71]. Fig. 2.8 is a schematic illustration of this size effect [72]. During the fabrication of micro channels by superplastic deformation of metals, the mould is filled by grain boundary sliding and grain rotation rather than intragranular deformation, which results in that micro components with sharp edges cannot be accurately formed by coarse grained metals.

If metals with fine grains and high angle grain boundaries can be reliably produced, they may be formed to microchannels by embossing. In an attempt to overcome the problems in coarse grained metals, ultra fined grained (UFG) aluminium alloys with grain size of ~ 1 μm have potential to be used to fabricate micro channels, which may be applied in the micro heat exchanger. Fabrication, microstructure, properties of ultra fined grained metals will be introduced in Section 2.5.

2.3.4.4 Nanoindentation as a method for characterising embossed metals

Characterization of the local mechanical properties of UFG components with features at the micron scale can be performed through nanoindentation. This indentation method will be applied in this work to characterise the embossed materials.

The hardness detected by nanoindentation depends on the indent size, which is the so-called indentation size effect (ISE) [73]. The ISE is generally attributed to geometrically necessary dislocations (GNDs) [74,75,76] generated in the plastic zone underneath the indent due to strain gradients [75,76]. (Manika and Maniks [77] attributed ISE to combination of surface effects, strain gradient effect and mass-transport by point defects, but no physical model was presented.) Decreasing indentation size gives rise to an increasing density of GNDs, and, hence, an increasing hardness. Understanding of the ISE is crucial to development of finite element (FE) models that incorporate GNDs. Thus the ISE has received intense interest and a range of models have been presented to analyse the measured hardness vs indentation depth relation.

Several works have analysed the ISE. In the Nix-Gao model [78], the GNDs are assumed to distribute in the hemisphere underneath the indenter with radius of a_c (projected contact radius), and the average density of GNDs, $\rho^{N-G}{}_{GND}$, is given by

$$\rho^{N-G}{}_{GND} = \frac{3}{2bh}\tan^2\theta_0 \qquad \text{Eq. 2.2}$$

where b is the Burgers vector, h is the indentation depth and θ_0 is the angle of conical indent surface to the sample planar surface. From this, it follows that the indentation hardness is only related to the indentation depth. This approach leads to the often applied equation [78]:

$$\frac{H}{H_0} = \sqrt{1+\frac{h^*}{h}} \qquad \text{Eq. 2.3}$$

where H is the indentation hardness, h is the indentation depth, h^* and H_0 are constants depending on the material and can be obtained by fitting the experimental results. The Nix-Gao model provided a good fit to the measured ISE of (111) single crystal copper, cold worked polycrystalline copper, (100) single crystal silver and (110) single crystal silver with the indentation depth larger than 150 nm [78]. Two parameter models, such as the Nix-Gao model, show increasing deviation from measured nanoindentation hardness at low indentation depths (typically lower than 150 nm) [78,79,80, 81,82]. In attempts to clarify these deviations, a number of modifications of the model have been proposed, see e.g. [83,84]. All of these methods provided some improvements, but often at the expense of introducing new fittable parameters.

Chicot [83] considered the nanoindentation hardness and micro-indentation hardness separately, i.e. using different H_0 and h^* values when predicting the nanoindentation hardness and micro-indentation hardness. The Chicot model improved the nanoindentation hardness predictions but still failed to accurately predict the hardness at the transitional zone (from 200 nm to 400 nm) and the nanoindentation hardness at the very small depth (under 100 nm). In addition, the physical meanings of the parameters of H_0 and h^* that are different for microscales and nanoscales are not clear.

Swadener et al [79] assumed the indentation depth is proportional to the contact radius to the power n (n >1). The GND density was then calculated following the Nix-Gao model. The Swadener et al refined model provided a better prediction but it still deviated the experimental results at lower indentation depth. Both of Chicot model and Swadener et al model showed improvements as compared to the Nix-Gao model, but regions of poor fit to data remained.

Abu Al-Aub [84] assumed the GND and statistically stored dislocation (SSD) density should be coupled by a power and also considered the strengthening contribution by intrinsic stress. This provides:

$$\left(\frac{H-H_{\mathrm{y}}}{H_0-H_{\mathrm{y}}}\right)^{\beta}=1+\left(\frac{h^*}{h_{\mathrm{c}}}\right)^{\beta/2} \qquad \text{Eq. 2.4}$$

where H_{y} is the hardness contribution by the intrinsic stress, β is a constant and determined as 0.77-1.2 by fitting. The latter equation provides a better prediction of the nanoindentation hardness but still can not accurately predict the nanoindentation hardness at very low indentation depth (see section 7.2.5.4). Feng and Nix [81] incorporated f in Nix-Gao model and assumed f follows an exponential relation with indentation depth h introducing two new coefficients. Therefore, there are four fittable parameters in the predicting function, which adds extensive flexibility allowing fitting to virtually any dataset.

Huang et al. [85] studied the ISE using the continuum theory of mechanism-based stain gradient plasticity (CMSG) [86] based on Taylor dislocation model by finite element (FE) method, in which the density of GNDs is given by:

$$\rho^{Huang}{}_{GND}=\bar{r}\frac{\eta}{b} \qquad \text{Eq. 2.5}$$

where $\bar{r}$ is Nye factor, η is the strain gradient. This work showed a good correlation with the ISE of several metals, but it fails to predict the nanoindentation hardness with indentation depth less than 150 nm because the tip rounding effect has not been considered.

Published work on the ISE shows that the existing formulations of models loose accuracy in predicting measured nanoindentation hardness for indentation depth

below about 150 nm whilst some approaches need a large number of fittable parameters to account for measured nanoindentation hardness. This can lead to doubts on the range of validity of the theoretical approaches. A new model or a modified model with improved accuracy and down to a smaller indentation depth is needed to interpret and predict the indentation size effect.

2.4 Micro-heat exchangers

The first studies of micro heat exchangers to be used in very-large-scale integrated (VLSI) circuits were reported in 1981 by Tuckerman and Pease [8]. The rapid progress in the microelectronic industry during the 1970s and 1980s had brought a steady increase of the density in the packaging of electronic equipment with the desire to achieve greater computational power and speed. Although per-transistor power dissipation had declined substantially as devices had been scaled down, the increased density on chips had caused a significant increase in per-chip power dissipation. As a consequence, more heat was generated from the electronic circuits and should be removed by small and highly efficient heat exchangers.

Tuckerman [87] showed that conventional liquid heat exchanger technology could be scaled down to micro scale dimensions and applied to silicon chips. A direct contact and cold plate hybrid technology was used, where laminar water flowed in the micro-passages. A very high heat transfer efficiency was achieved because heat exchangers with micron scale of passages can provide a thermal resistance smaller by orders of magnitude than that provided by conventional cooling schemes.

With the progress in microfabrication technique and the increasing requirement of highly efficient and compact heat exchangers in other fields, the design and fabrication of micro heat exchangers have been further researched.

2.4.1 Classification of micro heat exchangers

Conventional heat exchangers have been classified by the transfer processes, geometry, heat transfer mechanisms and flow arrangements. As to micro heat exchangers, there is not a definite classification because only several specific types of micro heat exchangers are studied and reported. Just like conventional heat exchangers, micro heat exchangers generally have either one or two fluidic passages. In the case of one passage, heat is transferred to the fluid from electrically powered

heater cartridges, or removed from the fluid by electrically powered elements like Peltier chillers. In the case of two fluidic passages, micro heat exchangers are usually classified by the orientation of the fluid passages to another as concurrent flow (Fig. 2.9 (a)), counter flow (Fig. 2.9 (b)) or cross flow devices (Fig. 2.9 (c) and Fig. 2.9 (d)). If a chemical reaction is conducted inside a micro heat exchanger, the latter is also called a microreactor.

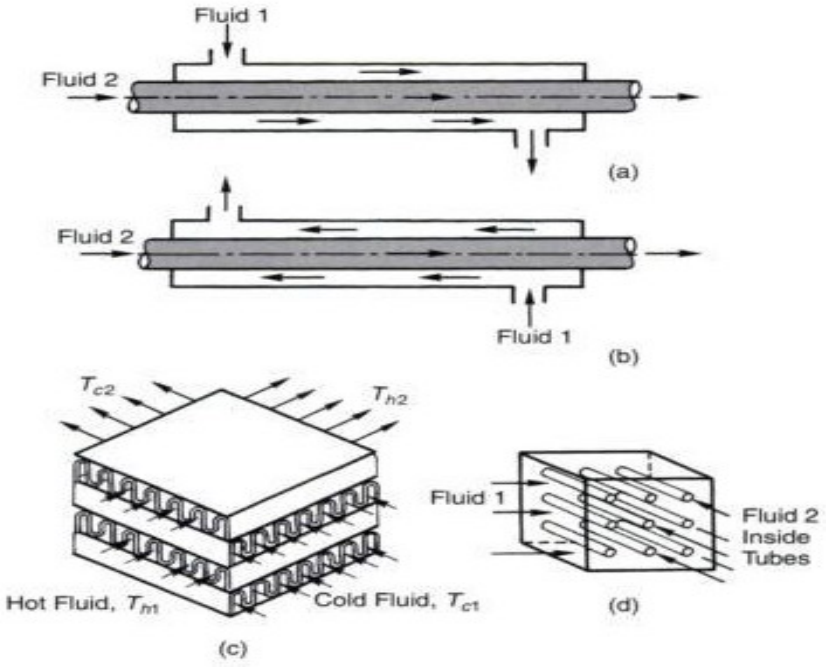

Fig. 2.9 Flow arrangement classifications: (a) concurrent-flow; (b) counter-flow; (c) cross-flow, both fluids unmixed; (d) cross-flow, fluid 1 mixed and fluid 2 unmixed [88].

The one fluidic passage micro heat exchangers, which were aimed to be used in VLSI field, were mostly researched at the early stage of development [8, 87]. In recent years, since 2000, most research was conducted on cross flow micro heat exchangers [64,89,90] because the fields of application are widened due to their high heat transfer efficiency.

2.4.2 Materials and forming methodology for micro heat exchangers

The advance in microfabrication, developed in the electronic and mechanical industries, makes it possible to manufacture flow channels ranging in depth from a few micrometers to hundreds of micrometers and produce micro heat exchangers.

Silicon was the main materials of early micro heat exchangers. Conventional heat exchangers, especially used in car industry, are mostly made of aluminium alloys or copper alloys because of their high thermal conductivity. However, conventional metal materials can not be applied in micro heat exchanger manufacture because precision machining was not available. The bulk micromachining technique in semiconductor industry was introduced to the fabrication of micro heat exchangers. Therefore, silicon became the main materials of micro heat exchangers. The first micro heat exchangers, in which ~400μm deep micro channels were etched in 500μm thick <110> oriented silicon wafers (Fig. 2.10), were manufactured using anisotropic etching and precision mechanical sawing techniques [87].

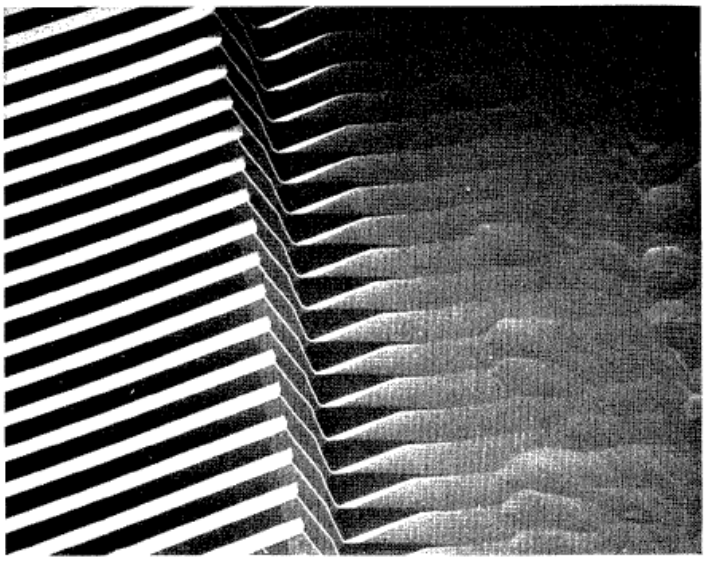

Fig. 2.10 SEM of microchannels etched in <110> silicon using KOH [87]

With the progress in diamond machining technique, copper was reported to be introduced to the manufacture of micro heat exchangers (Fig. 2.11) in 1994 [91]. Machining of thin copper foils with specially contoured diamond cutting tools was

applied in the production of small and very smooth fluid micro flow channels for micro heat exchanger applications. Heat exchanger plate wall thickness, as well as fin dimensions, may be carefully controlled and machined to dimensions on the order of tens of micrometers. The plates are stacked and bonded with the vacuum diffusion process to form a cross-flow, plate-type heat exchanger. The micro heat exchanger provided a volumetric heat transfer coefficient of nearly 45 MW/m^3K under very conservative design and operating conditions. This corresponds to a volumetric capacity nearly 20 times that of more conventional compact heat exchangers. High thermal capacity, coupled with low cost and ease of production, make these devices practical in areas where high thermal flux in a small volume is required.

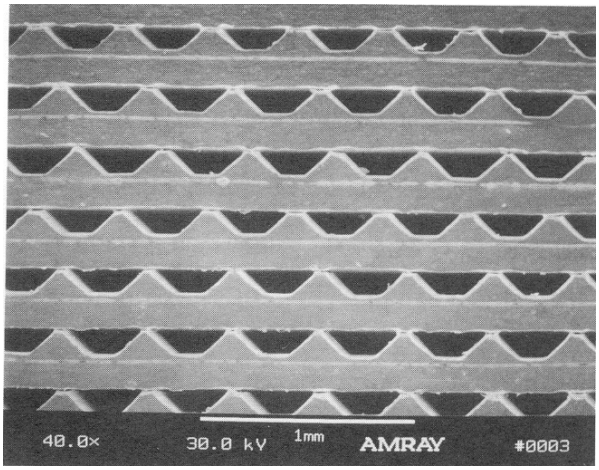

Fig. 2.11 A copper cross-flow micro heat exchanger fabricated by diamond machining [91]

Harris and co-workers [89, 92] firstly introduced the LIGA process to the fabrication of a cross flow micro heat exchanger, which was either made of PMMA (Fig. 2.12 (a)), or of Nickel (Fig. 2.12 (b)). The heat exchanger was fabricated by aligning and then bonding together two identical plastic parts that had been moulded using the LIGA process. The scale of the heat exchangers that were fabricated was approximately one order smaller than conventional scale heat exchangers and the heat transfer/volume was between 3–7 times greater. Relative to conventional scale heat exchangers, these heat exchangers provide extremely high rates of heat transfer/volume and relatively high ratios heat transfer/mass for given pressure drops.

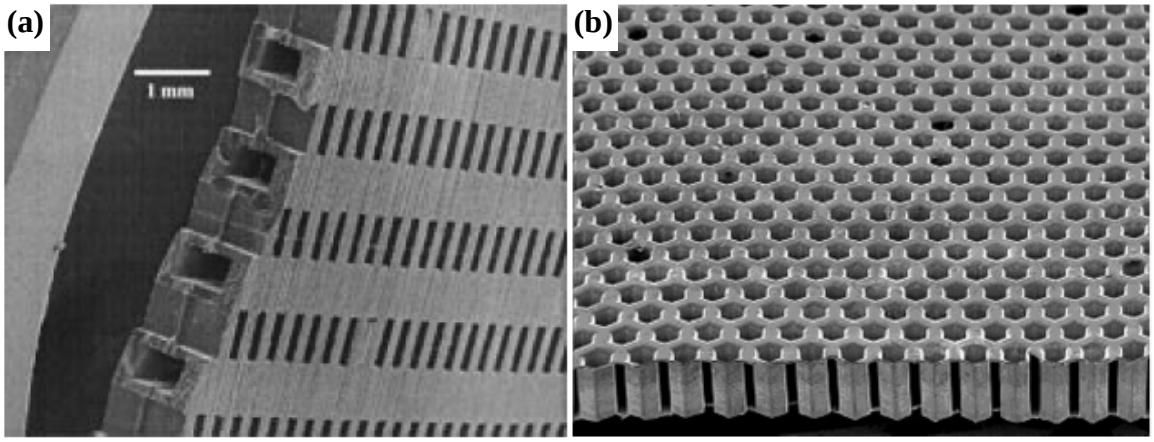

Fig. 2.12 Micro cross-flow heat exchangers made of (a) PMMA [89] and (b) Ni [92]

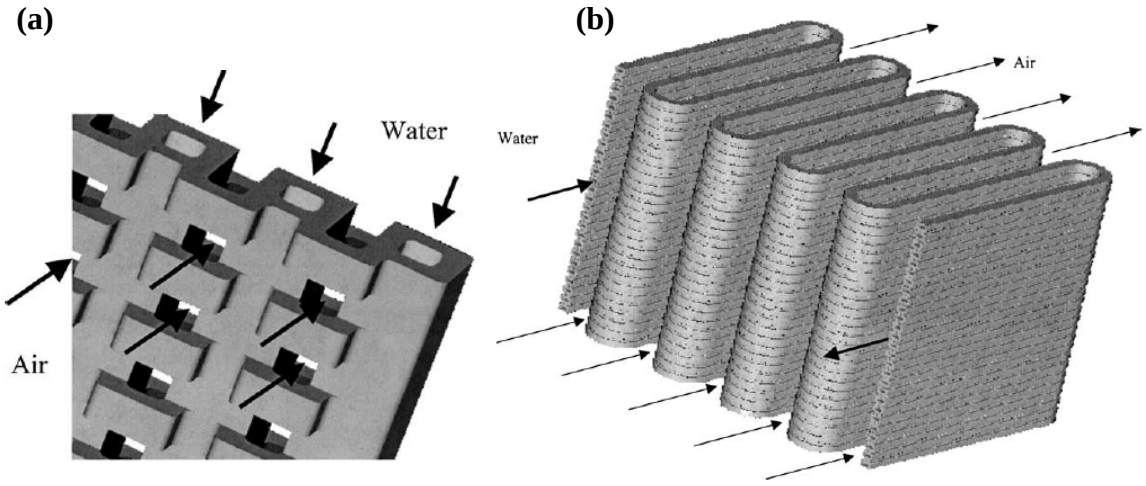

Fig. 2.13 (a) Passage of fluids in the extruded structure and (b) Serpentine heat transfer structure [93].

Gruss et al. [93] designed a cross-flow heat transfer surface with microchannels that could be manufactured industrially at a reasonable cost by extrusion either in aluminium or in polymers. In this paper, it is suggested that Harris design [89] of micro heat exchangers has several drawbacks. Firstly, the large sheet is very thin with a huge frontal air side area, making it difficult to use in real applications. Secondly, the technique used is limited in size to micro heat exchangers and is relatively expensive, as it uses sophisticated LIGA technology. Thirdly, the

fabrication of the structure demands precise joining of two half sheets, which is difficult to achieve without leaks. In order to avoid those drawbacks, Gruss designed a cross-flow micro heat exchanger by using a modified extruded structure. Following this process, a plate with micro channels is extruded, and slots are opened in the plate by milling (Fig. 2.13 (a)); thereafter the heat transfer structure is folded accordion-like (Fig. 2.13 (b)) in order to get a large air exchange surface with a small frontal area and a small air pressure drop. For aluminium alloys, the extruded channels size can be down to 0.6mm at industrial scale. The design and modelling of cross flow micro heat exchangers made of extruded structure is now finished but the fabrication and evaluation are underway.

A few metallic micro heat exchangers made of aluminium alloys, copper, titanium and stainless steel (Fig. 2.14), were fabricated in Karlsruhe Research Centre by using precision turning or precision milling, and were aimed for technical applications in thermal and chemical process engineering and in the laboratory [63,64, 94]. The machining is based on precision surface shaping of foils with microtools, diffusion bonding of a laminated foil stack, followed by welding of the microstructured core into housing. Cross-flow and counter-flow micro heat exchangers with micro channel or micro column structures have been developed for throughputs up to 7 ton water/h with a heat transmission power up to 200 kW. Overall heat transfer coefficients up to 54,000 W/m^2 K have been determined with water as test fluid.

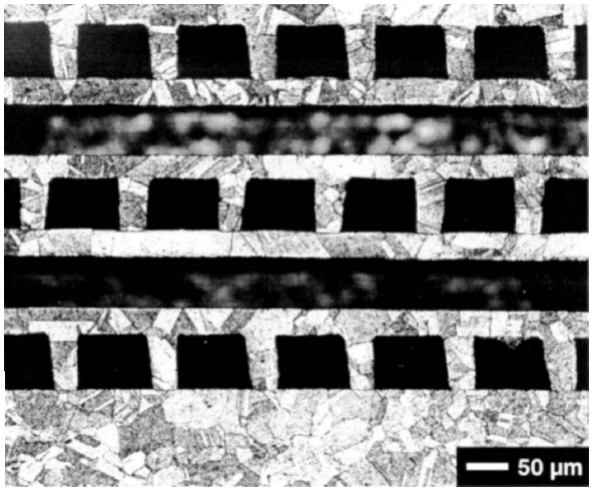

Fig. 2.14 Optical micrograph of a stainless steel cross-flow micro heat exchanger [63]

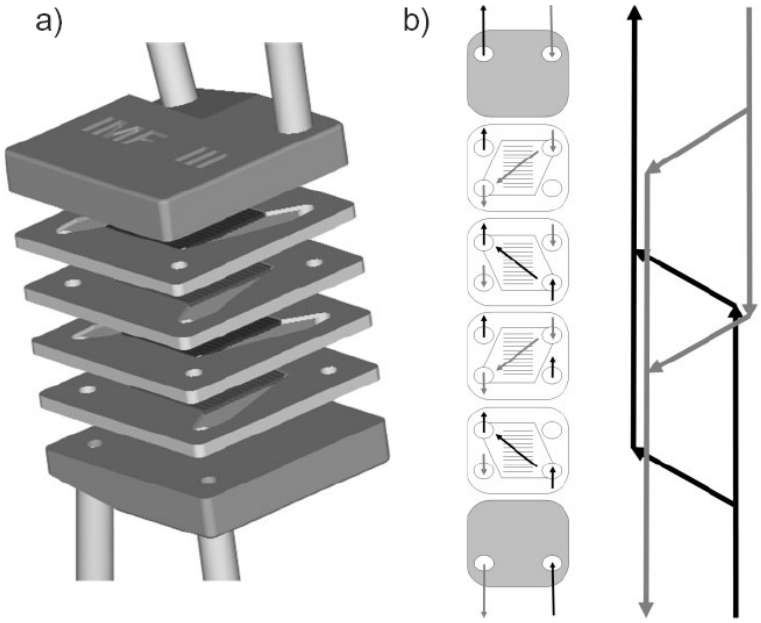

Fig. 2.15 Principle of a counter-flow micro heat exchanger with (a) two plates per passage and (b) guided mass flows [95]

A counter-flow ceramic micro heat exchanger was designed, fabricated and tested in 2005 [95]. The counter-flow micro heat exchangers were made up of 6 plates which included one cover plate, one base plate, 2 channel plates for cold medium and 2 channel plates for warm medium (Fig. 2.15). The plates were made of alumina ceramic by using a rapid prototyping process chain. Here, stereolithography was combined with a low-pressure injection moulding process for the rapid and precise manufacturing of ceramic components down to the micrometer range. Each plate contained 17 micro channels which were 250µm wide, 500µm high and 12.25mm long. The wall between the channels was 500µm thick. The separating layer between the passages was 1 mm thick. A micro heat exchanger, joined from sintered components using a glass solder, was applied as a prototype and checked for its performance at a system pressure of 8 bar. Heat transfer coefficients of up to 15kW/m^{2}K were reached.

2.5 Severe plastic deformation

Conventional metal forming methods that are extensively used in industry, such as rolling and extrusion, impose large plastic strains on work pieces. These large strains

may result in very fine-grained microstructures in metals and lead to some unique properties. Problems of such processing are that the size of the work piece is often continuously reduced in one or more directions and the fine-grained microstructure with unique properties can only be found in foil or filamentary materials that have limited use for structural applications. A number of processing methods have been reported [2] that impart a large plastic strain whilst the shape of the deformed sample does not change appreciably during the process. In addition, there is no limit to the strain that can be achieved in theory. Such deformation methods were called severe plastic deformation (SPD) [96].

SPD techniques, which were demonstrated as an effective approach to produce ultra fine grained (UFG) materials, refer to various experimental procedures of metal forming that may be used to impose large accumulated plastic strains on materials at room or elevated temperatures leading to exceptional grain refinement. A unique feature of SPD processing is that the high strain is imposed without any significant change in the overall dimensions of the workpiece. Another feature is that the shape is retained by using special tool geometries that prevent free flow of the material and thereby produce a significant hydrostatic pressure. The presence of this hydrostatic pressure is essential for achieving high strains and introducing the high densities of lattice defects necessary for exceptional grain refinement [2].

SPD Methods should meet the following requirements in the production of ultra fine-grained structures in bulk samples and billets[97]: (a) the capability of generating ultra fine-grained structures as well as the prevailing high angle grain boundaries, since only in this case can some unique properties be achieved, (b) the production of UFG materials with homogeneous microstructure and properties within the whole volume of a sample, and (c) the production of specimen without macro/micro defects such as mechanical damage or cracks. The SPD techniques which can meet the requirements through optimizing processing parameters and routes include high pressure torsion (HPT) [98], equal-channel angular pressing (ECAP, will be introduced in section 2.6) [99], Multi-directional forging (MDF) [100], accumulative roll bonding (ARB) [101], cyclic extrusion and compression (CEC) [102], repetitive corrugation and straightening (RCS) [103], and twist extrusion (TE) [104].

2.5.1 High pressure torsion

High pressure torsion (HPT) differs from conventional torsion by imposing a large hydrostatic pressure of up to several GPa during processing. The principle of HPT is illustrated schematically in Fig. 2.16 [98]. The HPT sample is in shape of disk, typically, in a diameter from 10 to 20 mm and a thickness of 0.2-0.9 mm [105, 106]. During HPT, the disk shaped specimen is put into an almost closed die and a compressing force is imposed on top of the sample. Then one or both contact platens impose a shear strain in the sample by rotating one of the platens (or both in opposite directions). A large accumulated strain and grain refinement can be achieved during several turns of rotations. This process can substantially refine the grain size, for instance the grain size of an Al-3%Mg-0.2%Sc can be refined to 0.15 μm after six turns of rotation at room temperature and pressure of 6 GPa [107]. Another advantage of the HPT technique is that it has the capability of refining the grain size during powder consolidation, which makes it possible to produce ultra fine grained materials from micrometer-sized metallic powders [108].

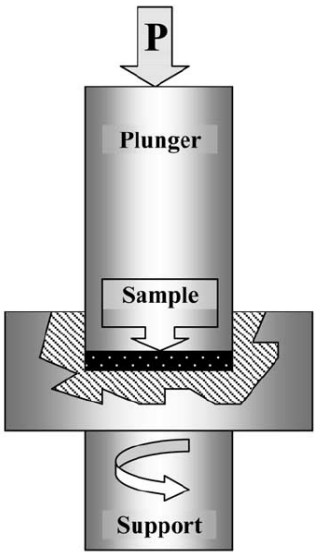

Fig. 2.16 The principle of HPT [98]

2.5.2 Multi-directional forging

Multi-directional forging (MDF, also called multiple forging) is a repetitive free forging operation in which the forging direction systematically changes. It was

developed by Salischev and co-workers [100]. Fig. 2.17 represents a schematic of the MDF process. The homogeneity of strain provided by MDF is lower than in that of both ECAP and HPT. However, MDF allows the generation of ultra fine grained structure in larger samples and in rather brittle materials since processing is carried out at high temperatures and specific loads are relatively low. A minimal grain size can be approached through optimizing the temperature and strain rate of deformation.

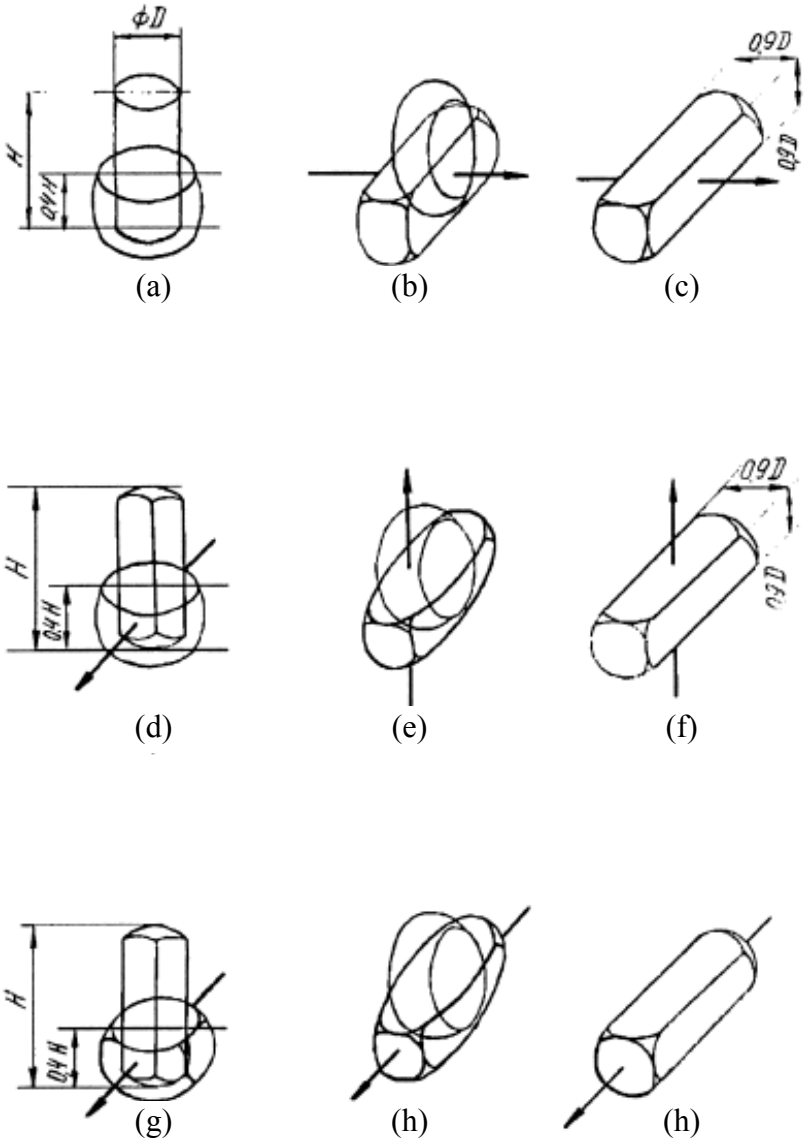

Fig. 2.17 The principle of MDF: (a), (b), (c) forging along the first axis; (d), (e), (f)-forging along the second axis; (g),(h), (i) forging along the third axis [100]

2.5.3 Accumulative roll bonding

Accumulative roll-bonding (ARB) is a process which can be applied to the grain refinement of sheet samples and can in principle scale up for commercial application

to large production quantities of sheet material. The principle of the ARB process is shown in Fig. 2.18. The ARB process combines stacking of sheet materials and conventional roll-bonding. Firstly, a strip with clean and oil-free surfaces is placed on top of another strip. The two layers of strips are bonded by rolling, which is same as in a conventional roll bonding process. The bonded material is cut at the middle of length. Two sectioned strips are again surface-treated, stacked and roll-bonded for another round of the process. The whole process can be repeated for a large number of times and is usually carried out at elevated temperature but below the recrystallization temperature. This is because rolling at the temperatures higher than recrystallization temperature will remove the accumulated strain while rolling at low temperatures usually causes insufficient ductility and bond strength [101].

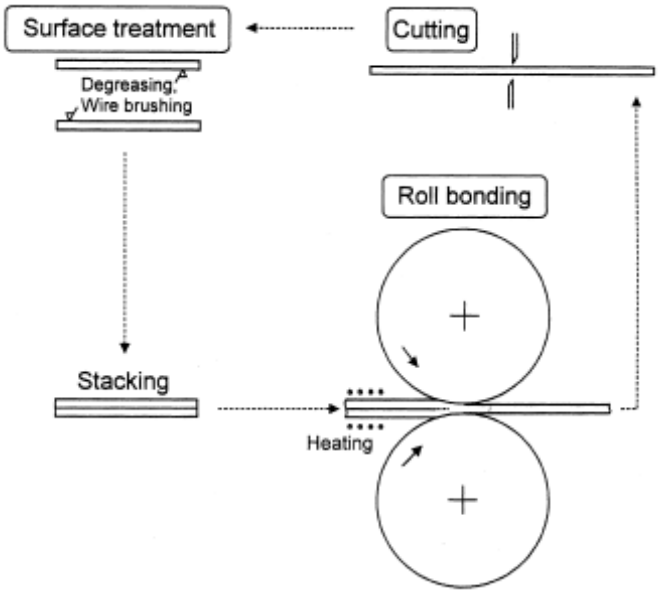

Fig. 2.18 The principle of ARB [101]

2.5.4 Cyclic extrusion and compression

Cyclic extrusion and compression (CEC) is performed by pushing a sample from one cylindrical chamber of diameter d_0 to another one with equal dimensions, through a die with smaller diameter d_m which is markedly smaller than d_0 [102]. The principle of CEC is illustrated in Fig. 2.19. Thus, the processing induces extrusion and the chambers provide compression so that, during one cycle, the material is pushed to first experience compression, then extrusion, and finally compression again. In the second cycle, the extrusion direction is reversed, leading to the same sequence of

deformation modes. The process can be repeated several times by pushing the sample back and forth to obtain a high accumulated strain.

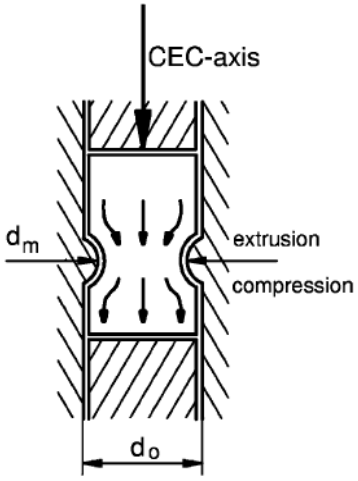

Fig. 2.19 The principle of CEC [102]

2.5.5 Repetitive corrugation and straightening

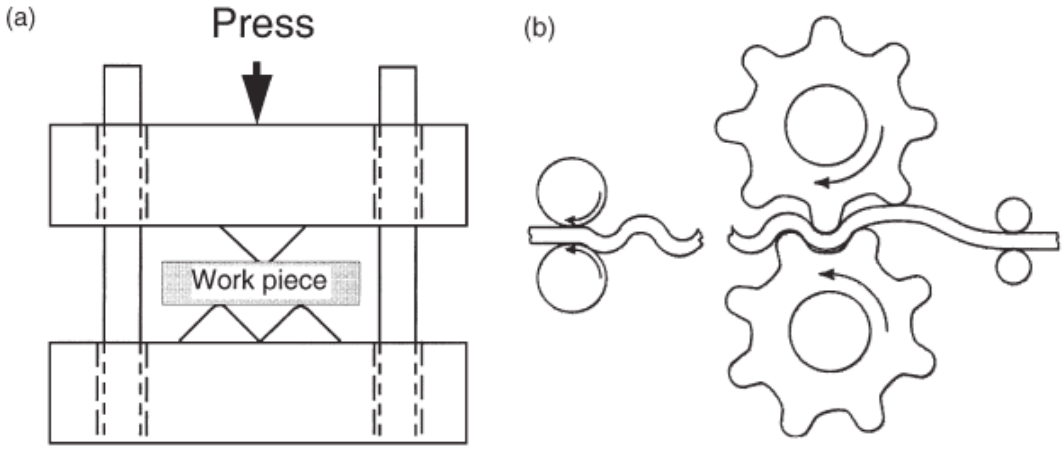

Fig. 2.20 The principle of RCS: (a) die set up for discontinuous RCS process and (b) set up for continuous RCS process [103]

Repetitive corrugation and straightening (RCS) involves the repeated rolling and straightening of a work piece. RCS shown in Fig. 2.20 (a) is a basic RCS cycle which consists of two steps: corrugation and straightening. The corrugation is carried out in a die set as shown in Fig. 2.20 (a) and straightening is performed between two flat platens using a processing cycle that may be repeated many times. The basic RCS is a discontinuous process. Fig. 2.20 (b) depicted a continuous version of the RCS

process. The work piece is corrugated by a system of gear-like rollers. The straightening is accomplished by pressing the corrugated work-piece between two flat platens. It is obvious that the continuous RCS process can be easily adapted to a rolling mill for industrial production of nanostructured metals and alloys [103].

2.5.6 Twist extrusion

The principle of twist extrusion (TE) is to obtain intense shear deformation via extrusion of rectangular cross section billets through a die with a twist channel (see Fig. 2.21).The shape and area of the channel cross section remain constant along the extrusion axis, while the channel is twisted around the extrusion axis. The shape of the cross section can be arbitrary (except for circular). Such a twist extrusion does not change the shape and area of the work piece cross section, which allows repetitive extrusion on a work piece to accumulate plastic strain [104].

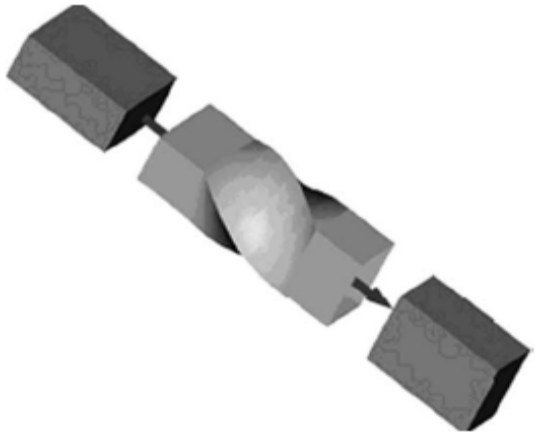

Fig. 2.21 The principle of TE [104]

2.6 Equal channel angular pressing

Equal channel angular pressing (ECAP) was invented by V.M. Segal [99], in Russia in the early 1980s. The original motivation of this design was to provide an ideal forming method that can produce large uniform plastic deformations but consume less energy than conventional forming processes. This technique became really popular at the end of 1990s when Valiev developed ECAP for refining the microstructure in order to achieve superior strength [109].

2.6.1 Principle of ECAP

The mechanism of ECAP is illustrated in Fig. 2.22 [110]. The die for ECAP is composed of two internal channels with identical cross-sectional area intersecting at an angle of Φ. Another angle of Ψ is defined by the outer arc at the intersection of the channels. During the pressing process, a lubricated billet with the same geometrical configuration as the channel is placed in the upper channel and then pressed out through the lower channel by applying a punch load using a plunger. This billet acquires an intense shear deformation at the intersection of the channels.

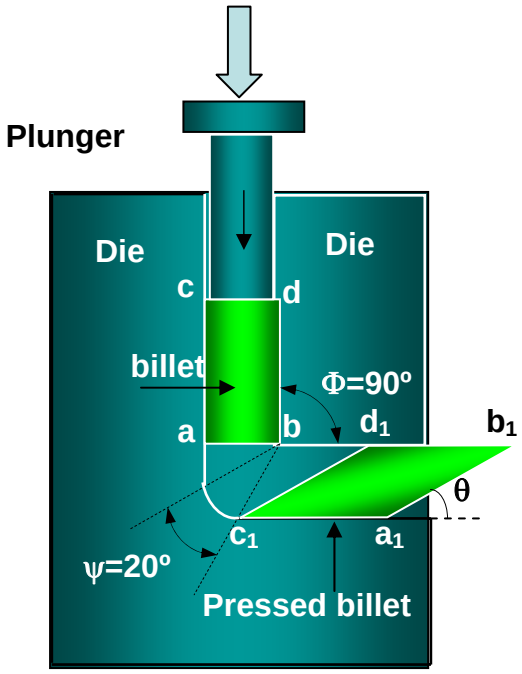

Fig. 2.22 The schematic of ECAP [110]

Since the shear deformation occurs without change in billet cross section shape, a severe plastic strain can accumulate by repeating the above process. The first equation used for calculating the accumulated strain was provided by Segal and his co-workers [111]. When the outer angle Ψ=0˚, and the inner angle Φ is arbitrary, according to [111], the accumulated shear strain value increment (ε_N) after N passes through the channels can be calculated by the Eq. 2.6:

$$\varepsilon_N = \frac{2N}{\sqrt{3}} \cot\frac{\Phi}{2} \qquad \text{Eq. 2.6}$$

Subsequently, Iwahashi et al. [112] extended the calculation to include also the arc angle, Ψ, and this led to the Eq. 2.7:

$$\varepsilon_N = \frac{N}{\sqrt{3}}\left[2\cot\left(\frac{\Phi}{2}+\frac{\Psi}{2}\right)+\Psi\cos\left(\frac{\Phi}{2}+\frac{\Psi}{2}\right)\right] \qquad \text{Eq. 2.7}$$

Eq. 2.7 has been verified to be accurate by finite element modelling [113] and experiments [114] when frictional effects were ignored. Eq. 2.7 indicates that the accumulated strain in a billet is approximately equal to 1 for each pass through a die with channel angles, Φ= 90˚, Ψ=20˚.

An alternative relationship for strain was proposed by Goforth et al. [115] in the form of:

$$\varepsilon_N = \frac{N}{\sqrt{3}}\left[2\cot\left[\frac{\Phi+\Psi}{2}+\Psi\right]\right] \qquad \text{Eq. 2.8}$$

When Ψ=0 (which is the minimum value) or Ψ=π-Φ (which is the maximum value for avoiding a reduction in the cross-sectional dimensions of the specimen as it passes through the die), Eq. 2.7and Eq. 2.8 become same form [116].

When Ψ=0:

$$\varepsilon_N = \frac{2N}{\sqrt{3}}\cot\frac{\Phi}{2} \qquad \text{Eq. 2.9}$$

When Ψ=π- Φ:

$$\varepsilon_N = \frac{N\Psi_{\max}}{\sqrt{3}} \qquad \text{Eq. 2.10}$$

And when Ψ is larger than 0 and smaller than π- Φ, the Eq. 2.7and Eq. 2.8 differ by less than 5% [116].

Apart from the number of billet passes through the channels, the rotation of macroscopic shear plane between each pass is also very important for microstructure refinement. There are typically four specific cases of deformation routes [117]. In

route A, the billet is pressed repetitively without rotation and the billet orientation remains unchanged at each pass. In rout B_A, the billet is rotated by 90˚ in alternate directions between each pass. In route B_C, the billet is rotated by 90˚ in the same sense between each pass. And in route C, the billet is rotated by 180˚ between passes. These four routes are illustrated schematically in Fig. 2.23 [118].

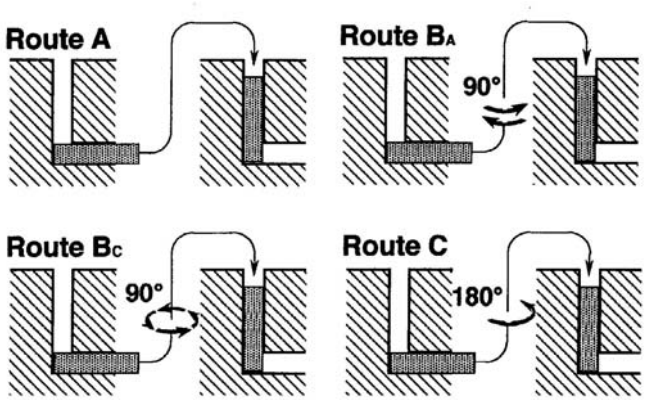

Fig. 2.23 The four processing routes in ECAP [118]

ECAP has many benefits. As mentioned, ECAP can be exerted on the billet repetitively to obtain severe plastic strain and to produce ultra fine grained (UFG) materials because the cross section of the billet remains unchanged after each pass. Compared with conventional plastic deformation techniques such as rolling and extrusion, ECAP can provide very large total deformation and fabricate UFG materials with relatively low punch pressure. Further, compared with other severe plastic deformation (SPD) methods such as high-pressure torsion (HPT) and multi-directional forging (MDF), ECAP can fabricate bigger bulk UFG materials with a more homogeneous microstructure and prevailing high angle grain boundaries by simple facilities. Also, compared with other top-down synthesis methods of nanostructure materials such as inert gas condensation and mechanical alloying [119], ECAP will not involve hazardous nano-powders and contamination.

2.6.2 Mechanisms of grain refinement in ECAP

ECAP has been used as a process to obtain remarkable grain refinement in coarse-grained materials since 1990s. A model for grain refinement was initially presented to explain the grain size reduction of Armco iron during high-pressure torsion by

Valiev et al. [120, 125]. In this model, the grains are considered to be gradually transformed from cellular structures. At the early stage of torsion deformation, a very high dislocation density emerges and forms intragranular structures with low angles of misorientation and thick cell walls (Fig. 2.24(a)). As the strain increases, the thickness of the cell walls decreases by recovery through a partial annihilation of dislocations of different signs that occurs at the cell boundaries (Fig. 2.24(b)). Ultimately, an excess of dislocations of only one sign remains on each boundary. And an array of ultra fine grains with high-angle non-equilibrium boundaries are formed (Fig. 2.24 (c)).

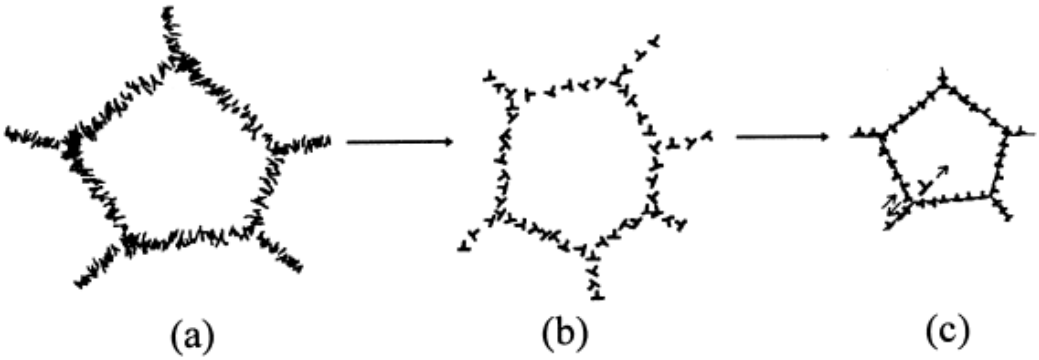

Fig. 2.24 Schematic model of dislocation structure evolution at different stages during severe plastic deformation [120].

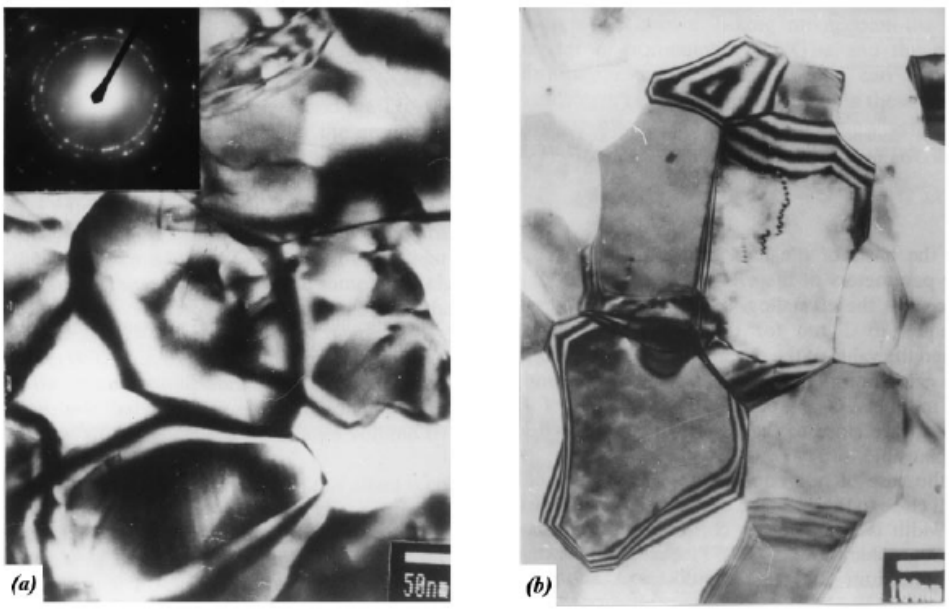

Fig. 2.25 TEM microstructure of the A1-4%Cu-0.5%Zr alloy: (a) HPT processed, (b) HPT and then annealed at 106˚C for 1 h [121].

The notions on non-equilibrium grain boundaries appeared for the first time in the Ref 122 where interactions of lattice dislocations with grain boundaries were investigated. The characterization of the non-equilibrium grain boundary is that excess crystal defects such as dislocations and voids store at grain boundary, which causes excess grain boundary energy and long range elastic stresses. The dislocations stored in grain boundaries were thought to have a crystallographic ordered structure and discontinuous distortions of such a structure cause the elastic stress fields. [122]

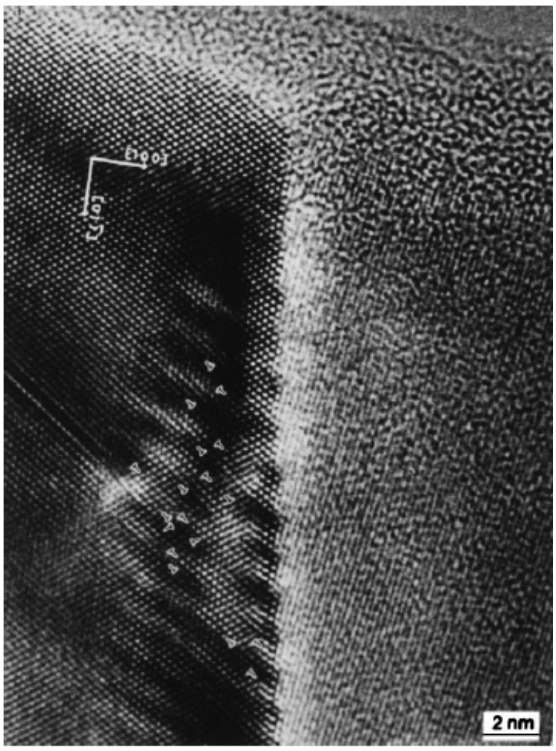

Fig. 2.26 Grain boundary structure of a nanostructured A1-3%Mg alloy observed by HREM. Edge dislocations are marked by the symbol ⊥ [123]

Grain boundaries in ultra fine-grained materials processed by SPD techniques have been shown to be in a non-equilibrium state through TEM/HREM investigations (Fig. 2.25, Fig. 2.26). Significant distortions of the crystal lattice can be observed near the grain boundaries, The figures also show a large amount of dislocations and other grain boundary defects (curved and wavy configurations) storing at or near grain boundaries [1].

Xu et al. [124] suggested that according to the Valiev model (Fig. 2.24), a gradually increasing refinement of the microstructure was predicted when the additional dislocations were continuously introduced during the straining process. However,

this is not consistent with the experimental observations when the model was applied to ECAP. In fact, both the widths of the elongated grains and the average sizes of the equiaxed grains are nearly unchanged after a pass of ECAP [124].

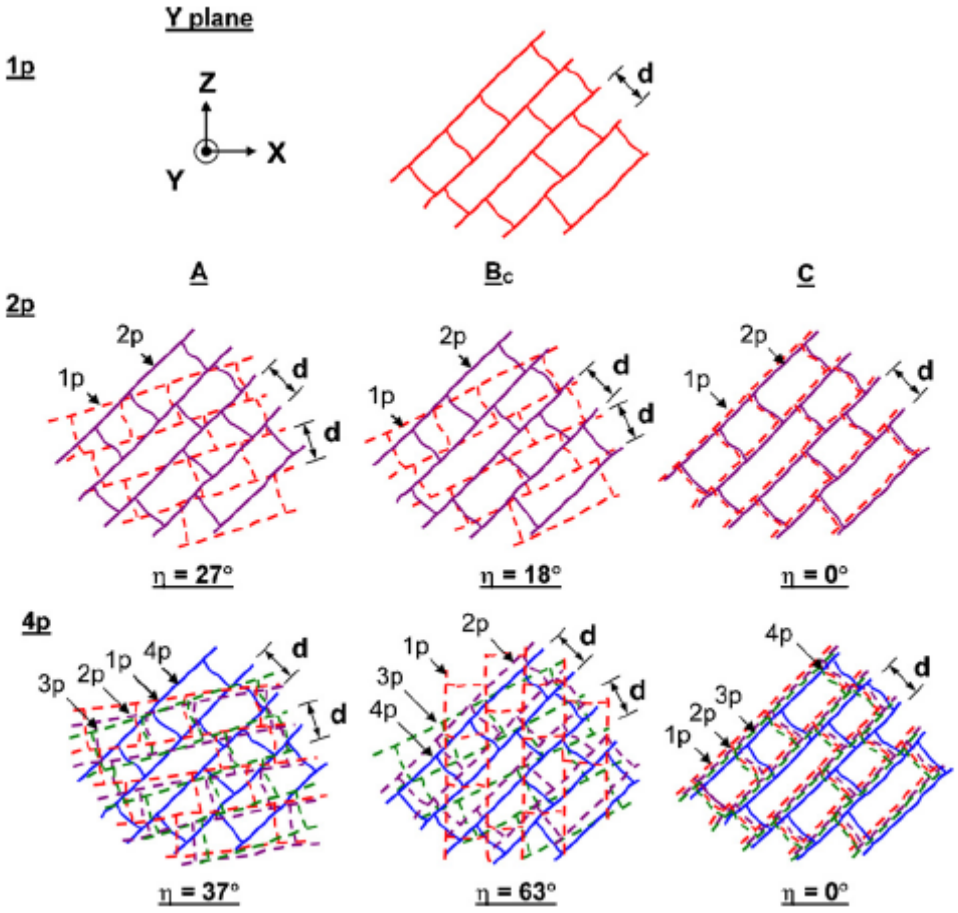

Fig. 2.27 A slip model for grain refinement in ECAP [125]

An alternative model based on an inter-relationship between the formation of subgrain boundaries and shear deformation was proposed by Xu et al. [124] and further developed by Langdon [125]. Fig. 2.27 is a schematic illustration of this model. The original grains become elongated to a band shape subgrain with the width of d when the billet passes the corner in the first pass (Fig. 2.27 1p). In the second pass, the elongated subgrain is further elongated (route C) because the shear plane remains in the same direction or sheared (route A and B_C) because the shear plane is changed to another direction (Fig. 2.27 2p). In the further passes, the shear deformation occurs (Fig. 2.27 4p). Especially when route B_C is used, several intersecting slip systems lead to a high density of dislocations and then these

dislocations re-arrange and annihilate. As a result, for route B_C, a reasonably equiaxed array of grains on each orthogonal section is formed, which is illustrated schematically in Fig. 2.28. By contrast, the development of an equiaxed microstructure is less advanced when using routes A and C because the shear plane is less changed than that of route B_C.

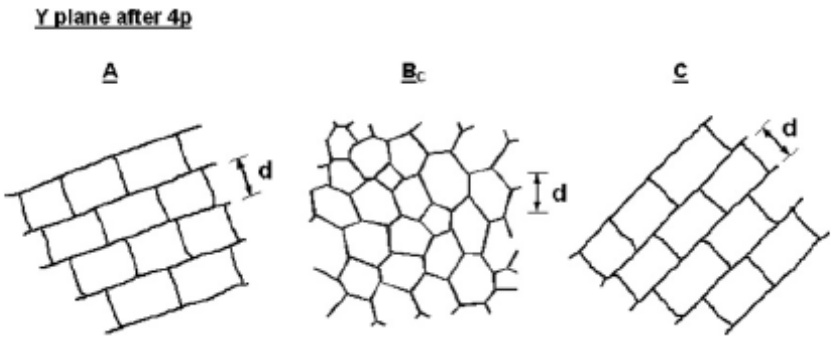

Fig. 2.28 The microstructures on the Y plane after four passes using route A, B_C and C [125]

2.6.3 Application of ECAP in aluminium alloys

ECAP of aluminium alloys has been studied extensively since the invention of this technique because the FCC crystal structure and good ductility of aluminium alloys make it easy to perform ECAP on them, especially on pure aluminium. After ECAP, both microstructures and properties of aluminium alloys are changed remarkably.

2.6.3.1 Microstructure of aluminium alloys after ECAP

Because shear deformation occurs at intersection of two channels in the ECAP die, the grain structure of aluminium alloys can be homogeneously refined to ultra-fine grained (UFG) materials. The original grain is sheared to a band-shaped subgrain after single pass of ECAP. The width of the band-shaped subgrain determines the equilibrium grain size of the pure aluminium after several passes of ECAP, which is about 1.2μm and larger than most materials processed by ECAP. It is possible to obtain much smaller grain sizes by alloying. As shown in the Table 2.1, the grain size of aluminium alloys can be down to about 0.2 μm after eight passes of ECAP [128, 129]. Some alternative procedures for decreasing the grain size are to combine

processing by ECAP with some other pro-ECAP or post-ECAP procedure such as rolling, extrusion and HPT, to decrease the ECAP temperature and to add a back pressure to the ECAP process.

Table 2.1 Microstructure and properties of aluminium alloys after ECAP

Materials	Condition of ECAP	Grain size (μm)		Maximum temperature for grain stability (K)	Elongation (%)	Reference
		As-received	After ECAP			
Pure Al	8p, Bc RT	190	1.2	N/A	~800	[126]
Pure Al	4p, Bc RT	1000	1.3	473	N/A	[137]
Al-0.2%Sc	8p, Bc RT	700	0.70	>750	200	[127]
Al-0.5%Mg-0.2%Sc	8p, Bc RT	500	0.48	>750	300-600	
Al-1%Mg-0.2%Sc	8p, Bc RT	200	0.36	>750	300-600	
Al-3%Mg-0.2%Sc	8p, Bc RT	200	0.2	>750	>2000	[128]
Al-3%Mg-0.2%Zr	8p, Bc RT	70	0.2	>570	>200	[129]
Al-3%Mg-0.2%Sc-0.12%Zr	6p, Bc RT	60	0.3	>750	>1000	
Al-2024 (Al-4%Cu-1.5%Mg-0.4%Mn)	8p, Bc RT	N/A	0.3	~700	300-500	[130]

The ultra fine grain processed by multiple ECAP passes is characterized by a high fraction of high angle grain boundaries [131]. Processing by ECAP involves a very high strain in each passage through the die so that very large numbers of dislocations are introduced into the material, which results in the presence of a high fraction of low angle non-equilibrium grain boundaries after a small number of passes. When the number of passes is increased, the subgrain boundaries evolve into high angle grain boundaries through the absorption of dislocations as discussed in section 2.6.2. Even after eight passes of ECAP, the grain boundaries are in high energy non-equilibrium configurations. For instance, the grain boundaries of Al-3%Mg after 8 passes of ECAP at room temperature and annealing for 1 hour at 423K are wavy and faceted, indicative of the presence of non-equilibrium grain boundaries [132].

Generally, the ultra fine grain is not thermal stable because the boundaries are in high energy non-equilibrium configurations.

2.6.3.2 Thermal stability of UFG aluminium alloys

Thermal stability of UFG Aluminum alloys with non-equilibrium grain boundaries has been extensively studied. This includes the influence of increasing temperature on the dislocation density within the grain and grain boundary, grain size, misorientations and grain boundary structure.

Cao et al. [133] studied the microstructure and hardness of ECAP processed pure Aluminum after annealing at 150-500˚C for 2 hours. Annealing at up to 210˚C led to a very slightly coarse microstructure with nearly unchanged subgrain size and grain size, whereas annealing at 240-500˚C made the microstructure coarsen rapidly. As a result, the hardness remained constant up to 180˚C, decreased rapidly at 210-300˚C and further slightly decreased at temperatures above 300˚C. The authors also studied the effect of annealing temperature on the average misorientation of pure aluminium after 10 passes of ECAP. During annealing up to 300˚C, there was a large continuous decrease in the number of subgrain boundaries with misorientation between 1.5˚ and 3˚, and a small decrease in the number of subgrain boundaries with misorientation between 3˚ and 9˚. The number of subgrain boundaries with misorientation between 9˚ and 15˚ remained approximately constant. The overall fractions of low angle grain boundaries (<15˚) decreased predominantly by elimination of the very low misorientation angle boundaries (<1.5˚).

Thermal stability of single phase aluminum alloys is not better than that of pure aluminum. Wang et al. [134] studied the microstructural stability of UFG Al-Mg alloy processed by ECAP during annealing at 170-530˚C for 1 hour. Annealing at 170˚C or 200˚C led to a small increase in the mean linear intercept grain size but the appearance of microstructure with both equiaxed and elongated grains coexisting remained the same as that in the as ECAP processed condition. After annealing at 230˚C for 1 hour, the microstructure was clearly split into unrecrystallized regions and recrystallized regions. Such a duplex microstructure was visible after annealing at temperature up to 275˚C, with an increase in the average grain size in both regions. At 290˚C and above, the alloy showed a fully recrystallized microstructure with a uniform distribution of grains separated by high angle grain boundaries.

Morris et al. [135] studied the microstructure of UFG Al-3Mg alloy processed by 8 passes of ECAP with a 120˚ inner angle die, and its evolution during isochronal annealing at 150-250˚C for 1 hour as well as for shorter times at 250˚C, where grain growth was very rapid. Annealing at 150˚C for 1 hour did not lead to any microstructure changes detectable by SEM, but a slight reduction of dislocation density and relaxation of cell boundaries into subgrain walls was observed by TEM. After annealing at 200˚C for 1 hour, almost equiaxed grains with the sizes of about 0.25μm were observed by SEM, whereas significant dislocation recovery, a slight increase in grain width and a slight reduction of grain length were observed by TEM. Converging beam diffraction and Kikuchi line patterns analysis showed that neighbouring grains in the unrecrystallized regions were generally misoriented by fairly low angles (less than 15˚), and the grains in the recrystallized regions were generally more randomly oriented. Annealing at 250˚C for 5-15 minutes led to slightly coarsened structures observed by SEM. The microstructure is fairly uniformly equiaxed with a grain size approaching 0.5-1μm. The changes of microstructure observed by TEM were: a general reduction of dislocation density both within grains and at grain boundaries, the retention of a significant amount of dislocations in some grains and the formation of subgrain/low angle boundaries by dislocation rearrangements. Annealing at 250˚C for 1 hour led to a duplex microstructure consisting of bands of slightly coarsened grains and regions of much coarser grains with grain size of 5-10μm due to the inhomogeneous recrystallization.

Aluminium alloys with additions of transition elements, such as zirconium and scandium, possess an improved thermal stability because the rate of grain growth can be controlled by fine and coherent precipitates such as Al_3Zr and Al_3Sc. Oh-ishi et al. [132] studied the influence of annealing temperature to microstructure of UFG Al-3Mg and Al-Mg-Sc alloys processed by ECAP. After isothermal annealing at 150˚C for 1 hour, the grain boundary structure and grain size of the Al-3Mg alloy were essentially identical to that of as-pressed conditions. The coarsening rates of the Al-3Mg alloy increased rapidly with the increase of the annealing temperature. In contrast, annealing at 400˚C for 1 hour made the average grain size of the Al-Mg-Sc alloy increase from 0.2 μm to 1 μm, with an evolution of the grain boundaries into configurations that are less curved and wavy. HREM investigations indicated the

motion of the grain boundaries were inhibited by the incoherent and spherical Al_3Sc particles which lie on the high angle grain boundaries.

Ning et al. [136] investigated the thermal stability of an Al-Mg-Mn alloy with Zr addition processed by ECAP at 350˚C and followed by water quenching or air cooling. After the air cooling process, the microstructure of the Zr-free alloy was much coarser than that of the Zr-containing alloy due to the static recovery and static recrystallization in the Zr-free alloy and Al_3Zr particles pinning the dislocation in the Zr-containing alloy. Annealing at 460˚C for 1 hour was applied to both alloys processed by ECAP followed by water quenching. The grain size of the Zr-free alloy increased to 181 μm due to secondary recrystallization. However, only very slight grain growth was observed in the Zr-contained alloy and the grain size only increased to 3.7 μm even after holding 1 hour at 460˚C because of Al_3Zr inhibiting the recrystallization.

Hasegawa et al. [137] studied the thermal stability of pure Al, Al-Mg and Al-Zr aluminum alloys after ECAP during annealing at 100˚C-500˚C for 1 hour. The fine and uniform microstructure of Al-Zr alloys can remain stable up to 300˚C with a slight grain growth. By contrast, annealing at 200˚C led to a duplex microstructure of large and small grains in pure Al and Al-Mg alloys due to abnormal grain growth. Also here the enhanced stability of the Al-Zr alloy was attributed to the precipitation of Al_3Zr particles which inhibit grain growth.

The thermal stability of many other commercial UFG aluminum alloys has been studied. An UFG Al-3wt%Mg-1wt%Li alloy with a composition based on commercial alloys AA5901 was obtained by spray casting and ECAP [138]. The thermal stability of the Al-3wt%Mg-1wt%Li alloy during annealing at 300-500˚C was studied. Isochronal annealing (for 1 hour) at temperatures up to 400˚C led to a limited amount of grain growth, for example, the grain size was 0.7 μm after holding for 1 hour at 400˚C. In contrast, when the annealing period was prolonged to 5 hours, a bimodal grain size distribution was observed due to abnormal grain growth. In an Al-3wt%Mg-2wt%Li alloy (i.e. with 1wt% more Li) the abnormal grain growth was not found until a much longer time of 35 hours at 400˚C. This was attributed to a significant increase in amount of Al_2LiMg particles which are distributed relatively homogeneously. The homogeneous distribution of the dispersoid particles inhibited

the abnormal grain growth during annealing. Mao et al. [139] studied the thermal stability of a 2024 (Al-4wt%Cu-1.5wt%Mg-0.4wt%Mn) aluminum alloy after ECAP. The UFG microstructure can remain up to 200˚C. After annealing at 300˚C for 1 hour, the grain size had been increased a little but was still at submicrometer scale.

Horita et al. [140] investigated the thermal stability of several commercial aluminium alloys (1100, 2024, 3004, 5083, 6061 and 7075) after 4, 6 and 8 passes of ECAP. After ECAP at room temperature for at least 4 passages, the alloys were statically annealed for 1 hour at 100˚C, 200˚C and 300˚C. The microstructure of all aluminium alloys did not change during 1 hour annealing at 100˚C. When the annealing temperature was increased to 200˚C, the dislocation density in the grains was reduced, the grain boundaries were clearer and the grain size were still at submicrometer level. However, annealing at 300˚C resulted in significant grain growth in the 1100, 3004, 5083 and 6061 aluminium alloys but limited grain growth in 2024 and 7075 aluminium alloys. Annealing of the 1100 and 3004 alloys after ECAP showed that the yield stresses, the UTS, and the elongations to failure remained reasonably constant within the region of constant grain size up to annealing temperatures of around 200˚C.

In summary, the thermal stability of UFG aluminium alloys processed by ECAP depends on many factors including strain, composition and second phase particles. A total effective strain of up to 8 leads to a homogeneous deformation of the whole sample and a uniform recrystallization during the annealing. The UFG microstructure of all aluminium alloys processed by ECAP, including pure aluminium, remains essentially unchanged up to 200˚C by comparison with the microstructure in as-pressed condition. The UFG aluminium alloys with fine and dispersed particles can be stable up to 400˚C because the precipitates restrict the movement of grain boundaries and the rate of grain growth is controlled. More data about thermal stability of UFG aluminium alloys processed by ECAP are shown in the Table 2.1.

2.6.3.3 Properties of aluminium alloys after ECAP

2.6.3.3.1 Strength and Ductility at room temperature

Pure aluminium has a good ductility because of its FCC crystal structure but has a low strength. The ultimate tensile strength (UTS) of annealed commercial pure

aluminium is about 50-70 MPa with an elongation of ~30%. Alloying and thermomechanical treatment can strongly improve the strength but the ductility will generally be reduced.

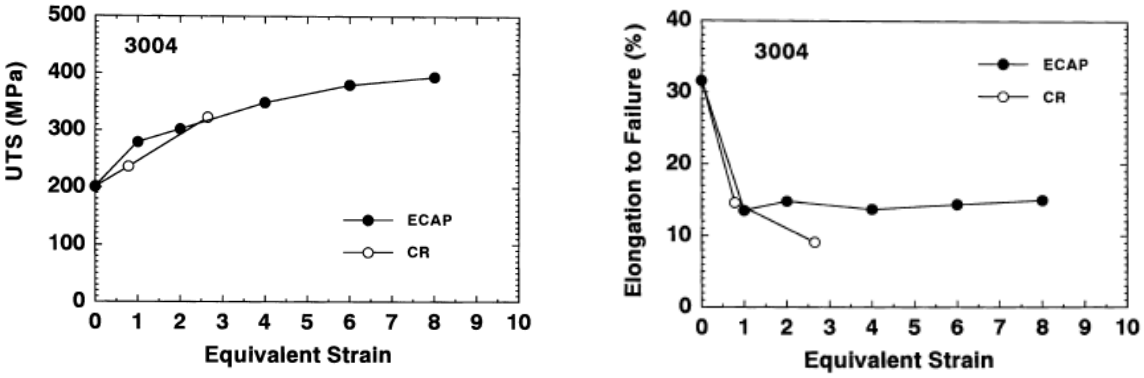

(a) UTS (b) elongation to failure.

Fig. 2.29 Comparison of tensile properties of cold rolling and ECAP for AA3004 [140]

Compared with conventional deformation process, such as rolling and extrusion, ECAP can lead to a stronger increase in the strength of non heat treatable aluminium alloys with an improved ductility of aluminium alloys. Horita et al. [140] compared the tensile properties of AA3004 (Al-1.15%Mg-1.0%Mn-0.44%Fe-0.2%Si-0.14%Cu) after cold rolling and ECAP. As illustrated by the data plotted in Fig. 2.29, the UTS of AA3004 processed by either cold rolling or ECAP increased monotonically with increasing equivalent strain. After 8 passes of ECAP, the UTS of AA3004 is higher than that of alloys processed by cold rolling. After one ECAP pass, the elongation to failure reduces from ~32% to ~14%, and there is nearly no change in the ductility with additional ECAP passes. By contrast, cold rolling decreases the ductility by a similar magnitude initially but thereafter the ductility continues to decrease with increasing rolling strain. Consequently, processing by ECAP leads to a greater retention of ductility and a higher strength than conventional cold-rolling.

The reason why UFG materials have both high strength and relative high ductility is not clear. Valiev et al. [141,142] considered that it was associated with the dominant deformation mechanisms changing from dislocation glide on preferred slip systems to grain boundary sliding and grain rotation. Grain boundary sliding is a diffusion-controlled process, it should occur preferentially at high temperatures where

diffusion rates are reasonably rapid. However, the fraction of high-angle grain boundaries is increased with increasing straining in the severe plastic deformation, and the number of grain boundaries per volume increases as the grain size is reduced. Also the grain boundaries of UFG materials are in non-equilibrium configurations. Therefore, it is reasonable to expect that the diffusion coefficient increases. So the deformation mode is changed to grain boundary sliding and grain rotation and ductility is enhanced.

Another interpretation of ductility enhancement was presented by the introduction of a bimodal distribution of grain sizes [143]. The materials, with a bimodal structure of micrometer size grains embedded in a larger grain matrix, exhibited an exceptionally high ductility but retained a very high strength because the embedded larger grains stabilize the tensile deformation of the material while the nanocrystalline grains provide strength.

Texture which has a strong effect on the strength and ductility of magnesium alloys [144] does not make an important contribution on the high strength and high ductility of aluminium alloys processed by ECAP. Only 1 basal slip system ((0002)<11$\bar{2}$0>) in magnesium alloys [145,146] except Mg-Li alloys [147] can be activated at room temperature because of their HCP crystal structure. Therefore the direction of base plane in magnesium alloys strongly influence the yield strength and elongation of magnesium alloys. Generally, the direction of (0002) plane in magnesium alloys tends to incline about 45^{o} to the pressing direction after ECAP [148], therefore the Schimid factor of basal slip system is nearly up to 0.5, which make basal slip system activate easily and increase the elongation. As contrast, 12 independent slip systems in aluminium alloys can be activated at room temperature because their FCC crystal structure. So the adjustment of texture during ECAP process does not have strong effect on strength and ductility of aluminium alloys.

2.6.3.3.2 Superplasticity

It is generally accepted that grain-boundary sliding is the main deformation mechanism of superplasticity [149] and a fine, stable and high-angle grain structure is key to achieving viable superplasticity for Al alloys. The UFG aluminium alloys processed by ECAP can meet all the requirements for superplasticity, which has been

introduced in Section 2.6.3.1. Actually, most aluminium alloys processed by ECAP can obtain superplasticity, which is shown in Table 2.1.

One of the advantages of UFG aluminium alloys processed by ECAP is the occurrence of superplasticity at high strain rate. An example is a commercial Al-Mg-Li-Zr alloy processed by ECAP, which achieved an elongation of 970% during a tensile test at 350˚C at a stain rate of $1.0\times10^{-1}s^{-1}$ [150]. The high strain rate superplasticity formally refers to the superplastic elongations occur at strain rates at and above $1.0\times10^{-2}s^{-1}$. Industrial superplastic forming is generally performed at stain rates ranging from $1.0\times10^{-3}s^{-1}$ to $1.0\times10^{-2}s^{-1}$. The high strain rate superplasticity will be attractive because it will decrease moulding time and improve the productivity.

The reason why UFG aluminium alloys can be deformed superplastically at high strain rate can be interpreted by following the equation for the steady state strain rate given by Langdon [151]:

$$\dot{\varepsilon}_{sp} = \frac{AD_{gb}Gb}{kT}\left(\frac{b}{d}\right)^2\left(\frac{\sigma}{G}\right)^2 \qquad \text{Eq. 2.11}$$

where $\dot{\varepsilon}_{sp}$ — the steady state strain rate

A — a dimensionless constant

D_{gb} — the coefficient for grain boundary diffusion

G — the shear modulus

b — the Burgers vector

k — Boltzmann's constant

T — the absolute temperature

d — the grain size.

Eq. 2.11 is derived from semiempirical Eq. 2.12 [152]

$$\dot{\varepsilon} = \frac{ADGb}{kT}\left(\frac{b}{d}\right)^{p}\left(\frac{\sigma}{G}\right)^{n} \qquad \text{Eq. 2.12}$$

which was established based on experimental investigations and theoretical considerations of the steady-state conditions in high temperature creep. Langdon [151] proposed a unified model for Rachinger sliding for all grain sizes based on theoretical analysis and superplastic experiments. This model leads to n=2, p=2 and D=D_{gb} for small grain sizes, therefore Eq. 2.12 appears to the form of Eq. 2.11.

ECAP is capable of producing UFG aluminium alloys with grain sizes in the range of hundreds of nanometres. A conclusion can be drawn using Eq. 2.11 that the strain rate associated with optimum superplasticity increases with the decreasing grain size, for instance, if the grain size reduces by ten times, strain rate will increase by a hundred times. Therefore the superplastic deformations can be performed at high strain rate.

Another advantage of UFG aluminium alloys processed by ECAP is that the superplasticity can be achieved at lower temperature. Superplasticity in conventional superplastic metals generally occurs at high temperatures because it is a diffusion-controlled process and diffusion rate is large at high temperatures. Typically, superplasticity temperature is around or slightly higher than $0.5T_{\mathrm{m}}$ where T_{m} is the melting point of the material in absolute temperature. As to UFG aluminium alloys processed by ECAP, the diffusion coefficient at the grain boundary increases because the grain boundaries are in the non-equilibrium configurations, the density of grain boundaries is increased because the grain size is in the submicrometer range. Therefore the superplastic deformation can be performed at lower temperatures.

2.7 Summary

Pure aluminium has a good electrical and thermal conductivity but a low strength. A small amount of Zr addition to aluminium significantly increases the strength and thermal stability with limited influence on thermal conductivity. Al-Zr alloys appear suitable to produce MEMS components that rely on thermal conduction, for instance a cross flow micro heat exchanger. However, fabrication of microchannels for (cooling) fluids by embossing using conventional coarse grained metals has some

problems, such as large embossing force, high failure rate of the mould and rounded channel edges. Those problems could be resolved by using UFG Al produced by SPD. UFG Al alloys processed by ECAP has a very small grain size (typically, ~ 1 μm) with a large fraction of high angle grain boundaries, which leads to superplastic forming at reduced temperatures with a smaller forming load. Additionally, the UFG Al can be formed to microchannels with sharp edges. Nanoindentation is a unique technique to characterize the mechanical property of MEMS components. The indentation size effect (ISE) need to be better understood before testing. The existing models for ISE can not accurately predict nanohardness over the entire range of indentations, especially for depths lower than 150 nm.

3 Design of Equipment

As part of the PhD project a range of equipment was designed, manufactured and commissioned. Design was performed by the author, with input from the supervisors and several individuals named below and in the Acknowledgements section. Manufacturing was done both in-house and by outside contractors; and commissioning was performed by the author.

3.1 ECAP facilities

An ECAP die and a plunger used for room temperature ECAP process were made of H13 tool steel by precision machining. Design of the die and the plunger were based on a tried and tested one provided by Prof. T.G. Langdon. The main dimensions were changed to fit the work space of available hydraulic press machine. The drawing of the plunger is illustrated in Fig. 3.1. The whole length of the plunger is 145.0mm and a thread head was in the one end for connection with the press. The work part of the plunger is 90.0mm in length and 9.68mm in diameter.

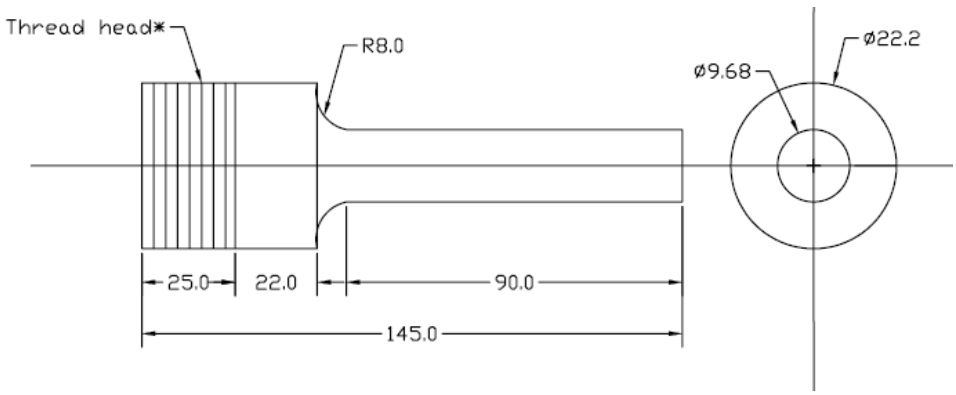

Fig. 3.1 A plunger for ECAP process

The drawing of the die is shown in Fig. 3.2. The ECAP die is machined from a steel block of dimensions 101.6 mm × 82.6 mm × 152.4 mm. The diameter of the upper channel is 9.7mm. The diameter of the bottom one is 9.5mm for the inner part and 9.9mm for the outer part. The inner angle (Φ) and outer angle (Ψ) between the two channels are 90˚ and 20˚ respectively. Two U-shape grooves are at both side of the die bottom for fixing with the press by clamps.

A second ECAP die to be used for elevated temperature has also been fabricated. The design is similar to the one for room temperature. Four additional holes were drilled on the ECAP die used at elevated temperature (Fig. 3.3). The holes are used to hold the heat cartridges for heating the die. The diameter of the cylindrical holes is 10.0mm with the tolerance of from +0.05 to +0.10.

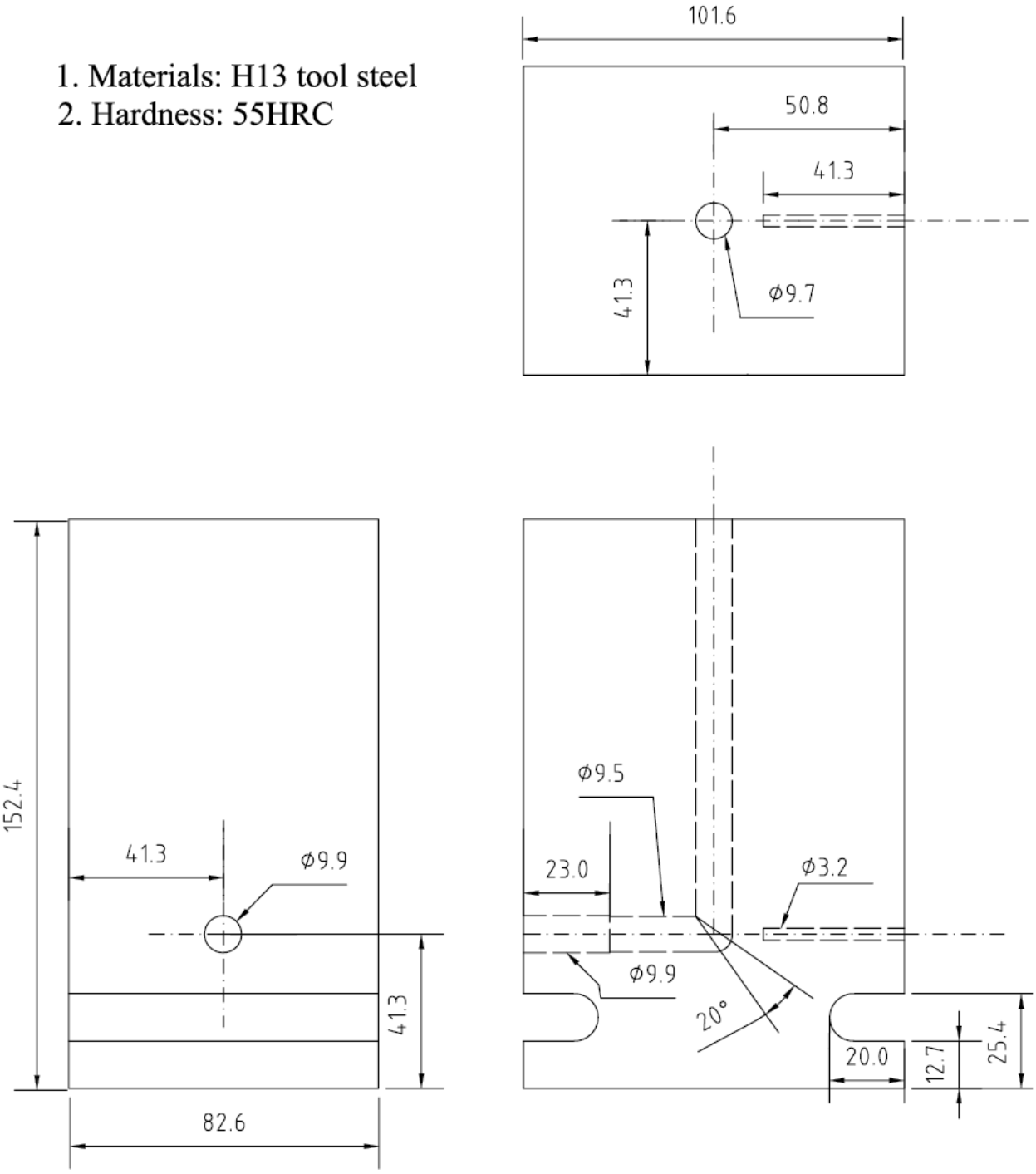

Fig. 3.2 The drawing of the ECAP die for room temperature processing

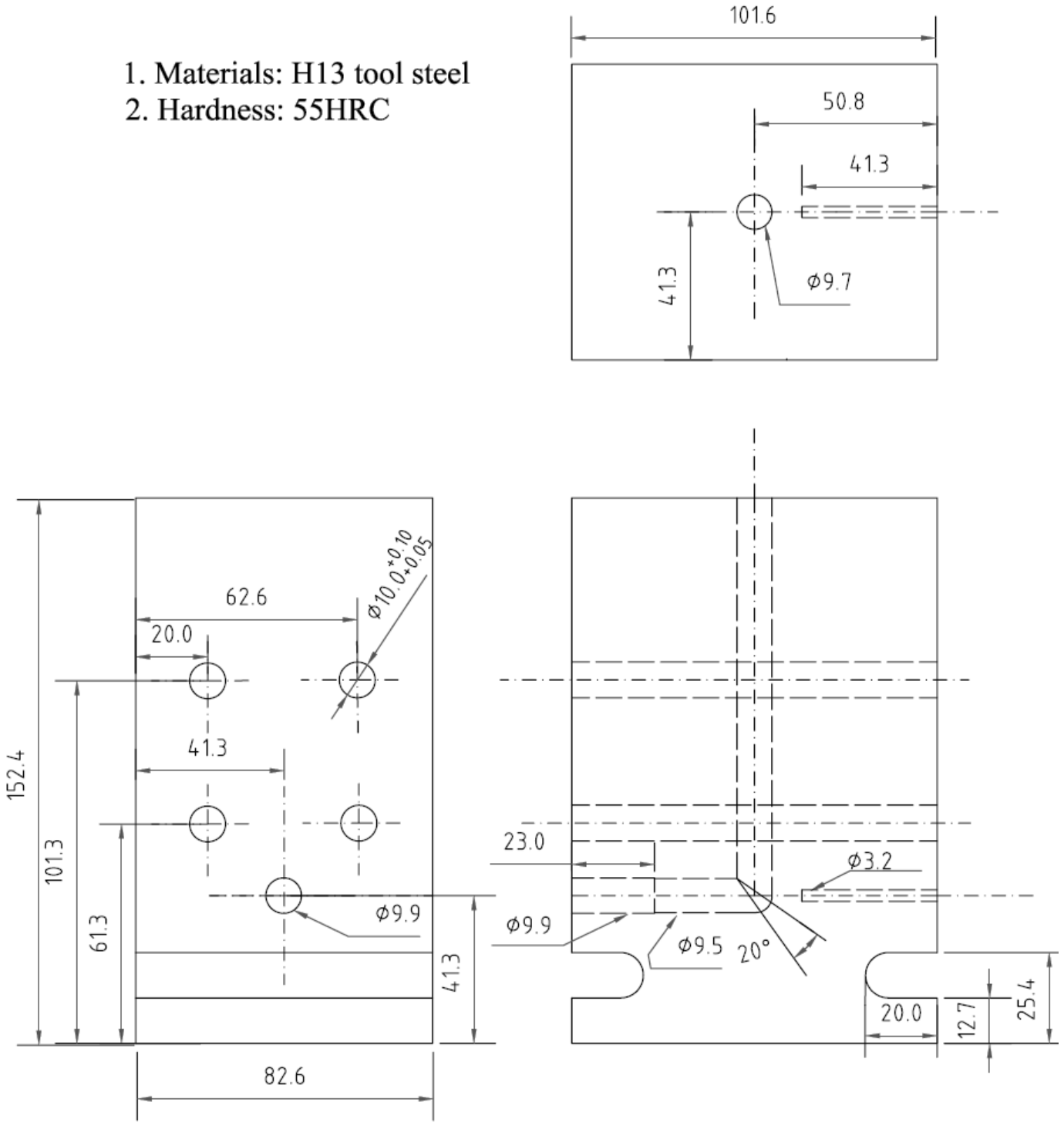

Fig. 3.3 The drawing of the ECAP die for elevated temperature processing

A 200 ton DMG hydraulic press is used to perform the ECAP process (see Fig. 3.4). The working distance is 85mm. The press has a speed control ranging from 0.01 to 50 mm/s. Two special clamps and an additional fixture were designed and fabricated to fix the plunger and ECAP die to the press. The ECAP process system with the die, the plunger and the fixture is illustrated in Fig. 3.4.

Fig. 3.4 ECAP process system

3.2 ECAP processing procedures

Specimen were lubricated with a suspension of MoS_2 in mineral oil ('ASO oil' supplied by Rocol) in order to reduce the friction between the plunger, specimen and the die. A careful alignment of the plunger and upper channel of the die was carried out to avoid the plunger bending. The plunger was pressed into the die at speed of 0.5mm/s and was pulled out at speed of 5mm/s. After one pass of ECAP, another specimen was put in the die to push out the first specimen. The ECAP process was conducted for 1, 2, 4, 8 and 12 passes respectively using route Bc [118] at room temperature.

3.3 Embossing Facilities

The embossing facilities(see Fig. 3.5) used in present experiments consist of loading system, platens, alignment system, connecting parts, heating system, cooling system, control system and die. Drawings of each part are shown in Appendix A.

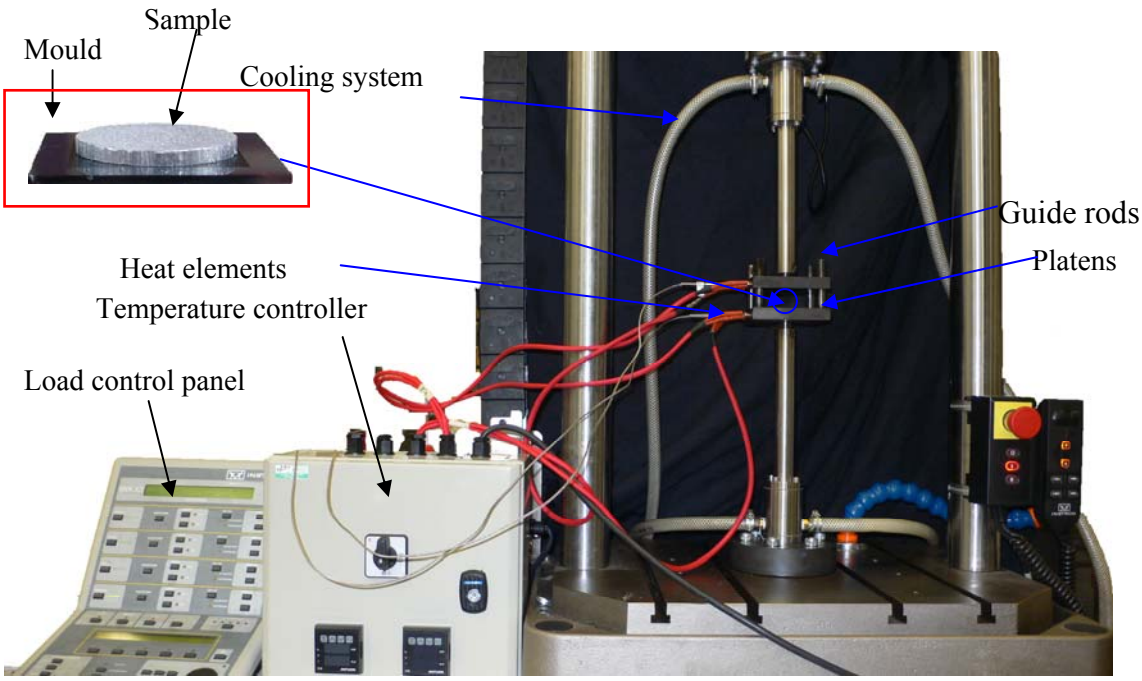

Fig. 3.5 The embossing setup showing different components used in the experiments; the inset photo in a red box shows the sample and the silicon mould.

Loading system The embossing process was carried out on a 9510 Instron hydraulic testing machine. It can be controlled by force and position. The load capacity of this machine is 10 kN. The load can be increased by the means of ramp and cycle. The position of the top beam can be changed to adjust the distance between the top beam and bottom stage. The moving distance of the working punch is between -52 cm to +52 cm.

Platen design The platens are critical components of the embossing facilities. The platens are designed to support the work piece and the die and maintain their orientation. The platens are made of mild steel and have dimensions of 80 mm × 80 mm × 20 mm. Holes in each corner of the two platens, are to provide the means for an accurate alignment. Two position marks are made in the centre of both two work surfaces for attaching the work piece and the die. The bottom and top platens are designed to be attached the bottom base and the top beam of the Instron machine, respectively. The work surface of both two platens is carefully polished to obtain a smooth and flat work surface. Two holes are drilled through each platen to contain the heat elements. A blind hole is drilled in each platen to contain a thermal couple.

The end of the blind hole is under the position marks to accurately measure the sample temperature.

Alignment system The alignment is a critical issue for designing a suitable embossing facility. The size of the channel to be embossed is in the micrometer range, so any minor deviation will lead to a flawed product, and can even cause damage of the micro silicon die. The purpose of the alignment design is to make the work surface of the two platens parallel. This is achieved in two ways. One is to limit the tolerance of the platens and connecting parts through precision machining. The other is through connecting the two platens by four guide rods, which is schematically presented in Fig. 3.6, see also Fig. 3.5 and Appendix A for dimensions. The guide rods are fixed to the bottom platen though which the top platen slides in vertical direction. The guide rods are lubricated and have a carefully designated tolerance, so that the top platen can slide smoothly along the guide rods.

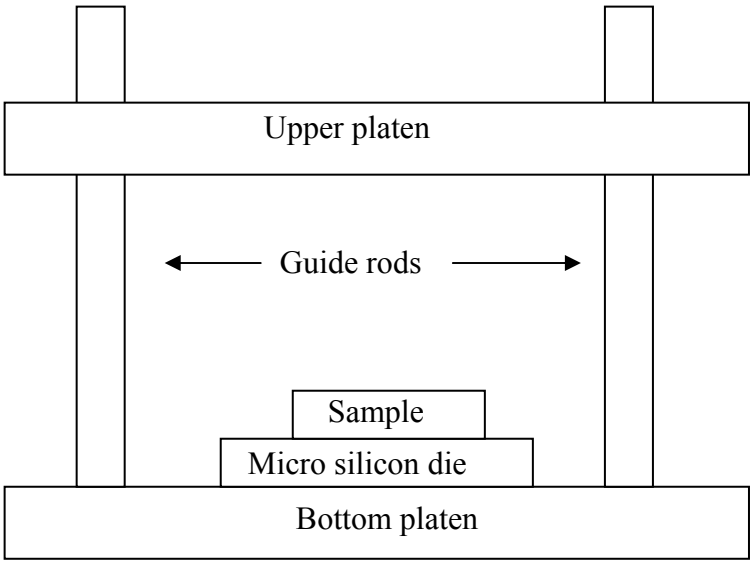

Fig. 3.6 Schematic drawing of embossing rig equipped with guide rods.

Connecting parts Two stainless steel shafts are used to connect the platens to the load cell and the bottom base of the Instron machine. The shafts are 210 mm long and 28 mm in diameter. The long axis of the shafts is perpendicular to the end surface in 0.05 degree.

Heating system The heating system consists of heating elements, control unit, and thermo couples. The four heating elements are 80 mm long rods in diameter of 9.8

mm and provide a maximum power of 2000 kW. The two thermo couple wires are encapsulated in a 40 mm long rod in diameter of 6 mm; they measure temperature with accuracy of ±0.2 ˚C. The controlling unit uses PID temperature control. During heating, the heat elements and thermal couples are put in the holes of the platens. One thermal couple controls two heat elements in the same platen.

Cooling system The design incorporates a water cooling system to prevent the load cell and Instron machine frame from being heated through gradually dissipation. Two water chambers made of stainless steel are used. One is installed between the load cell and the connecting shaft to secure the load cell, the other is fixed between the machine base and the other connecting shaft. The chambers are divided into two cavities by a plate in order to increase the water flow time in the chamber. Tap water is used as the coolant, with possible further modifications to incorporate a coolant recirculating system.

Control system Position and force controls are realized through the Instron machine. A separate temperature control unit is used to control the heating cartridges to achieve the embossing temperature.

Fabrication of micro silicon die The micro silicon die has been fabricated by the PEGASUS™ DRIE source from Surface Technology System plc. The DRIE process is illustrated schematically in Fig. 3.7. Firstly, a thin layer of silicon oxide or silicon nitride is put on the wafer and used as an etch mask for DRIE (Fig. 3.7 step 1). Secondly, the photolithography is carried out using a layer of UV-photo resist. The current resist is S1818 model negative resist from Shipley Corporation with a thickness of 2μm. After that, a glass mask with pattern is carefully aligned to the silicon wafer, and the photo resist is exposed (Fig. 3.7 step 2). Thirdly, the silicon oxide or nitride layer is etched using RIE and the pattern will be transferred to it (Fig. 3.7 step 3). Fourthly, the photo resist is removed by a solvent (Fig. 3.7 step 4). Finally, the substrate silicon wafer will be etched by DRIE (Fig. 3.7 step 5).

During this process, design and fabrication of the glass mask for photolithography are very important because the final configuration of the wafer depends on the pattern on the mask. In this work, initially only one mask is planned to be used. The mask is designed to contain 69 chips. The sketch of mask design shown in Fig. 3.8

was drawn using AutoCAD, which is only for presenting. The drawing of mask design for DRIE was completed on professional software named L-edit.

There are 4 types of chips in these 69 chips. Type A are chips that have a uniform channel width, with the width of grating equal to that of channel. Type A chip is illustrated in Fig. 3.9. There are 45 type A chips with channel width of 3μm, 5μm, 10μm, 25μm and 50μm respectively, and 9 chips for each channel width. Type B has mixed channel width with two dimensions, see Fig. 3.10. The combination of channel width includes 3μm and 5μm, 5μm and 10μm, 10μm and 25μm, and 25μm and 50μm. There are 4 chips for each combination and in total there are 16 type B chips. Type C chips have uniform diameter cylinders on it and the distance between cylinders is equal to the diameter, as illustrated in Fig. 3.11. There are 4 type C chips with the cylinder diameter of 3μm, 5μm, 10μm and 25μm, and 1 chip for each diameter. Type D chips have uniform side length cubes on it and the distance between cubes is equal to the side length. Type D chip is illustrated in Fig. 3.12. There are 4 type D chips with the side length of 3μm, 5μm, 10μm and 25μm, and 1 chip for each side length. Type A and type B chips are used to fabricate the micro heat exchangers components. The type C and type D are used to comparison.

After the mask is fabricated, the various chips with different layout and dimensions can be obtained by different etching time to get different etching depth in the DRIE process. Therefore the different channel widths and depths can be achieved with one mask. Prof M. Kraft and Dr Zakaria Moktadir provided important input in the design process of the microsilicon die.

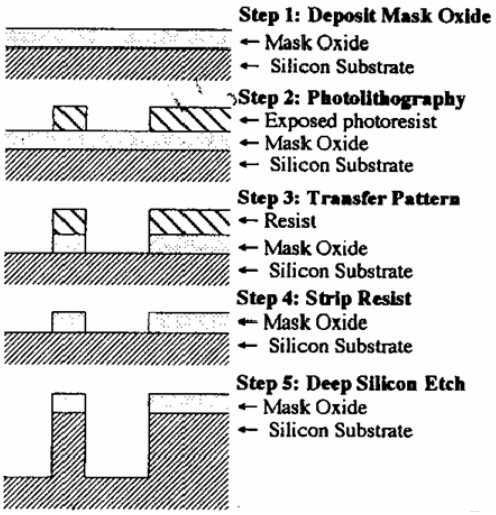

Fig. 3.7 DRIE process with different channel width in a wafer.

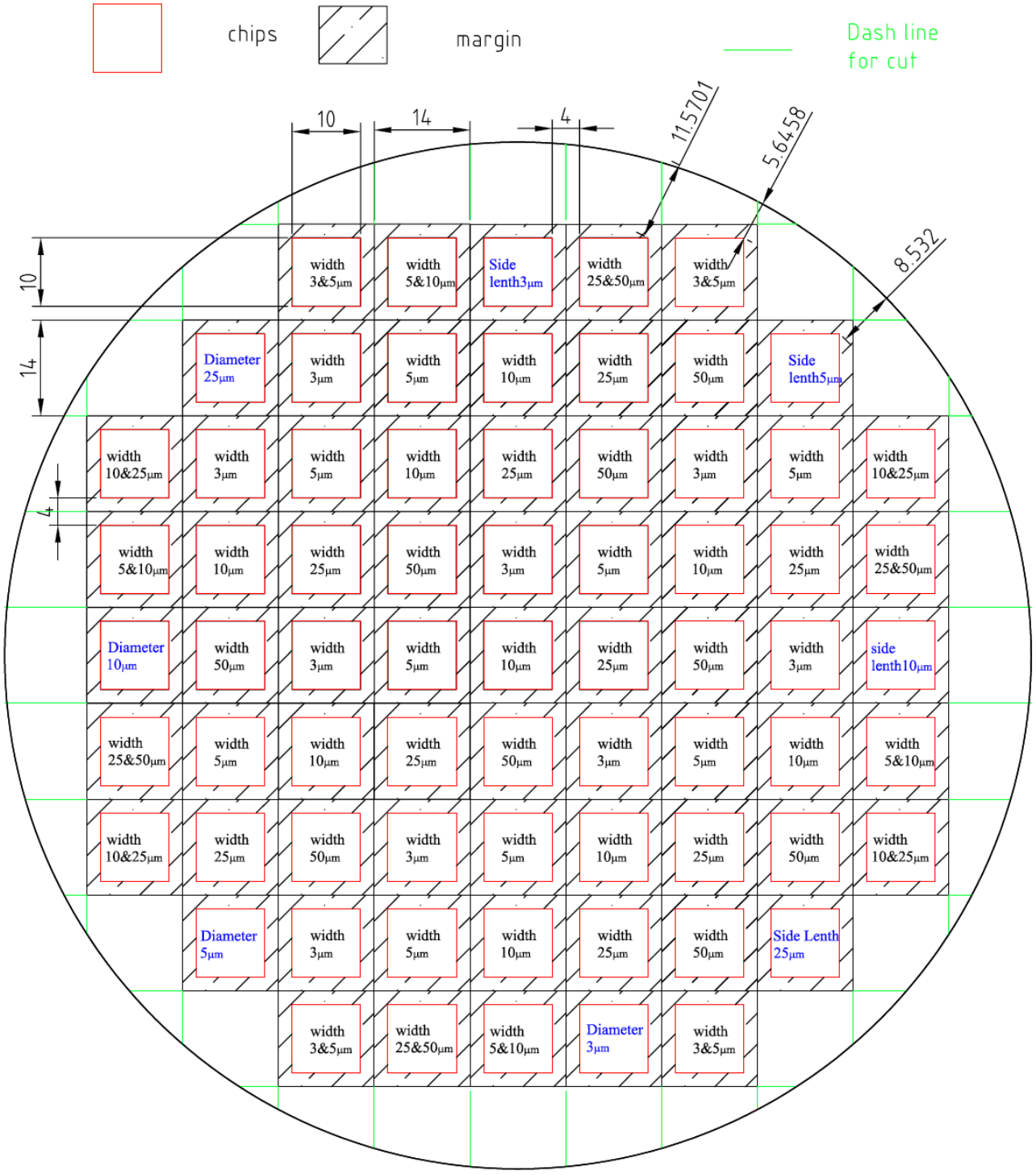

1.Depth of channel: 3, 5, 10, 25 and 50 μm.
2.One wafer one depth. Totally 5 wafers.
3.In one wafer:
i. 5 channel width dimensions are chosen, 3, 5, 10, 25 and 50 micrometers.
ii. 9 pieces chips for each single dimension.
iii. 4 kinds of chips with two mixed channel width dimensions, which are 3&5, 5&10, 10&25 and 25&50, are put in the edge of the wafer. 4 pieces for each.
iv. Groove grating equals to groove width.
v. 4 kinds of cubic array with side length 3, 5, 10, 25 micrometers. Space length equal side length. 1 piece for each.
vi. 4 kinds of cylinder array with diameter 3, 5, 10, 25 micrometers. Space length equal diameter. 1 piece for each.
vii. total 9*5+4*4+1*4+1*4=69 pieces chips for one wafer.

Fig. 3.8 Mask design

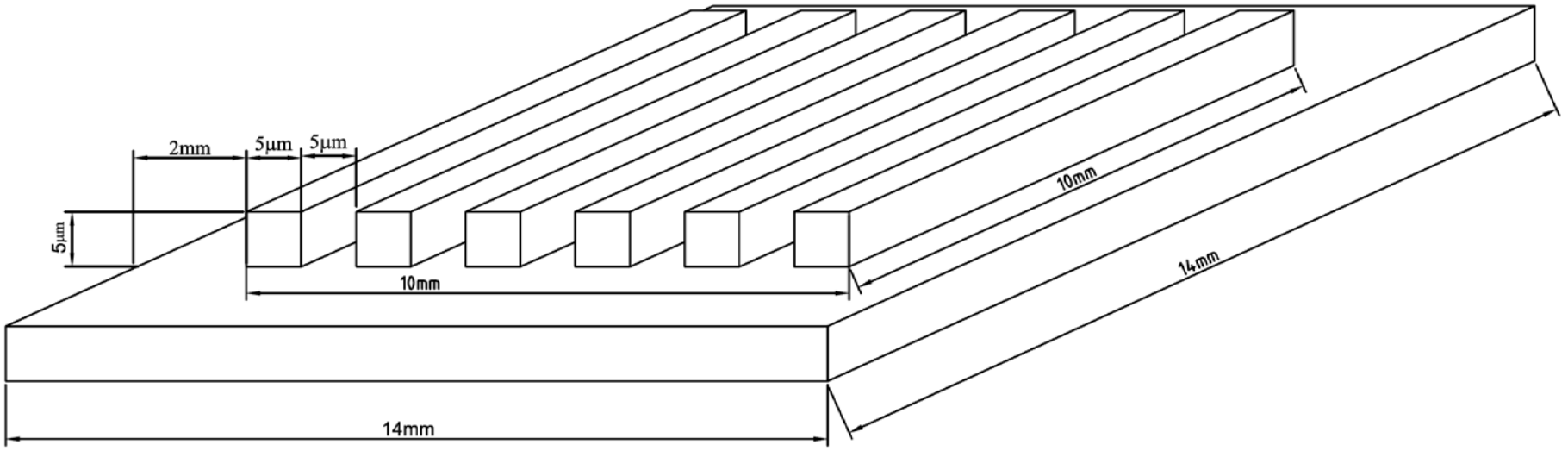

Fig. 3.9 the schematic drawing of type A chips

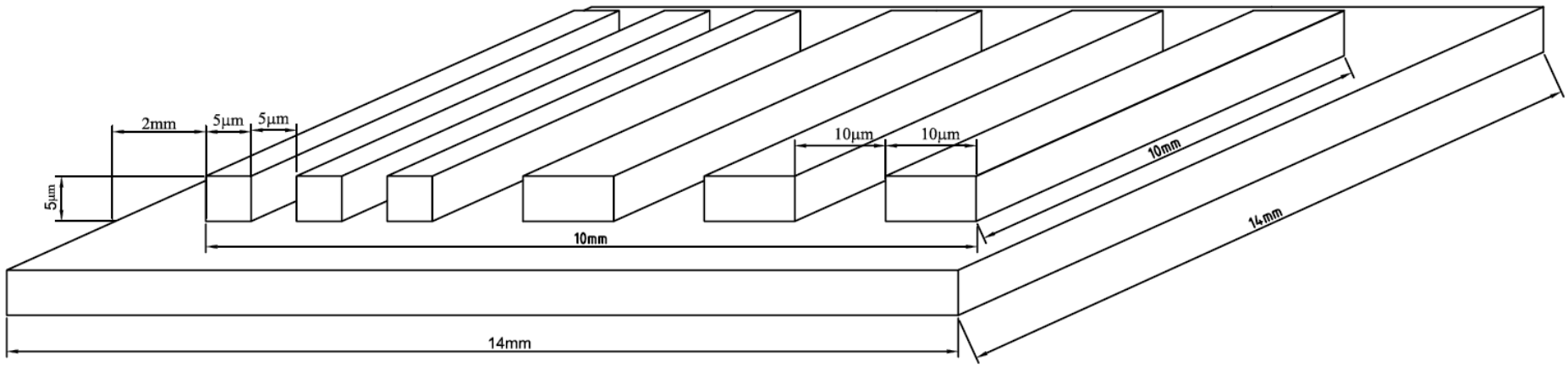

Fig. 3.10 the schematic drawing of type B chips

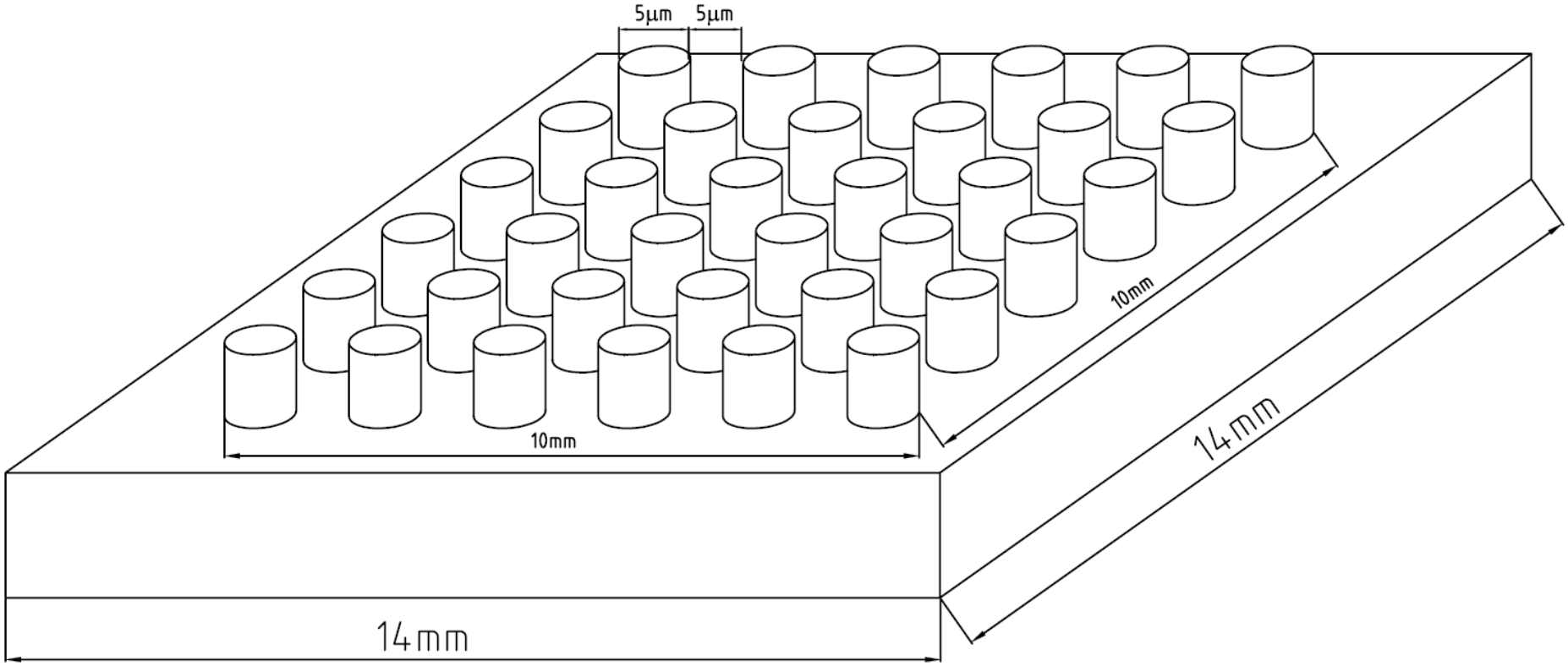

Fig. 3.11 the schematic drawing of type C chips

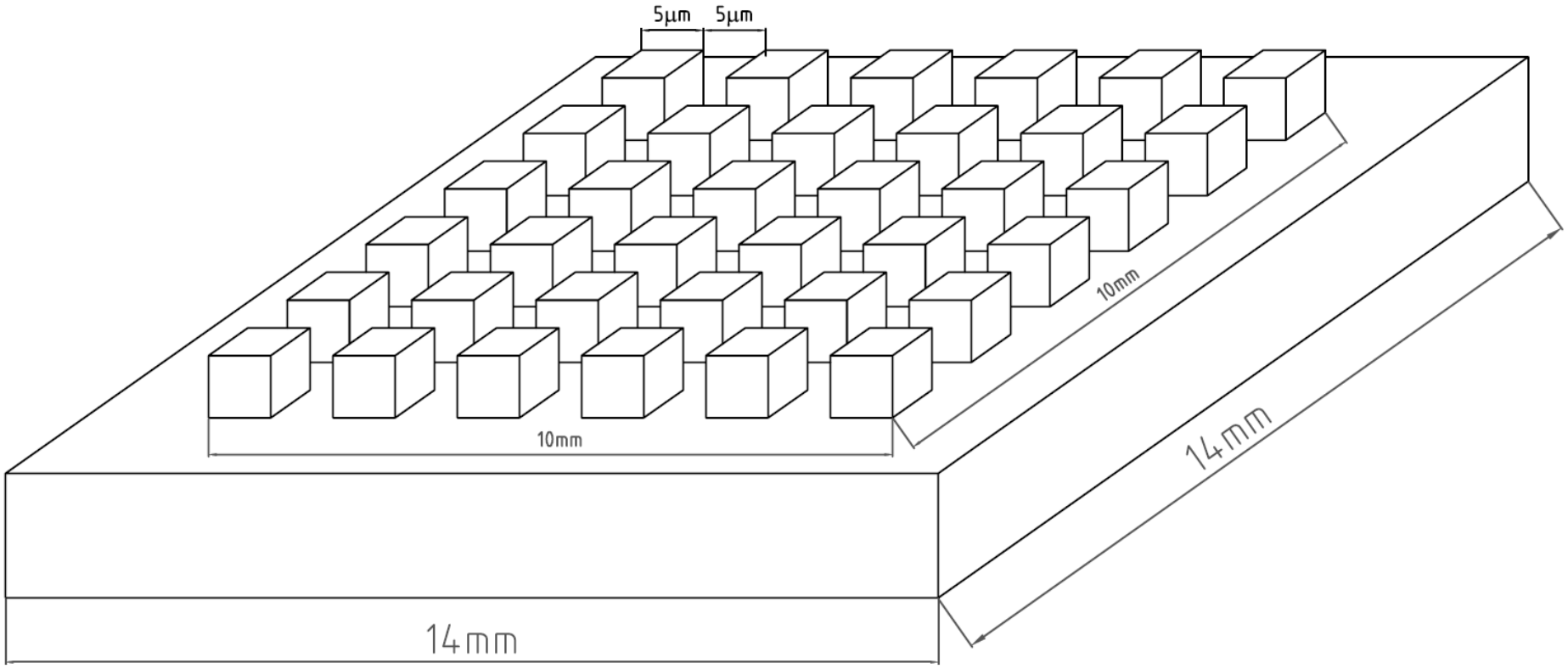

Fig. 3.12 the schematic drawing of type D chips

3.4 Embossing process and procedures

The embossing process involves three steps: rig set up, heating the micro silicon die and work piece to work temperature, and hot embossing. 1 mm thick samples in diameter of 9.6 mm were machined from ECAP-processed billets with broad faces perpendicular to the longitudinal direction. The circular surface was ground by abrasive papers from 600 grits to 1200 grits then polished to mirror-like surface. The embossing process was carried out on the circular surface by the micro silicon die.

The main steps in the procedures are as follows:

Rig set up

Adjust the position of the Instron beam.

Connect all the parts together in the order of load cell, water chamber, shaft, upper platen, guide rods, bottom platen, shaft, water chamber and Instron base.

Adjust the alignment and ensure the upper platen can slide smoothly along the guide rods to the bottom platen.

Set up heating system.

Connect the water passages of the cooling system.

Heating

Put micro silicon die on the bottom platen and the aluminium foil on the die.

Set the temperature parameters on the temperature control unit.

Switch on heating elements and water valve.

Embossing process

Switch off the heating elements after the aluminium foil and the micro silicon die have been held for 5 minutes at the desired temperature.

Move the upper platen to touch the aluminium foil in the mode of position control.

Change to the mode of force control and set the forcing parameters on Instron control panel, then start embossing.

Demoulding

Raise the upper platen and take out the embossed foil.

4 Material, Testing and Microstructural Analysis

This section introduces the material, testing, microstructural analyses methods and experimental procedures involved in current study. The main stages of the project are as follows. Firstly, a suitable aluminium alloy with good thermal conductivity, good formability and high thermal stability is chosen. Secondly, ECAP is performed on it to produce an UFG aluminium alloy. The microstructure of the UFG aluminium alloy is analyzed by EBSD and TEM. Thermal stability of the UFG aluminium alloy is tested using microhardness test. Thirdly, the channel size of the micro heat exchanger is designed, and then micro silicon dies for embossing are fabricated by DRIE. Fourthly, the UFG aluminium alloy is embossed, and then the embossed alloy is inspected by SEM, FIB and nanoindentation.

4.1 Materials

Three aluminium alloys were used in this investigation; they are a commercial Al-1050 aluminium alloy, an Al-0.15Zr and an Al-0.16Zr-0.17Si-0.19Fe aluminium alloy. Al-1050 was chosen because it is cheap and easy to obtain, easy to process by ECAP, whilst it can be embossed at room temperature. Al-1050 was purchased from Wilsons Plc in the form of rod bar. The bar is 4m long and 9.53mm in diameter. Prior to ECAP, the bar was cut to ECAP samples of 65mm in length. Al-015Zr and Al-0.16Zr-0.17Si-0.19Fe were considered because of their expected thermal stability and superplasticity. They were supplied in plate with thickness of 12mm and width of 60mm, in as cast condition. The plates without heattreatment were subjected to ECAP after being cut into ECAP samples by electrical discharge machining (EDM). The chemical compositions of three alloys are shown in Table 4.1. The compositions are actual compositions obtained by chemical analysis (tested by BODYCOTE).

Table 4.1 Composition of aluminium alloys used in this study

Component	Al Wt. %	Cu	Fe	Mg	Mn	Si	Ti	Zr	Zn	Other, each
Al-1050	99.65	0.01	0.18	0.01	< 0.01	0.12	0.02	-	< 0.01	< 0.01
AlZr	Bal	< 0.01	< 0.01	< 0.01	< 0.01	< 0.01	< 0.01	0.15	< 0.01	< 0.01
AlZrSiFe	Bal	< 0.01	0.19	< 0.01	< 0.01	0.17	< 0.01	0.16	0.01	< 0.01

4.2 Heat treatment

To evaluate the thermal stability, the three UFG aluminium alloys after different passes of ECAP were heated to from 200˚C to 500˚C with step size of 50˚C, with a 30 minute hold at each temperature.

In order to study strengthening mechanism and microhardness inhomogeneity, Al-1050 processed by one pass of ECAP were annealed for 0.5 h at 200 ˚C, 250 ˚C, 275 ˚C, 300 ˚C, 325 ˚C, 350 ˚C and 375 ˚C, respectively.

4.3 Microhardness testing

Microhardness was tested on an MHT-1 model micro Vickers hardness tester. For thermal stability evaluation, 2mm thick samples were cut from the middle of ECAP processed billet for three alloys up to 12 passes. The circular surface was ground by abrasive papers from 600 grits to 1200 grits. Microhardness testing was carried out on the circular surface. Five individual values were measured in centre area for each sample. Distance between each indent was larger than five times of indent size. 300g force was applied and held for 15 second.

For a study of strengthening mechanisms (see Section 6), samples of 2 mm thickness were machined from ECAP-processed Al-1050 billets and heat treated Al-1050 billets along the longitudinal direction for microhardness testing. The circular surface was ground by abrasive papers from 600 grits to 1200 grits. Microhardness testing was carried out on the circular surface. As shown in Fig. 4.1, individual values of the microhardness were measured on two lines across the diameter of the circular surface from top to bottom in an incremental step of 0.5 mm. The distance between two lines is 0.5 mm and the endpoints of both two lines are 0.75 mm to the sample edge. The indentations were removed by grinding and polishing after the hardness values of every point were measured. The values were marked as A, A*, B and B* etc. The second hardness measurement was carried out at the same positions with the first measurement. The values were marked as A_1, A_1*, B_1 and B_1* etc. The hardness of each point was calculated through averaging the measurements of four individual indentations on the equivalent locations. For instance, the hardness at point A was calculated by averaging the hardness obtained from indentation at the equivalent positions A, A*, A_1 and A_1*. A force of 300 g was applied on all the samples except

for the softer 350 ˚C and 375 ˚C heat treated samples, where a 100 g load was applied. Holding time is 15 second for all microhardness testing.

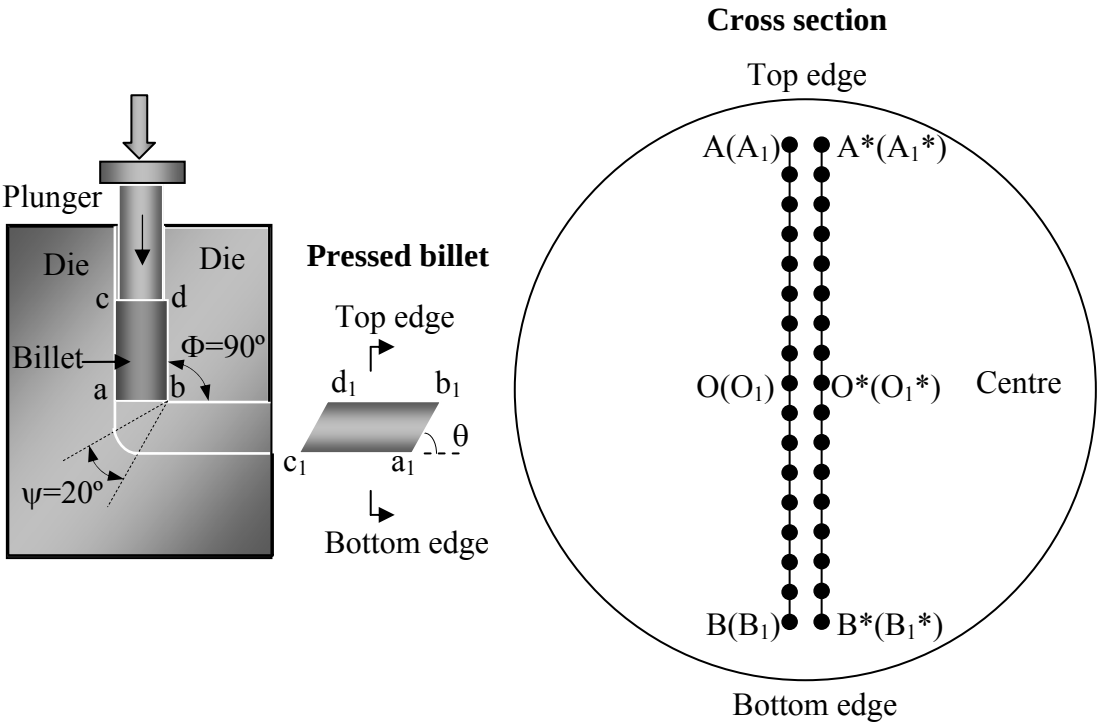

Fig. 4.1 Schematic illustration of cross section of the ECAP-processed Al-1050 billet for microhardness measurement.

4.4 Electron backscattered diffraction

Electron backscattered diffraction (EBSD) is used to characterize the microstructure as well as grain and subgrain boundary misorientation distribution in as-received, ECAP processed, heat treated and embossed alloys. Orientation imaging microscopy (OIM) was based on automatic indexing of electron backscattered diffraction patterns. The equipment used is a JEOL JSM6500F thermal field emission gun scanning electron microscope (FEG-SEM) equipped with an HKL EBSD detector and HKL Channel 5 software.

The samples used for EBSD analysis were 10 mm long and cut from the middle of ECAP processed specimen. The OIM was obtained from the cross section perpendicular to the extruded direction. The samples were first mechanically ground

by SiC paper, from 600 to 4000-grit. Then the sample was electropolished employing an electrolyte composed of 33vol% nitric acid and 67vol% methanol. The electropolishing was carried out with a DC voltage of 20-30V for a period of 30 seconds. The electrolyte was cooled to and maintained at a temperature of -30˚C with liquid nitrogen additions.

For EBSD samples were tilted so that the sample normal was at an angle of 60 degrees relative to the incident electron beam. The accelerating voltage was set to 15kV. Step sizes were between 0.1 and 8μm. A large step size of 8μm was used for as-received coarse samples. Smaller step sizes between 0.1μm and 1μm were used for ECAP processed sample in order to obtain better accuracy for the refined grain.

For observation of microstructure homogeneity of Al-1050 after one pass of ECAP, the OIM maps were obtained from the cross section perpendicular to the longitudinal direction of ECAP-processed billets and heat treated billets. The position of EBSD analysis were marked as A, O and B (see Fig. 4.1). For misorientation angle distributions the lowest cut off angle was set about 1˚ higher than the angle at which an apparent drastic increase in boundary angle density occurs. This apparent increase is due to local deformation and noise, and is thus eliminated from the experiments.

For observation of cross section of embossed Al, the cross section surface was prepared by focussed ion beam (FIB) milling (see section 4.9). The OIM maps were obtained from the milled surface of the cross section of the embossed samples. The step size was 0.1 μm. To characterize grain size, intercept lengths were determined using an automated procedure. For misorientation angle distributions the lowest cut off angle was set at 1˚.

A mean linear intercept method was used to measure the average grain size. The mean linear intercept length was determined by laying 50 uniformly distributed test lines on the OIM and counting the number of times that grain boundaries were intercepted. Grain sizes were calculated by dividing the line length by intercept number and magnification. All grain size values in this thesis are mean intercept lengths unless indicated otherwise.

4.5 Transmission electron microscopy

Transmission electron microscopy (TEM) is performed on ECAP processed Al-Zr alloys using a JEOL 3010 microscope operating at 300 kV. 500μm thick slices are cut from ECAP processed specimens perpendicular to the extrusion exit direction using electrical discharge machining (EDM). Subsequently the slices are ground to reduce the thickness to 40μm by 1000-grit SiC paper, and disks of 3mm in diameter are punched out from these slices. Twin jet polishing is employed to thin the disks to perforation using an electrolyte composed of 33% nitric acid and 67% methanol at a temperature of -30˚C.

4.6 Confocal laser system

A Taicaan Xyris 4000 Confocal Laser System was used to observe the surface topography of micro silicon dies for embossing. The motor and sensor specifications were shown in Table 4.2. The actual dimension of the groove width and depth of the die was also measured. The measuring area and step size were adapted to the groove size.

Table 4.2 Taicaan Xyris 4000 Confocal Laser System specifications

Motor			Sensor			
Travel	Resolution	Max Speed	Illumination Source	Spot size	Measurement Range	Sensor Resolution
25mm	0.1μm	25mm/ sec	670nm Laser (Visible Red)	2μm	0.6mm	0.01μm

4.7 Optical microscopy

The topography of the selected embossed samples and cross sections of embossed samples were observed by an Olympus BH-2 optical microscope (OM) equipped with a Prosilica digital CCD camera. The same microscope was used to observe the cross sections of embossed samples after nanoindentation test.

4.8 Scanning electron microscopy

A JEOL JSM 5910 scanning electron microscopy (SEM) was used to compare the surface topography of micro silicon die and that of aluminium components fabricated

by embossing. The actual dimension of the groove width and depth of the aluminium components was also measured by SEM.

4.9 Focussed ion beam microscopy

A Carl Zeiss XB1540 Focussed ion beam (FIB) was used to characterize the microstructure on the cross section of the embossed UFG Al-1050. The FIB was operated at 30 kV with ion beam current of 200 pA. To save milling time, before FIB milling, the embossed samples were cold mounted in transparent resin in direction of channels perpendicular to resin bottom surface, following cutting, grinding and polishing until a sharp and clear channel profile was observed. The milled surface was analyzed by EBSD.

4.10 Nanoindentation

The nanohardness distribution over the cross section of the embossed UFG Al-1050 was characterized by nanoindentation. The embossed UFG Al-1050 was cut perpendicular to the direction of the straight channels, then cold mounted in transparent resin at room temperature. The mounted sample was ground by SiC paper up to 4000-grit followed by rough polishing using one micron diamond paste and fine polishing using Struers OP-S suspension. The nanoindenter used is manufactured by Micro Materials Ltd, UK, equipped with a Berkovich tip. The instrument is positioned on an anti-vibration base and is enclosed in a temperature controlled cabinet which provides a thermally stable environment. The temperature is controlled at 25 ºC (with expected stability ± 0.1 ºC) inside the cabinet, and about 24 ºC outside. The indentation depths were set as 100 nm, 200 nm, 300 nm, 400 nm and 800 nm. The loading/unloading rate was 3 mN/s.

5 Analyzing Ultra Fine Grained Al Alloys

The microstructure and mechanical properties of Al alloys are significantly changed through ECAP processing. The initial passes of ECAP cause a substantial grain refinement with an inhomogeneous microstructure, whilst the later passes of ECAP lead to a further grain refinement with a more homogeneous microstructure. In this section, the evolution of microstructure and texture of UFG Al alloys during ECAP were analyzed by EBSD and TEM to understand mechanisms of grain refinement in Al alloys during ECAP. A predictive model for grain refinement is provided.

5.1 Results

5.1.1 Electron backscattered diffraction analysis

5.1.1.1 Grain sizes and grain boundaries in Al-1050

The grain structures of Al-1050 alloys before and after ECAP processing as determined by EBSD are shown in Fig. 5.1. Dark thick lines are used to represent high angle grain boundaries with misorientation angle greater than 15˚. The gray fine lines represent low angle grain boundaries of which the misorientation angle is smaller than 15˚ and greater than 2˚. Misorientations less than 2˚ were ignored in order to remove the noise.

The average grain size (mean intercept length) of as-received AAl050 alloys is 44 μm, which is shown in Fig. 5.1(a). After one pass of ECAP process, the grain structure became inhomogeneous. The grain size was refined to 15 μm (Fig. 5.1(b)), and many fine subgrain surrounded by low angle grain boundaries can be observed in the grain. In the further passes, the grain size was further refined to 11 μm for two passes (Fig. 5.1(c)), 4.9 μm for four passes (Fig. 5.1(d)), 1.3 μm for eight passes (Fig. 5.1(e)) and 0.88 μm for 12 passes (Fig. 5.1(f)). The comparison of grain size of Al-1050 alloy processed by ECAP for different passes is shown in Table 5.1.

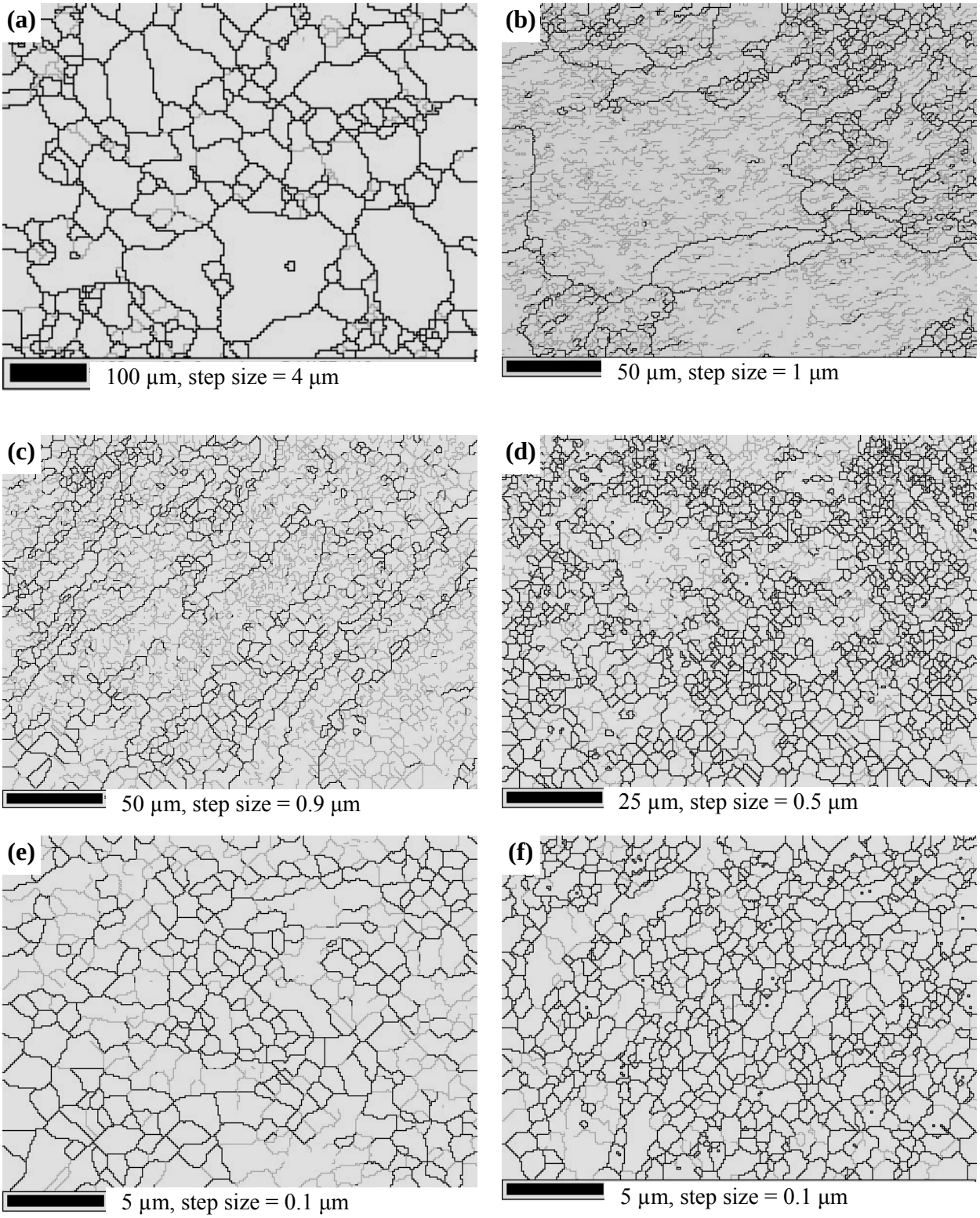

Fig. 5.1 Microstructure of Al-1050 alloys from EBSD (a) in the as-received conditions and processed by ECAP for (b) 1, (c) 2, (d) 4, (e) 8 and (f) 12 passes.

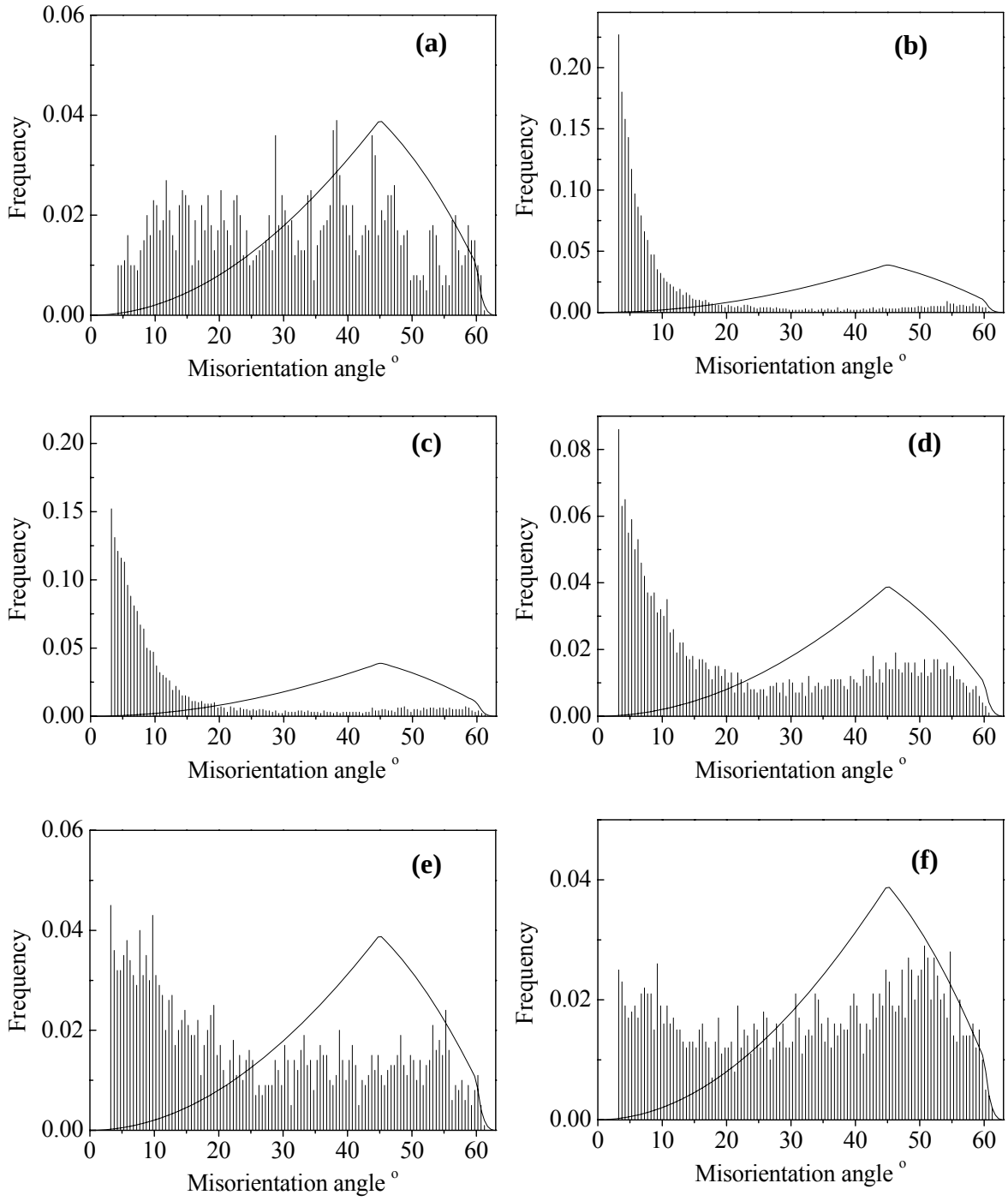

Fig. 5.2 Grain boundary misorientation distribution for Al-1050 alloys (a) in the as-received conditions and processed by ECAP for (b) 1, (c) 2, (d) 4, (e) 8 and (f) 12 passes. The curves in the figures represent the theoretical misorientation distribution of randomly oriented grains [153]

Fig. 5.2 shows the misorientation distribution of Al-1050 alloy in as-received conditions and after 1, 2, 4, 8 and 12 passes of ECAP, respectively. The curves in all the figures represent the theoretical misorientation distribution of randomly oriented grains [153]. In as-received condition, the fraction of high angle grain boundaries (HAGBs) and low angle grain boundaries (LAGBs) are about 87% and 13%, respectively (Fig. 5.2 (a)). The average misorientation is ~32˚. After one pass of ECAP process, the fraction of low angle grain boundaries increases steeply from 13% to 69%, and the average misorientation decreases to 15˚ (Fig. 5.2 (b)). After two passes of ECAP, the misorientation distribution was nearly the same as that after one pass of ECAP (Fig. 5.2 (c)). On further passes of ECAP, the fraction of high angle grain boundaries increases to 62% (Fig. 5.2 (d)), 67% (Fig. 5.2 (e)) and 84% (Fig. 5.2 (f)) for 4, 8 and 12 passes of ECAP, respectively. The average misorientation increases to 33˚ after 12 passes of ECAP (see Table 5.1).

Table 5.1 The comparison of grain size, fraction of HAGBs and LAGBs and average misorientation of Al-1050 alloy processed by ECAP for different passes

	As-received	1 pass	2 passes	4 passes	8 passes	12 passes
Grain Size, μm	44	15	11	4.9	1.3	0.88
Fraction of HAGBs, %	87	31	32	62	67	84
Fraction of LAGBs, %	13	69	68	38	33	16
Average misorientation, ˚	32	15	15	25	24	33

5.1.1.2 Texture in Al-1050

The texture formed during ECAP process has been analysed. It is first compared with a description based on a simple shear deformation [154], which is denominated as Simple Shear Model in this work. In this model, the simple shear is considered to be only significant deformation mode in ECAP [155].The simple shear under ideal ECAP conditions occurs along the x` direction on the y` plane (Fig. 5.3 (a)). For FCC materials, the most ideal slip systems in the simple shear are those with a slip

direction parallel to the shear direction or a slip plane parallel to the shear plane, that is, the {111}<uvw> and the {hkl}<110> slip systems. The main ideal slip systems are illustrated in Fig. 5.3 (b) [156] by the (111) pole figure projected on the y plane. The corresponding Miller indices are shown in Table 5.2 [157].

Fig. 5.4 shows the (100) and (111) pole figures of Al-1050 alloy in as-received condition prior to ECAP. Both pole figures are projected on the x plane (Fig. 5.3 (a)) and the normal direction of these pole figures is parallel to the longitudinal direction of the rod-shaped sample. The pole figures show a <100> fibre texture and a <111> fibre texture. The <100> fibre texture is a little stronger than the <111> fibre texture although both of them are weaker than that of conventional extrusion texture.

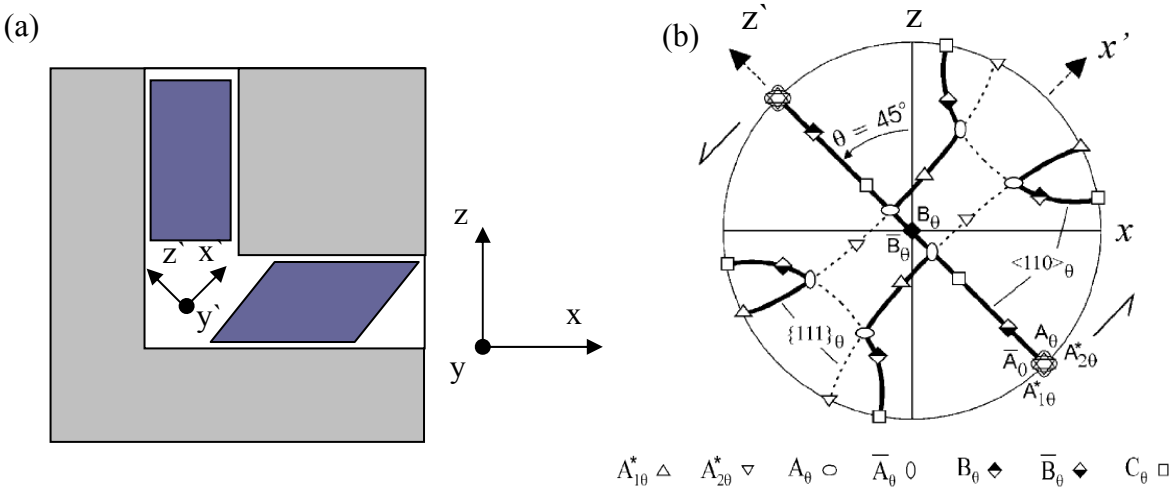

Fig. 5.3 (a) Illustration of ECAP process and (b) (111) pole figure projected on y plane showing the main ideal slip system in simple shear [156].

Table 5.2 Main ideal slip system in simple shear [157]

Notation	Miller indices
A^*_1	$(111)[\bar{1}\bar{1}2]$
A^*_2	$(1\bar{1}1)[1\bar{1}2]$
A	$(1\bar{1}1)[110]$
$\bar{A}$	$(\bar{1}1\bar{1})[\bar{1}\bar{1}0]$
B	$(1\bar{1}2)[110]$
$\bar{B}$	$(\bar{1}1\bar{2})[\bar{1}\bar{1}0]$
C	{001}<110>

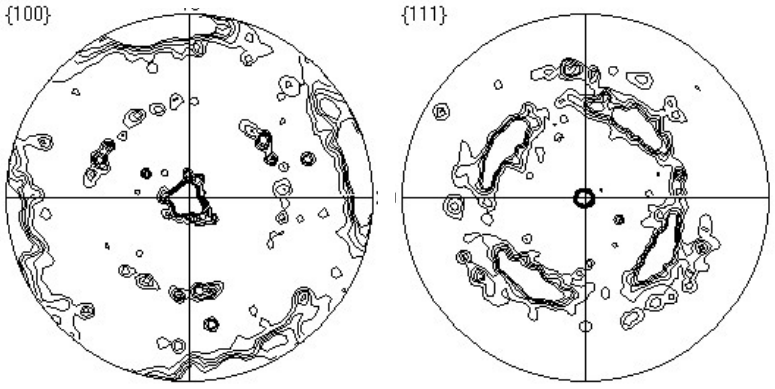

Fig. 5.4 (100) and (111) Pole figures of Al-1050 alloys in the as-received conditions projected on x plane

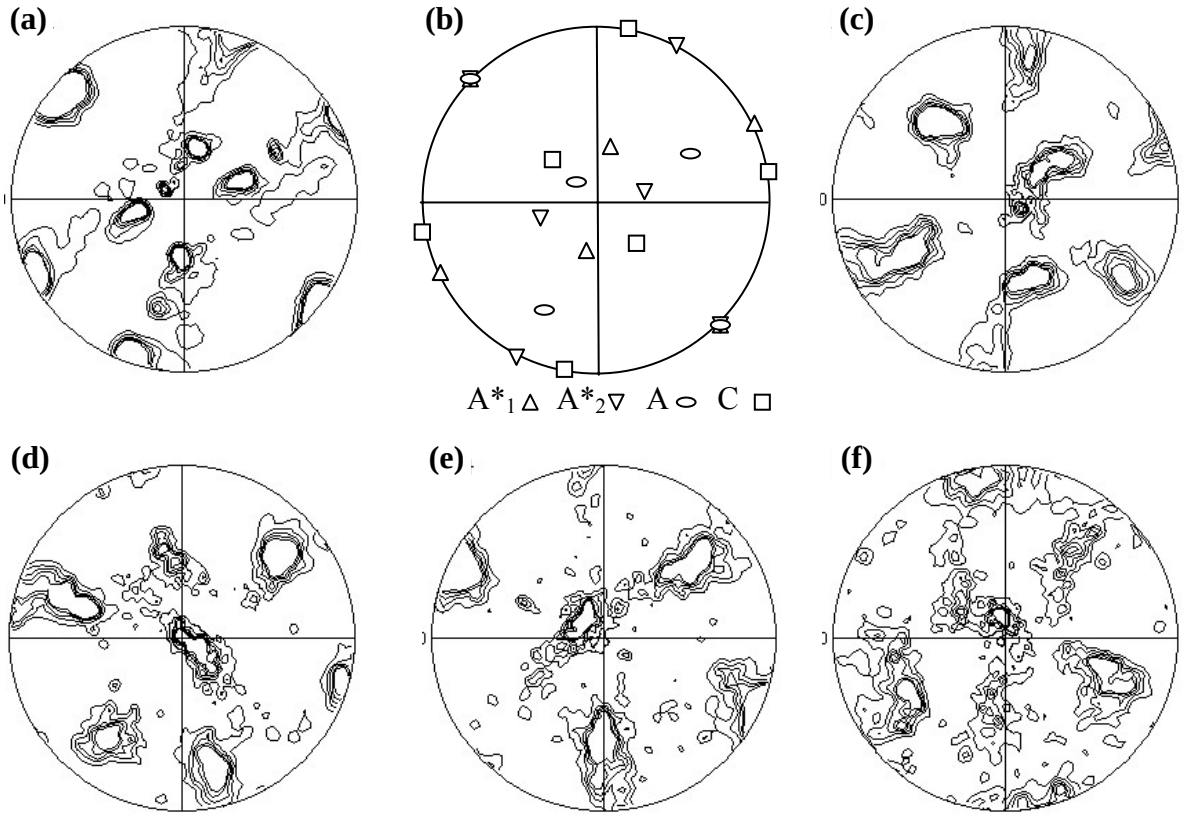

Fig. 5.5 (111) Pole figure projected on y plane of Al-1050 alloys processed by ECAP for (a) 1 (c) 2 , (d) 4, (e) 8 and (f) 12 passes; (b) the ideal slip systems in the Simple Shear Model (with slip systems not evident in the experimental pole figure being taken out).

The (111) pole figures on the y-projection plane of Al-1050 alloy after 1, 2, 4, 8 an 12 passes of ECAP are shown in Fig. 5.5. Comparison of the pole figure of Al-1050 after one pass of ECAP (Fig. 5.5 (a)) with the Simple Shear Model shows that the measured EBSD pole figures fit this model. The A^*_1, A^*_2, A and C slip systems are involved (Comparing with Fig. 5.4 (b)), while the A^*_1, A^*_2 and A components are much stronger and C components are much weaker. After additional passes of ECAP from 2 to 12, the texture evolution shown in the pole figures shows little crystallographic regularity. This is interpreted to be due to the rotation by an angle of 90˚ between passes, which results in the main ideal slip systems not aligning to the ideal simple shear orientations any more. Notably, the texture becomes weaker and more random with the increasing number of ECAP passes.

A recent model [158] for ECAP deformation suggests that the shear occurs on two shear planes during the ECAP deformation. One occurs on z` plane along x` direction (named main shear plane, MSP), the other occurs on x` plane along z` direction (named secondary shear plane, SSP) (see Fig. 5.3(a)). This model is denominated as Two Planes Shear Model in this thesis. In this model, it is considered that the A* and B slip systems are unlikely to be activated in the aluminium alloys after one pass of ECAP at room temperature. So only A and C slip systems are considered.

5.1.1.3 EBSD on AlZr alloy

The AlZr alloy in as-received (as-cast) condition has a grain size of 0.7mm. EBSD data shows a casting fibre texture of <100> along the longitudinal direction of the sample for ECAP. The microstructure of AlZr alloy after different passes of ECAP is shown in Fig. 5.6. The coarse microstructure in as-received condition was dramatically refined after only one pass of ECAP. The grain size of AlZr alloy after one pass of ECAP is 10.5 μm, while the microstructure is not homogeneous and the shear bands can be observed (Fig. 5.6 (a)). The grain size decrease with the increase of ECAP passes. After two passes of ECAP, the grain size was refined to 9.8 μm, but the microstructure is still inhomogeneous and some crossing sheared bands can be observed (Fig. 5.6 (b)). 4 passes of ECAP made the microstructure more homogeneous and with a finer grain size of 3.5 μm (Fig. 5.6 (c)). After 8 passes of

ECAP, the OIM figure showed a very homogeneous microstructure with a further refined grain size of 1.8 μm (Fig. 5.6(d)).

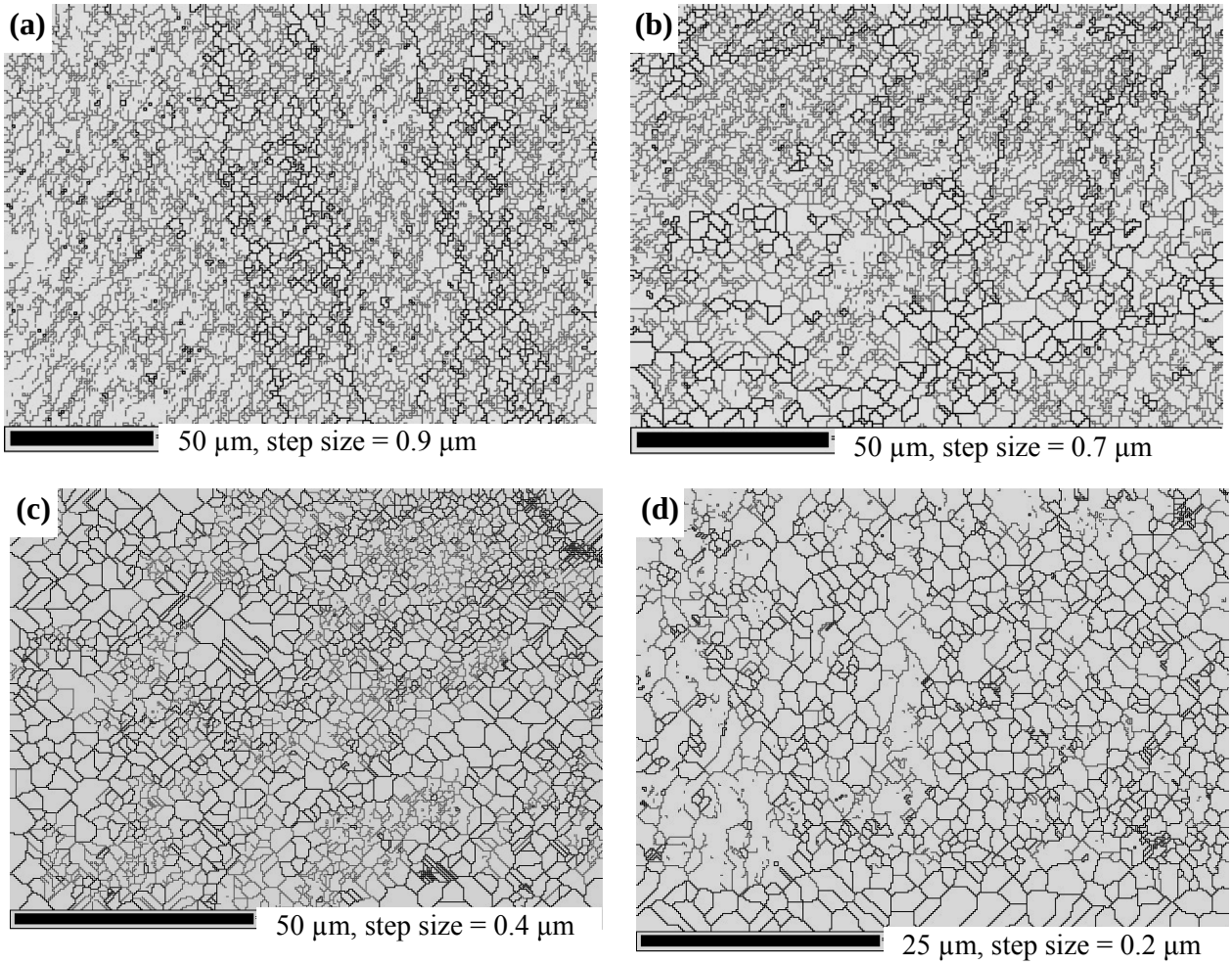

Fig. 5.6 Microstructure of AlZr alloys processed by ECAP for (a) 1, (b) 2, (c) 4 and (d) 8 passes.

Fig. 5.7 shows the misorientation distribution of AlZr alloys after different passes of ECAP. After one pass of ECAP, there is an obvious decrease of the fraction of HAGBs being observed, while the fraction of LAGBs increases dramatically (Fig. 5.7 (a)). The fraction of HAGBs increases with the increase of the passes of ECAP. After 8 passes of ECAP, the misorientation distribution in the high angle part is close to the theoretical distribution curve for randomly oriented grains, while another peak of misorientation distribution is observed in low angle part (Fig. 5.7 (d)). The fraction of HAGB of AlZr alloys after 1, 2, 4 and 8 passes of ECAP are 0.27, 0.41, 0.65 and 0.77, respectively.

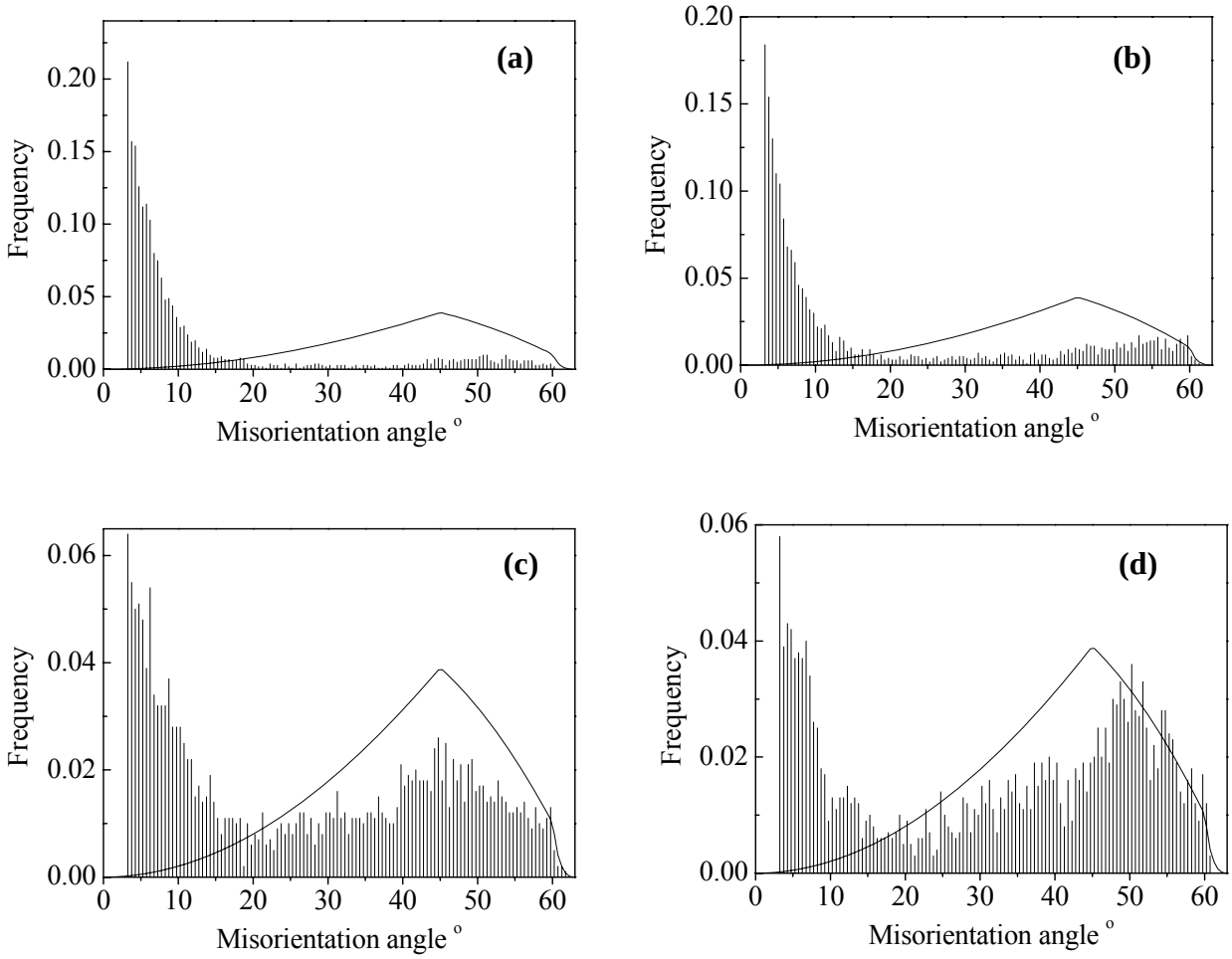

Fig. 5.7 Misorientation distribution of AlZr alloys processed by ECAP for (a) 1, (b) 2, (c) 4 and (d) 8 passes. The curves in the figures represent the theoretical misorientation distribution of randomly oriented grains [153]

Fig. 5.8 shows (111) pole figures of AlZr alloy after different passes of ECAP. Unlike Al-1050 after one pass of ECAP, the pole figures of ECAP processed AlZr alloy does not fit in pole figures predicted by either of the two models mentioned above. However, if the pole figures of AlZr alloy after 1, 2, 4 and 8 passes of ECAP are rotated by 45˚ around the y axis in the counter clockwise direction, both the A slip system in the Simple Shear Model (Fig. 5.3(b)) and A_{MSP} in the Two Planes Shear Model [158] can be observed in the (111) pole figures of AlZr alloy after all passes of ECAP with a small deviation (see Fig. 5.8(a-d)). This indicates that the {111}<110> slip system is activated on the x plane during ECAP. In work on a pure

Al single crystal similar pole figures were obtained after one pass of ECAP [159, 160]. In work on these single crystal alloys, the {111}<110> slip system was the only one which was observed by EBSD and TEM. The {111}<110> slip system in both the AlZr alloy in current work and Al single crystal in the literature [159,160] are not activated on the ideal shear plane (x` plane in Fig. 5.3(a)). This is because the {111}<110> slip system in as-received materials are not close to the ideal shear plane. In the pole figures of AlZr alloy after 2, 4 and 8 passes of ECAP (Fig. 5.8(b-d)), the A texture of Simple Shear Model (or A_{MMP} texture of Two Planes Shear Model [158]) shown after 1 pass of ECAP is observed and co-exist with some random textures.

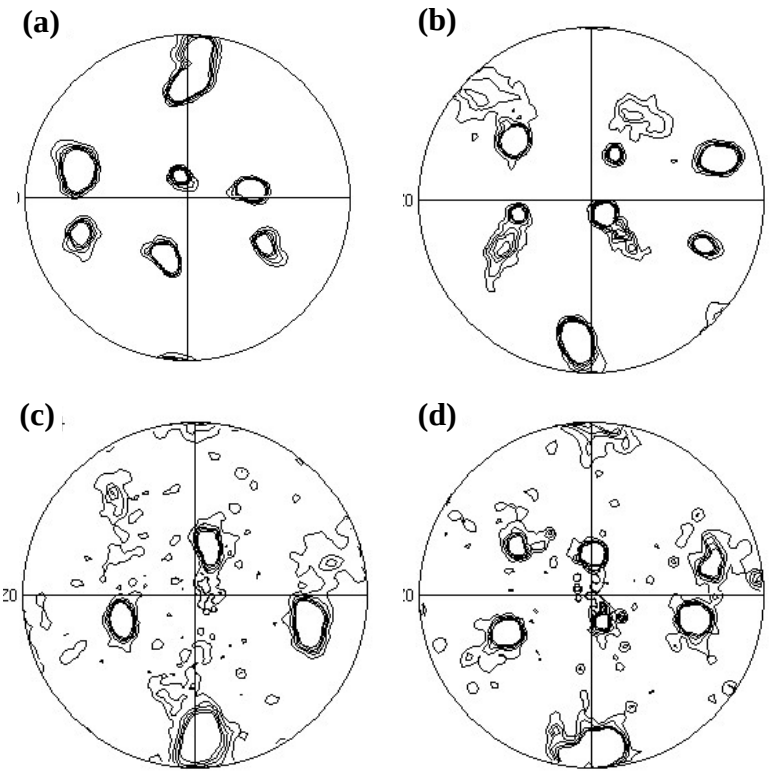

Fig. 5.8 (111) Pole figures of AlZr alloys processed by ECAP for (a) 1, (b) 2, (c) 4 and (d) 8 passes.

5.1.1.4 EBSD on AlZrSiFe alloy

The AlZrSiFe alloy is also received in cast condition. The grain size is 0.5 mm. A casting fibre texture of <100> is detected along the longitudinal direction of the sample for ECAP. Fig. 5.9 shows the microstructure of AlZrSiFe alloy after different

passes of ECAP. The coarse microstructure in as-received condition was dramatically refined after only one pass of ECAP. The grain size of AlZrSiFe alloy after one pass of ECAP is 4.5 μm, while the microstructure is not homogeneous and many subgrains can be observed (Fig. 5.9 (a)). After two passes of ECAP, the grain size was refined to 4.1 μm, but the microstructure is still inhomogeneous (Fig. 5.9 (b)). 4 passages of ECAP made the microstructure more homogeneous and a finer grain size of 4.0 μm is observed (Fig. 5.9 (c)). After 8 passes of ECAP, the OIM figure showed a homogeneous microstructure with a grain size further refined to 1.0 μm (Fig. 5.9 (d)).

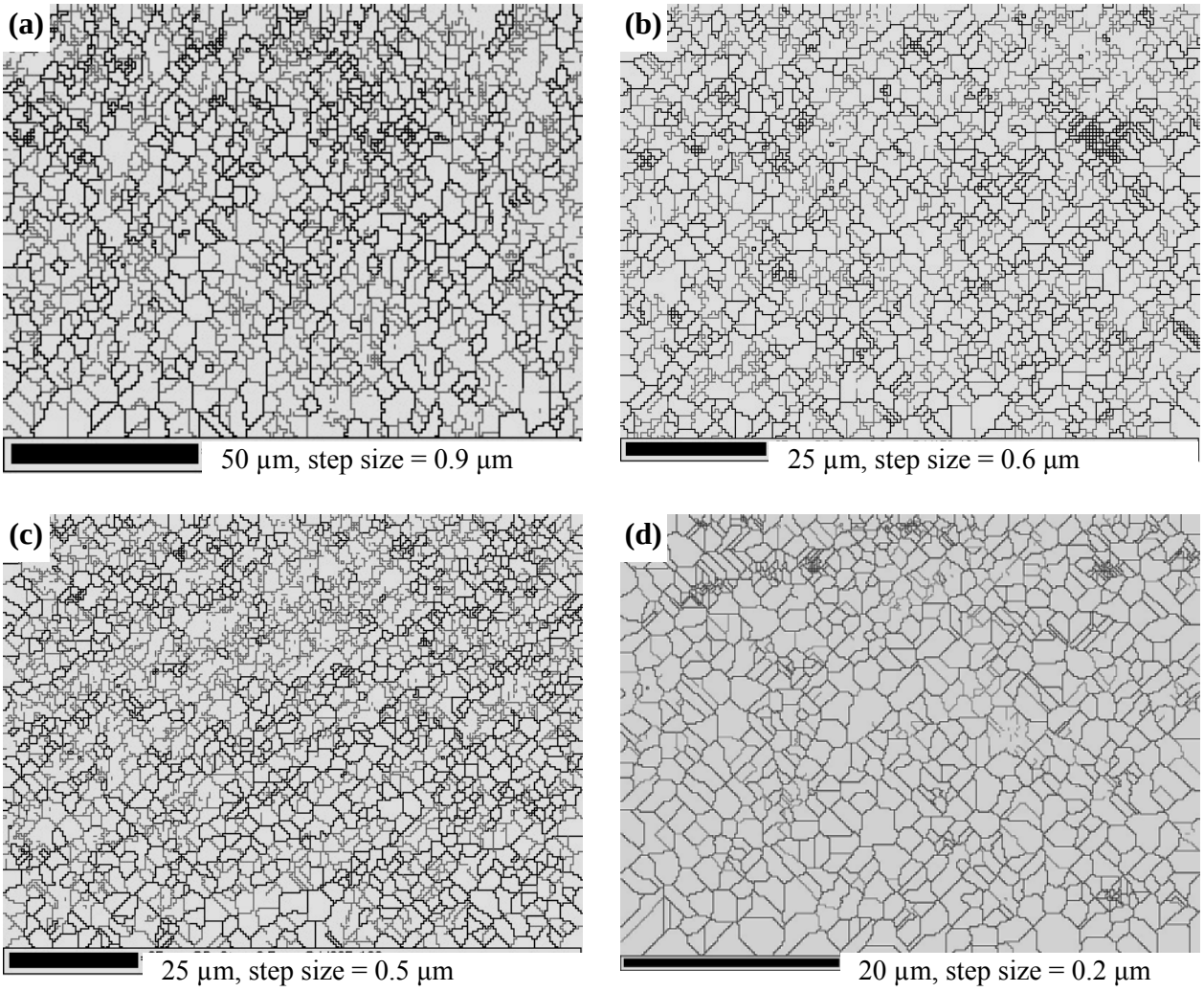

Fig. 5.9 Microstructure of AlZrSiFe alloys processed by ECAP for (a) 1, (b) 2, (c) 4 and (d) 8 passes.

The misorientation distribution of AlZrSiFe alloys after different passes of ECAP is shown in Fig. 5.10. On one pass of ECAP, the HAGB fraction decreases, while the amount of LAGB increases dramatically (Fig. 5.10 (a)). The amount of HAGB increases slightly after two passes and four passes of ECAP (Fig. 5.10 (b) and (c)). After 8 passes of ECAP, the amount of HAGB has increased dramatically and the misorientation distribution in the high angle part is close to the theoretical distribution curve for randomly oriented grains. However, the misorientation distribution at lower angle ($3° < \theta < 25°$) part remains somewhat higher than the theoretical distribution for randomly oriented grains (Fig. 5.10 (d)). The fraction of HAGB of AlZrSiFe alloys after 1, 2, 4 and 8 passes of ECAP are 0.54, 0.61, 0.55 and 0.90, respectively.

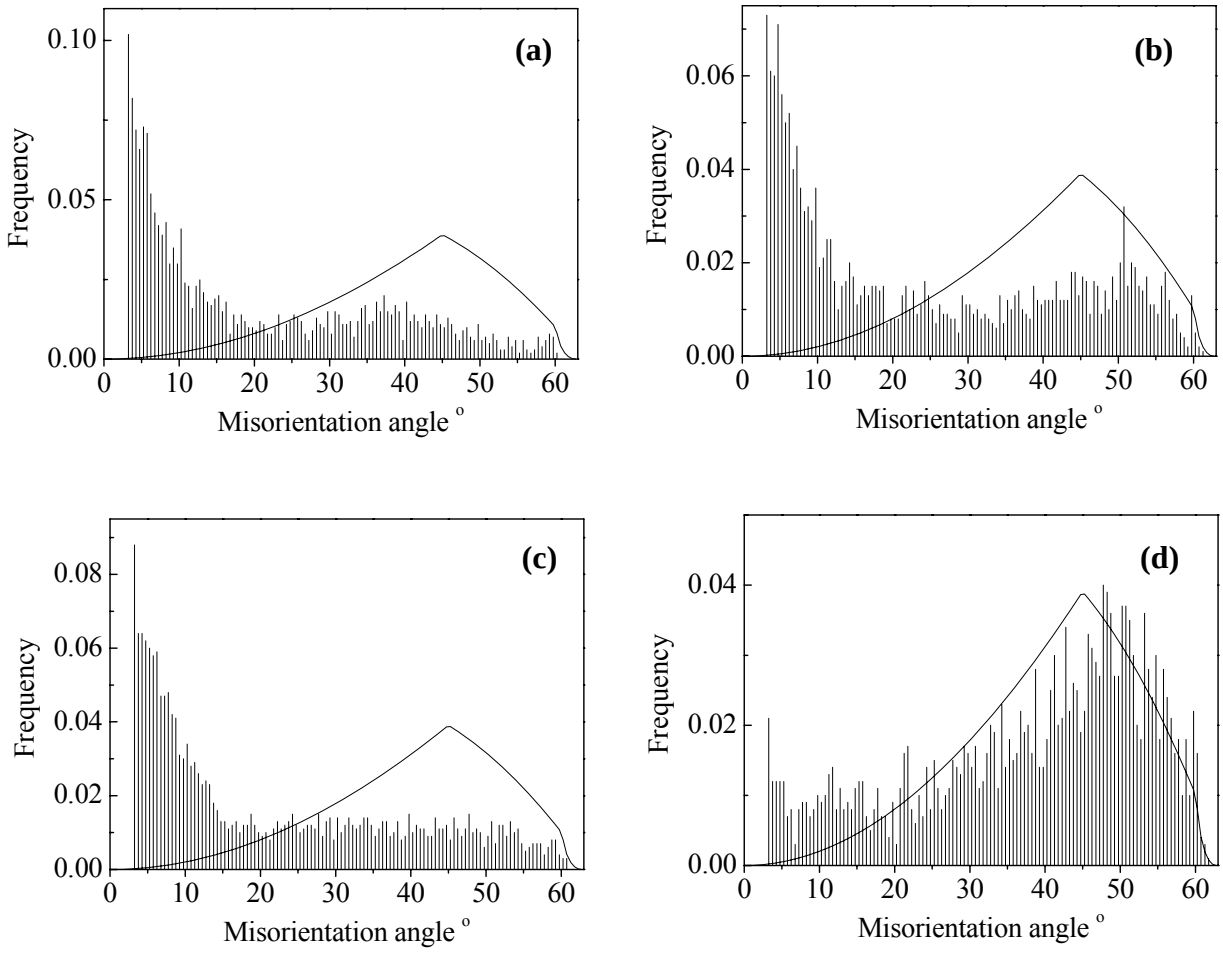

Fig. 5.10 Misorientation distributions of AlZrSiFe alloys processed by ECAP for (a) 1, (b) 2, (c) 4 and (d) 8 passes. The curves in the figures represent the theoretical misorientation distribution of randomly oriented grains [153]

Fig. 5.11 shows (111) pole figures projected on the y plane for the AlZrSiFe alloy after different passes of ECAP. Most of those pole figures do not show any similarity with the Simple Shear Model or the Two Planes Shear Model except the pole figure of the AlZrSiFe alloy after two passes of ECAP. The pole figure of the AlZrSiFe alloy after two passes of ECAP (Fig. 5.11 (b)) shows similarities with that of the AlZr alloy after ECAP (Fig. 5.8(b)), that indicates the {111}<110> slip system is activated in the AlZrSiFe alloy after two passes of ECAP. The pole figures of the AlZrSiFe alloy after 1, 4 and 8 passes of ECAP do not show any regularity even after being rotated. This is probably because of coarse microstructure and non-preferential texture in the as-received material. The texture evolution of the AlZrSiFe alloy during ECAP is similar with that of the Al-1050 and the AlZr alloy. The texture tends to be weak, close to random, and becomes more random with increasing number of passes.

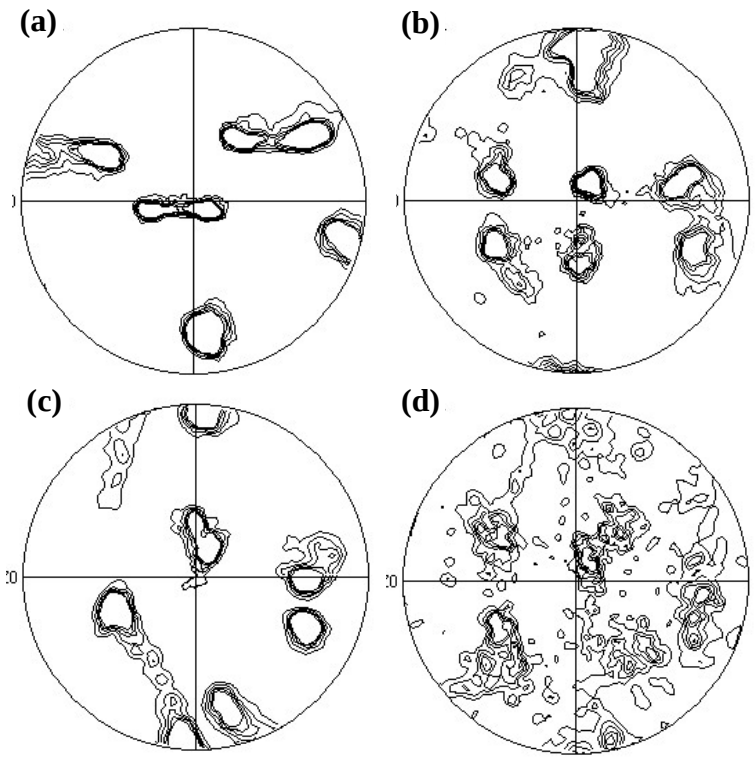

Fig. 5.11 (111) Pole figures of AlZrSiFe alloys processed by ECAP for (a) 1, (b) 2, (c) 4 and (d) 8 passes.

5.1.2 Transmission electron microscopy

Fig. 5.12 shows a range of TEM micrographs of the AlZr alloy after 1, 4 and 8 passes of ECAP. The shape of grains is found to develop from an elongated shape into an equiaxed shape, and the size of the grains decreases with increasing number of passes (i.e. with increasing accumulated plastic strain). After one single pass of ECAP, the microstructure consists of an array of band-shaped subgrains (Fig. 5.12 (a)). The spacing between each band is approximately 0.6μm. A high density of tangled dislocations inside the grain and parallel dislocations at grain boundaries can be observed (Fig. 5.12 (b)).

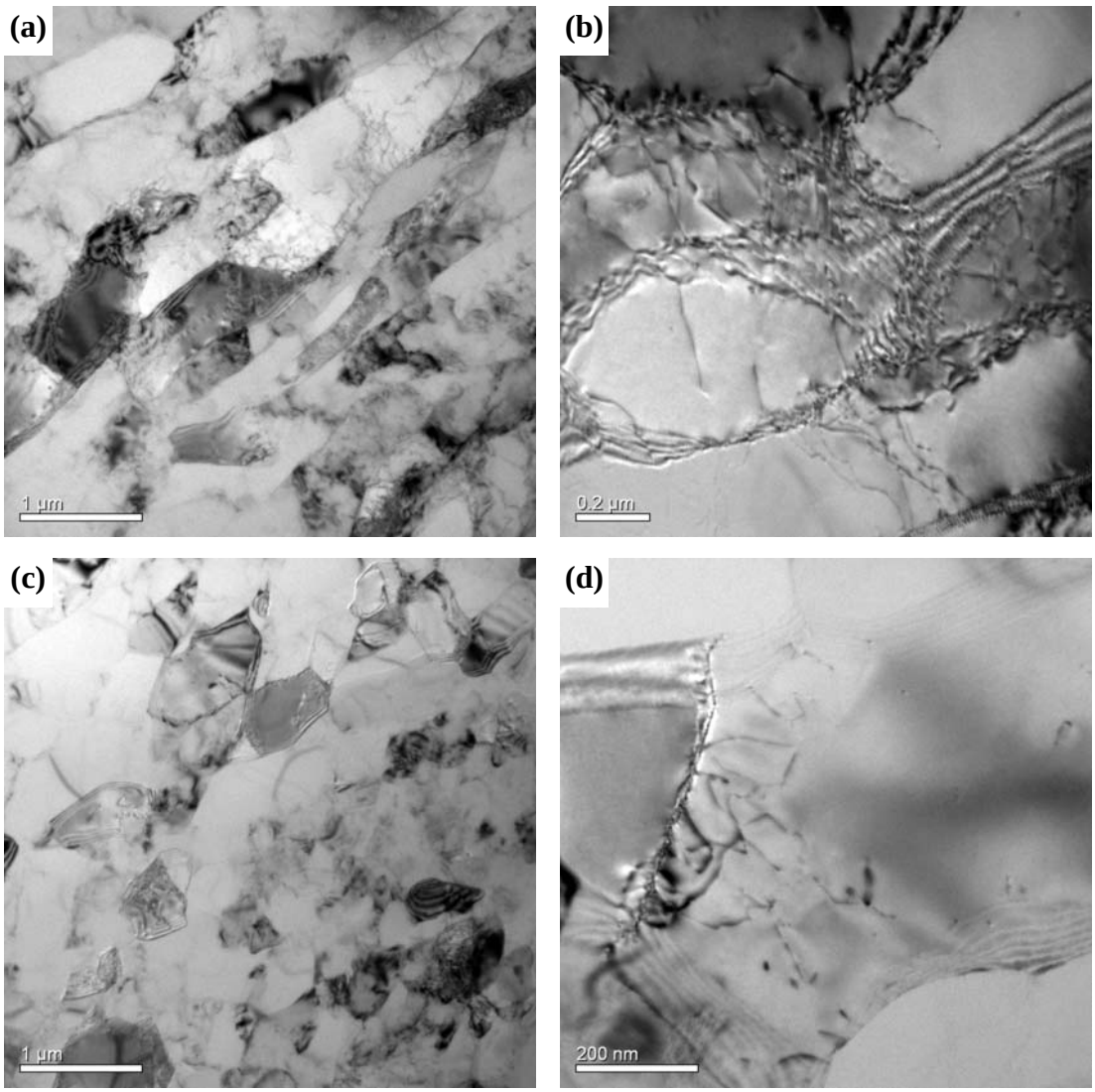

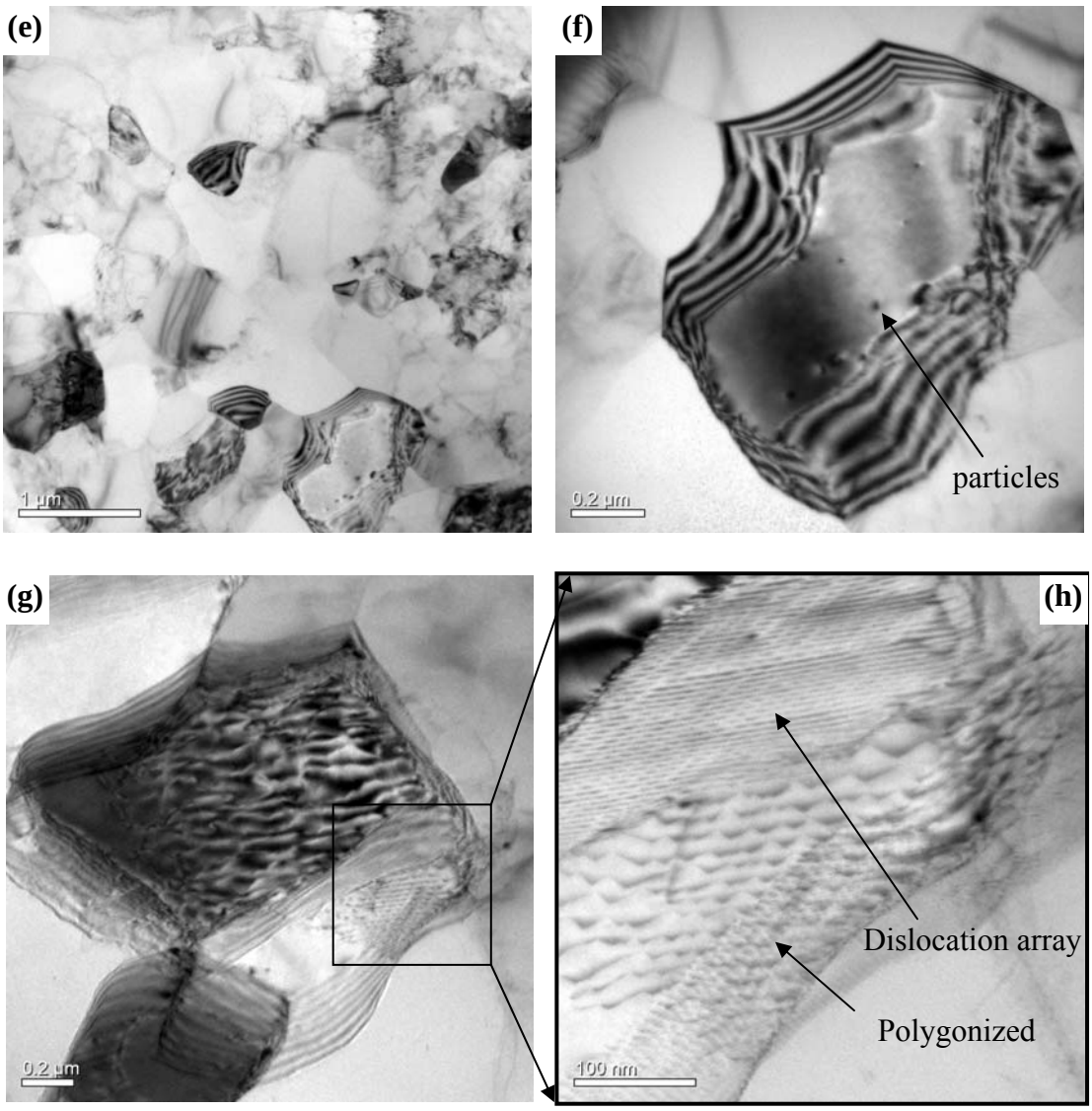

Fig. 5.12 TEM micrographs showing the structural evolution of AlZr alloy after (a), (b) 1; (c), (d) 4 and (e), (f),(g), (h) 8 passes of ECAP.

After 4 passes of ECAP, the band-shaped subgrains are replaced by equiaxed grains with sizes of about 0.5 µm (Fig. 5.12 (c)). The density of dislocations both inside the grain and in the grain boundary decreases with increasing number of passes (Fig. 5.12 (d)). After 8 passes of ECAP, the grains are still equiaxed and the size is further refined to 0.4µm (Fig. 5.12 (e)). The dislocations inside the grains are distributed inhomogeneously, with patches of relatively high density as well as dislocation free patches (Fig. 5.12 (f)), which is a product of the annihilation of dislocations of different signs. The dislocations at the grain boundary exist in two forms, one form is polygonized dislocation wall (Fig. 5.12 (h)), similar to those described by

Humphreys and Hatherly in their well known book on recovery and recrystallization [161]. This wall is composed of the excess dislocations left after the first stage of dislocation annihilation. The other is a parallel dislocation array (Fig. 5.12 (h)). The dislocation spacing in the parallel dislocation array is much smaller than that in the polygonized dislocation wall. That indicates the parallel dislocation wall is the transition state between the polygonized dislocation wall and the formation of a grain boundary. These forms of dislocations were also reported in pure aluminium after 8 passes of ECAP by Chang et al. [162].

5.2 A model of grain refinement

Microstructure in section 5.1.1 shows grain size reduces with the increasing passes of ECAP. The grain refinement during ECAP depends on total strain, route [163], temperature, alloy composition and backpressure. A recent predictive model of grain refinement during SPD gives an accurate grain size by involving most of above factors [164]. In this model the structure evolution during ECAP at the early stage of deformation, a very high dislocation density is introduced, which leads to the formation of an intragranular structure consisting of cells with thick cell walls and low angles of misorientation.

5.2.1 The model

Density of the generated dislocations during SPD is assumed to follow the Kocks-Mecking-Estrin (KME) model [165, 166, 167, 168] (see Eq. 5.3). On increasing deformation, dislocations are continuously generated, and accumulate at the cell wall/grain boundary. As a result, the thickness of the cell walls decreases, the misorientation between cell walls increases and the cell wall transforms gradually into a grain boundary. The basic calculation procedure of the model is given in Eq. 5.1-Eq. 5.7. The increase in strength $\Delta\sigma$ due to dislocation density ρ is considered to follow classical equation given in Eq. 5.1, where α_1 is a constant, G is the shear modulus, b is the Burgers vector and M is Taylor factor. To calculate rate of dislocation generation it is assumed that over a limited range of deformation (1 to 5%) the increase in strength $\Delta\sigma$ and plastic strain ε_p obey a parabolic relationship with a proportion factor of K_A (see Eq. 5.2). The value of K_A can then be obtained from

tensile tests, and it can be compared by a predictions from Eq. 5.6 which incorporates composition and non shearable obstacles (mostly precipitates and dispersoids) (see Ref [164]). The prediction of K_A involves mean free path related to density of geometrically necessary dislocations (GNDs) and the new concept of density of chemically necessary dislocations (CNDs). The Al alloy that contains a larger amount of fine non-shearable particles and solute atoms with high bond energy (for instance, Mg) tends to generate a higher density of GNDs and CNDs during ECAP, i.e. have a smaller free path value, bigger K_A value and smaller grain size (see Eq. 5.1-Eq. 5.7). The dislocation density in grains was ignored since it is much smaller than the dislocation density in the grain boundary, then the grain (in a Poisson-Voronoi shape) size d is related to the dislocation density by Eq. 5.6 and calculated by Eq. 5.7, where Sv is boundary area per unit volume, θ and $\bar{\theta}$ are misorientation and average misorientation angle between cells/grains, respectively, $\bar{L}$ is the mean lineal intercept length. In Eq. 5.6, ρ_{GB} can be obtained by total strain when substituting Eq. 5.1 in Eq. 5.2. Experimental measurements show that $\bar{\theta}$ is relatively constant.

$$\Delta\sigma = M\tau = M\alpha_1 Gb\sqrt{\rho} \qquad \text{Eq. 5.1}$$

$$\Delta\sigma = G\alpha_1\sqrt{\frac{Mb}{l_d}}\sqrt{\varepsilon_p} = K_A\sqrt{\varepsilon_p} \qquad \text{Eq. 5.2}$$

$$\frac{d\rho}{d\gamma} = (bl_d)^{-1} - k_2\rho \qquad \text{Eq. 5.3}$$

$$\rho_g = \gamma\left(M\left[\frac{Gb\alpha_1}{K_A}\right]^2\right)^{-1} \qquad \text{Eq. 5.4}$$

$$K_A = C_2 GM^{1/2}b^{1/2}\left(\left[\frac{f}{2r}\right]^2 + \sum\left[B_i x_i\right]^2\right)^{1/4} + K_A^0 \qquad \text{Eq. 5.5}$$

$$\rho_{GB} = \int 1.5\frac{\theta}{b}dS_{V,def} \cong 1.5\frac{\bar{\theta}}{b}S_V = 1.5\frac{\bar{\theta}}{b} * \frac{2}{\bar{L}} = 1.5\frac{\bar{\theta}}{b} * \frac{2.91}{d} \qquad \text{Eq. 5.6}$$

$$d \cong 2.91/S_{v,def} = 1.5 * 2.91 \frac{\bar{\theta}}{\rho_{GB} b} \qquad \text{Eq. 5.7}$$

5.2.2 The modelling results

The predicted and measured grain size of three Al alloys after different passes of ECAP are shown in Fig. 5.13. The grain size here is an average value for all grains with misorientation angles in whole range. The grain size is defined by assuming the grain shapes to be of Poisson-Voronoi construction [169] which provides that the grain size is 1.455 times the intercept length. The values of grain size in other sections of this thesis are intercept length. This model only predicted the grain size of UFG Al with ECAP pass number larger than a specific value, typically 3 because mean misorientation angle $\bar{\theta}$ starts to approach or approaches a constant value, which is independent to composition and varies little with increasing strains (see Fig. 5.2, Fig. 5.7 and Fig. 5.10).

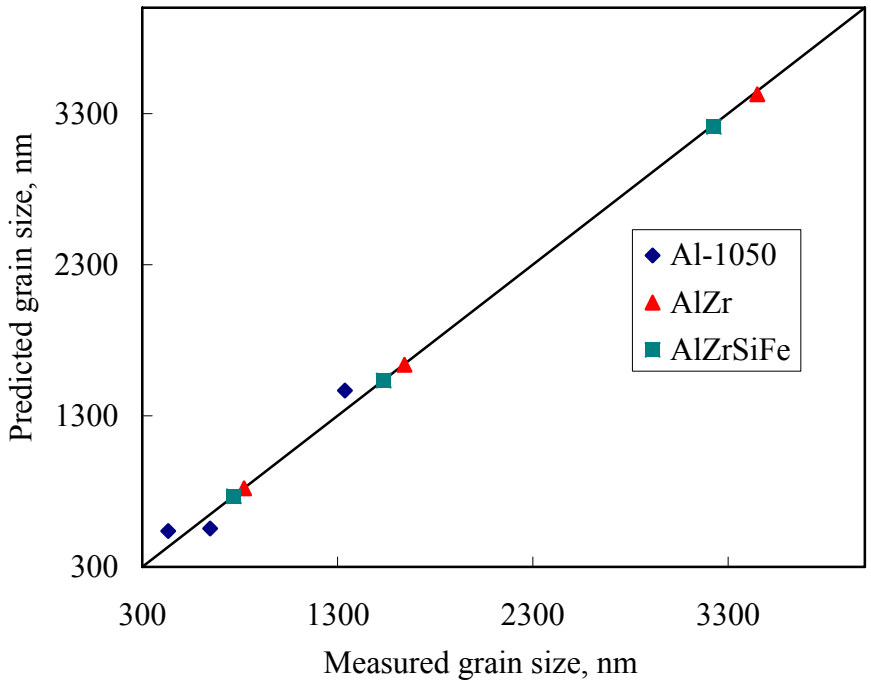

Fig. 5.13 Measured and predicted grain size of UFG Al alloys processed by two or more passes of ECAP

The predicted grain size fits the measured grain size very well. The root mean square error (RMSE) is 64 nm. This model is also applicable for a wide range of other Al

alloys, such as Al-Mg, Al-Cu, Al-7075 and Al-6082 [164]. After a large strain provided by ECAP or HPT, the grain size of these Al alloys is well predicted with good accuracy. In fact, the model is more accurate (smaller RMSE) for the present dilute alloys as compared to the wide range of alloys in [164]. This may be due to the measurement of particle size and volume fraction of the Al alloys with high amount of alloying elements having a limited accuracy, which will impact on prediction accuracy.

5.3 Summary

The UFG Al alloys were produced by ECAP at room temperature. After eight passes of ECAP, the grain size of three alloys was around 1 μm. The texture evolution strongly depends on the initial condition. The texture tends to become weaker with increasing passes of ECAP. A model of grain refinement was reported. A large amount of dislocations were generated during ECAP and most of the generated dislocations form or move to cell wall/grain boundaries. The average misorientation angle tends to approach a constant value after a number of passes of ECAP. A model from grain size refinement based on average amounts of dislocations generated fits the measured grain sizes with a high accuracy.

6 Strength/Microhardness of UFG Al Alloys Processed by ECAP

This section reports the Vickers hardness of three UFG Al alloys processed by various passes of ECAP. To study the thermal stability the UFG Al alloys, the hardness of annealed UFG Al alloys at different temperature were also measured. Furthermore, to study the inhomogeneity of the UFG Al alloys after one pass of ECAP, the distribution of microhardness and microstructure on the cross section of ECAP processed billets was measured before and after annealing at different temperatures. A new model of strength/microhardness of UFG Al alloys is presented.

6.1 Results

6.1.1 Thermal stability of UFG structure

Like all worked metals, the UFG materials processed by ECAP will recrystallize when they are held at high temperature. The recrystallization temperature may be determined through measuring the grain size changes with increasing temperature. Microhardness testing of the UFG materials can also reflect the recrystallization temperature because of the (Hall-Petch) relationship between the grain size and the yield strength. In present work, the three UFG aluminium alloys after different passes of ECAP were heated to from 200˚C to 500˚C with step size of 50˚C, with a 30 minute hold at each temperature. Microhardness results of the three UFG aluminium alloys after each heat treatment step are shown in Fig. 6.1, Fig. 6.2 and Fig. 6.3.

6.1.1.1 Microhardness of Al-1050 annealed at various temperatures

The variation of the Vickers microhardness with temperature is shown in Fig. 6.1 for Al-1050 UFG alloy after 1, 2, 4, 8 and 12 passes of ECAP. Inspection shows that at low temperature (200˚C), the microhardness increases with increasing number of ECAP passes. The microhardness of the sample after one pass of ECAP is 43MPa, and it is increased to 50MPa after 12 passes of ECAP. All samples show a decrease in microhardness with the increase of the temperature. The initial rate of decrease

increases with number of passes of ECAP, so that trends are reversed at 300˚C and the microhardness decreases with increasing number of ECAP passes. At and after 350˚C, the microhardness of all samples is nearly identical and constant: at this stage recrystallization is completed for all samples.

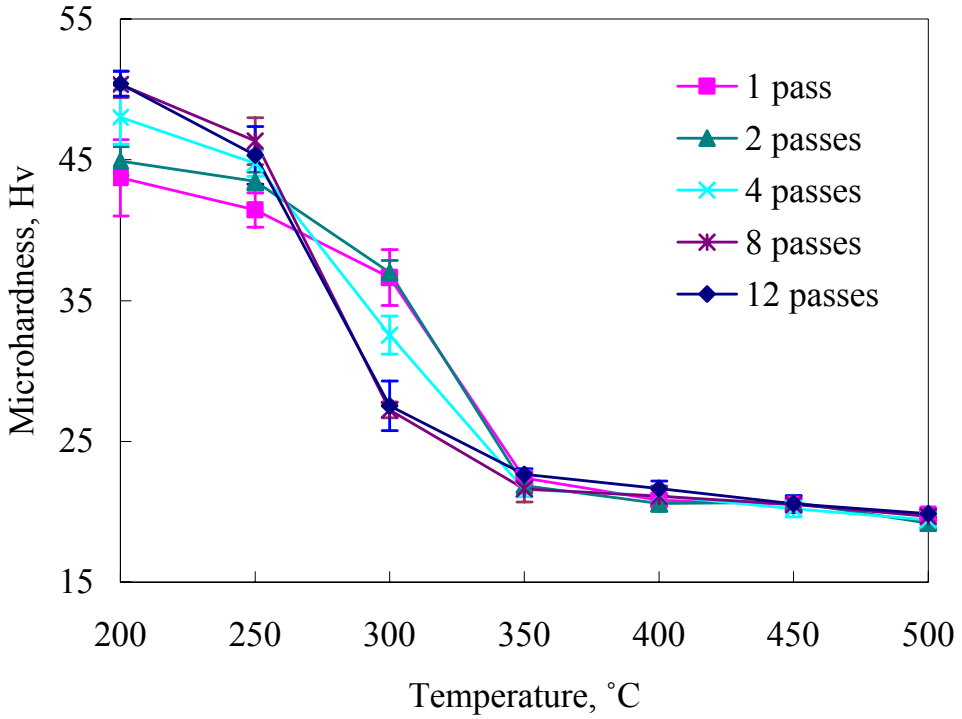

Fig. 6.1 Microhardness of UFG Al-1050 at elevated temperature. The error bars in the figure define a symmetrical confidence interval by plus-minus standard deviation.

6.1.1.2 Microhardness of AlZrSiFe after annealing at various temperatures

Similar microhardness-temperature curves are shown in Fig. 6.2 for AlZrSiFe alloy after 1, 2, 4 and 8 passes of ECAP. Whilst most trends are similar, the main difference between the results of the Al-1050 alloy and that of the AlZrSiFe alloy is that the recrystallization is shifted to higher temperatures. It is also noted that the hardness after ECAP is somewhat higher.

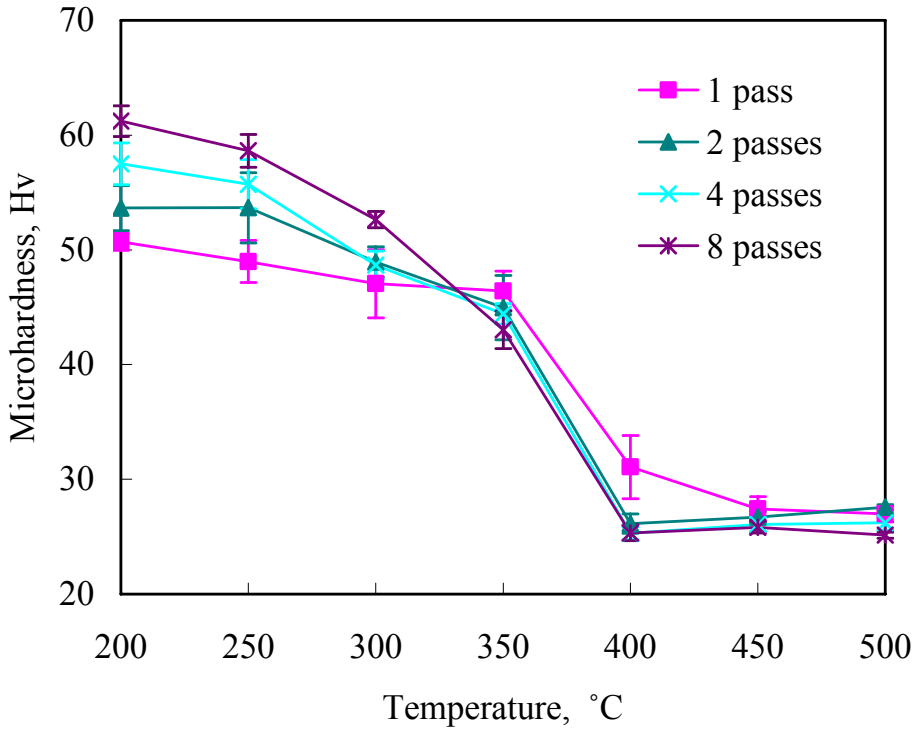

Fig. 6.2 Microhardness of UFG AlZrSiFe at elevated temperature. The error bars in the figure define a symmetrical confidence interval by plus-minus standard deviation.

6.1.1.3 Microhardness of AlZr alloy after annealing at various temperatures

Fig. 6.3 shows the microhardness-temperature curves of the AlZr alloy. Whilst most trends are similar, the main difference between the results for the other alloys is that there is hardly any change in hardness with increasing number of ECAP passes. A steep drop occurs in all the microhardness curves at 350˚C. At and after 400˚C, the microhardness of all samples become to almost constant: recrystallization is completed at this stage.

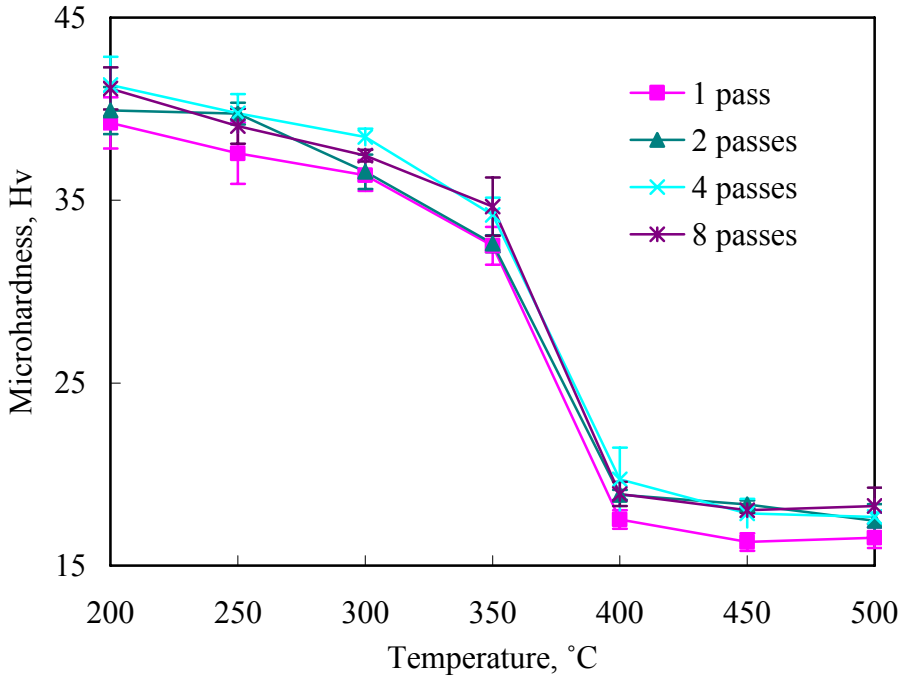

Fig. 6.3 Microhardness of UFG AlZr at elevated temperature. The error bars in the figure define a symmetrical confidence interval by plus-minus standard deviation.

6.1.1.4 Discussion on annealling behaviour of UFG Al alloys

The changes in microhardness of Al-1050 and AlZrSiFe following ECAP passes and post-ECAP annealing are similar. At lower annealing temperature, e.g. at or below 200˚C, the microhardness increases with increasing number of passes. This is because the grain size decreases with increasing accumulated strain, as was evidenced by the EBSD results in Section 5.1.1. In addition, the fraction of HAGBs and dislocation density in the samples increase with increasing accumulated strain. This was confirmed in EBSD and TEM results in Section 5.1.1. With increase of the annealing temperature, the microhardness of all samples decreases and the gap between the microhardness of alloys after lower strain deformation and higher strain deformation becomes small. Eventually, at a specific temperature, 300˚C for Al-1050 and 350˚C for AlZrSiFe, the microhardness of alloys with lower initial accumulated strain surpass that of alloys after with higher initial accumulated strain. This phenomenon can be interpreted by the stored energy. The higher strain deformation

involves more point defaults and dislocations, i.e. more stored energy, and the alloy with higher stored energy will start to recover and recrystallize earlier. Annealing at higher temperature leads to completion of the recrystallization and grain growth of the alloys after both lower and higher strain deformation. The microhardness will tend to the same value.

6.1.2 Local microstructure and microhardness of Al-050 processed by ECAP

The local microstructure and mechanical properties of aluminium alloys processed by ECAP have been studied extensively since the invention of this technique [124, 170]. But the relationship between the inhomogeneous microstructure and mechanical properties after ECAP is still not clear. Especially, there are few reports on how the enhanced strength of aluminium after ECAP is quantitatively related to dislocation density and grain size. Aluminium experiences a severe deformation during ECAP that leads to a high strength with a high density of dislocation and a significantly decreased grain size. It is often suggested that the enhanced yield strength of aluminium alloys after ECAP is due to the refined grains, with the contribution of dislocation density receiving little mention. In this section, microhardness testing was carried out on the cross section of ECAP-processed billet to measure the microhardness distribution over the cross section. To facilitate the identification of the contribution of dislocation density to the yield strength, a series of heat treatments were performed on the ECAP-processed billets to lower the dislocation density through recovery with minor grain size changes. The microstructure of the interested area was observed with the objective of determining the relationship between the nonuniform microhardness and the local microstructure.

6.1.2.1 Microhardness of the ECAP-processed billet

The microhardness distribution on the cross section of the ECAP-processed billet (as defined in Fig. 4.1) is shown in Fig. 6.4. The error bars in the figure define a symmetrical confidence interval by plus-minus standard deviation. (The reported standard deviations refer to the standard deviations obtained from 4 indentations for each data point. Hence measurement accuracy of the mean can be estimated to be a factor 2 better.) The average microhardness of the as pressed billet on the top edge (0.75 mm to the edge) is 42 ± 1.2 Hv while the counterpart on the bottom edge is 39

± 4.2 Hv. The microhardness increases on approaching the center, where the average microhardness is 48 ± 1.4 Hv.

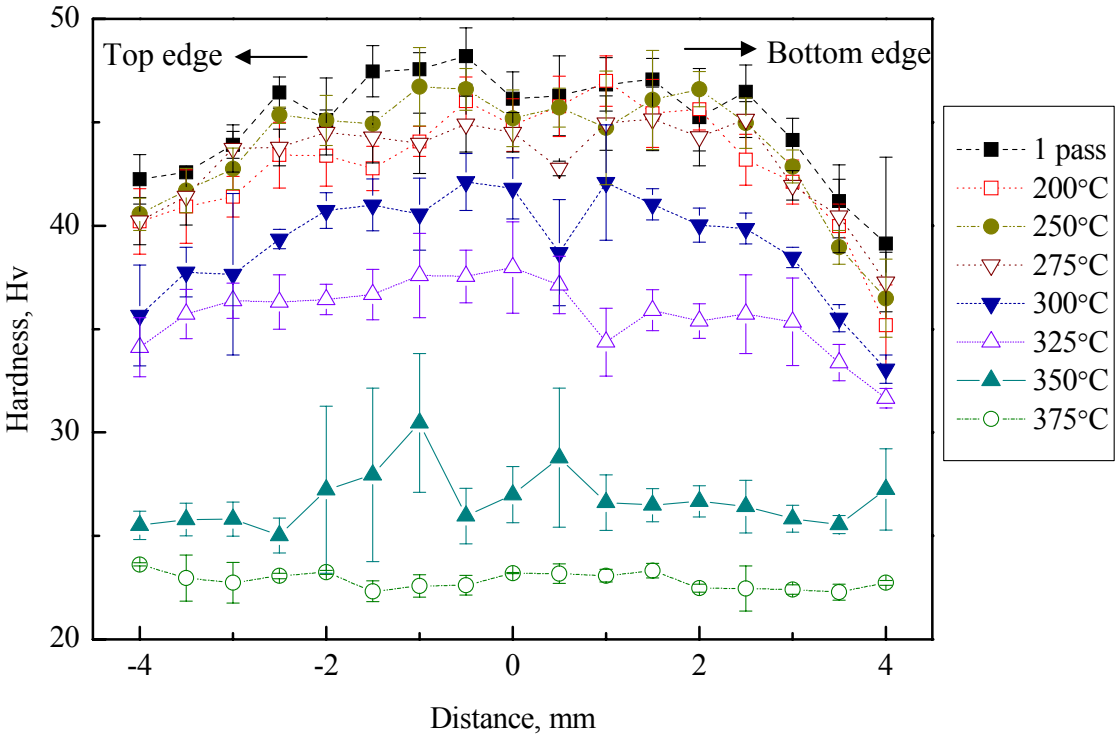

Fig. 6.4 The average microhardness distribution over the cross section from the top edge to the bottom edge of the ECAP-processed billet (one pass of ECAP) and the heat treated billet (one pass of ECAP plus annealing at various temperatures). The error bars are defined as plus-minus standard deviation.

6.1.2.2 Microstructure of the ECAP-processed billet by EBSD

To investigate the origins of the variation of the microhardness across the circular surface, microstructure at the top edge (Mark A), the center (Mark O) and the bottom edge (Mark B) on the circular surface of the ECAP-processed billet (see Fig. 4.1) has been observed by EBSD. Fig. 6.5 (a), (c) and (e) show the microstructure of the top edge, the centre and the bottom edge of the ECAP-processed billet. Dark thick lines are used to represent grain boundaries of which the misorientation angle is greater than 15˚. The grey fine lines represent subgrain boundaries of which the misorientation angle is smaller than 15˚ and greater than 4˚. Misorientations less than 4˚ were ignored in order to remove noise. The average grain sizes at the top edge, the center and the bottom edge, as calculated by the mean linear intercept method, are 8.2 μm, 26 μm and 19 μm.

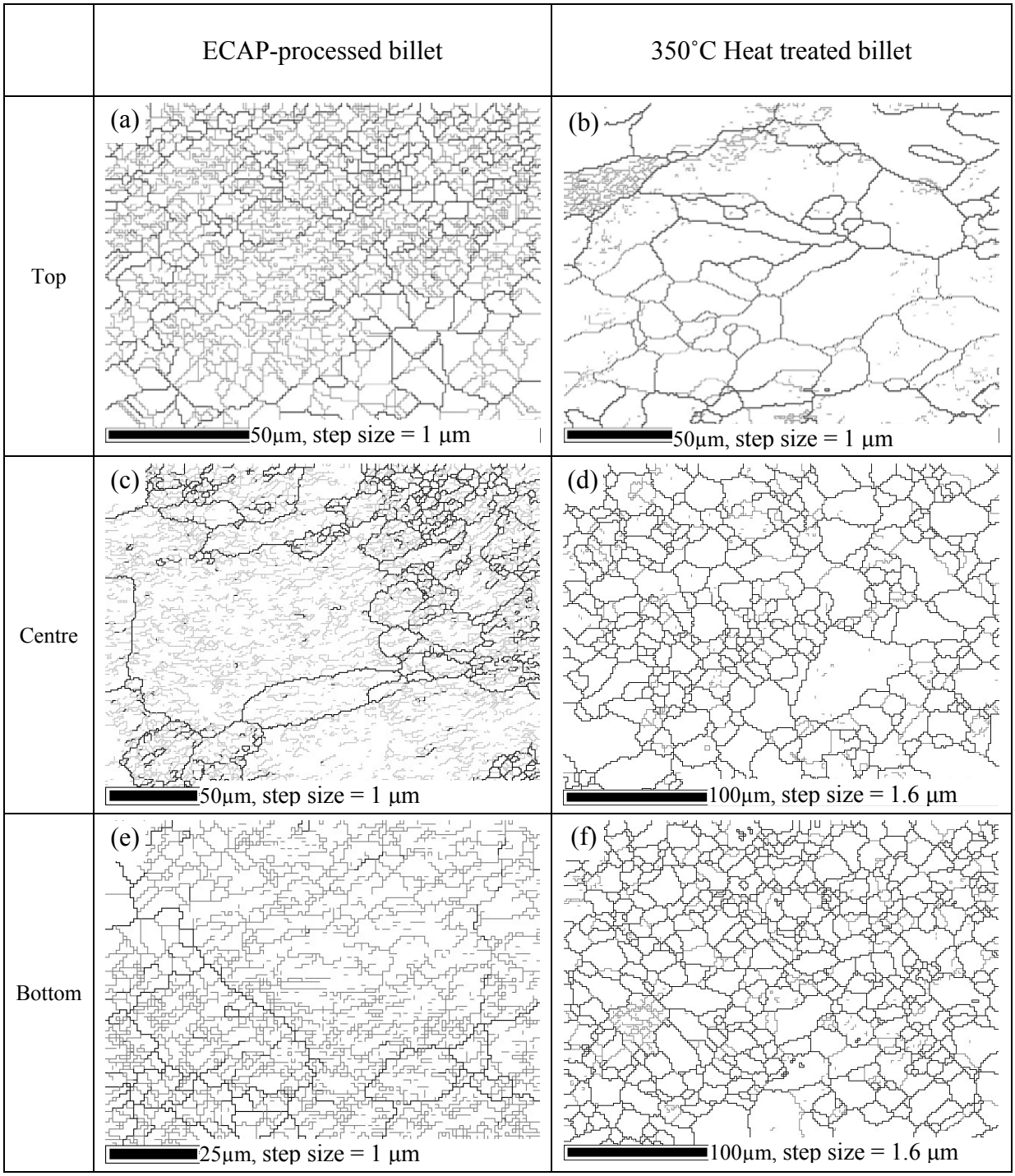

Fig. 6.5 The microstructure of the billet cross section at (a), (b) the top edge, (c), (d) the centre and (e), (f) the bottom edge. (a), (c) and (e) are from the ECAP-processed billet; (b), (d) and (f) are from the 350 ˚C heat treated billet.

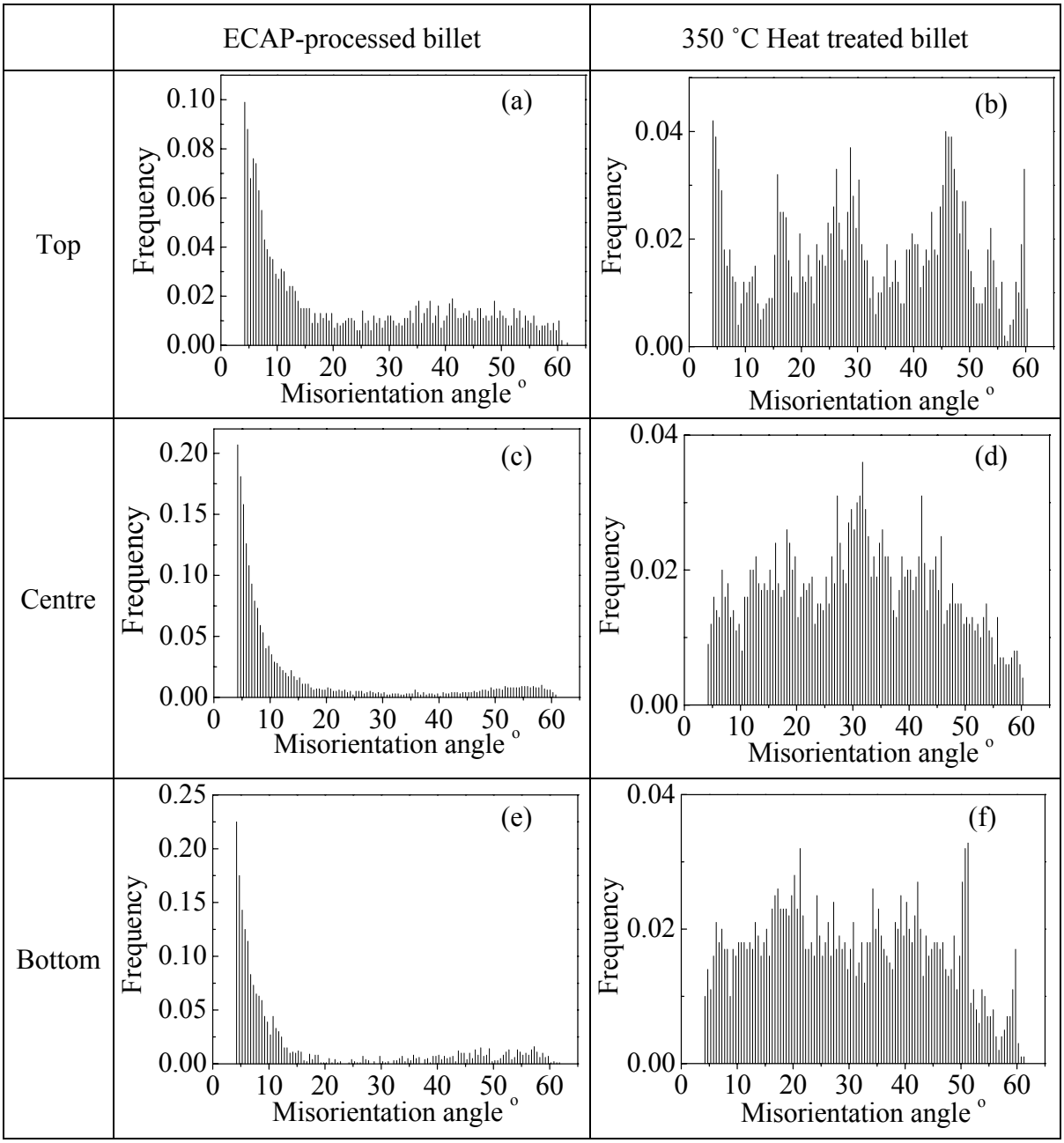

Fig. 6.6 Misorientation distribution of (a), (c), (e) the ECAP-processed billet, and (b), (d), (f)350 ˚C heat treated billet at (a), (b)the top edge, (c), (d)the centre and (e), (f)the bottom edge. The curves in the figures represent the theoretical misorientation distribution of randomly oriented grains [153]

After 1 pass of ECAP, a large amount of subgrains with low angle grain boundaries (LAGB) appears in the original coarse grains due to the severe strain at the

intersection corner of the die. Fig. 6.6 (a), (c) and (e) show the misorientation distribution of the top edge, the centre and the bottom edge. The fraction of LAGB is 47 % at the top edge, 75 % at the centre and 73 % at the bottom edge.

It is worth noting that among the three positions, the centre has the highest microhardness, whilst also the grain size is largest at this location. Hence, grain boundary strengthening is not the dominant strengthening mechanism. Conventional strengthening mechanisms can further include solid solution strengthening, precipitation/dispersion strengthening, dislocation strengthening and grain boundary strengthening. The composition of Al-1050 is close to pure aluminium and the microhardness difference occurs in the same billet so that the solid solution strengthening and precipitation/dispersion strengthening are not significant.

In order to identify the dislocation hardening contribution to the difference of microhardness among the top edge, the centre and the bottom edge of the circular surface, a series of recovery heat treatments were carried out to decrease the dislocation density with limited grain size changes.

6.1.2.3 Microstructure of the heat treated billet

Fig. 6.5 (b), (d) and (f) show the microstructure of the top edge (Mark A), the center (Mark O) and the bottom edge (Mark B) on the circular cross section surface of the billet heat treated for 0.5 h at 350 ˚C. The average grain sizes at the top edge, the center and the bottom edge are 21 μm, 12 μm and 11 μm, respectively. The grain size at the centre and the bottom edge decreased after annealing due to the recrystallization in the billet processed by ECAP. The high density of dislocations in the ECAP-processed billets, and the related high stored energy, caused recrystallization during annealing. The recrystallization has not fully completed and some subgrain boundaries and wavy grain boundaries can still be seen in Fig. 6.5 (d) and (f). However, the grain size at the top edge increased slightly after annealing at 350 ˚C due to the recrystallization and the grain growth.

Fig. 6.6 (b), (d) and (f) show the grain boundary misorientation angle distribution at the three locations for the pressed and heat treated 0.5 h at 350 ˚C sample. Heat treating at 350 ˚C for 0.5 h causes a drastic reduction in LAGB. The fraction of LAGB is 17 % at the top edge, 17 % at the centre and 18 % at the bottom edge.

6.1.2.4 Microhardness of the heat treated billet

Fig. 6.4 also includes the microhardness distribution on the circular cross section surface of ECAP-processed billets after annealing at various temperatures. With increasing annealing temperature, the microhardness at each position decreases and the difference in average microhardness between locations reduces. For example, after annealing at 350 ˚C, the average microhardness of the top edge, the centre and the bottom edge are close together at 25.5 Hv, 27.0 Hv and 27.3 Hv, respectively. However, the variation in microhardness for equivalent positions as measured by the standard deviation appears to increase with heat treatment temperature up to 350 ˚C. The reduction in difference in microhardness among the top edge, the centre and the bottom edge after heat treatment is due to recovery and recrystallization [161]. The deviation of the individual microhardness value at equivalent positions, as reflected in the standard deviation in Fig. 6.4 can be explained by a partially recrystallized microstructure (see Fig. 6.5 (b), (d) and (f)). When measuring microhardness through multiple microhardness indentations (four in this study), the individual hardness value will be slightly higher when measured on the unrecrystallized area; and slightly lower when measured on the recrystallized area. This effect causes a rise in the standard deviation between the hardness values for the equivalent points.

6.2 Discussion of strengthening mechanism of the ECAP-processed aluminum

During ECAP the strain experienced by billet is homogeneous throughout most of the billet, but the billet experiences an inhomogeneous strain at the corner of the die, which has been revealed by experiment [114, 158] and modeling [113]. The deformation in the middle of the billet is generally thought to predominantly follow the single shear model while the deformation in both the top edge and the bottom edge are more complex, being influenced by friction, back pressure and channel intersection angle [1,3]. The uneven deformation inevitably leads to inhomogeneous microstructure and strength of the billet after ECAP. After one pass of ECAP, the microhardness of the billet centre is higher than that of the bottom edge and the top edge while the grain size of the billet centre is bigger than that of the bottom edge and the top edge as well.

To analyse strength variations in the present Al-1050 alloy, it is first noted that the yield strength of fully annealed Al-1050 (28 MPa, see [171]) is about 18 MPa higher than that of pure Al. The limited strength of Al-1050 is mostly due to solution strengthening (from the limited amount of dissolved elements) and strengthening due to a limited amount of hard intermetallic particles (mostly Si and Fe containing phases). These two strengthening contributions are very small and will not significantly vary through the present ECAP and heat treatment. Thus strength variation should be due to variations in grain boundary strengthening and dislocation strengthening. Hence our microhardness results and analysis suggests that the uneven deformation results in the dislocation density of the centre being higher than that of the edge. The heat treatment experiments support this hypothesis. After annealing at 350 ˚C for 0.5 h, the microhardness of the center is close to that at the edges because the dislocation density difference between the center and the edges has been removed during the heat treatment with limited grain size changes because of the recrystallization.

6.3 A model for microhardness/strength of the alloys after ECAP

According to a general strength model for polycrystalline Al alloys, the yield strength is given by the following equation [172,173]:

$$\sigma_y = \Delta\sigma_{gb} + M\tau_{tot} \qquad \text{Eq. 6.1}$$

where σ_y is yield strength, $\Delta\sigma_{gb}$ is the strengthening due to the presence of grain or subgrain boundaries, M is a factor often referred to as the Taylor factor and τ_{tot} is the critical resolved shear stress (CRSS). Contributions to τ_{tot} include intrinsic CRSS, solid solution strengthening, strengthening by dislocations inside the grains and precipitation strengthening. For the present alloys, only the intrinsic CRSS and the dislocations inside grain are significant contributions to the CRSS because of the low solid solubility of alloying elements and absence of precipitates. The contribution to the yield strength by intrinsic CRSS, solid solution strengthening and precipitation strengthening are taken as a constant term σ_0 because they are virtually constant

compared with the contribution of grain size and dislocation density during ECAP and heat treatment. Therefore, the Eq. 6.1can be written as:

$$\sigma_{\mathrm{y}} = \Delta\sigma_{\mathrm{gb}} + \sigma_0 + M\tau_{\mathrm{d}} \qquad \text{Eq. 6.2}$$

where τ_{d} is the strengthening by dislocations inside the grains. The grain boundary strengthening contribution consists of subgrain boundary strengthening and grain boundary strengthening. The effect of subgrain boundaries to the strength is lower than that of a HAGB. Generally, $\Delta\sigma_{\mathrm{gb}}$ is expressed as a function of grain size [174], and as conventionally processed metals have a very low fraction of LAGBs, the distinction between LAGBs and HAGBs can be neglected. But in the present investigation, a high density of LAGBs was observed in the ECAP processed billets and a substantial proportion of the LAGBs have remained in the heat treated billets (see Fig. 6.5). Here, we consider that at low misorientation angle, strengthening will decrease with decreasing misorientation angle [175]. This effect is captured through introducing λ, the ratio of subgrain boundary strengthening contribution to grain boundary strengthening contribution. Following [174,176] it then provides:

$$\Delta\sigma_{gb} = \alpha_2 Gb\left[\lambda f_{sub}\left(\frac{1}{\delta}\right) + (1 - f_{sub})\left(\frac{1}{d}\right)\right] \qquad \text{Eq. 6.3}$$

where α_2 is a constant (equalling 2 see Ref [176]), G is the shear modulus of Al, b is the Burgers vector, δ is the subgrain size, d is the grain size. f_{sub} is the fraction of LAGB.

We will approximate the dislocation strengthening, τ_{d}, by considering an averaged dislocation density. The τ_{d} can generally be expressed by [177]:

$$\tau_{\mathrm{d}} = \alpha_1 Gb\sqrt{\rho_{\mathrm{l}}} \qquad \text{Eq. 6.4}$$

The dislocation density of the microstructure in the heat treated billet is inhomogeneous due to the partial recrystallization. The recrystallized microstructure has a lower dislocation density while the unrecrystallized one has a higher one. Therefore the dislocation contribution τ_{d} of the heat treated billet can be expressed as:

$$\tau_d = \alpha_1 Gb\left[(1-f_{\mathrm{Rec}})\sqrt{\rho_1} + f_{\mathrm{Rec}}\sqrt{\rho_2}\right] \quad \text{Eq. 6.5}$$

In Eq. 6.4and Eq. 6.5, α_1 is a constant (about 0.3 [177]) and f_{Rec} is the recrystallized volume fraction. ρ_1 and ρ_2 are dislocation density in the unrecrystallized grain and recrystallized grains, respectively.

When Eq. 6.2-Eq. 6.5 are substituted into Eq. 6.1, the yield strength for the ECAP-processed billet and the heat treated billet can be expressed as:

$$\sigma_y = \sigma_0 + M\alpha_1 Gb\sqrt{\rho_1} + \alpha_2 Gb\left[\lambda f_{Sub}\left(\frac{1}{\delta}\right) + (1-f_{Sub})\left(\frac{1}{d}\right)\right] \quad \text{Eq. 6.6}$$

$$\sigma_y = \sigma_0 + M\alpha_1 Gb\left[(1-f_{\mathrm{Rec}})\sqrt{\rho_1} + f_{\mathrm{Rec}}\sqrt{\rho_2}\right] + \alpha_2 Gb\left[\lambda f_{sub}\left(\frac{1}{\delta}\right) + (1-f_{sub})\left(\frac{1}{d}\right)\right] \quad \text{Eq. 6.7}$$

6.3.1 Modelling of strengthening of Al alloys after various passes of ECAP

Before calculating the microhardness/yield strength of Al alloys, we will discuss the dislcoation density in the alloys. A large amount of dislocations are generated during ECAP. The total amount of generated dislocations per volume in Al alloys, calculated using Eq. 5.4, is larger than 10^{16} m^{-2} after 2 passes of ECAP, whilst the mean dislocation densities measured by XRD or TEM are typically only about 10^{14} m^{-2} [178,179,180,181,182,183]. The difference is due to the generated dislocations forming or moving to cell walls/grain boundaries [120] and only a small amount of dislocations store in the grains. Reported mean dislocation densities after various passes of ECAP range for various Al alloys with different compositions (see Table 6.1), are in the range 10^{14} m^{-2} - 10^{15} m^{-2}. It is time-consuming to measure dislocation density by TEM to obtain a reliable value by counting dislocations number in a large area. Alternatively, dislocation density of Al alloys after ECAP can also be obtained through mean free path for dislocation movement.

Table 6.1 Measured dislocation density for several Al alloys subjected to cold deformation (incl ECAP) and the total amount of dislocations generated per volume. [164]

Alloy	Process	strain	$\rho \times 10^{14}$ m^{-2}		Method	Ref
			meas	total pred		
Al-3Mg-0.4Cu	Cold roll	0.1	2.7	10	TEM	184
Al-3Mg-0.4Cu	Cold roll	0.6	5	18	TEM	184
Al-6082	ECAP	1.0	4	18	XRD	178
Al-7075	ECAP	2.0	9.4	142	TEM	179
Al 97wt%	ECAP	4.0	3.8	118	TEM	180
Al-1Mg	ECAP	6.0	4	280	XRD	181
Al-3Mg	ECAP	4.0	27	389	XRD	182
Al-7Si	ECAP	7.0	1	168	TEM	183

If we consider dislocations are separated by rectangle blocks of dislocation-free zone with side length of average free path ($\bar{l}$), then, dislocation density in grains is provided by:

$$\rho_{ig} = \frac{\bar{L}^2 / \bar{l}^2}{\bar{L}^2} = \frac{1}{\bar{l}^2} \qquad \text{Eq. 6.8}$$

where $\bar{L}$ is the average intercept length and $\bar{l}$ is mean free path.

Detailed inspections of Table 6.1 show that deformed Al alloys with Mg additions, Cu additions and/or particles have larger dislocation densities than other Al alloys. This is thought to be due to the chemically necessary dislocations and geometrically necessary dislocations (see [164]). The bonds of Al atoms and/or dissolved atoms (for instance, Mg) will break and form new bonds between an Al atom and a dissolved atom during ECAP. As a result, the free energy increases. To avoid this energy increase, chemically necessary dislocations will be created. On the other hand, coherent or semi coherent interfaces between particles and Al matrix cause a strain gradient in the Al matrix, then extra geometrically necessary dislocations will be created [177].Thus, non-shearable particles and dissolved elements both contribute to dislocation generation. The dislocation generation is related to mean free path (see Eq. 5.3) [164], and the mean free path is further related to non-shearable particles

[177] and dissolved elements [164]. In other words, both non-shearable particles and dissolved elements are obstacles of dislocation movement and influence the mean free path, cell walls/grain boundaries and forest dislocations in grain should also be considered to contribute the mean free path because last two terms are also obstacles of dislocation movement. Therefore, the free path for dislocations movement due to particles, dissolved elements, cell walls/grain boundaries and forest dislocations, can be calculated as:

$$\overline{l}^{-2} = l_{\mathrm{p}}^{-2} + l_{\mathrm{ch}}^{-2} + l_{\mathrm{gb}}^{-2} + l_{\mathrm{D}}^{-2} \qquad \text{Eq. 6.9}$$

where $l_{\mathrm{p}} = \dfrac{2r_{\mathrm{p}}}{f_{\mathrm{p}}}$ [164, 177], $l_{\mathrm{ch}} = \sqrt{\sum \left[B_i x_i\right]^2}$ [164] and $l_{\mathrm{gb}} = \overline{L}$. l_{p} is mean free path caused by hard, non shearable particles, f_{p} is volume fraction of particles, r_{p} is the mean radius of particles. l_{ch} is mean free path caused by dissolved elements, x_{i} are the concentrations of dissolved alloying elements i and B_{i} are constants. l_{gb} is mean free path caused by cell walls/grain boundaries, l_{D} is mean free path caused by forest dislocations. l_{D} is considered as constant because a large amount of dislocations are created during ECAP and the dislocations in grain are in state of thermodynamical equilibrium, the redundant dislocations with high energy have formed or moved to cell walls/grain boundaries. The value of l_{D} is determined by fitting.

Table 6.2 Average free path of Al-1050, AlZr and AlZrSiFe alloys after various passes of ECAP

	Average free path, μm		
	AlZr	AlZrSiFe	Al-1050
1 pass	0.169	0.169	0.169
2 passes	0.169	0.168	0.168
4 passes	0.169	0.168	0.168
8 passes	0.166	0.166	0.155
12 passes			0.154

For AlZr, AlZrSiFe and Al-1050 alloys l_{p} and l_{ch} are larger than 20 μm [164], which means they have no significant influence in the latter equation. The values of l_{gb} are equal to the average intercept lengths, which are shown in Table 6.3-Table 6.5. The values of l_{D} are determined as 0.17 μm through fitting measured microhardness and

predicted microhardness. The average free path values for dislocation movement in present three Al alloys are shown in Table 6.2.

The predicted dislocation densities in the grains of ECAP processed Al-1050, AlZr and AlZrSiFe alloys are shown in Table 6.3-Table 6.5. The yield strength of Al-1050, AlZr and AlZrSiFe alloy after various passes of ECAP can be calculated using Eq. 6.6, in which α_1 , α_2, λ, G, b and M were taken as 0.3 [177], 2 [176], 0.5, 26 GPa [185], 0.286 nm and 3 [186], respectively. σ_0 was taken as 28 MPa for Al-1050 [171], 14 MPa for AlZr alloy and 78 MPa for AlZrSiFe alloy, which are the yield strengths of each alloy in fully annealed condition. d, δ and f_{sub} were measured from EBSD results. The results of the model calculations are shown in Table 6.3-Table 6.5 and Fig. 6.7.

Table 6.3 Microhardness predictions of AlZr alloy after different passes of ECAP and values of parameters for microhardness calculation

	1 pass	2 pass	4 pass	8 pass
ρ, m^{-2}	3.48×10^{14}	3.49×10^{14}	3.52×10^{14}	3.61×10^{14}
f_{sub}	0.73	0.52	0.35	0.23
$l_{gb,}$ δ, μm	2.1	1.7	1.3	0.81
d, μm	10.5	9.78	3.5	2.6
σ_0 , MPa	14	14	14	14
$\Delta\sigma_{gb}$, MPa	3.0	3.0	4.6	6.4
$\tau_{d,}$ MPa	41.6	41.7	41.9	42.4
σ_y, MPa	125	125	127	131
HV_{cal}	39.6	39.6	40.3	41.3
HV_{exp}	39.2	39.9	41.3	41.1

Table 6.4 Microhardness predictions of AlZrSiFe alloy after different passes of ECAP and values of parameters for microhardness calculation

	1 pass	2 pass	4 pass	8 pass
ρ, m^{-2}	3.49×10^{14}	3.53×10^{14}	3.54×10^{14}	3.62×10^{14}
f_{sub}	0.468	0.459	0.459	0.107
$l_{gb,}$ δ, μm	2	1.2	1.1	0.8
d, μm	4.5	4.1	4.0	1.0
σ_0 , MPa	50	50	50	50
$\Delta\sigma_{gb}$, MPa	3.5	4.7	5	14.3
$\tau_{d,}$ MPa	41.7	41.9	42.0	42.4
σ_y, MPa	162	164	164	175
HV_{cal}	51.1	51.7	51.9	55.2
HV_{exp}	50.7	57.5	57.5	61.2

Table 6.5 Microhardness predictions of Al-1050 alloy after different passes of ECAP and values of parameters for microhardness calculation

	1 pass	2 pass	4 pass	8 pass	12 pass
ρ, m^{-2}	3.49×10^{14}	3.52×10^{14}	3.56×10^{14}	4.15×10^{14}	4.19×10^{14}
f_{sub}	0.69	0.68	0.38	0.33	0.16
l_{gb}, δ, μm	2.0	1.2	1.0	0.38	0.37
d, μm	14.72	11.23	4.87	1.31	0.88
σ_0, MPa	28	28	28	28	28
$\Delta\sigma_{gb}$, MPa	2.9	4.6	4.7	14	17.4
τ_d, MPa	41.7	41.9	42.1	45.4	45.7
σ_y, MPa	139	141	142	160	164
HV_{cal}	44.0	44.7	44.9	50.6	51.9
HV_{exp}	43.7	44.9	48.0	50.4	50.4

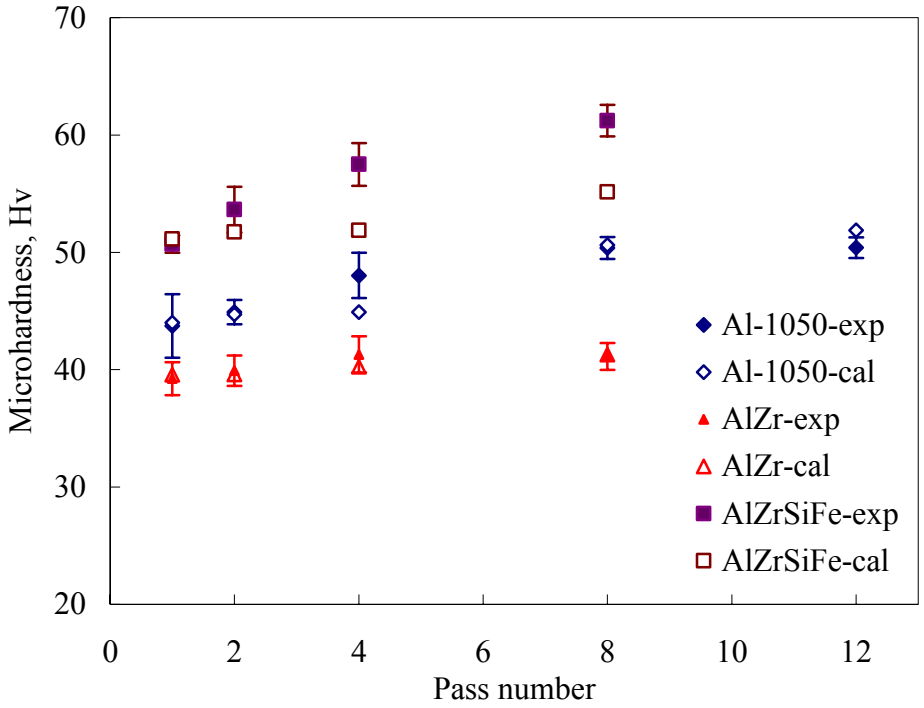

Fig. 6.7 Predicted and measured microhardness of Al-1050, AlZr and AlZrSiFe alloys after different passes of ECAP. The error bars in the figure define a symmetrical confidence interval by plus-minus standard deviation.

The microhardness of Al alloys is approximately proportional to the yield stress through the expression $HV=C\sigma_y$ [187] (The C value will be further discussed in Section 6.3.2 and Section 7.2). The value of C was taken as 3.16, which is the average value of worked Al-1050 with Vickers hardness ranging from 32 to 48 [227]. This value was used to calculate HV_{cal} in Table 6.3-Table 6.5 and Fig. 6.7. The each

value of HV_{exp} in Table 6.3-Table 6.5 was measured through five individual hardness values obtained from the microhardness tests, which are then averaged. Comparing the value of HV_{exp} and HV_{cal} shows the microhardness predicted by modelling is close to the experimental data, especially for AlZr alloy for which the model accurately predicts microhardness in all passes with average deviation within 1 %. The model also accurately predicts the microhardness of Al-1050 except for the material after four passes, where the predicted microhardness is 7 % lower than average measured microhardness but still in the range of standard deviation. The model also accurately predicts the microhardness of AlZrSiFe after one and two passes of ECAP but it fails to accurately predict the microhardness after four and eight passes of ECAP. This is thought to be due to refinement of intermetallic particles. The AlZrSiFe alloy has more alloying elements than the AlZr and Al-1050 alloys. Prior to ECAP this alloys in the as cast condition and the primary phases are coarse Al_3Zr, Al_3Fe with a small amount of α-AlFeSi particles distributed along grain boundaries. Thus, the free path caused by non-shearable particles is very large. After several passes of ECAP, the coarse second phases will break and refine to fine and more homogenously distributed particles, causing the strengthening contribution to non shearable particles to increase. Moreover, the free path caused by non-shearable particles decreases and dislocation density in the grain will significantly increase. For instance, if the particles are refined to 15 nm in diameter (estimated from TEM, see Fig. 5.12 (f)), the predicted microhardness is 61 Hv, which includes an increase of 9 Hv caused by precipitates strengthening [188] and an increase of 1 Hv caused by increased dislocation density in the grains.

6.3.2 Modelling on microhardness inhomogeniety of Al-1050 after one pass of ECAP

In Section 6.1.2 it was demonstrated that the microhardness inhomogeneity on the cross section of ECAP processed Al-1050 is mainly due to the difference of dislocation densities between billet centre and edges. This can also be interpreted by the present strengthening model. In the model, the parameters α_1, α_2, G, b, M and δ are taken as 0.3 [177], 2 [176], 26 GPa [189], 0.286 nm, 2.6 [190] and 1.3 μm [124], respectively. The other parameters can be obtained from the experimental data on Al-1050 presented here (see Table 6.6). d can be measured from the OIM data (Fig. 6.5). f_{sub} can be calculated through misorientation distribution figure (Fig. 6.6 (a), (c) and

(e)). f_{Rec} is determined from Fig. 6.6 (b), (d) and (f) as the area in the OIM map occupied by grains that have no interior low angle grain boundaries.

The dislocation density in the unrecrystallized grain (ρ_1) is calculated using Eq. 6.8 (see also [227]). The calculated values (see Table 6.3-Table 6.5), are close to value estimated from measurements on Al-6082 after one pass of ECAP at room temperature which provided a dislocation density of 4×10^{14} m^{-2} [178]. The dislocation density in the recrystallized grain (ρ_2) is estimated as 1×10^{13} m^{-2}, which is the typical dislocation density of annealed aluminium alloys [161].

Table 6.6 Strength predictions for the ECAP-processed billet and the heat treated billet.

parameter	ECAP- processed Al-1050 billet			350 ˚C heat treated Al-1050 billet		
	Top edge	Centre	Bottom edge	Top edge	Centre	Bottom edge
ρ_1, $\times10^{14}$ m^{-2}	4	4	4	4	4	4
P_2, $\times10^{13}$ m^{-2}				1	1	1
f_{sub}	0.473	0.746	0.73	0.170	0.166	0.180
f_{Rec}				0.759	0.688	0.723
δ, μm	1.3	1.3	1.3	1.3	1.3	1.3
d, μm	8.2	26	19	21	12	11
σ_0, MPa	28	28	28	28	28	28
$\Delta\sigma_{gb}$, MPa	3.70	4.48	4.44	1.58	2.01	2.16
τ_d, MPa	39.1	39.1	39.1	13.4	17.1	16.0
σ_y, MPa	149.0	149.8	149.7	71.9	81.3	78.1
HV_{cal}	49.7	50.2	50.1	25.5	26.6	26.1
HV_{exp}	42.2	48.2	39.1	25.5	27.0	27.3

In the classic works on grain size strengthening, it is generally interpreted by pile-up of edge dislocations [191, 192]. The stress concentration by the pile-up edge dislocation at the subgrain/grain boundaries leads to the dislocation activated in the neighbouring grain. The length of pile-up edge dislocations is proportional to the grain size so that the dislocation movement in a materiel with a larger grain size is easier to transfer to the neighbouring grains by the same strain. Thompson et al. [193] studied the grain size strengthening in 1970s by introducing a microstructurally sensitive composite model based on Ashby's concept of statistically stored dislocations (SSDs) and geometrically necessary dislocations (GNDs) [177]. In the

last decade, many works [194,195,196,197,198,199,200,201] were focused on studying grain strengthening employing SSDs and GNDs, in which the SSDs are stored in the grain interior and the GNDs are distributed in grain boundary regions due to strain gradients. When the amount of GNDs stored in grain boundary regions is large enough, the dislocation in the adjacent grain will be activated due to stress concentration. Both the pile-up model and the GND model indicate the effectiveness of grain boundaries in strengthening will depend on the misorientation angle between them. A smaller misorientation angle between the two grains makes it easier to transfer the dislocation movement to the neighbour grain at the same slip system. Therefore, the subgrain boundary strengthening effect is smaller than the grain boundary and the value of λ is between 0 and 1. In the present study, λ is estimated as 0.5. The value of λ estimation has a limited influence on the strength modelling results because the experiment results and the following modelling results show the grain size only contributes a very small part to the yield strength. The results of the model calculations are shown in Table 6.6.

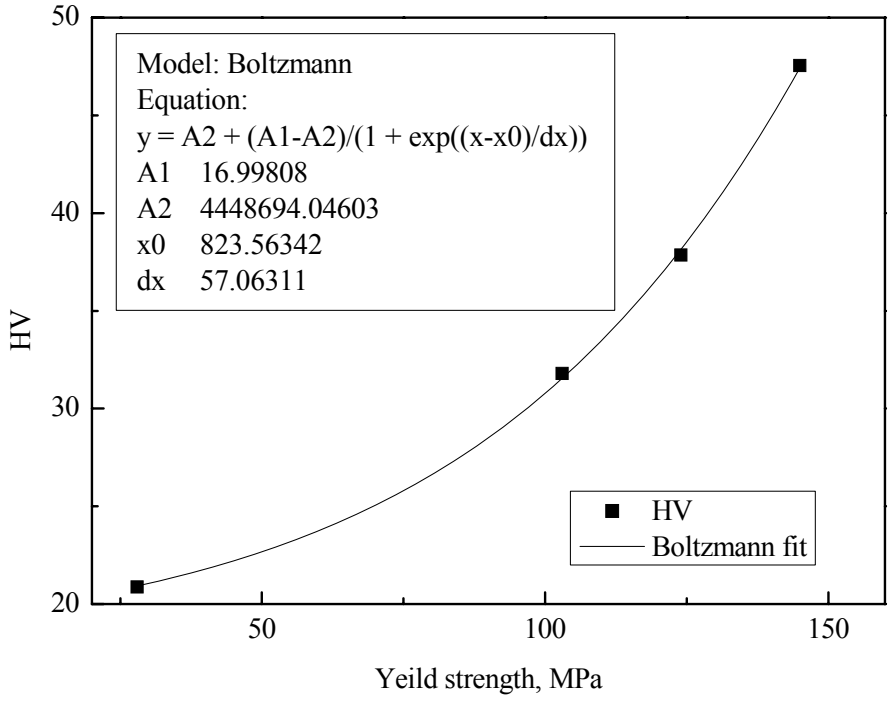

Fig. 6.8 The relationship between microhardness and yield strength of Al-1050.

In order to compare the yield strength modelling results and measured microhardness, the relationship between hardness and yield strength of Al-1050 alloy is present in Fig. 6.8. The solid squares in Fig. 6.8 are four groups of values of Vickers hardness

(HV) and yield strength of Al-1050-O, Al-1050H14, Al-1050H16 and Al-1050H18, which are obtained from reference [171] (see Table 6.7). The Vickers hardness (HV) in Table 6.7 is converted from Brinell hardness (HB) using HB = 3.76211+0.826368HV [202]. The curve in Fig. 6.8 is the fit curve using Boltzmann model. The fit equation and parameters values are also shown in Fig. 6.8. The hardness calculated from this relationship (HV_{cal}) is listed in Table 6.6.

Table 6.7 Hardness and yield strength of Al-1050 at various states of heat treatments [171]

	HB	HV	Yield strength, MPa
Al-1050-O	21	20.9	28
Al-1050-H14	30	31.8	103
Al-1050-H16	35	37.8	124
Al-1050-H18	43	47.5	145

The modelling results in Table 6.6 show a reasonably good correspondence between measured and predicted hardness. This indicates that the present model may form a sound basis for predicting and analysis strength of severe plastically deformed metals. The model indicates that the strength contributed by dislocation density is much higher than the strength contributed by grain size in both ECAP processed billet and heat treated billet. This is consistent with findings by Gubicza et al [181], who showed that for various severely plastically deformed alloys the yield strength can be predicted well by Eq. 6.2 and Eq. 6.4, disregarding GB strengthening, for dislocation densities measured through X-ray diffraction line broadening. Comparing the values of HV_{exp} and HV_{cal} shows the microhardness of the heat treated billet achieved by modelling is close to the experimental data, suggesting that the model captures the different strengthening effects well. However, the modelled microhardness of the ECAP-processed billet slightly deviates from the experimental microhardness. The modelling microhardness at the top edge, the centre and the bottom edge are all around 50 Hv while the experimental microhardness at those positions is 42 Hv, 48 Hv and 39 Hv. This deviation is thought to be due to the same dislocation density (4×10^{14} m^{-2}) being used in Eq. 6.6 to calculate the microhardness of the ECAP-processed billet at the top edge, the centre and the bottom edge. The present results indicate that the dislocation density at different areas of the ECAP-processed billet could be slightly higher or lower than 4×10^{14} m^{-2} due to the inhomogeneous strain during ECAP.

To verify these suggestions about differences in local dislocation density one might attempt dislocation density measurements through transmission electron microscopy (TEM). However, it should be realized that dislocation density will be inhomogeneous and that accuracy of dislocation density measurement in TEM on severely plastically deformed Al alloys is typically associated with confidence of at best about ±20 % [184]. Hence, it is unlikely that the variations in dislocation density between the different areas can be efficiently detected by TEM, and hence TEM was not attempted.

6.4 Summary

The evolution of microstructure and mechanical properties of Al-1050, AlZr and AlZrSiFe alloys after various passes of ECAP was studied through experiments and modelling. After one pass of ECAP, the grain size significantly decreases and microhardness increases substantially due mainly to the generation of large amounts of dislocations. Furthermore, both microstructure and microhardness is inhomogeneously distributed on the cross section of the UFG Al-1050. The microhardness is larger in the centre whilst the grain size is also large in the centre. The microhardness inhomogeneity is caused by the difference between dislocation density in the centre and edges due to inhomogeneous deformation, which has been justified by experiments on annealed billets and the strengthening model. After additional passes of ECAP, the grain is continuously refined and microhardness increases.

The UFG microstructure and relatively higher microhardness is stable up to 200˚C. Annealing at higher temperature leads to recovery, recrystallization, grain coarsening and a decrease in microhardness. According to the model, the microhardness decreases with the increasing annealing temperature because the density of dislocations stored in the grains during ECAP is reduces due recrystallization. The refined grain size contributes the yield strength/microhardness but it is not main strengthening contribution compared with dislocation strengthening.

7 Nanoindentation of UFG Aluminium Alloys

In this chapter, nanoindentation hardness experiments of UFG Al-1050 processed by two passes of ECAP are reported. The nanohardness was measured by nanoindenter equipped with a Berkovich tip at deferent indentation depths. The main part of this Chapter deals with a model that was developed to interpret the indentation size effect (ISE). The model considers the tip wear effect causing a rounded tip, the plastic zone size and various strengthening contributions, including geometrically necessary dislocations. The model differs from existing models on several critical details and it is justified through comparison with our own experimental data and experimental data in the literature. The model developed will be further expanded and applied in the subsequent Chapter.

7.1 Results

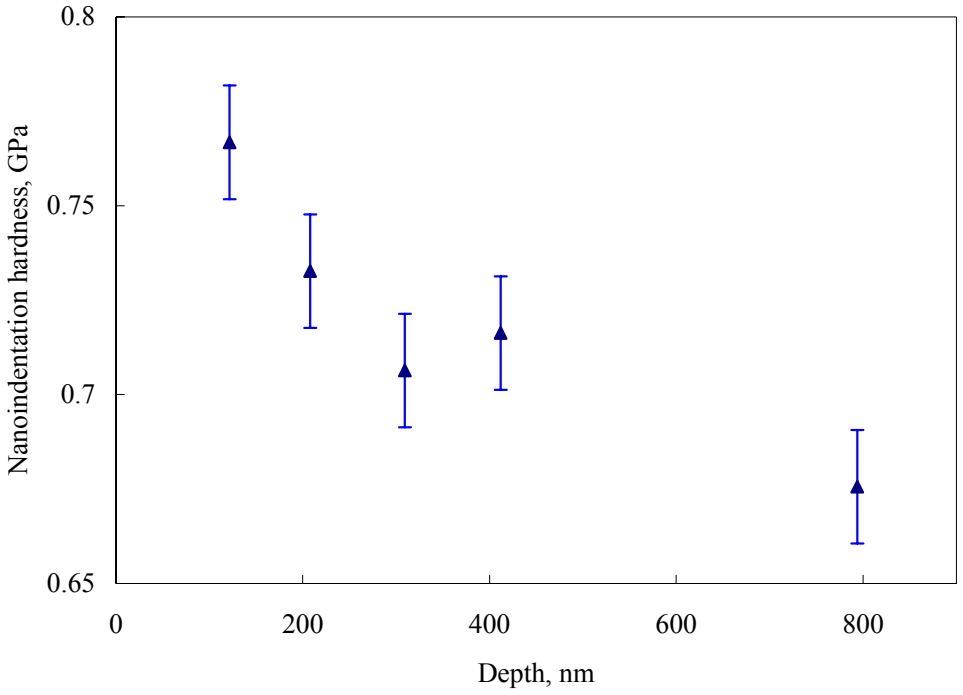

Fig. 7.1 The influence of indentation depth on nanoindentation hardness of UFG Al-1050 processed by two passes of ECAP.The error bars are defined by standard deviations.

The nanoindentation hardness of UFG Al-1050 processed by two passes of ECAP was measured at different indentation depths. The measured results are shown in Fig. 7.1. The nanoindentation hardness shows a significant indentation size effect (ISE), i.e. the indentation hardness values decrease with the increasing indentation depth. Moreover, the nanoindentation hardness of UFG Al-1050 after two passes of ECAP is much higher than the Vickers hardness of this same alloy in same condition, for instance, the nanoindentation hardness is 0.78 GPa at the indentation depth of 800nm while the Vickers hardness is only 0.44 GPa (see Fig. 6.7).

7.2 A model of indentation size effect for a blunted tip.

In the present model, we consider that the main cause for deviations from existing models is due to deviation from the ideal pyramid shape of the tip. This tip rounding can be due to wear and localised nanoscale fracture at the tip, which in practice will be unavoidable. A rounded tip has been considered in some works [79,203], which provide an improved fit to experiments, but still failed to fully explain deviations. Huang, Hwang, Nix and co-workers [204,205,206] studied the tip rounding effect using CMSG theory in an FE analysis. They predicted that the indentation hardness increases with the increasing indentation depth when the indentation depth is lower than the height of the rounded tip; then decreases with the increasing indentation depth when the indentation depth is larger than the height of the rounded tip. A test of the model reported in [206], using hardness data of MgO, indicated that their model of the tip rounding effect alone can not explain these experimental results.

Apart from the tip radius effect, adjusting the assumed size of the plastic zone underneath the indent has also been considered in several works to provide a more accurate hardness prediction. Feng and Nix [81] and Durst et al [207,208] considered the radius of the plastic zone under the indent is f times larger than the radius of the contacted area. Feng and Nix [81] assumed the f value is continuous factor varying with the contact depth in an exponential function, whilst Durst et al [207, 208] assumed f is fixed for specific materials. The modified models provide good predictions for different materials at the expense of using a range of fitting parameters; with f values from 1 to 2.6.

Furthermore, the intrinsic stress, grain boundaries, precipitates and solid solution atoms should be considered in the hardness prediction model especially for cold worked alloys. Qiu et al [209] studied the effect of intrinsic stress on the ISE of single crystal tungsten and found the intrinsic stress strongly influences the proportional factor of the square of the indentation hardness H^2 and the reciprocal of the indentation depth h^{-1} provided by Nix-Gao model.

7.2.1 Aims of the model

The influence of strain gradient effects needs to be included in the formulation of the constitutive behaviour of materials at micro-scale [210, 211] and a number of gradient plasticity models accounting for these effects have been proposed (see e.g. [212,213]). One example of an experiment revealing the strain gradient effect is nanoindentation, in which the hardness detected has been shown to depend on the indent size, which is the so called indentation size effect (ISE) [73]. The ISE is generally explained using the so-called 'mechanism-based gradient plasticity theory' in which geometrically necessary dislocations (GNDs) [74,75,76] generated in the plastic zone underneath the indent due to strain gradients play a key part. Decreasing indentation size gives rise to an increasing density of GNDs, and, hence, an increasing hardness. Understanding of the ISE is crucial to development of FE models that incorporate GNDs. Thus the ISE has received intense interest and a range of models have been presented to analyse the measured hardness vs indentation depth relation. This range of differing models can lead to doubts on the range of validity of the theoretical approaches. The objective of the present work is to show that existing and new data on the indentation size effect can be modelled with improved accuracy and down to a smaller indentation depth using a model in which we incorporate an accurate description of a blunted indenter tip and various additional strengthening effects, all within the mechanism-based gradient plasticity theory. The model is based on analytical equations, and is hence computationally highly efficient.

7.2.2 Generation of GNDs.

In this section an improved calculation of the ISE in the case of a non-perfect (rounded) indenter tip is provided to avoid the many approximations involved in [203]. Radius of a rounded tip is considered to be a fixed value. The rounded tip can

be considered as comprised of two parts: a spherical cap and a conical frustum (see Fig. 7.2).

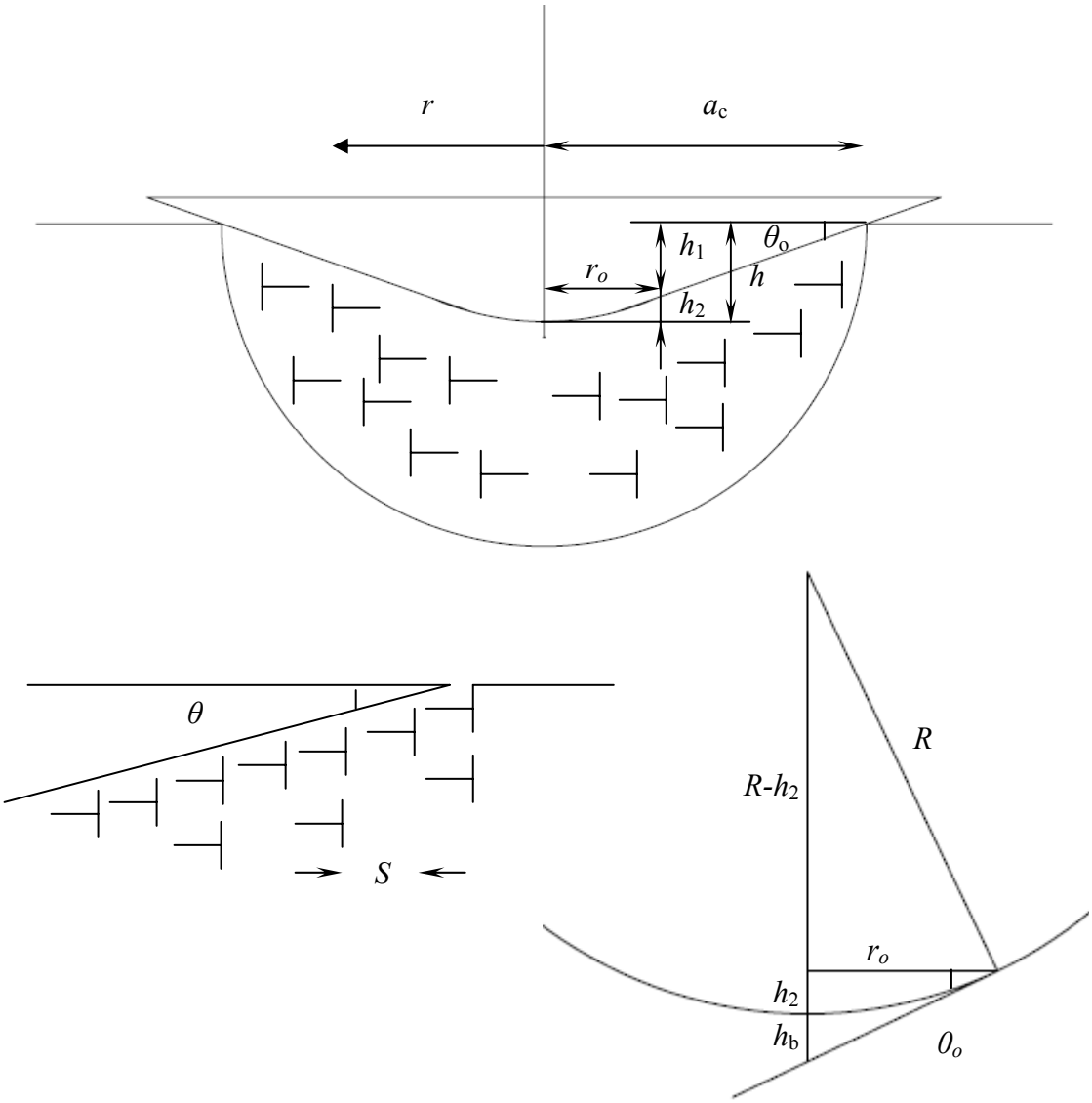

Fig. 7.2 Schematic sketch of distribution of GNDs underneath the rounded conical tip [78]

We will take $a_{pz} = fa_c$, where $f > 1$ [81, 207], a_{pz} and a_c are the radius of the plastic zone and the contact area. With reference to Fig. 7.2 it can be seen that:

$$h = h_1 + h_2 \qquad \text{Eq. 7.1}$$

$$\frac{r_0}{R} = \sin\theta_0 \qquad \text{Eq. 7.2}$$

$$h_2 = R - \sqrt{R^2 - {r_0}^2} \qquad \text{Eq. 7.3}$$

$$\tan\theta = \frac{b}{S} \qquad \text{Eq. 7.4}$$

$$\tan\theta_0 = \frac{h_1}{a_c - r_0} \qquad \text{Eq. 7.5}$$

where h is indentation depth, h_2 is the height of the spherical cap, r_0 is the radius of the bottom surface of the spherical cap as well as the top surface of the conical frustum. From Eq. 7.1 to Eq. 7.5 follows,

$${r_0}^2 - \frac{2h_2}{\sin\theta_0} r_0 + {h_2}^2 = 0 \qquad \text{Eq. 7.6}$$

Solving the latter equation and taking into account that $\frac{r_0}{h_2} > \cot\theta_0$ (see Fig. 7.2) provides:

$$r_0 = \frac{1+\cos\theta_0}{\sin\theta_0} h_2 \qquad \text{Eq. 7.7}$$

Substituting Eq. 7.7) to Eq. 7.5) provides:

$$a_c = \frac{h_1}{\tan\theta_0} + r_0 = \frac{h_1}{\tan\theta_0} + \frac{1+\cos\theta_0}{\sin\theta_0} h_2 = h\cot\theta_0 + h_2 / \sin\theta_0 \qquad \text{Eq. 7.8}$$

$$R = \frac{r_0}{\sin\theta_0} = \frac{1+\cos\theta_0}{\sin^2\theta_0} h_2 = \frac{1}{1-\cos\theta_0} h_2 \qquad \text{Eq. 7.9}$$

$$h_\mathrm{b} = \frac{1}{\cos\theta_0} h_2 \qquad \text{Eq. 7.10}$$

where h_b is blunting distance (see Fig. 7.2). The total length of GND $\lambda(h)$ comprises of two parts

$$\lambda(h) = \lambda_1(h_1) + \lambda_2(h_2) \qquad \text{Eq. 7.11}$$

where $\lambda_1(h_1)$ stands for the length of GND underneath the conical frustum while the $\lambda_2(h_2)$ stands for the length of GND underneath the spherical cap. $\lambda_1(h_1)$ and $\lambda_2(h_2)$ are given by:

$$\lambda_1 = \int_{r_0}^{a} 2\pi r \frac{dr}{S} = \int_{r_0}^{a} 2\pi r \frac{\tan\theta_0}{b} dr = \frac{\pi \tan\theta_0}{b}(a_c{}^2 - r_0{}^2) \qquad \text{Eq. 7.12}$$

$$\lambda_2 = \int_{0}^{r_0} 2\pi r \frac{dr}{S} = \int_{0}^{r_0} 2\pi r \frac{\tan\theta}{b} dr = \int_{0}^{\theta_0} \frac{2\pi R^2 \sin^2\theta}{b} d\theta = \frac{\pi R^2}{b}(\theta_0 - \sin\theta_0 \cos\theta_0) \qquad \text{Eq. 7.13}$$

The radius of the plastic zone is taken as f times of the contact radius, therefore, $V = \frac{2}{3}\pi f^3 a_c{}^3$. Substituting Eq. 7.7~Eq. 7.13 into $\rho = \frac{\lambda(h)}{V}$, provides the GND density, ρ_{GND}

$$\rho_{GND} = \frac{3\tan^2\theta_0}{2bf^3\left(h+h_b\right)}\left(1 + \frac{(\theta_0 - \tan\theta_0)\sin\theta_0\cos\theta_0}{(1-\cos\theta_0)^2} \cdot \frac{h_b{}^2}{\left(h+h_b\right)^2}\right) \qquad \text{Eq. 7.14}$$

In Eq. 7.14), θ_0 is 19.7° for a Berkovich tip, which can be obtained from indent shape parameters. The value of h_b can be obtained by measurement using atomic force microscope (AFM) or scanning electron microscope (SEM). Alternatively, it can also be obtained by fitting the indent shape correction equation. The contact area according to current model is,

$$A_c = \pi a_c{}^2 = \frac{\pi}{\tan^2\theta_0}(h+h_b)^2 \qquad \text{Eq. 7.15}$$

The above expressions are valid for $h>h_2$. The corresponding equations for $h<h_2$, i.e. for a purely spherical indent, are given as follows:

$$\begin{aligned}\lambda(h) &= \int_{0}^{r} 2\pi r \frac{dr}{S} = \int_{0}^{r} 2\pi r \frac{\tan\theta}{b} dr = \int_{0}^{\theta} \frac{2\pi R^2 \sin^2\theta}{b} d\theta = \frac{\pi R^2}{b}(\theta - \sin\theta\cos\theta) \\ &= \frac{\pi}{b}\left[R^2 \arccos(1-h/R) - (R-h)\sqrt{2Rh-h^2}\right]\end{aligned} \qquad \text{Eq. 7.16}$$

where, $\theta = \arccos(1 - h/R)$ and R=1883.5 nm (see Eq. 7.9). Substituting Eq. 7.16 in $\rho = \frac{\lambda(h)}{V}$, provides the GND density as:

$$\rho_{GND} = \frac{3(\theta - \sin\theta\cos\theta)}{2bf^3 R\sin^3\theta} = \frac{3\left[R^2\arccos(1-h/R) - (R-h)\sqrt{2Rh-h^2}\right]}{2bf^3(2Rh-h^2)\sqrt{2Rh-h^2}} \quad \text{Eq. 7.17}$$

In this case the projected contact area is given by

$$A_c = \pi a_c^{\,2} = \pi R^2\sin^2\theta = 2\pi Rh - \pi h^2 \quad \text{Eq. 7.18}$$

In contrast to this, Alkorta et al [203] made a range of approximations and suggested:

$$A_c = \pi a^2 = \pi\tan^2\phi\cdot h_f^{\,2} + 2\pi R h_f \quad \text{Eq. 7.19}$$

i.e,

$$a = \tan\phi\sqrt{h_f^{\,2} + \frac{2R}{\tan^2\phi}h_f} \quad \text{Eq. 7.20}$$

where a is the radius of contact area, ϕ is complementary to θ_0, h_f is the depth and R is the radius of rounded tip.

7.2.3 Strength model

The Nix-Gao model and most of its derivatives [78,79,81] only consider the dislocation strengthening, whilst other strengthening contributions remain unspecified and are part of the fittable parameter H_o. In the current study, the grain boundary strengthening including subgrain boundary and grain boundary and remaining minor strengthening contribution are also considered as well as the dislocation strengthening, using the expression [172, 173,214]:

$$\sigma_y = \Delta\sigma_{gb} + M\,\tau_{tot} = \Delta\sigma_{gb} + M\,[\Delta\tau_0 + \Delta\tau_{ss} + (\Delta\tau_D^{\,2} + \Delta\tau_{ppt}^{\,2})^{1/2}] \quad \text{Eq. 7.21}$$

where σ_y is yield strength, $\Delta\sigma_{gb}$ is the strengthening due to the presence of grain or subgrain boundaries, M is a factor often referred to as the Taylor factor. τ_{tot} is the critical resolved shear stress (CRSS) of the grains. The hardness is expressed as

$$H = C\,\sigma_y \quad \text{Eq. 7.22}$$

where C is a constant. To simplify the expressions, the contributions to the yield strength by intrinsic CRSS (τ_0), solid solution strengthening (τ_S) are taken as a constant term σ_0, whilst at this stage precipitation hardened materials are avoided (ie. $\Delta\tau_{ppt}$=0). The value of constant C is generally taken as 3 in the literature for conventional hardness test [187]. However, the nanoindentation hardness is generally 10-30% higher than the Vickers hardness for many metals even using a large indentation depth to avoid the ISE [215]. The difference between nanoindentation and Vickers hardness is partly due to the former being defined by projected area while the latter is defined by contact area, which would induce a difference of about a factor 1/sin(136˚/2)=1.08 (the vertex angle of Vickers tip is 136˚). Therefore, the proportionality constant C_2 for nanoindentation hardness is somewhat larger that that for Vickers hardness (see also section 7.2.5.2), i.e.:

$$H\mathrm{v} = C_1\sigma_y = C_1\left[\sigma_0 + \Delta\sigma_{gb} + M\alpha_1 Gb\sqrt{\rho_{SSD}}\right] \qquad \text{Eq. 7.23}$$

$$H\mathrm{n} = C_2\sigma_y = C_2\left[\sigma_0 + \Delta\sigma_{gb} + M\alpha_1 Gb\sqrt{\rho_{SSD} + \rho_{GND}}\right] \qquad \text{Eq. 7.24}$$

where Hv is the Vickers hardness, Hn is the nanoindentation hardness, α_1 is a constant (about 0.3 [75]), G is the shear modulus of Al, ρ_{SSD} is the density of the statistically stored dislocations. (As shown in section 7.2.5.2, for aluminium C_1 = 3.16.)

7.2.4 Model predictions

To evaluate the present model and compare it to other models, the GND density predicted by the Nix-Gao model, Alkorta et al [203] model and the current model are calculated and presented in Fig. 7.3 (b is taken as 0.286 nm, the value for Al). Fig. 7.3 shows that the current model (taking h_2 = 110 nm) predicts a much milder ISE than the Nix-Gao model. For large indentation depth (typically h> 400 nm) the GND density predictions in current model and Nix-Gao model with f=1.76 converge. The current model predicts an ISE that is clearly very different from the Alkorta et al [203] model. This is due to the approximations made in the latter model.

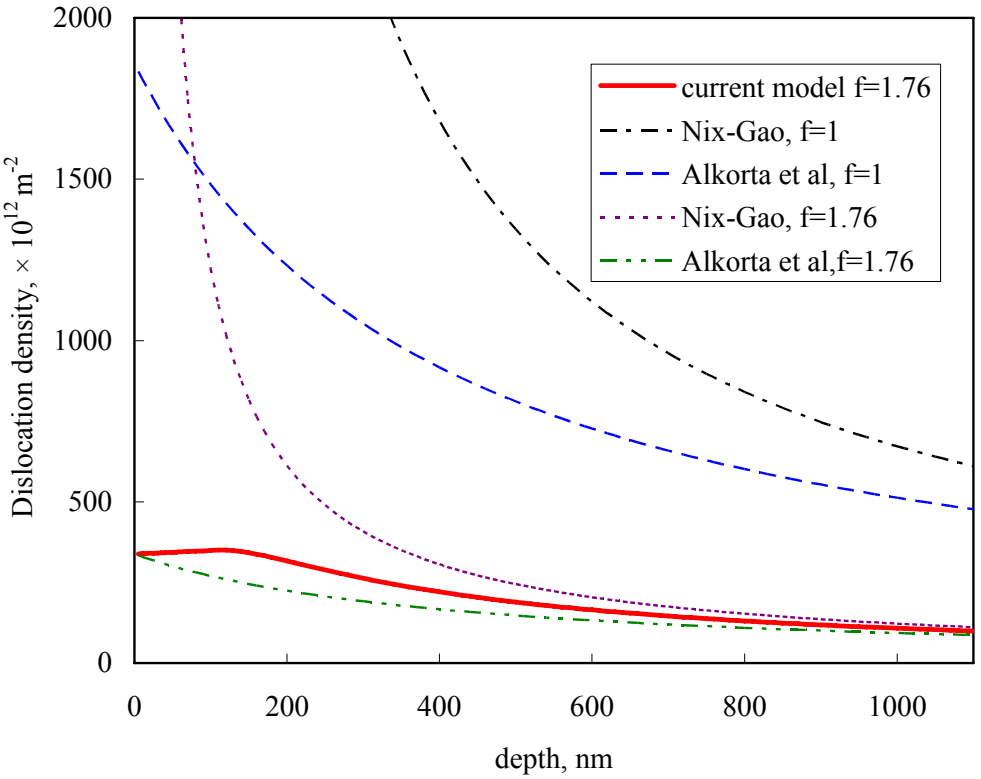

Fig. 7.3 Comparison of GND density predicted by various models

The calculated GND density (see Fig. 7.3) and nanoindentation hardness (see Fig. 7.7) predict a reverse ISE when the indentation depth is lower than h_2. Both experimental and finite element modelling results have proved the reverse ISE using a spherical tip [79,216]. When the indentation depth is larger than h_2 the current model shows a slower ISE than the Nix-Gao model because of the blunt tip (see Fig. 7.3).

The Nix-Gao model and its derivatives including the current model calculate the average GND density underneath the indent by assuming the GNDs are being stored in a hemisphere with a specific radius. The radius of the plastic zone in current model is assumed to be f times the radius of the original Nix-Gao model. This is broadly in line with experiments [217] and finite element modelling [218,219]. The finite element modelling has determined that value of f ranges from 0 to 3.5, which depends on material and other parameter values such as M and C_2 [218].

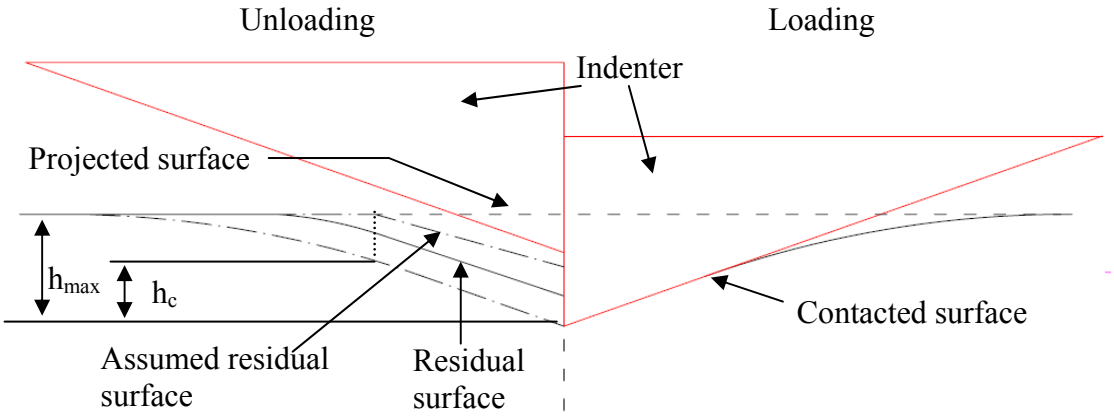

Fig. 7.4 Illustration of contacted area, residual area, assumed residual area and projected area during nanoindentation

C_2 is defined as the ratio of nanoindentation hardness to yield strength, whilst C_1 is the ratio of Vickers hardness to yield strength. This difference can be attributed to the nanoindentation and Vickers hardness being calculated using different areas. As shown in Fig. 7.4), Vickers hardness is obtained by dividing applied force by the residual contacted area whilst nanoindentation hardness is calculated using the projected area which is calculated using contact depth h_c (alternately referred to as the plastic depth, h_p). If the residual projected area is used to calculate the Vickers hardness, the Hv value would be 8% higher than the real Hv value but still lower than the nanoindentation hardness. It is assumed that unloading from h_{max} to residual depth (see Fig. 7.4) is pure elastic [220], and then the projected area is underestimated by using h_c, which is calculated using h_{max} by the Hertz equations [221]. In fact, the unloading is elastic and plastic [215], therefore the residual area is larger than the assumed residual area used for nanoindentation calculation (see Fig. 7.4). The reverse plasticity is different for different materials so that Hn/Hv depends on material.

Determination of h_2 is critical in current model. As shown in Fig. 7.5, the GND density predicted by the current model is close to that predicted by the Nix-Gao model with the same f value when h_2 value is close to zero, whilst the GND density at lower indentation depth dramatically decreases with increasing h_2 value. The blunting distance h_b of different commercial nanoindenters has been determined to be 6.1 nm to 28.8 nm [222,223,224]. Using Eq. 7.10 this is equal to a range of values for h_2 of 5.7 nm ~ 27 nm. The h_2 value of a new tip produced by precision polishing

will be at the lower end of this range, but it will increase due to wear of the tip. Therefore the h_2 value that will be determined in the current work (see section 7.2.5.1 below) is only correct for our nanoindenter at the time the experiments were performed.

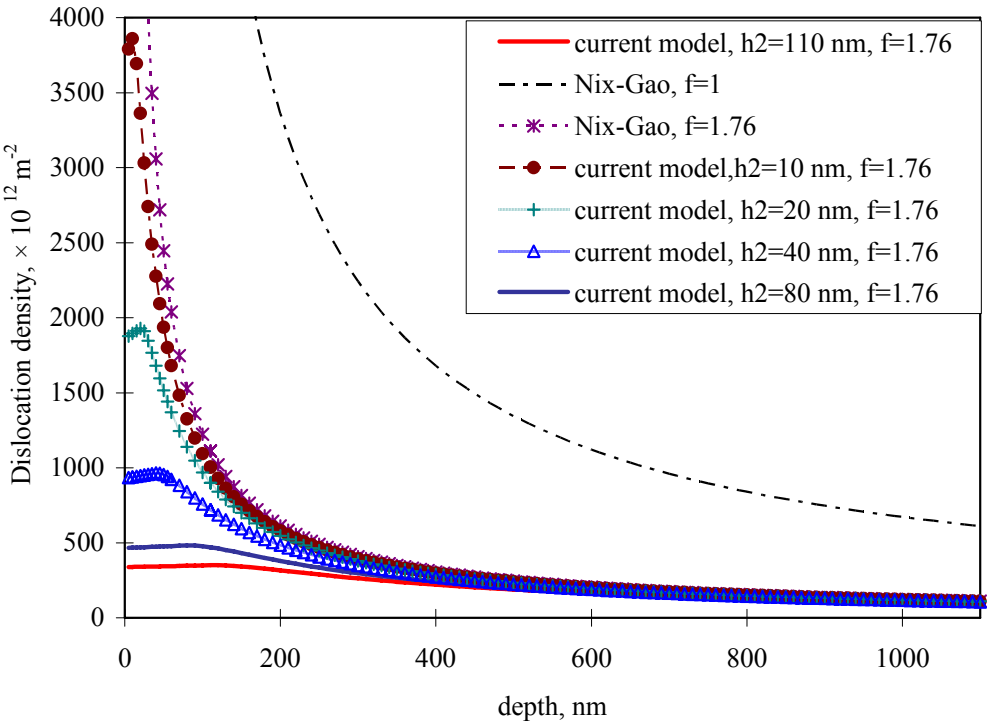

Fig. 7.5 Influence of rounded tip on the GND density created under different indentation depth.

7.2.5 Modelling Results and Model Verification

7.2.5.1 Determining the blunted tip radius.

To apply the above model in the analysis of nanoindentation data first h_b for the indenter needs to be obtained. An effective way of achieving this is through calibration experiments on a calibration material with known properties. In this work, this calibration was achieved by performing a series of indentations with loads varying from 0.5 mN to 500 mN on fused silica. The elastic modulus, hardness and Poission's ratio of this calibration material are known, and from these experiments the area values at specific depth were obtained and plotted in Fig. 7.6. By fitting the area and depth data using Eq. 7.15 h_b is determined as 117 nm. The fit (Fig. 7.6) is

excellent (root mean square error (RMSE) 0.090 × 10 ^{6} nm ^{2}) providing confidence that the treatment of the rounded tip (section 7.2.2) is at least an accurate approximation.

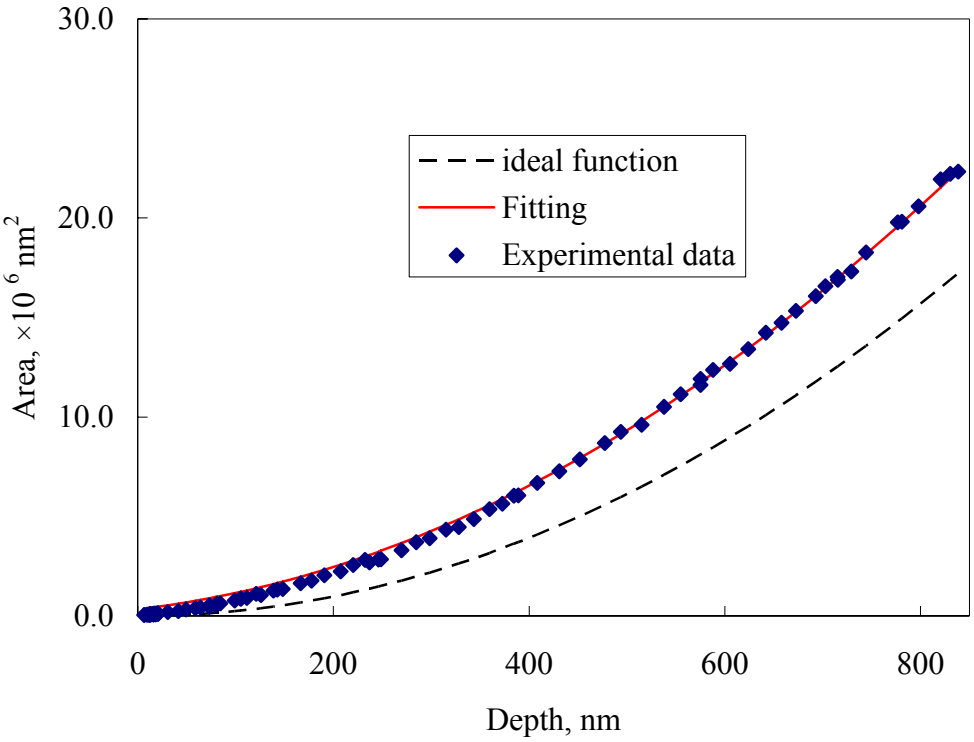

Fig. 7.6 Fitting of $h_{b.}$ The blue cubes are the area function measured by experiments; the dash line is ideal function for the sharp tip; the red line is fitting curve using Eq. 7.15.

7.2.5.2 Predicting nanoindentation hardness of UFG Al-1050.

To provide a critical assessment of the model nanoindentation tests were performed on a material for which the ISE has not been tested previously, with a microstructure that contains substantial strengthening contributions besides the GNDs, whilst the parameters in the model are known to a good accuracy. UFG Al-1050 was selected. We will first show that all parameters are (essentially) known.

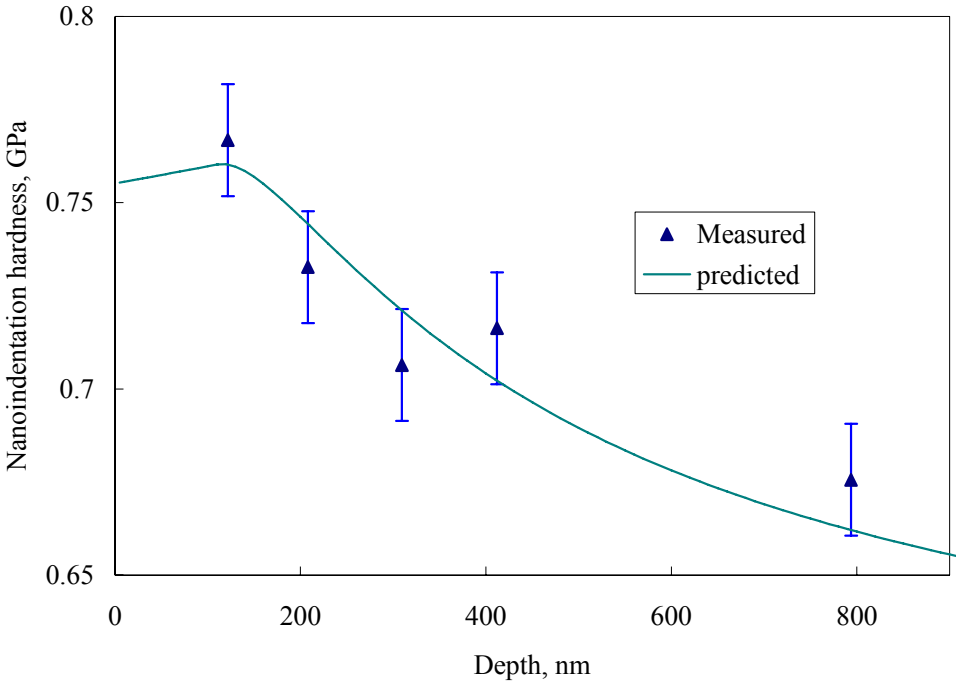

Fig. 7.7 Measured and predicted nanoindentation value against the indentation depth. The error bars are defined by standard deviations.

It was shown before that the C_1 value for worked Al-1050 ranges from 3.05 to 3.28 [227], we will here take C_1 as the average over that range, i.e. C_1=3.16. Work on a range of alloys [215] has shown that nanoindentation hardness is 10-30% higher than the Vickers hardness, in the current work we will take C_1/C_2 of Al-1050 as equal to that of Cu (0.8 [215]). The Vickers hardness of the present UFG Al-1050 was measured to be 44 Hv. The σ_0 of Al-1050 is taken as 28 MPa [171], which is the yield strength of Al-1050 in fully annealed condition. The value of $\Delta\sigma_{gb}$ is calculated using the approach outlined in [214], which provides $\Delta\sigma_{gb}$= 5 MPa (see also [227]). M and G are taken as 2.6 [190] and 26 GPa [189], respectively. This leaves just f to be fitted. We would expect f to be close to the value of 1.9 determined for single crystalline copper, annealed polycrystalline copper, UFG copper and polycrystalline iron [207].

The predicted nanoindentation hardness with a fitted value f = 1.76, is presented in Fig. 7.7. A very good correspondence is found with RMSE of 0.011GPa. The measured and predicted nanoindentation values are plotted in Fig. 7.8.

Fig. 7.7 shows the measured and predicted nanoindentation hardness as a function of the indentation depth. The predicted values successfully captured the measured trend. The nanoindentation hardness decreases with increasing indentation depth but the rate of decrease is slow when the depth is larger than 400 nm.

The present data shows a higher scatter than experimental data on polycrystalline and single crystal materials reported in a range of papers. This is due to the more inhomogeneous nature of the present UFG Al-1050 (see Ref [227]). This, however, does not impinge on the main conclusion here, i.e. the good predictions of the nanoindentation hardness.

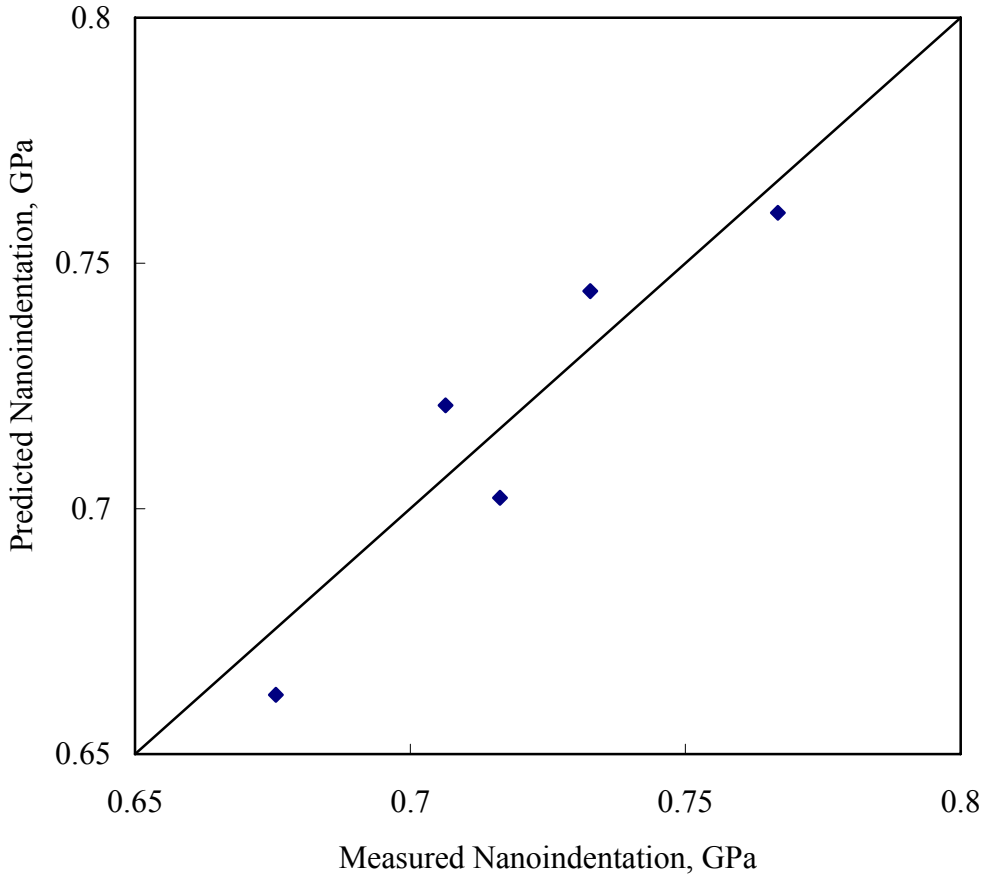

Fig. 7.8 Measured and predicted nanoindentation value of UFG Al-1050. The indentation depth ranges from 100 nm to 800 nm.

7.2.5.3 Predicting dislocation densities

In a further test for the model we will predict dislocation densities and compare those against measured values by Demir et al [225] for (111) copper single crystals. In the latter work dislocation densities were obtained from analysis of cross sections of deformed material under a rounded tip with diameter of 1 μm using 3-D EBSD. (Note that in Fig 2 in Ref [225] depth are mislabelled). The average values of measured GND densities at different indentation depths have been replotted in Fig. 7.9, and various model predictions are included in the figure. The GND density increases with the indentation depth, and this is captured well by the present model if the value of f is set to 1.4. (The slightly larger deviation between predicted and measured value for the data point at the larger indentation depth could be because the radius value (reported to be R = 1 μm [225]) of the tip having increased due to wear. The current model would give good predictions for all the four GND densities if R = 1.3 μm.)

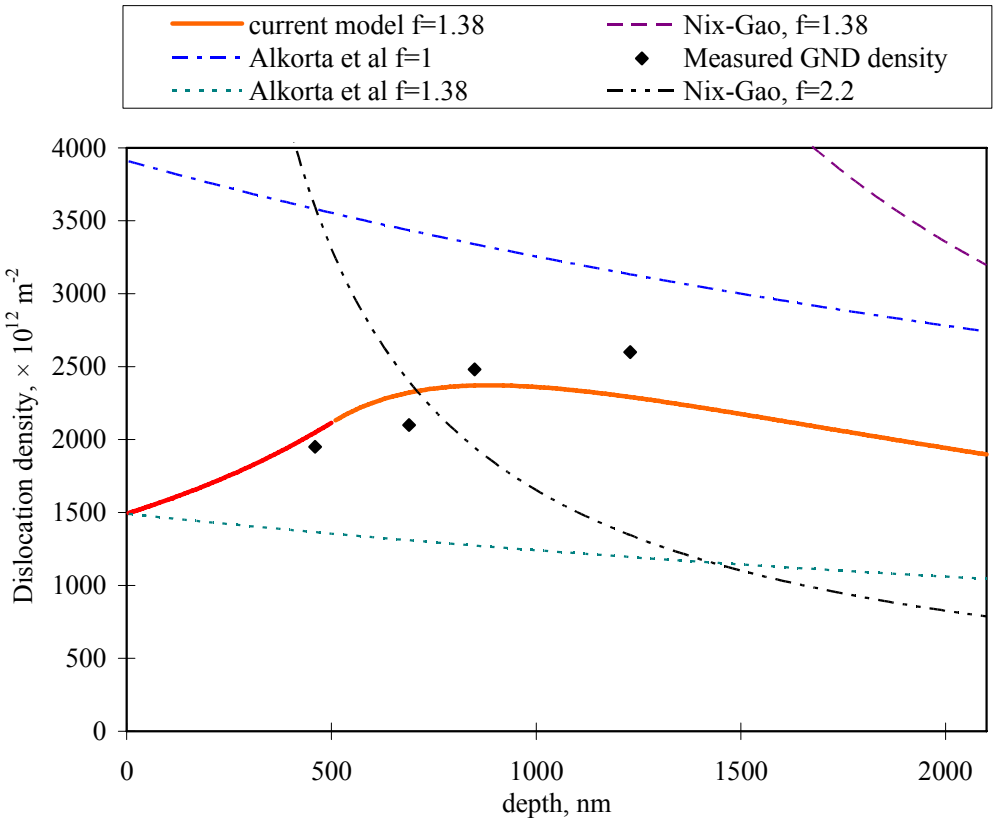

Fig. 7.9 Evolution of measured and predicted GND density of (111) copper single crystal with the indentation depth. The measured data are taken from [225]. A 60° conical tip with a rounded tip in diameter of 1 μm was used.

Fig. 7.9 shows that the models for a sharp indenter (the Nix-Gao model [78], the Abu Al-Rub model [84] and the Durst et al model (the Nix-Gao model with an adjustable f [207,208])), predict dislocation densities that are very different from the ones measured underneath the spherical indenter. The Huang et al model [206] assumes the GND density is constant when the indentation depth is less than a specific value h^*_{nano}. If taking the height of the tip in spherical cap part (500 nm) as the h^*_{nano} value, the GND densities predicted by Huang et al model [206] are 5-12 times larger than experimental results (not shown in Fig. 7.9 because they are out of range). The GND density predicted by the original Alkorta et al model [203], i.e. with f=1, is much larger than the experimental results. Adjusting f will bring values broadly within range but this model will fail to predict that the GND density increases with the indentation depth at lower depth. The reason for this is two fold. Firstly, the Alkorta et al model assume the contact area and indentation depth follows Eq. 7.19, which causes the GND density predicted to be much lower than that predicted by current model (except for h approaching 0 where the two models converge, but that is not a realistic indentation). Secondly, Alkorta et al [203] calculate the total length of the GNDs based on the approximation:

$$\lambda = \int_0^{h_f} \frac{2\pi}{b} r(h)\mathrm{d}h = \frac{2\pi \tan\phi}{b} \int_0^{h_f} \sqrt{h^2 + \delta h}\mathrm{d}h\,, \quad \delta = \frac{2R}{(\tan\phi)^2} \qquad \text{Eq. 7.25}$$

i.e.,

$$r(h) = \tan\phi \sqrt{h^2 + \frac{2R}{\tan^2\phi} h} \qquad \text{Eq. 7.26}$$

Eq. 7.25 is correct only when the depth is large, i.e., $r(h) > r_0$ (see Fig. 7.2). However, without justification Alkorta et al extend Eq. 7.25 to apply at lower indentation depth, i.e. $r(h) < r_0$. The second assumption leads to the Alkorta et al model predicting an incorrect trend at lower indentation depth. As a result of these inaccurate approximations the Alkorta et al model is only accurate for h=0 and for the limit for high h, typically h>>500 μm, leaving the model to be inaccurate in the range that is relevant.

From this section we conclude that where other models fail, our model predicts the correct magnitude and trend in dislocation densities under a spherical indenter.

7.2.5.4 ISE of several FCC metals

As a final test for our model we will compare its predictions against published nanoindentation ISE data for a range of materials.

ISE in Ir-0.3wt%W

Swadener et al. [79] measured nanoindentation hardness and microhardness of annealed Ir-0.3wt%W (with 60 ppm Th by weight) at the indentation depth from 150 nm to 50000 nm. The nanoindentation hardness was measured using the Oliver-Pharr method [220], i.e. through determining the contact depth (h_c) by Hertz elastic equations during loading and unloading, then converting h_c to projected contact area using an area function. In Fig. 7.10 the measured data [79] are compared with model predictions. In the current model, G and b were taken as 217 GPa [79,206] and 0.271 nm [79, 206]. The yield strength of the Ir-0.3wt%W is 338 MPa (determined from data in [79,206]) and the value of $\sigma_0 + \sigma_{GB}$ is estimated as $0.8\sigma_y$, which is reasonable for an annealed alloy. The other parameters, including C_1, C_2 and M, were taken as the same values with Al-1050. The radius of rounded tip, R, plastic zone factor, f, and Vickers hardness Hv were determined as 288 nm, 1.94 and 3.0 GPa by fitting to the experimental nanoindentation data.

As shown in Fig. 7.10 and Fig. 7.11, the predicted nanoindentation hardness by the current model fits the experimental results to a very high accuracy and within the standard deviation of the experimental data. Furthermore, the values for the 3 parameters as determined by fitting are reasonable. Firstly, the value of R (determined to be 288 nm, which corresponds to a blunting distance of 18 nm) is between the radius of a new Berkovich tip (about 50 nm) and the value at which a worn tip will generally be reported as a defective tip (~500 nm) [83]. Secondly, the f value of Ir-0.3wt%W determined by the present model (1.94) is closed to the f value of Al-1050 (1.76). Furthermore, Durst et al [208] determined f for coarse-grained copper, UFG copper, coarse-grained aluminium and UFG aluminium as 1.9, which is also close to current determination. Finally, the Hv value determined by the present model (3.0 GPa) is close to the measured microhardness (2.6GPa) determined at large depth by Swaderner et al [79].

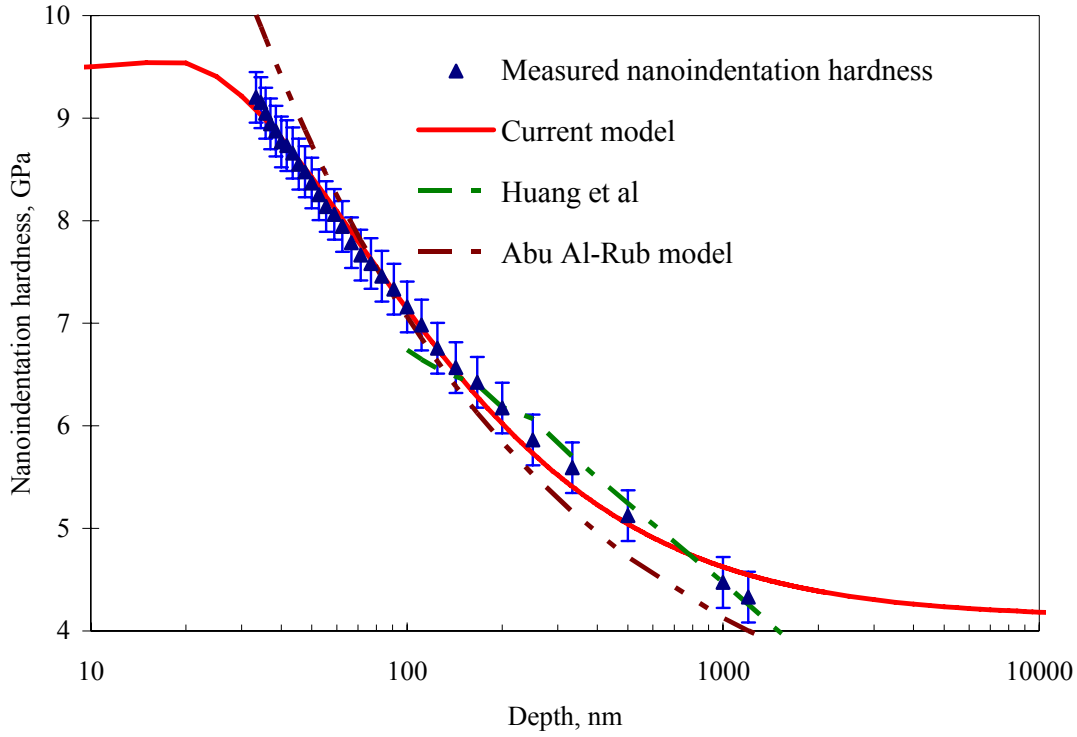

Fig. 7.10 Comparison of the prediction of the nanoindentation hardness of annealed Ir-0.3wt%W by Huang et al model [206], Abu Al-Rub model [84] and current model. The nanoindentation hardness data are taken from [79].

Fig. 7.10 also shows nanoindentation hardness of Ir-0.3wt%W predicted by the Huang et al [206] model and the Abu Al-Rub model [84]. In their model, Huang et al [206] assume the GND density reaches a maximum value, which is called maximum allowable GND density when the indentation depth h is less than a specific value h^*_{nano}. The value of GND density is related to h^*_{nano}, the value of which is determined by fitting. As seen in Fig. 7.10, predictions using the Huang et al [206] model broadly capture the trend, but the increasing deviation between prediction and measured values for decreasing depth suggests that this model will fail for depths less than 100 nm. Huang et al [206] did not provide predictions for the nanoindentation with depths less than 100 nm. The Abu Al-Rub model [84] also fails to accurately capture the trend producing an overestimate at indentation depths under 100 nm but an underestimate at the indentation depths larger than 100 nm. A summary of the accuracies achieved by the various models is presented in Table 7.1.

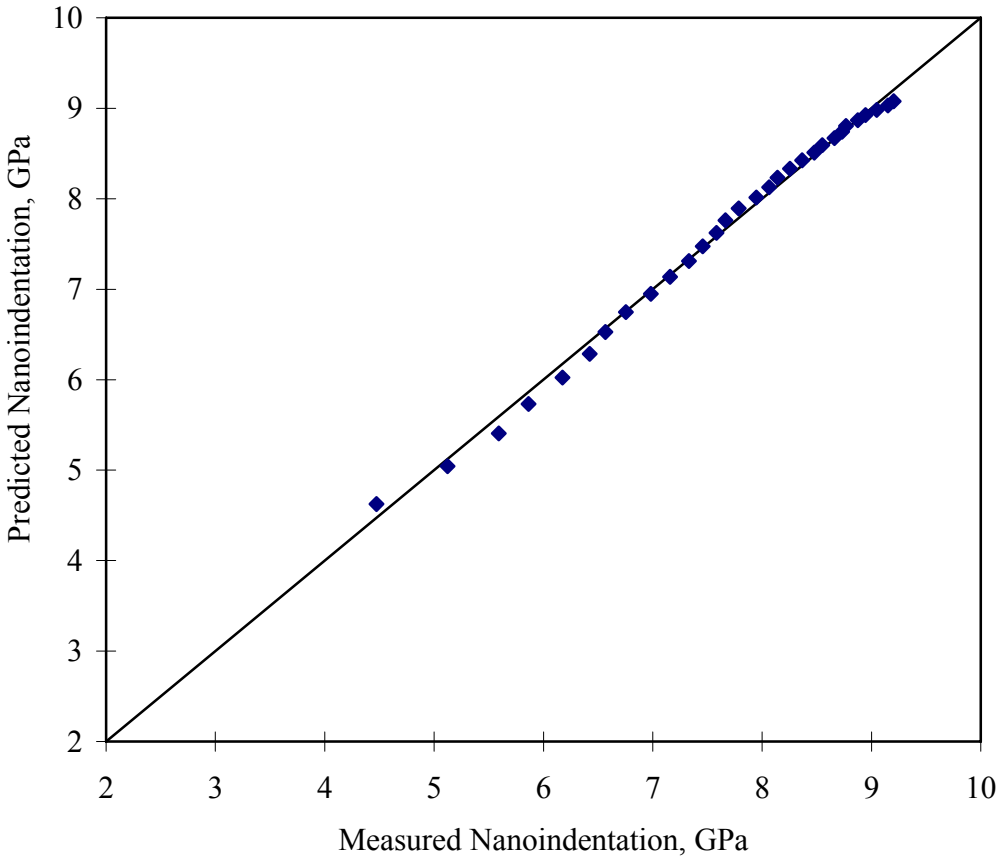

Fig. 7.11 The measured nanoindentation hardness of annealed Ir-0.3wt%W and predicted nanoindentation by the current model. The experimental data were taken from [79].

It is worth noting that in Ref [79] microhardness was measured using a microhardness tester equipped with a Berkovich tip for lower depths and a Rockwell hardness tester for larger depths. The indent area was measured by a video microscope system, i.e. the measured area is residual area, which is different with the projected contact area determined in nanoindentation hardness. As a result, the microhardness measured in Ref [79] can not be simply considered as the nanoindentation hardness with a higher indentation depth because the ratio of hardness to yield strength (C) is different in nanoindentation hardness and microhardness.

ISE in single crystal MgO

Feng and Nix [81] measured nanoindentation hardness of single crystal MgO. The experimental data are replotted in Fig. 7.12. In the current model, a fixed f value was

used. The value of b, G and intrinsic stress of MgO were taken from [81, 206] as 0.298 nm, 126 GPa and 0.18 GPa The remaining parameters were taken as the same values used for Al-1050. The prediction curve is shown in Fig. 7.12. The values of f, Hv and R were determined as 1.13, 6.9 GPa and 764 nm by fitting. The exponential relationship between f and h determined by Feng and Nix [81] provides an average f value for $0<h<500$ nm of 1.11, which is close to current f value. The current Hv value (6.9 GPa) is 25% lower than the nanoindentation hardness with large indentation depth (9.19 GPa, see Fig. 7.12), which is reasonable because the nanoindentation hardness is 10-30% higher than Vickers hardness using the same load [215]. The radius of the blunting tip was determined as 764 nm in current model, i.e. the blunting distance h_b is 47 nm (see Eq. 7.9 and Eq. 7.10), which has been proved by the experimental data in Fig. 7.12 where the nanoindentation hardness starts to decrease when the indentation depth is lower than 50 nm. Thus the values of all three fitted parameters, f, Hv and R, are very close to values that can be experimentally determined through direct experiments.

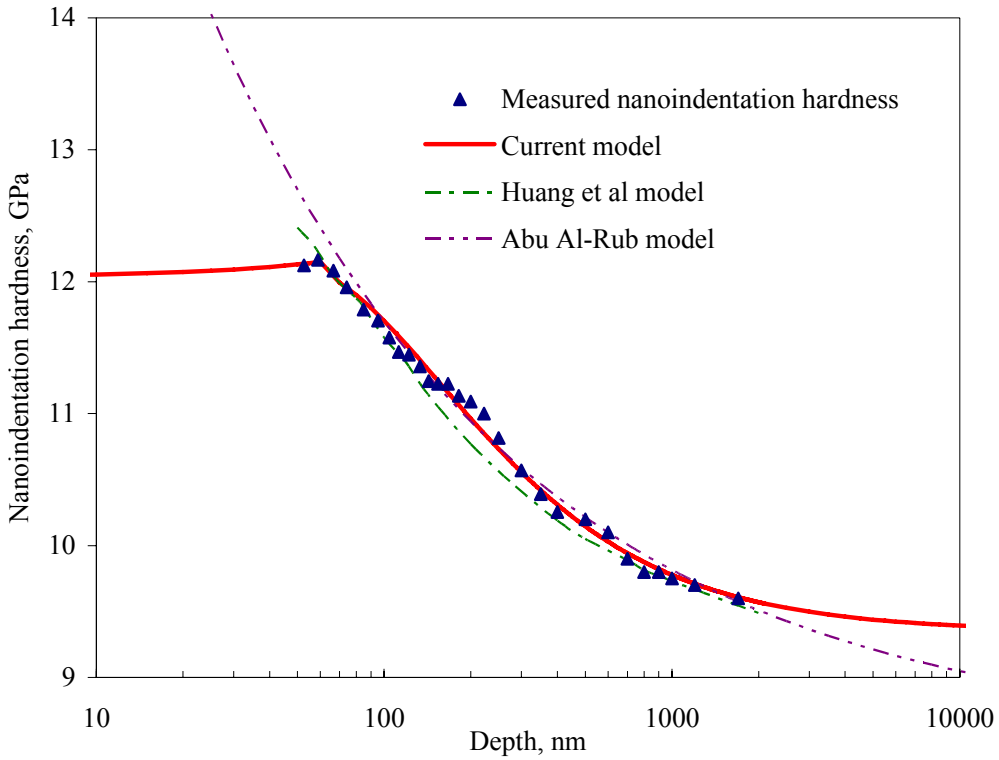

Fig. 7.12 Comparison of the prediction of the nanoindentation hardness of single crystal MgO by Huang et al model [206], Abu Al-Rub model [84] and the current model. The nanoindentation hardness data are taken from [81].

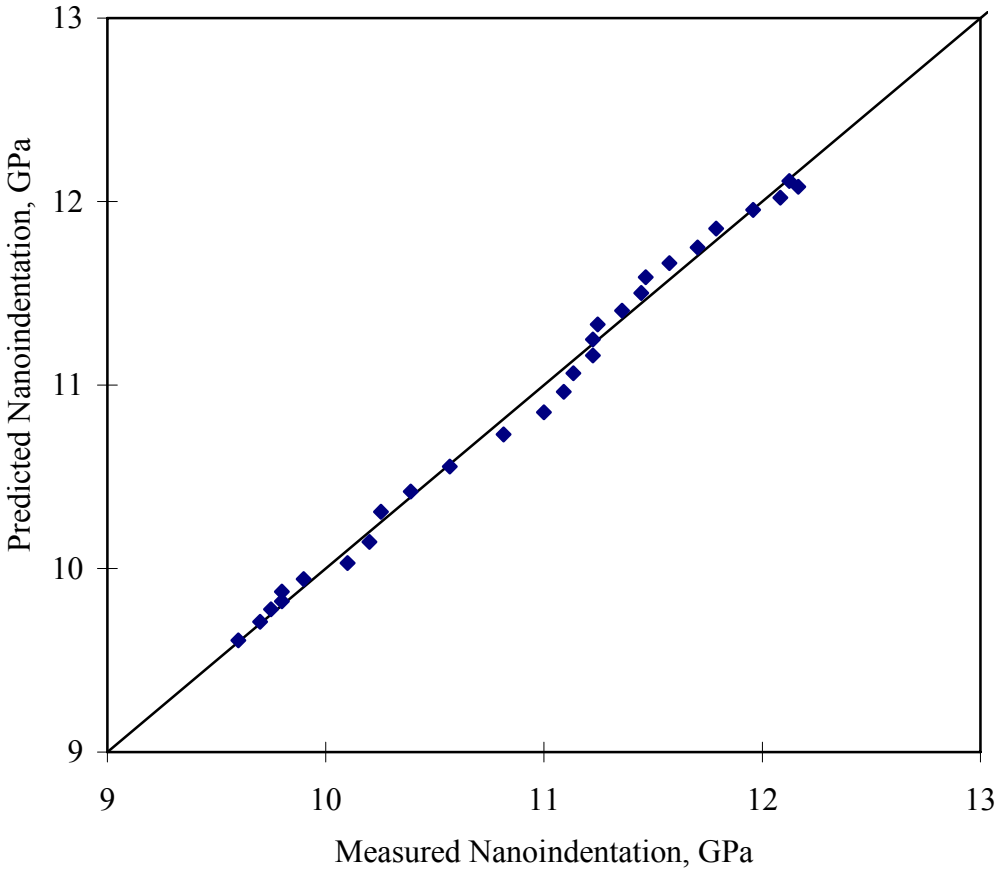

Fig. 7.13 The measured nanoindentation hardness of single crystal MgO and predicted nanoindentation by the current model. The experimental data were taken from [81].

Predictions by Huang et al model [206] and Abu Al-Rub model [84] are also shown in Fig. 7.12. For both models, predictions are close to the experimental data, but the fit is not perfect, especially when it is considered that 3 or 4 parameters are fitted, in many cases with little justification provided for the values obtained. In contrast, the current model fits the experimental data near perfectly, whilst, as shown above, the values of the 3 fitted parameters can be justified to within a few percent. RMSE of the fits are presented in Table 7.1. At low indentation depth, the current model predicts the indentation hardness decreases with decreasing depth because of the tip radius effect. The tip radius will not have a considerable effect on the ISE when the radius is less than 300 nm (h_2 <20 nm, see Fig. 7.5). The Huang et al model [206] contains a maximum allowable GND density when the indentation depth is less than a specific value, i.e. the GND density is constant at small indentation depth. The Abu Al-Rub model [84] even omits the tip radius effect, and both models have a relative

good fitting for a relative sharp Berkovich tip. However, when the tip radius is large, particularly for a conical tip with a small cone angle (see section 7.2.5.3), the tip radius will significantly influence the GND densities at small indentation depth and the Huang et al model [206] and the Abu Al-Rub model [84] will not provide valid predictions. At large indentation depth, the current model predicts the nanoindentation hardness decreases with the depth at a low rate, which coincides with the experimental data. For the whole range of the experimental indentation depth, the hardness predicted by the current model fits the measured hardness to a very high accuracy (see Fig. 7.13), with root mean square error of 0.068 GPa (2.5% of the range of values).

Summary of ISE data

We further made model predictions for single crystal Cu and work hardened Cu (experimental data are from ref [226]), and the RMSE values are reported in Table 7.1. The predictions are good over the entire range (80 nm to 2000 nm). Nix and Gao [78] excluded the nanoindentation hardness with indentation depth less than 150 nm because their model substantially deviates from the experimental data at lower depth. (Fitting the experimental data of single crystal Ag in Ref [74], replotted by Nix and Gao [78], was not attempted. This is because in that data set the residual projected area was used to calculate the nanoindentation hardness, and this unusual measured quantity can not be directly compared with the present model.)

7.2.6 Discussion of the model

In the above we have shown that a computationally friendly analytical model for the ISE can be derived which incorporates a blunted nanoindenter tip and an effective plastic zone size that scales with the indent size. It is shown that the indenter size can be determined through calibration experiments. The model is tested against nanoindentation data and dislocation density data, and is shown to be substantially more accurate than existing models. Model parameters can in many cases be determined from independent experiments, and where fitting is necessary they are within ranges that can be justified. We thus conclude that the present model is very useful in analysis nanoindentation ISE data, and can solve some of the issues regarding the ISE that have hitherto remained unexplained. Specifically, the model

shows that where several existing models showed (largely unexplained) deviations with measured data at small indentation depths (typically 30 – 150 nm), the present model does provide good fits in that range. This shows quantitatively that deviations from earlier models can be (largely) due to the tip rounding artefact. This improved understanding will be further exploited in the next chapter, where nanoindentation is used to study embossed UFG Al alloys.

It is further noted that if we consider that the effects for even smaller indentations, which involve a pop-in event occurring during the transition from elastic to plastic loading, are reasonably well understood (see Durst et al [208]), it thus appears that the entire ISE over all indentation sizes can be fully explained on the basis of the strain gradient plasticity and GNDs.

Table 7.1 RMSE of nanoindentation hardness predictions by there models for two Alloys.

	RMSE of prediction			Source of exp data
	Huang et al model [206]	Abu Al-Rub model [84]	Present model	
Ir-0.3wt%W	201 MPa [a)]	412 MPa	92 MPa	[79]
MgO	141 MPa	137 MPa	68 MPa	[81]
Single crystal Cu	-	-	45 MPa	[226]
Work-hardened Cu	-	-	22 MPa	[226]
Al1050	-	-	106 MPa	Present work
Fitted parameters	3	4	1 [b)], 2 [c)],3 [d)]	

a) Model only predicts 100-1000 nm range. RMSE error is for that limited range.
b) Only the value of f is fitted for Al-1050 and single crystal Cu.
c) f and R are fitted for work hardened Cu.
d) f, Hv and R are fitted for Ir-0.3wt%W and MgO.

7.3 Summary

The nanohardness of UFG Al-1050 measured by nanoindenter show an indentation size effect. A model employing the concept of geometrically necessary dislocations was established to interpret the indentation size effect for an indenter with a tip worn to a rounded shape. Conclusions are drawn as follows:

- The blunting distance h_b (and tip radius) can be determined by fitting the area function.

- The ratio of nanoindentation hardness to the yield strength (C_2) is larger than that of the Vickers (micro) hardness to the yield strength (typically, C_1=3.16).
- The current model successfully predicts the GND density increases with the increasing indentation depth at lower depth under the rounded conical tip.
- The current model for indenter with worn tip accurately fits the experimental ISE data of a range of materials where other models have proved to be inaccurate.

8 Embossing of UFG Aluminium

If metals with a fine pattern of channels, typically below 10μm, can be reliably produced, then they may find application in a range of new or improved microdevises. One relevant device is a micro heat exchanger, which is a crucial component of many microelectromechanical systems (MEMS). Their efficiency is determined predominantly by size and density of cooling channels and the heat conductivity of the material from which it is fabricated. Fine, high density channels in a metal with high conductivity can strongly improve efficiency as compared to incumbent heat exchanger technology.

In the previous section, the microstructure and properties of UFG aluminium alloys processed by ECAP have been analyzed. In this section, the UFG aluminium alloys were embossed to MEMS components with microchannels using the micro silicon die. Topography, microstructure and hardness of the embossed UFG foils at different temperatures and embossing forces were analysed with a view to understanding the mechanisms and to optimize the embossing process. The topography of micro silicon dies before and after embossing was observed by the confocal laser system, SEM and optical microscopy. The topography and microstructure of the embossed foil of UFG aluminium alloys were observed and analyzed by optical microscopy, SEM, FIB and EBSD. Hardness distribution on the cross section of embossed UFG Al was characterized by nanoindentation. Starting from the model outlined in the previous chapter, a model was developed to interpret the indentation size effect, hardness distribution on the cross section and embossing force. The model considered the tip rounding effect, plastic zone size, strengthening contribution by intrinsic stress, GNDs and grain boundaries.

8.1 Results

8.1.1 Micro silicon die

The SEM images of the micro silicon die are shown in Fig. 8.1. The SEM images show a clear pattern of channels etched on chips with sharp and straight sidewalls. A smooth bottom of the channel is observed for all sizes of channels. However, a scallop can be observed on the side wall of the channels. The scallop is due to the

cyclic alternation between etch and passivation steps (Section 3.3). The depth values measured from the SEM images are close to the designed value: the depth of the channel with width of 3 μm, 5 μm, 10 μm and 25 μm are measured as 9.48 μm, 9.86 μm, 10.03 μm and 9.96 μm, respectively. The accuracy is plus/minus 0.01μm.

(a)

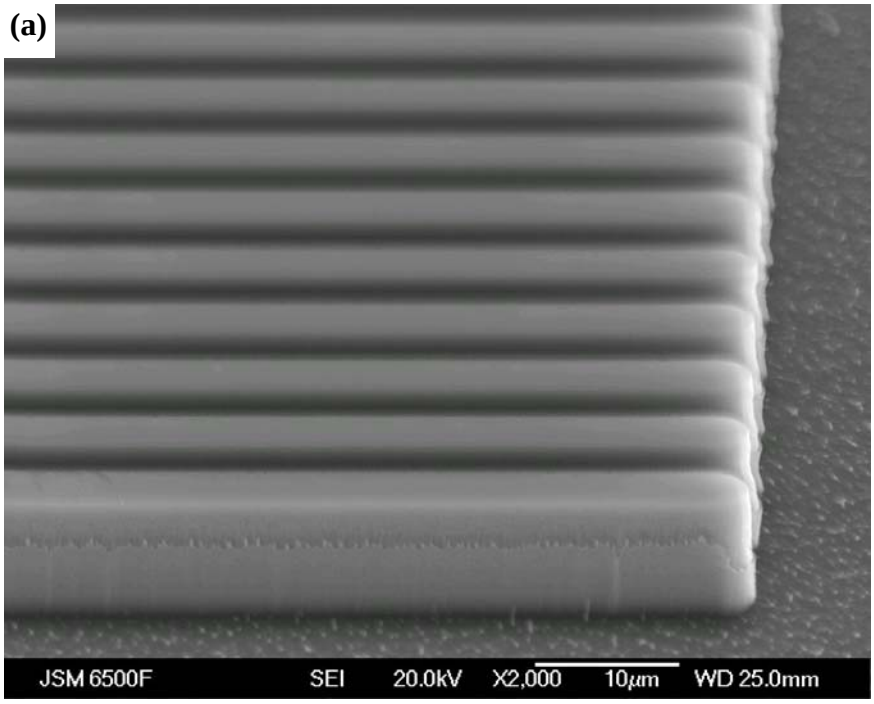

(b)

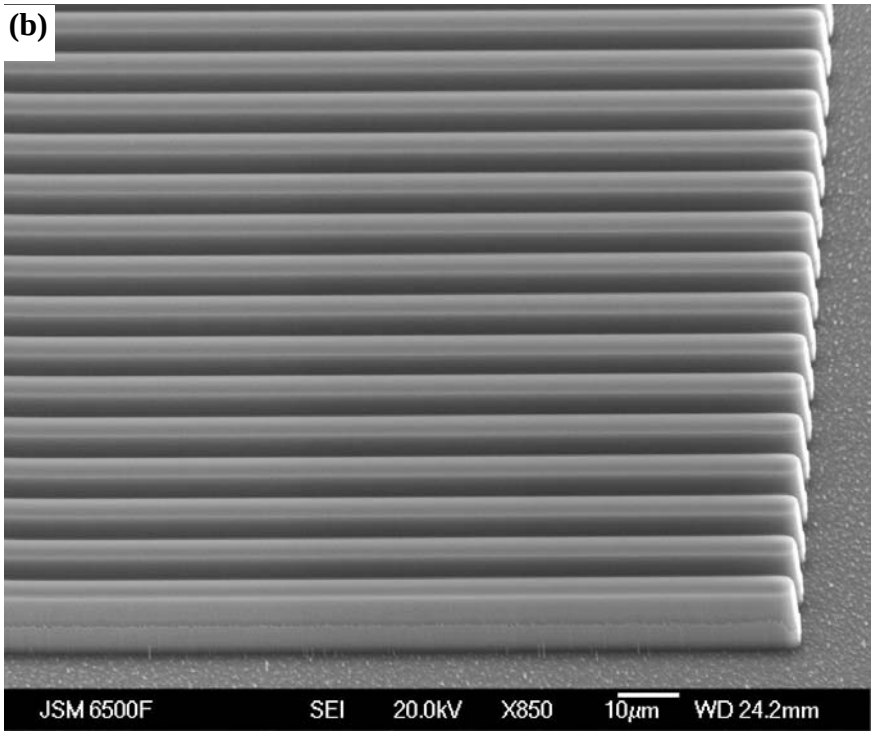

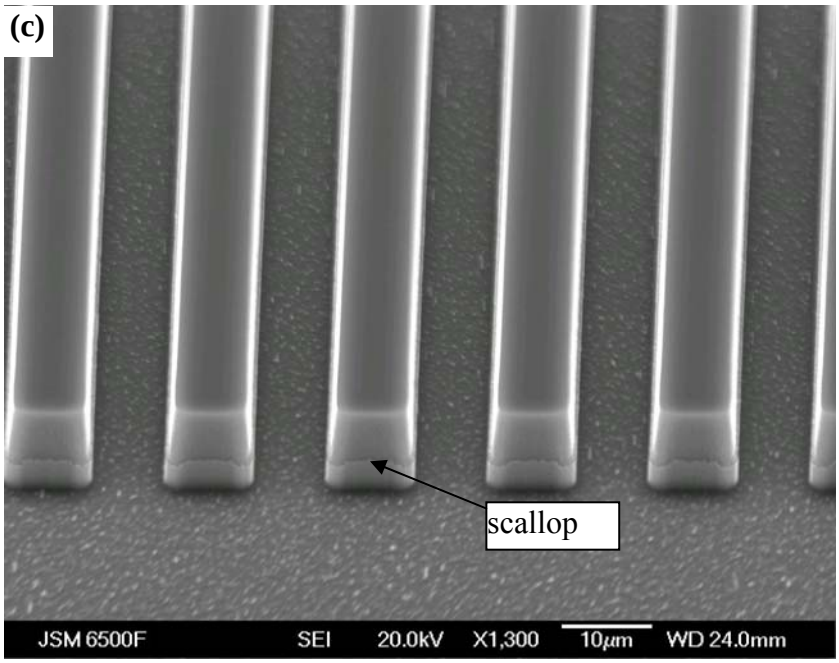

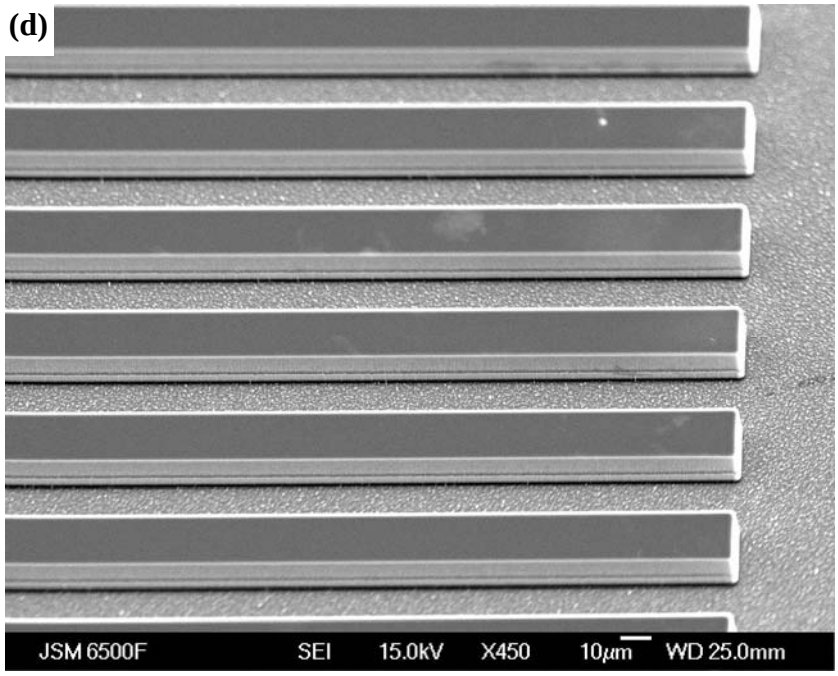

Fig. 8.1 SEM image of micro silicon die with the channel depth of 10 μm and width of (a) 3 μm, (b) 5 μm, (c) 10 μm and (d) 25 μm.

The channel depths measured by the confocal laser system are shown in Table 8.1. The measured depths of all channels in designed width of 3μm are inaccurate due to the bigger spot size and the step size settings. Ignoring these measurements we can note that the measured channel depth are close to the designed depth. The measured

depths of channels with designed depth of 3 μm are somewhat higher than the designed depths, while the measured depths of the channels with the designed depth of 5 μm are slightly lower than the designed value, but deviations are less than 0.5 μm; the measured depths of the channels with the designed depth of 10 μm are about 9.90 μm, which is very close to the designed value; the measured depths of the channels with the designed depth of 15 μm are 2 μm lower than the designed value. The topography of micro silicon dies are shown in Appendix B.

Table 8.1 Dimensions of channels measured by confocal laser system

Designed channel size, μm		Measured channel depth, μm					
Depth	Width	Value 1	Value 2	Value 3	Value 4	Value 5	Ave.
3	3	1.90	2.10	1.84	2.07	1.79	1.94
3	5	3.91	3.46	3.20	3.29	3.63	3.50
3	50	3.15	3.18	3.02	3.06	3.08	3.10
5	3	4.57	4.92	4.15	4.89	4.87	4.68
5	5	4.68	4.58	4.45	4.77	4.31	4.56
5	10	4.58	4.55	4.45	4.62	4.37	4.51
5	25	4.58	4.52	4.37	4.39	4.64	4.50
5	50	4.55	4.74	4.64	4.53	4.62	4.62
10	3	7.75	8.24	7.36	7.60	7.85	7.76
10	5	10.18	9.89	9.80	10.05	9.90	9.96
10	10	9.95	10.05	9.70	10.02	9.96	9.94
10	25	9.87	9.71	9.61	9.94	10.18	9.86
10	50	9.65	9.88	10.07	10.02	9.90	9.90
15	3	5.51	8.52	8.70	9.51	7.80	8.04
15	5	13.12	12.69	12.47	12.86	13.95	13.02
15	10	13.03	13.31	12.71	13.32	13.22	13.12
15	25	13.22	13.12	13.47	12.63	13.08	13.10
15	50	13.30	12.80	13.02	12.75	13.86	13.15

8.1.2 Cold embossing

8.1.2.1 Embossing force

The Al-1050 sample after two passes of ECAP was cut into foils perpendicular to the longitudinal direction yielding thin disks. The 0.5 mm thick foils were ground, polished and subsequently embossed by the micro silicon die with the 10 μm deep and 10 μm wide channels at room temperature. If the embossing process is considered as similar to a hardness test, the embossing force required can be

estimated as the Vickers hardness of the embossed materials multiplied by the embossed area, i.e.:

$$F = H_V S \qquad \text{Eq. 8.1)}$$

where F is the embossing force, H_V is the Vickers hardness (in GPa), S is embossed area. For Al-1050 after two passes of ECAP H_V is 0.44 GPa. For the present samples the pressed surface is half times sample area and thus the embossing force for Al-1050 after two passes of ECAP is estimated as 16 kN at room temperature.

The above embossing force is calculated on the assumption that the micro silicon die is absolutely parallel to the aluminum foil surface and fully touches the aluminium foil during the embossing process. In practice, this ideal situation is difficult to realize because of the roughness of the foil and the inaccurate alignment of platens, the micro silicon die and the foil. So 5 kN, 8kN and 9kN embossing forces (the maximum load of the press is 10kN) are chosen in order to avoid that the stress concentration damages the micro silicon die.

8.1.2.2 Microscale topography of cold embossed foils

When the embossing force was set at 5 kN, only one third of the foil surface was embossed. Fig. 8.2 (a) shows the optical microscopy (OM) image of the embossed area of the foil. In this figure, the pattern on the micro silicon die was fully transferred to the foil surface. Fig. 8.2 (b) shows a high magnification SEM image of the embossed area of the foil. Some micro cracks along the longitudinal direction of the channel can be observed on the top of the grating. Some micro defects are also observed on the edge of the grating top. The defects arose because the edge of that part was broken when the micro silicon die was pressed into the foil or taken out from the foil.

Fig. 8.3 (a) and (b) show the cross section of the foil mounted in resin, ground and subsequently electropolished. The electropolishing caused preferential removal of Al material near the edge of the sample, and thus this sample preparation method is imperfect and the sample was not suited for detailed microscopy or EBSD. This experiment does confirm however that the channel depth is close to 10 μm, which is the designed embossing depth.

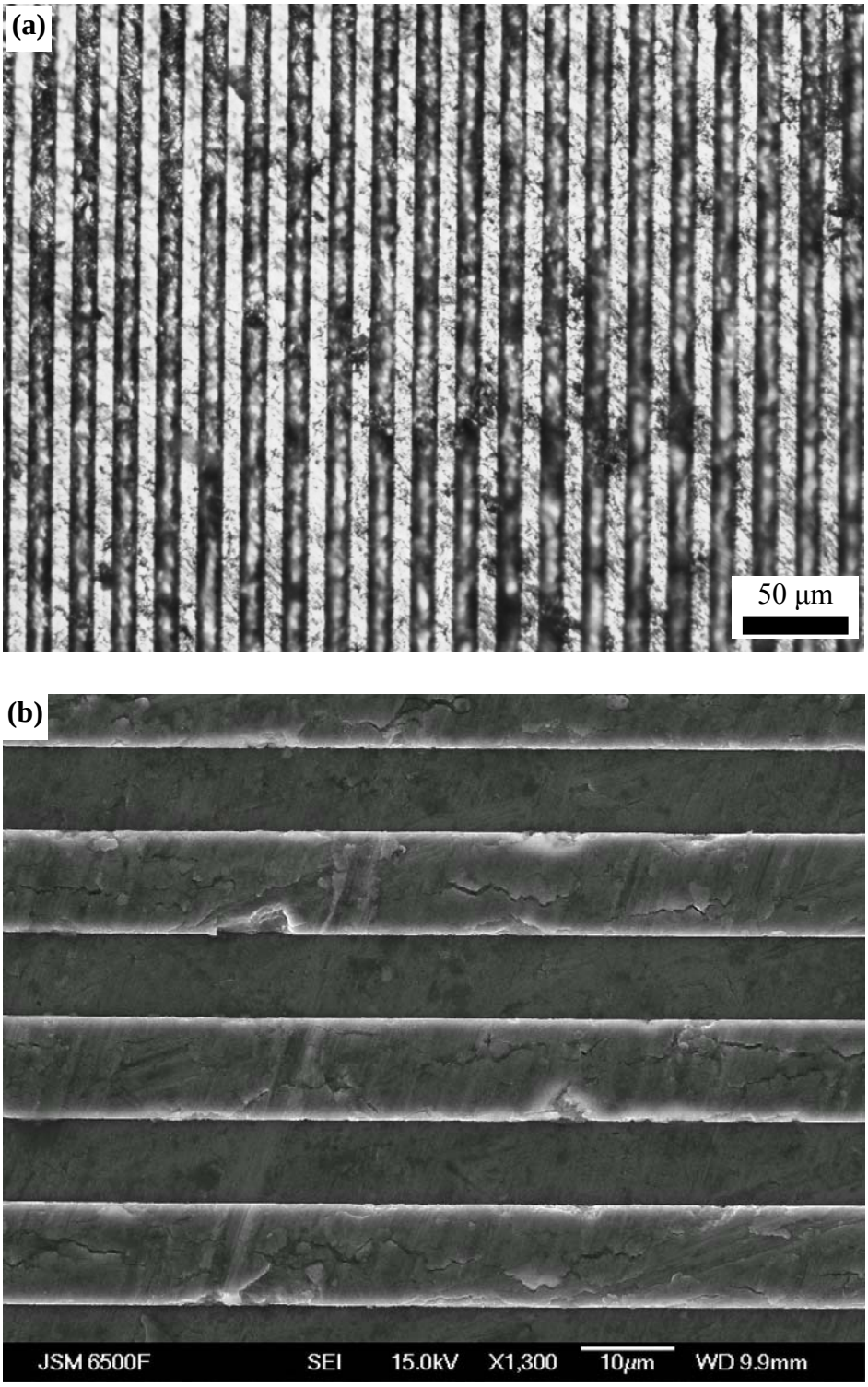

Fig. 8.2 Embossed topography of the UFG Al-1050 foil after two passes of ECAP, embossing force: 5 kN. (a) optical micrograph; (b) SEM image.

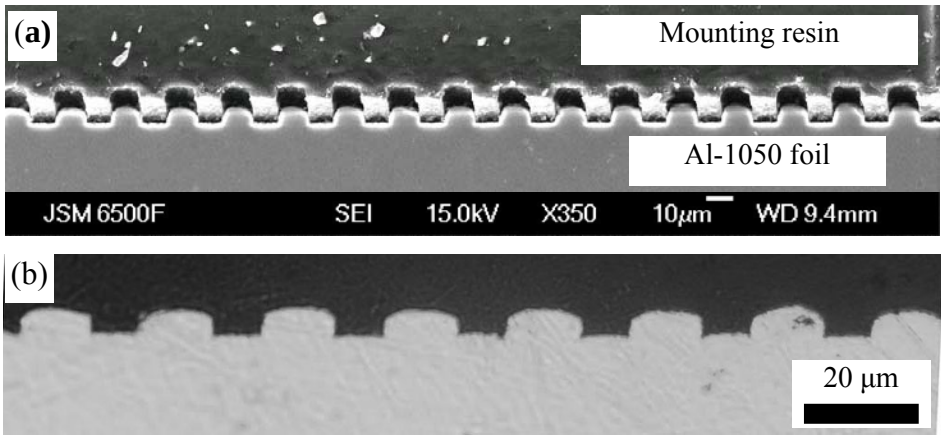

Fig. 8.3 The cross section of the embossed UFG Al-1050 foil, (a) two passes of ECAP, SEM image; (b) eight passes of ECAP, OM image.

Fig. 8.4 shows a SEM image for a transition zone from the embossed area to the unembossed area on the surface of Al-1050 foil embossed by 5kN force. The pattern on the micro silicon die was not fully transferred to the surface of the foil. The scratches on the original surface of the foil can still be observed. The channel depth gradually changed from shallow in the embossed area to zero in the unembossed area.

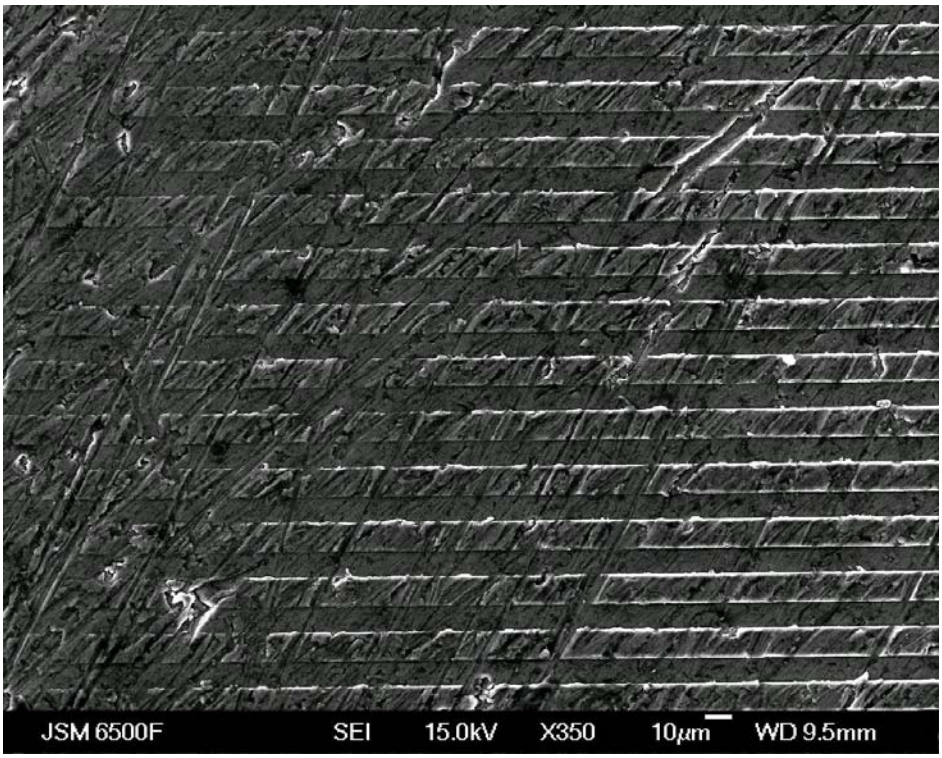

Fig. 8.4 SEM SEI image showing the topography of a transition zone from the embossed area to unembossed area on the surface of the Al-1050 foil embossed by 5kN force.

From the above experiments, it must be concluded that embossing set-up used does not allow full transfer of the patterns on the micro silicon die to the Al-1050 foil at room temperature. The embossing is not uniform due a combination of factors. One is the uneven thickness of the Al-1050 foil following cutting, grinding and hand polishing. Another factor is the inaccurate alignment. The micro silicon die and the foil were connected to platens, shafts, chambers and upper beam and bottom base, respectively, so that the tolerances between each part will superimpose to a certain amount of inaccurate alignment. The uneven thickness and inaccurate alignment causes the micro silicon die to not be perfectly parallel to the aluminum foil surface and thus it will not fully contact the aluminum foil during the embossing process. A further cause is the inappropriate embossing force.

An increase of the embossing force did not improve the uniformity of the pattern, with two thirds of the sample area unembossed even when the embossing force was increased to 8kN or 9kN. Only a small part of aluminium foil surface was embossed when the embossing force was set as 5 kN, while more areas were embossed when the embossing force increased from 5 kN to 9 kN. However, the failure rate of the silicon mould significantly went up because of the stress concentration. Fig. 8.5 shows the optical microscopy image of the well embossed area on the surface of Al-1050 foil embossed by 8kN force and 9kN force. The pattern was fully transferred to the foil surface, which is the same as the foil embossed by 5kN force (see Fig. 8.2(a)).

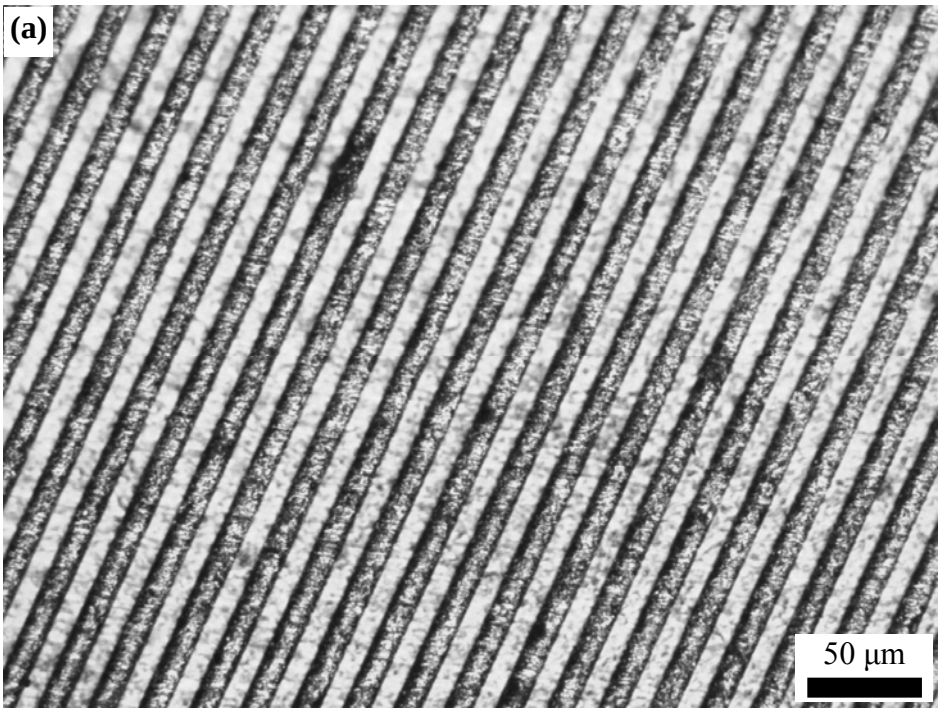

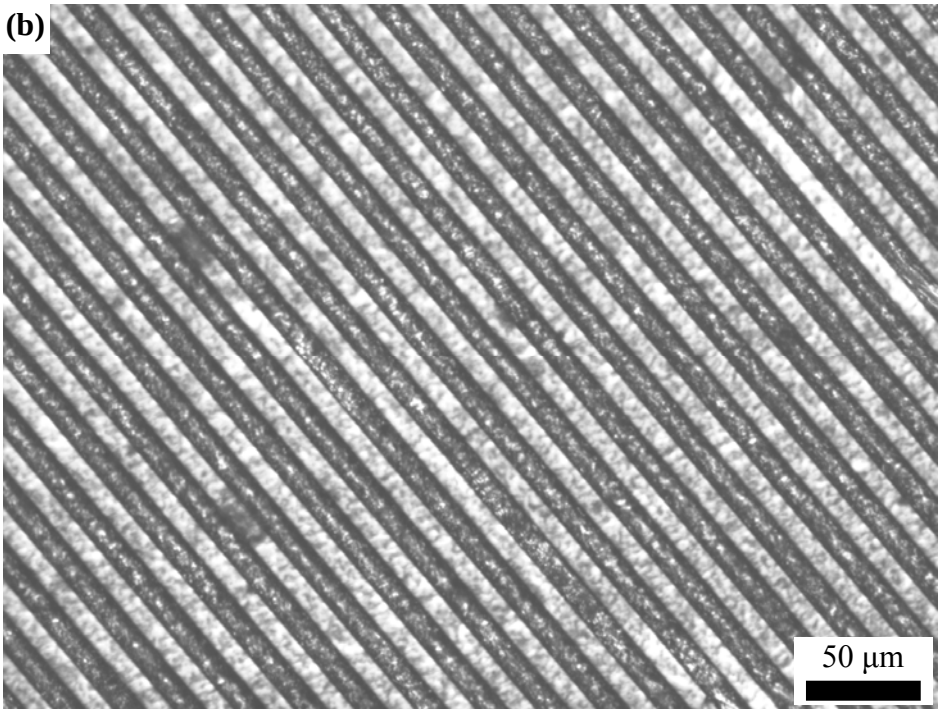

Fig. 8.5 The optical microscopy topography of the Al-1050 foil embossed by (a) 8kN force, (b) 9kN force.

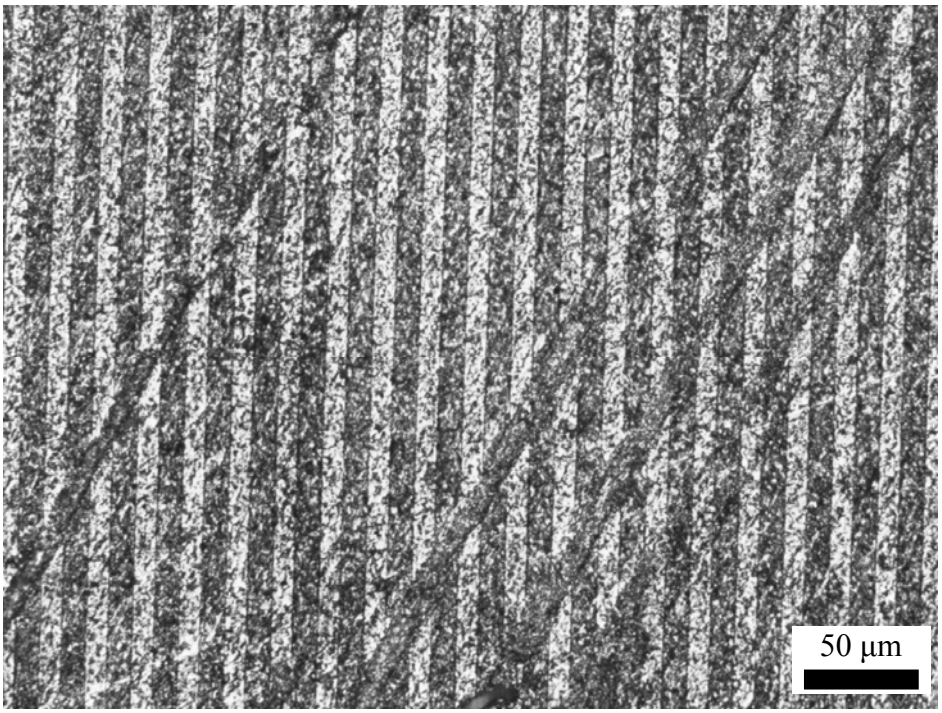

Fig. 8.6 The optical microscopy image for the uniform pattern on the surface of the Al-1050 foil embossed by 9kN force.

A uniform pattern on the surface of the Al-1050 foil was occasionally obtained by embossing at a 9 kN force. Fig. 8.6 shows the optical microscopy image of the uniform pattern on the surface of Al-1050 foil. The pattern covers the whole surface of the foil, however the channel is shallow and the scratches on the original surface of the foil can still be observed. This is because the embossing force (9kN) is insufficient. The largest embossing force used in current work is 9 kN because the maximum force of the machine is 10 kN. According to the analysis in Section 8.1.2.1, the theoretical embossing force for Al-1050 after two passes of ECAP should be 16 kN at room temperature.

Embossing at elevated temperature appeared a suitable way to resolve the problems encountered with the embossing because of the low yield strength of the aluminium at high temperature, whilst the uneven thickness of the foil can be evened out through creep when the embossing force is gradually applied at high temperature. That work is presented in Section 8.1.3.

8.1.2.3 Microstructure and nanoindentation hardness on cross section of the embossed UFG Al

The hardness distribution on the cross-section of embossed UFG Al-1050 foils was measured by nanoindentation. A map of 10×10 testing points was set up close to the edge of the cross-section (see Fig. 8.7). Distance between columns and rows was 30 μm. The maximum indentation depth was set as 800 μm with a loading and unloading rate of 3.0 mN/s and a 5 s dwell at maximum load. A plot of the indentation hardness against the distance to the edge of the cross-section is provided in Fig. 8.8. (The hardness value obtained from an indent on a scratch was removed.) The nano indentation hardness is 0.68 GPa near the centre of the cross-section and increases on approaching the edge. The average hardness value at 20μm from the edge is about 0.8 GPa.

Fig. 8.9 (a) is a FIB image taken on the cross-section of the UFG Al-1050 foil. The smooth part in the image centre had been milled by FIB and shows orientation contrast allowing grains to be identified. The subgrain size near the embossed channel is much smaller than that at the centre of the sample. The grain size and fraction of high angle grain boundaries (HAGB) were measured by EBSD at the milled position. The orientation mapping (OIM) image shown in Fig. 8.9 (b)

demonstrates that a large amount of subgrains arise close to the embossed surface while the band-like microstructure at the centre remains similar to that seen prior to embossing.

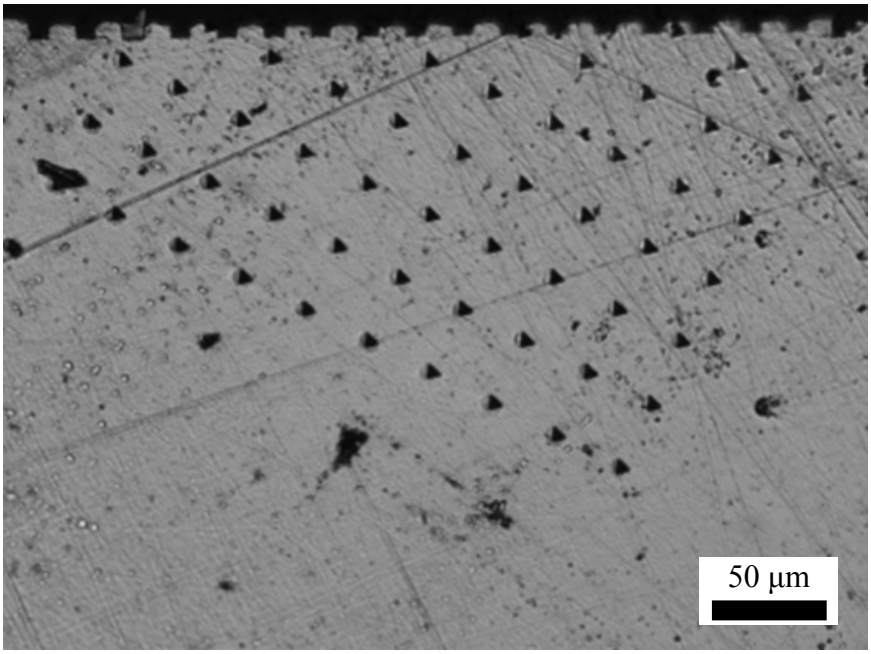

Fig. 8.7 Indentation mapping on the cross-section of embossed UFG Al-1050 foil

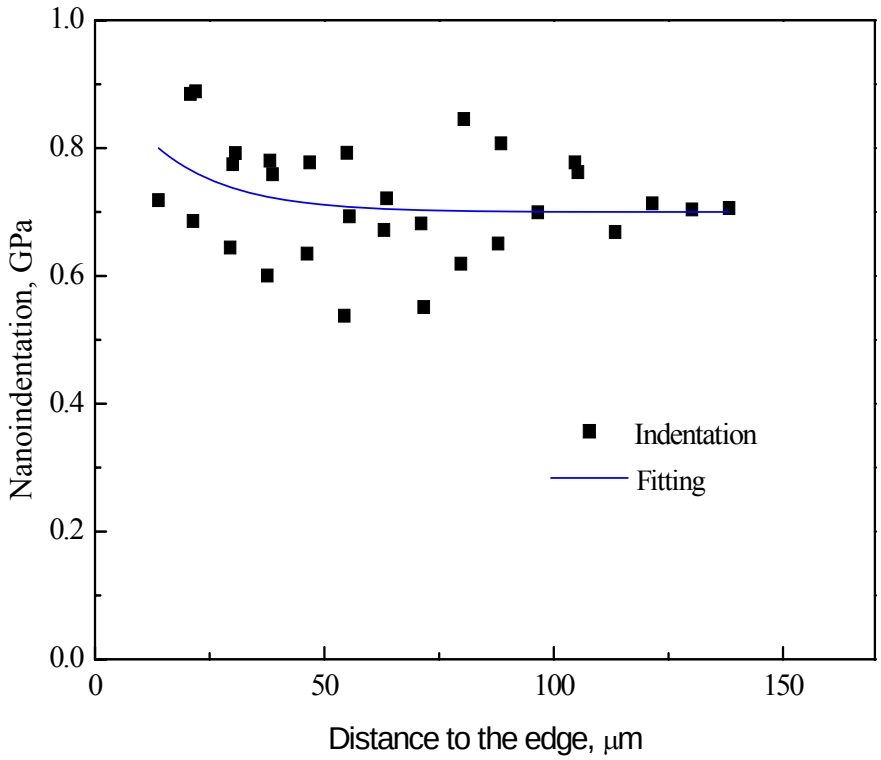

Fig. 8.8 Nanoindentation hardness distribution over the cross-section of the embossed UFG Al-1050 foil produced by two passes of ECAP.

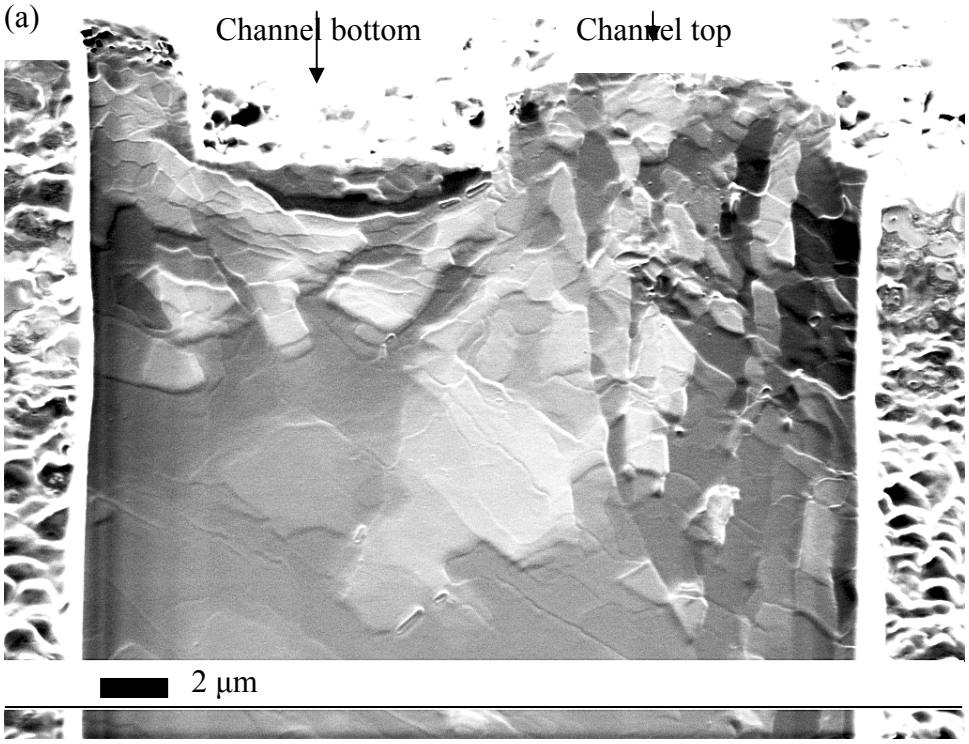

Fig. 8.9 Microstructure on the cross-section of cold embossed UFG Al-1050 produced by two passes of ECAP, (a) FIB image, (b) OIM image by EBSD , where dark lines are grain boundaries with misorientation angle larger than 15°, Grey lines are subgrain boundaries with misorientation angle less than 15° and larger than 3°.

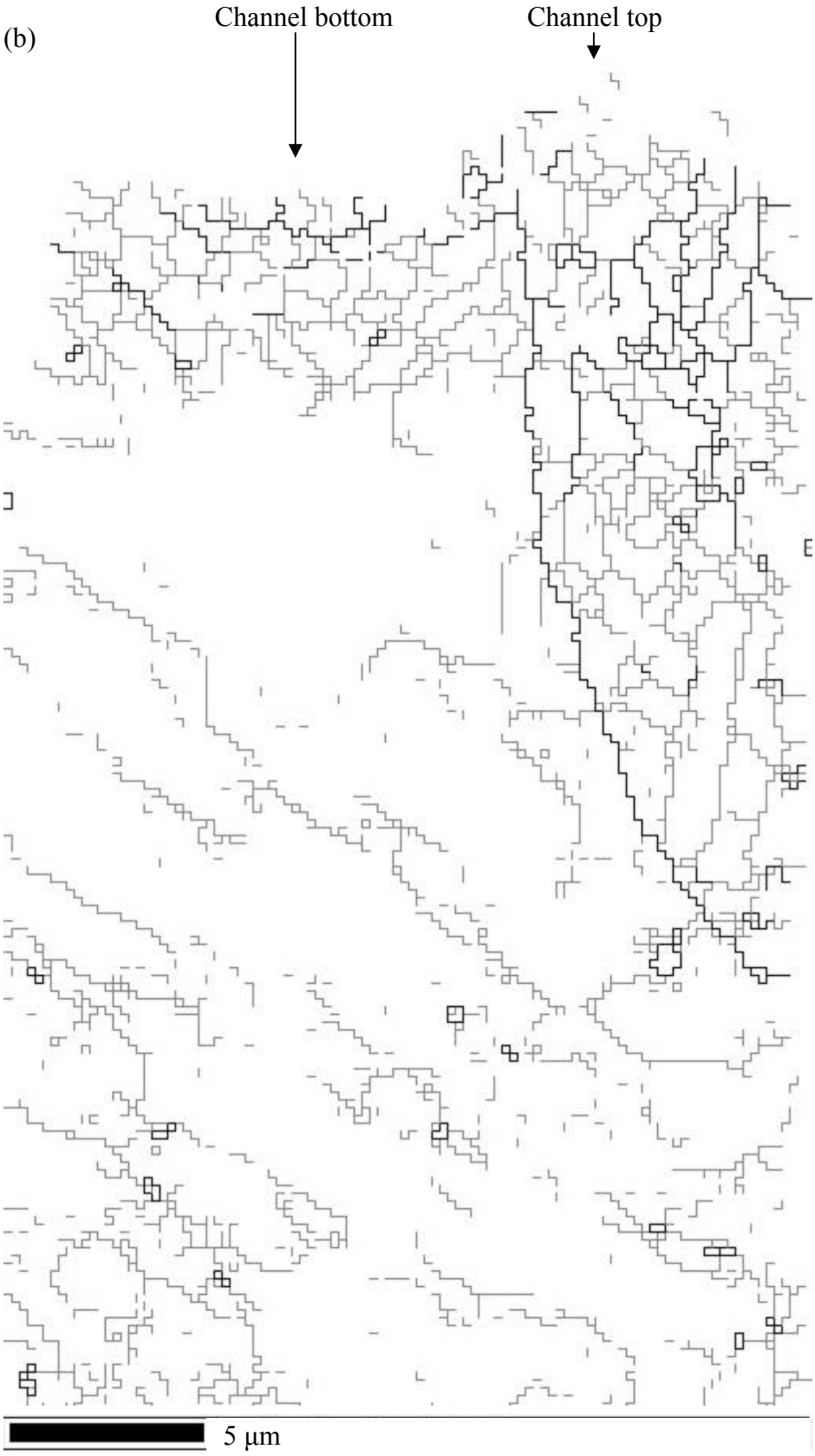

Fig. 8.9 continued

8.1.3 Hot embossing

Hot embossing was carried out on the same basic facility used for the cold embossing. A heating system and a cooling unit were specially designed to fit the machine. Based on hardness data in Fig. 6.1, 300 ˚C was selected as the embossing temperature. At this temperature the hardness of UFG Al-1050 dramatically decreased after annealing for half an hour but was still higher than that of fully annealed samples, which indicates the recrystallization has not completed and grains have not grown [227] (see Fig. 6.1). This is considered an optimum condition for embossing. A force of 3 KN was applied during embossing at 300 ˚C. The loading rate was 50 N per second. Holding time was 300 seconds.

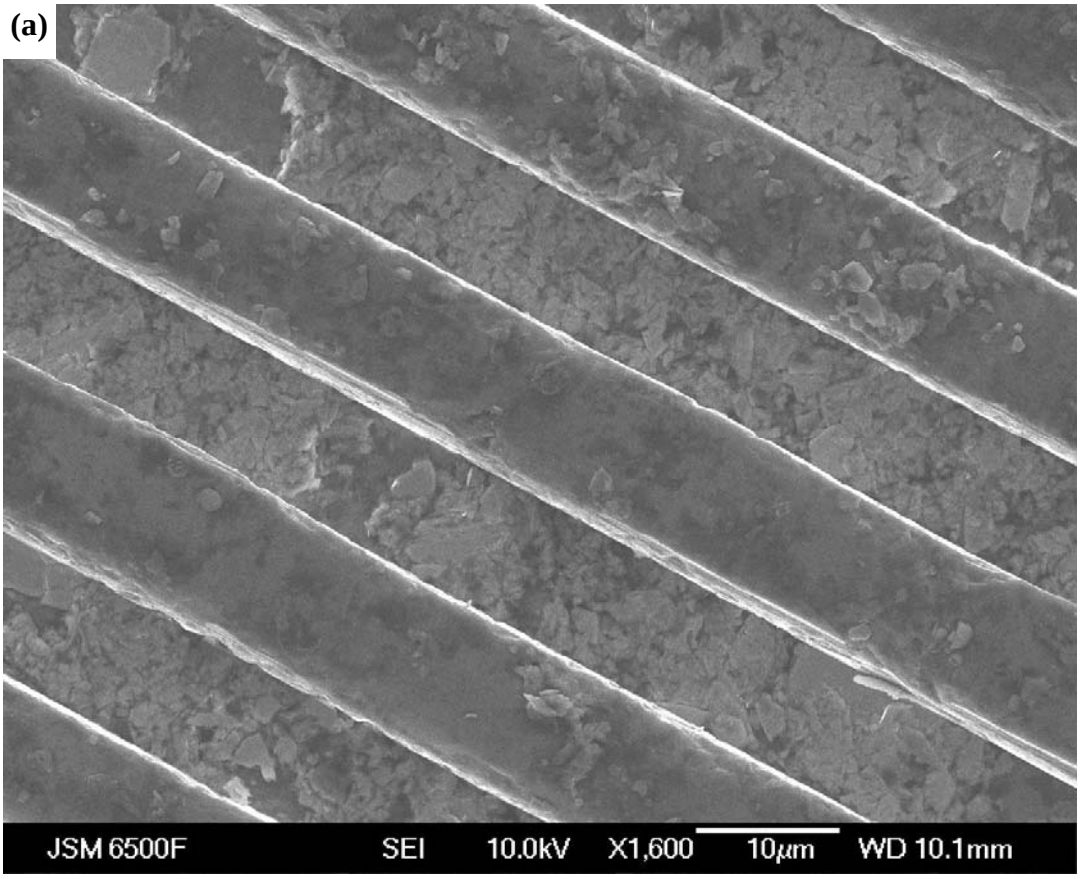

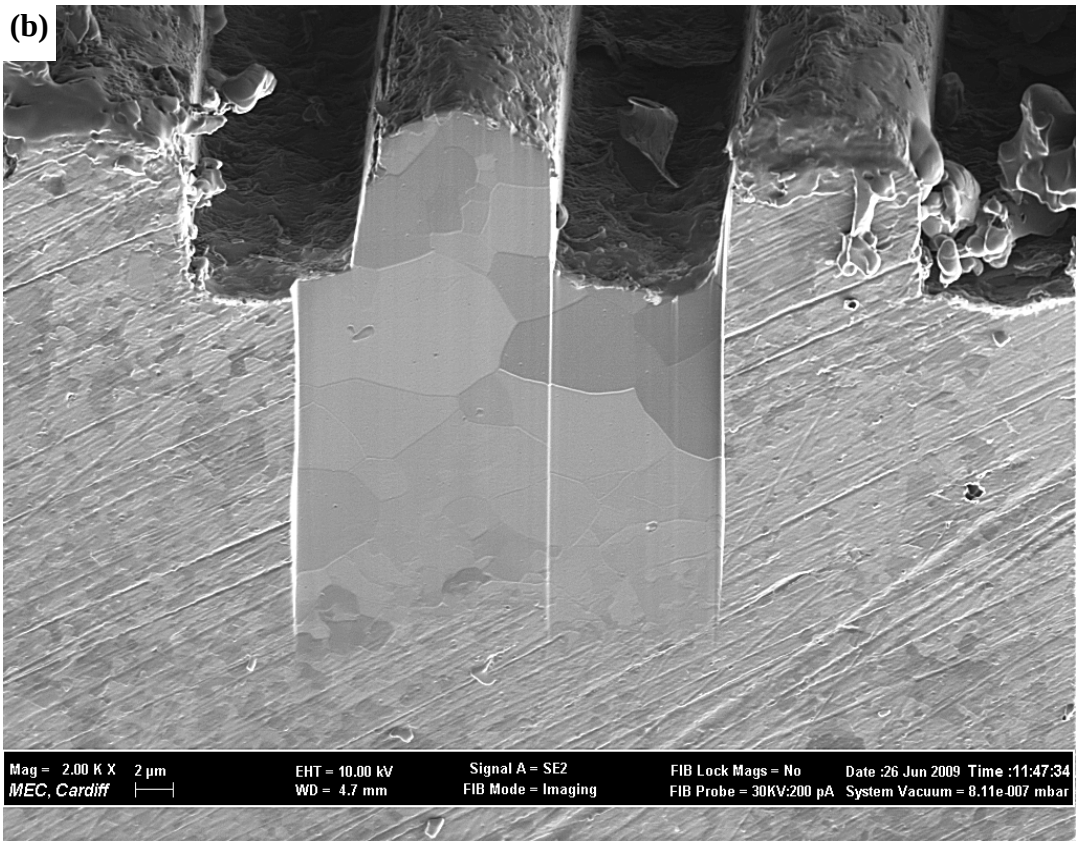

Fig. 8.10 300 ˚C embossed UFG Al-1050 produced by eight passes of ECAP, (a) Secondary electron SEM image of the top surface; (b) Secondary electron FIB image of the cross-section.

Since a lower embossing force was applied for embossing at 300 ˚C, the failure rate of silicon moulds significantly dropped, and no failures were observed in 20 pressings. Additionally, hot embossing led to a full pattern transfer from the silicon mould to the UFG aluminium foils. Fig. 8.10 (a) shows a typical SEM image of the surface of the UFG Al-1050 alloy foil embossed at 300 ˚C. The flake-like contaminants are MoS_2 used as solid lubricants. Cracks and defects, which were observed on cold embossed samples, were not observed after the hot embossing. Fig. 8.10 (b) is a FIB image of the cross-section of the UFG Al-1050 foil. The smooth part in the image centre had been milled by FIB and shows an orientation contrast. Fig. 8.10 (b) demonstrates that the depth of the channel reaches the designed value (10 µm). Moreover, the average grain size is still lower than 5 µm after hot embossing. The channel edges are not perfect sharp because the Al-1050 with growing grains fails to entirely fill the micro silicon die due to recrystallization.

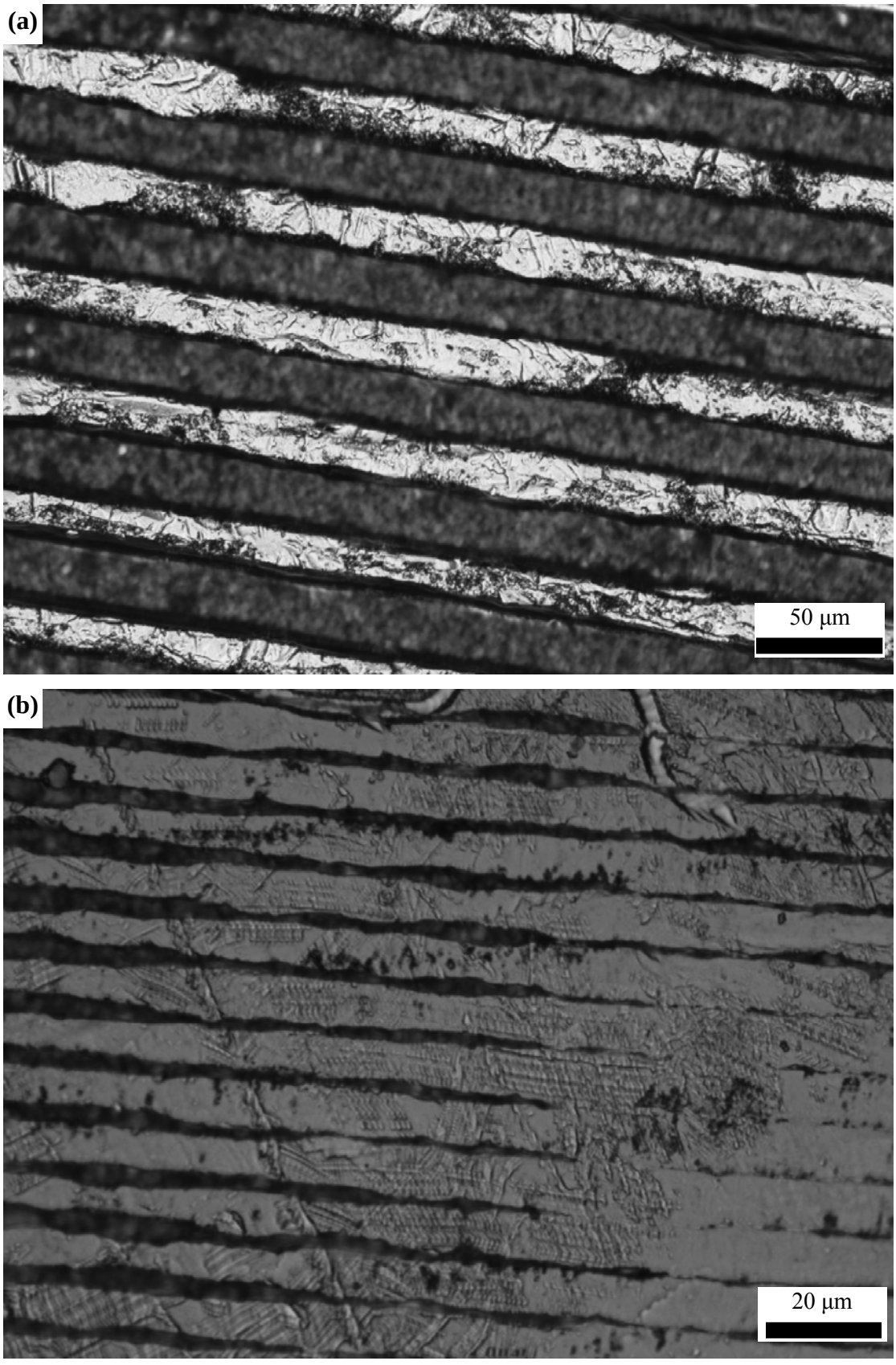

Fig. 8.11 Optical image of 300 ˚C embossed coarse-grained Al-1050 with the channel size of (a) 25 μm wide and (b) 5 μm wide.

Embossing of coarse-grained Al-1050 foils at 300 ˚C has also been attempted. Fig. 8.11 shows the topography of embossed surface of the coarse-grained Al-1050 taken by an optical microscope. The pattern on the surface was designed as parallel straight 10 μm deep channels with width of 25 μm and 5 μm. Compared to the embossed UFG foil, the channel top of the coarse-grained foil is rougher.

Unlike the UFG foil, the channel top of the coarse-grained foil shows many shear bands, which are thought to be caused by arrays of dislocations slipping in the same direction. The grain size of the Al-1050 in as-received condition is around 50 μm, which is two times bigger than the channel width. As a result, a channel on the silicon mould is likely to be filled by a single grain in the transverse direction, and in that case dislocation movement is restricted to slipping on a preffered plane and direction. This leads to shear bands when the dislocations move out to the material surface. The OM image of the coars-grained Al-1050 foil embossed by a silicon mould of 5 μm in channel width in Fig. 8.11 (b) shows a more clear shear band. The pattern on the silicon mould has not been fully transferred to the coarse-grained foil and clear parallel shear bands can be seen on the surface. The angle between two crossed shear bands is 60˚, which is consistent with the shear bands being caused by dislocation slipping on the (111)<110> slipping system.

8.2 Summary on embossing

The present experiments show good promise for application of the embossing to UFG Al foil at elevated temperature, whilst embossing of Al foil with conventional grain size and embossing at room temperature were both prone to processing problems.

Under room temperature embossing only one third of the foil surface was patterned when the embossing force was set at 5 kN, rising to about 50-70% when the embossing force was set to 7kN or 9kN (the maximum load of the press is 10kN). Additionally, the failure rate due to the broken silicon mould dramatically increased when the embossing force was raised from 5 kN to 9 kN.

Hot embossing shows a full transfer of the pattern from the micro silicon die to the UFG Al. The embossing force significantly decreases, which leads to a significant drop of failure rate of the mould. However, the channel edges are slightly rounded.

The rounded edges of the micro channels are mainly attributed to the large grain size compared with the channel size, although a spring back effect may also have a minor contribution. The micro channels made of UFG Al-1050 (1 μm grain size) are improved as compared to the coarse grained variant, but still do not possess perfect right angle edges. According to the theory in Section 5.2, the Al alloys with large value of K_A, e.g. Al-Mg alloys, could reach smaller grain size with the same strain. (For instance, Al-3Mg and Al-3Mg-(Sc-Zr) alloys were refined to 0.2-0.3 μm after eight passes of ECAP [129,137].) Fabrication of micro channels using the UFG Al-Mg alloy is a potential way to obtain microchannels with sharp edges and needs to be further studied in the future work.

8.3 A model of micro embossing of UFG Al alloys

The current model aims to study the influence of the channel size on the embossing force and hardness distribution underneath the embossed surface on the cross section by nanoindentation. Since the features of both embossing and nanoindentation are in micron or submicron scales with strain gradient, geometrically necessary dislocations (GNDs) will be created underneath the embossed surface and lead to a size effect. Following some of the same principles as the nanoindentation model outlined in the previous chapter, a model was created to analyse the embossing force and nanoindentation hardness distribution on the cross sections of embossed UFG materials with feature sizes in the range of a few micrometers. The intrinsic stress and grain boundary strengthening contribution are also considered in current model.

8.3.1 The model

Embossing leads to inhomogeneous deformation, and hence geometrically necessary dislocations exist. The distribution of the GNDs is estimated using a method similar to that in the previous chapter for nanoindentation. The length of a single GND is assumed to be L and the number of GNDs is:

$$N_{GND}=D/b \qquad \text{Eq. 8.2)}$$

where D is the channel depth (see Fig. 8.12). The generated GNDs are assumed to store in a semi-cylinder underneath the embossed surface. The length of the semi-cylinder is L and radius of the semi-cylinder is $f\times W/2$, where W is the channel width. The GND density underneath the embossed surface is thus given by:

$$\rho_{GND}^{E} = \frac{2D/b\,L}{1/2\,\pi(fW/2)^2 L} = \frac{16D}{\pi(fW)^2} \qquad \text{Eq. 8.3)}$$

For embossing, f should be somewhat larger than for nanoindentation because the tool used in embossing is in shape of cuboid whilst the nanoindenter uses a Berkovich tip. Therefore, using a same f value to calculate the plastic zone during embossing with the nanoindentation will lead to underestimate the plastic zone. On the other hand, the volume of the plastic zone is overestimated because a larger indented volume caused by embossing has been taken in account in the plastic zone. We will here estimate f to be the same as that for nanoindentation. The modelling results (see section 8.3.2) will indicate that this approximation is valid.

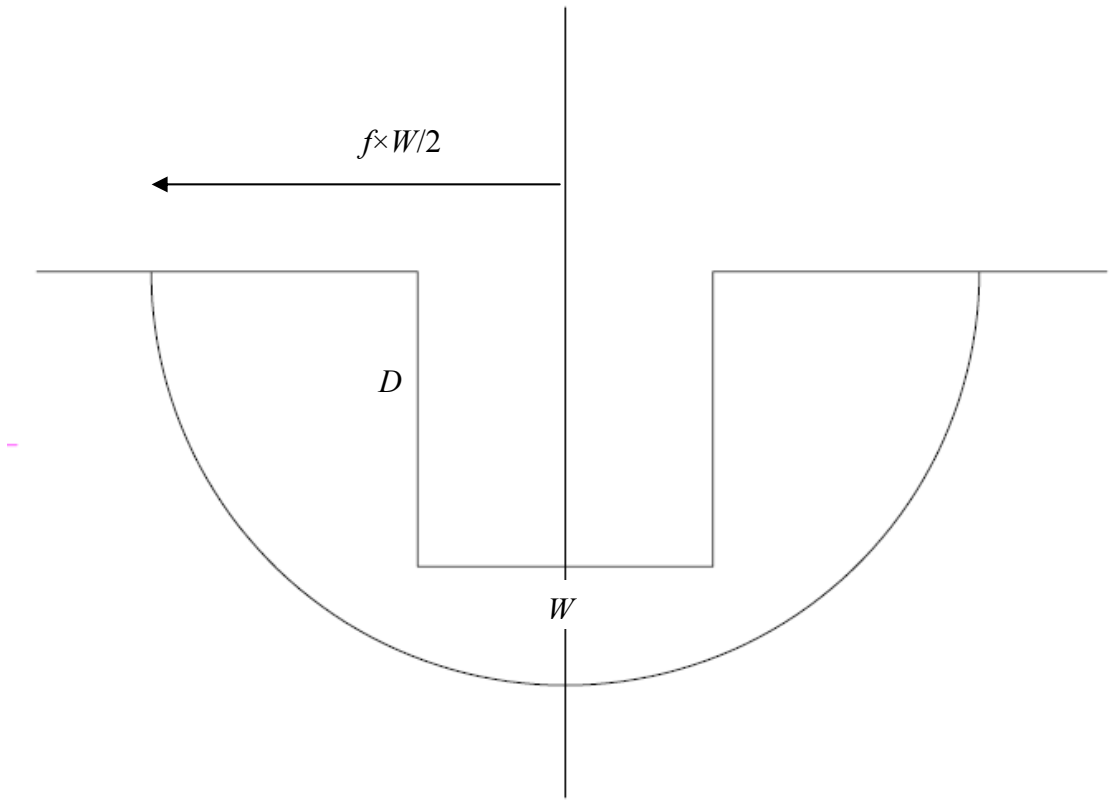

Fig. 8.12 Schematic sketch of GND distribution underneath the embossed surface, D is the channel depth and W is channel width.

In the present embossing work, the embossed channel size, W, ranges from 3μm to 50μm which is in the same order of magnitude with the indent crater side length of the nanoindentation test, so the embossing force can be estimated using the similar equation as the nanoindentation calculation, i.e.:

$$F = H_n^E A_E \qquad \text{Eq. 8.4)}$$

where F is the embossing force, H_n^E is the nanoindentation hardness, A_E is embossed area. The samples used for embossing are discs of 4.5 μm in diameter. The pattern on the discs is a series of parallel straight channels with 1:1 grating; therefore the embossed area is half of the sample area. Through combining Eq. 8.4) with Eq. 7.24) with replacement of ρ_{GND} by $\rho_{\mathrm{GND}}^{\mathrm{E}}$ one obtains an expression for the embossing force:

$$F = 1/2\pi {R_{\mathrm{E}}}^2 * C_2 \left(\sigma_0 + \sigma_{\mathrm{GB}} + M\alpha_1 Gb\sqrt{\rho_{\mathrm{GND}}^{\mathrm{E}} + \rho_{\mathrm{SSD}}} \right) \qquad \text{Eq. 8.5)}$$

where R_{E} is the diameter of the embossed sample.

The creation of GNDs during embossing will cause an inhomogeneous hardness distribution near the indented ridges close to the surface of the embossed sample where the strain gradient is large. This phenomenon can be quantitatively explained by the extra GNDs stored. The GNDs created during embossing contribute to the hardness following Eq. 8.6):

$$H\mathrm{n} = C_2 \left[\sigma_0 + \sigma_{\mathrm{GB}} + M\alpha_1 Gb\sqrt{\rho_{\mathrm{GND}}^{\mathrm{E}} + \rho_{\mathrm{SSD}} + \rho_{\mathrm{GND}}} \right] \qquad \text{Eq. 8.6)}$$

8.3.2 Modeling results

Fig. 8.13 shows the predicted embossing force of the UFG Al-1050 against the embossing width. The minimum embossing force is 16 kN in the limit for large width, and the force rises to 16.3 kN at a width of 50 μm and increases further to 17.5 kN at the width of 25 μm. At further reductions in width the increase in force becomes ever steeper.

Table 8.2 shows the nanoindentation difference between edge and centre on the cross-section of the UFG Al-1050 at various indentation depths predicted using Eq. 8.6). The nanoindentation difference increases with increasing indentation depth.

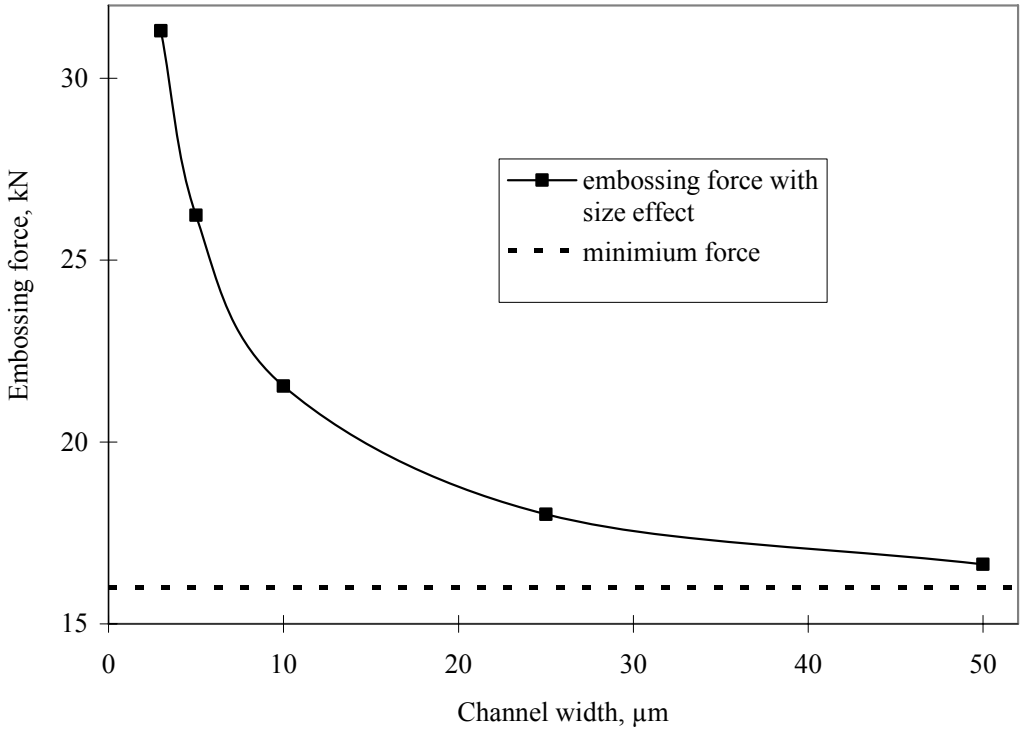

Fig. 8.13 Predicted embossing force against the embossing width

Table 8.2 Predicted nanoindentation hardness difference between edge and centre on the cross-section of the UFG Al-1050 at various indentation depths.

Indentation depth, nm	Hn, GPa		ΔHn, GPa
	edge	centre	
100	0.814	0.754	0.060
200	0.804	0.741	0.063
300	0.79	0.722	0.068
400	0.779	0.706	0.073
800	0.757	0.674	0.083

8.3.3 Discussion of the model

8.3.3.1 Indentation size effect in UFG alloys and coarse grained (CG) alloys

Fig. 8.14 shows variation of the calculated nanoindentation hardness of UFG Al-1050 and CG Al-1050 with the indentation depth. The nanoindentation hardness of UFG Al-1050 is higher than the CG Al-1050 for the whole range of indentation

depths and the ISE for UFG Al-1050 is stronger than for CG Al-1050. This is because ρ_{SSD} of the UFG Al-1050 is larger and contributes more to the nanoindentation hardness as compared to the CG Al-1050. This difference is experimentally confirmed in Ref [208], in which the ISE of a CG Al in grain size of 40 μm and an UFG Al in grain size of 300 nm are compared*. The yield strength of UFG Al was 150-170 MPa measured by the tensile test [228]. In the work of Manika and Maniks [77], no ISE was observed for the fine grained copper and aluminium when the indent size is comparative or larger than the grain size. Manika and Maniks [77] attributed to the strong effect of grain boundaries as barriers for dislocations and concluded the grain boundaries suppress the ISE. However, this appears unlikely as the contribution of grain boundary strengthening of aluminium alloys is very limited compared with dislocation density strengthening [172,227]. The findings of Manika and Maniks [77] can be fully explained by the current model. When the indent size is two times larger than the grain size, the indentation size will be larger than 400nm- 1200 nm (given grain size is 1- 3 μm). As shown in Fig. 8.14, the ISE at such large indentation depth is very limited for fine or ultra fine grained aluminium because the GND density is not the determining factor of the nanoindentation hardness at large indentation depth.

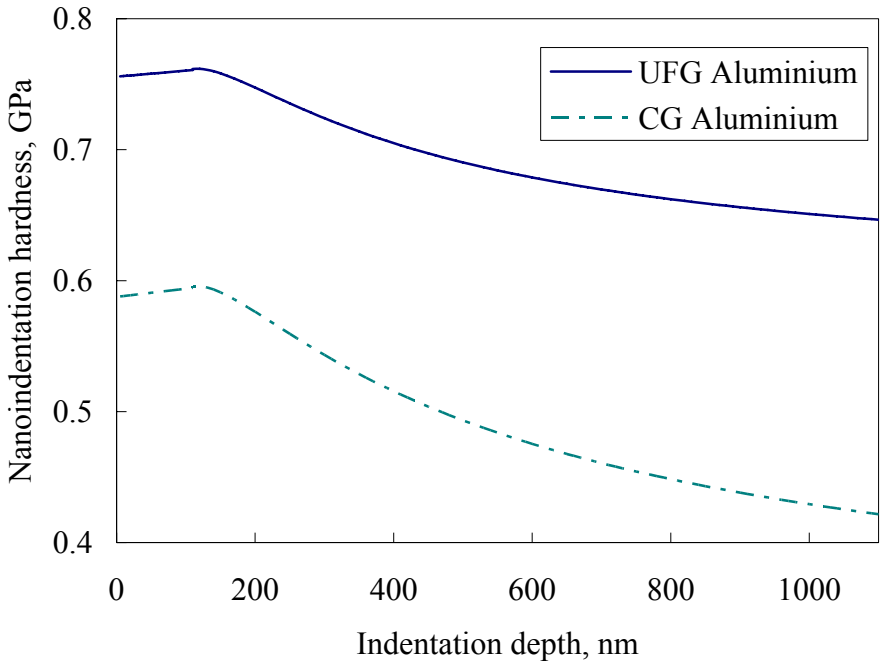

Fig. 8.14 Comparison of ISE in UFG Aluminium and CG Aluminium

* It is worth noting that the yield strength of UFG Al assumed in Ref [208] (200 MPa) is inaccurate.

8.3.3.2 Influence of embossing force on the embossing quality

The pattern that was transferred from the mould to the UFG aluminum is a series of parallel straight channels with 1:1 grating. The width of the channel is same as the depth, which ranges from 3 μm to 50 μm. A problem during room temperature embossing using the 10 μm wide channeled mould is that only one third of the foil surface was patterned when the embossing force was set at 5 kN. The rate rose to about 50% when the embossing force was set to 7kN or 9kN (the maximum load of the press is 10kN). Moreover, it was found that pattern transfer is easier using a mould with a larger channel size than the mould with a smaller channel size. The reason of these problems and limitations are explained by the data in Fig. 8.13. The minimum embossing force required for a pattern with very large channel size is 16kN. The pattern with a smaller channel size needs a larger embossing force to be transferred from the mould to the UFG aluminium because a larger density of GNDs underneath a smaller channel. One potential solution is to increase the embossing force to get the UFG aluminium fully embossed but increasing failure rate of the fragile mould will be unavoidable. Another solution is hot embossing which has been studied in detail in section 8.2.

8.3.3.3 Evaluating hardness homogeneity over the cross section of embossed UFG Aluminium using nanoindentation

The hardness under the embossed surface is higher than that at the centre of the material, which has been detected by nanoindentation in depth of 800 nm (see Fig. 8.8). However, the hardness difference between the subsurface and the centre has not been detected by nanoindentation using depth of 100nm, 200nm, 300nm and 400 nm. This is because the nanoindentation difference between the subsurface and the centre decreases with the decreasing indentation depth (see Table 8.2) since the GND density is the determining factor at lower indentation depth. Additionally, the nanoindentation hardness difference between the subsurface and the centre is in the range of measurement error and fluctuations when the indentation depth was set under 400 nm thus making this difference undetectable. Therefore, using nanoindentation with a larger indentation depth seems necessary to detect the hardness difference between the centre and subsurface according to the results shown in Table 8.2. A plot of the data from Table 8.2 (Fig. 8.15) shows that the hardness difference between the edge and the centre increases with increasing indentation

depth. It may seem that a larger indentation depth might detect this hardness difference because this hardness difference is close to the hardness deviations. However, the larger indentation depth leads to a larger indent size and a large plastic zone so that the distance between two indents and the distance to the sample edge has to be set to a large value. For instance, a distance of 30 μm was set from the indent to the sample edge and the same distance was set from two adjacent indents for the nanoindentation in depth of 800nm. This distance is too large to accurately detect the GNDs under the embossed surface. A potential way to detect the hardness difference between the subsurface and the centre is through using a relatively small indentation depth, meanwhile minimizing the deviation range by using a high precision machine, carefully polishing and accurate calibration.

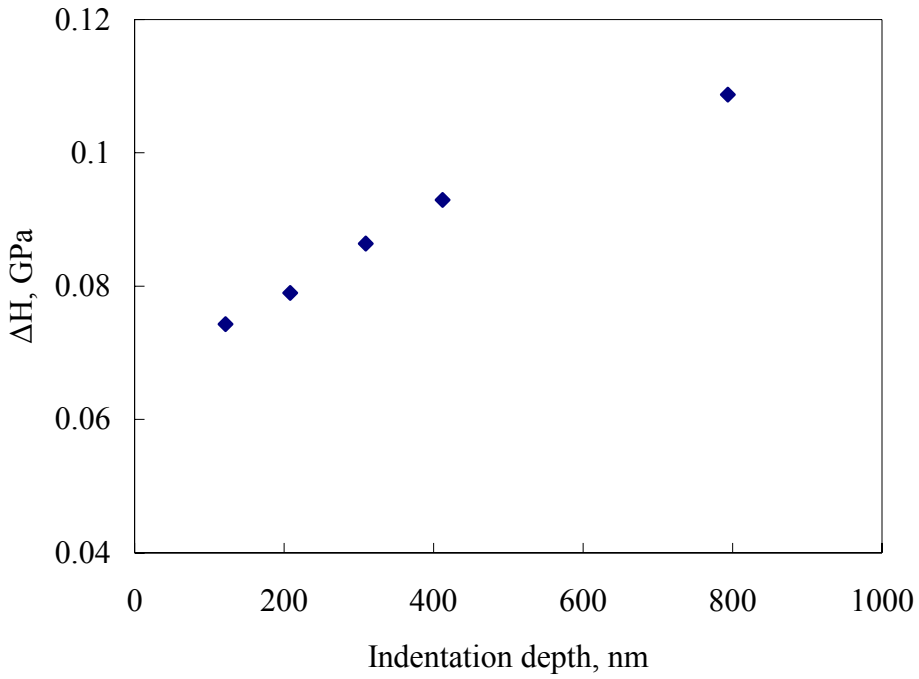

Fig. 8.15 Predicted nanoindentation difference between edge and centre on the cross-section of the UFG Al-1050 at various indentation depths

8.4 Summary

UFG Al-1050 alloys produced by ECAP were embossed to a MEMS component with microchannels at room temperature. The hardness distribution on the cross section of the embossed UFG Al-1050 was measured by nanoindentation. A model

employing the concept of geometrically necessary dislocations was established to interpret hardness distribution on the cross section and predict the embossing force. Conclusions are drawn as follows:

- The nanoindentation hardness at the edge is larger than that at the centre of the cross section of the embossed UFG Al-1050 because of the GND introduced by embossing

- The nanoindentation hardness at the cross section is accurately predicted by the current model with consideration of tip rounding effect, plastic zone size, strengthening contribution of intrinsic stress and grain boundaries.

- Embossing force increases with the decreasing channel size because of the GND underneath the embossed surface that has been successfully predicted by the current model.

9 General Discussion

SPD techniques have attracted researchers' interests since they were developed in 1980s. Especially in the last decade, many works on SPD have been reported. The published works are mainly focused on microstructure, basic mechanic properties and modelling of SPD processed materials. SPD processed materials have many attractive advantages, such as an ultra fine grain size, a large fraction of HAGBs and high speed superplasticity at intermediate temperature, but application of those techniques are rarely attempted in conventional industries because the volumes of SPD processed materials are relative too small as well as expensive. In the present thesis, we used SPD processed materials for the fabrication of MEMS components, an application in which the size of HPT processed materials is sufficient. This project involved material selection, ECAP processing and evaluations after each step with the future objective of fabrication of a micro heat exchanger with high heat transfer efficiency.

9.1 Materials selection

The materials that can be fabricated into micro heat exchangers should have at least three advantages as follows: a) fine grain size in order to obtain a high formability; b) high thermal stability during hot embossing and c) high thermal conductivity for providing a micro heat exchanger with high thermal efficiency. Al-1050 was chosen in present project because it is soft and widely available at low cost. Al-Zr alloys were selected due to their high thermal conductivity, high thermal stability and relative small grain size after ECAP. The embossing works in Chapter 8 indicate the fine grain size is crucial to obtain sharp channel edges. After eight passes of ECAP the grain size of AlZr and AlZrSiFe are about 1μm (see section 5.1.1), which is not small enough to obtain a perfect sharp channel edge if taking into account the channel is 10 μm wide and 10 μm deep. The Al alloys with a relative large grain size will cause rounded channel edges, which is expected to be detrimental to the bonding quality during later bonding process and with an increased possibility of leakage.

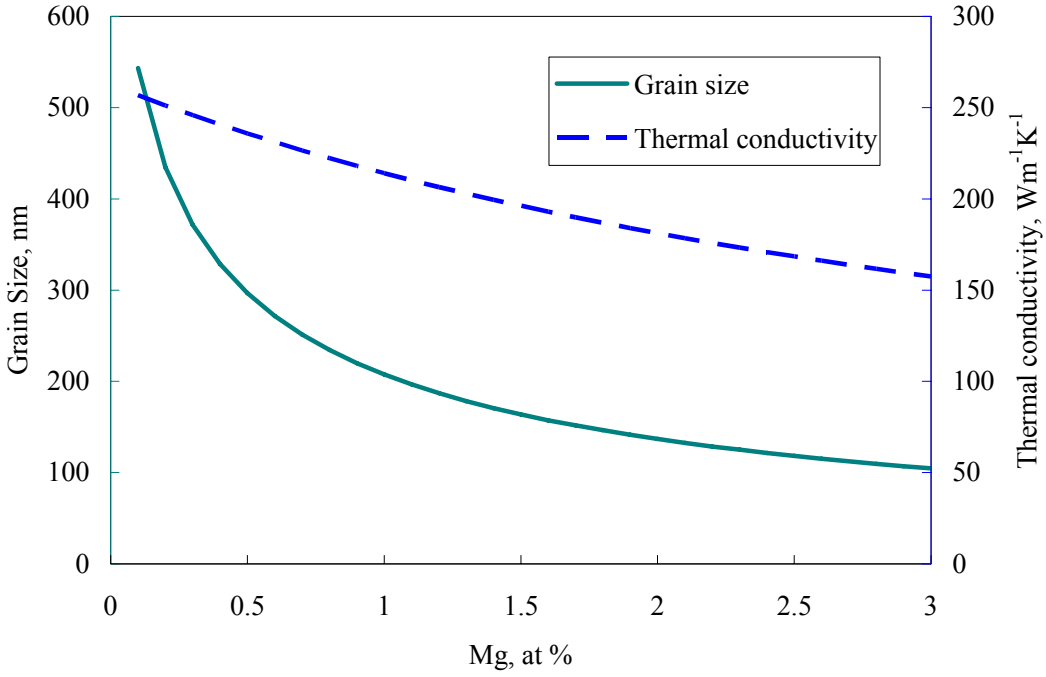

Fig. 9.1 Effect of Mg contents on grain refinement and thermal conductivity of Al-Mg alloys after eight passes of ECAP. The equation of electrical resistivity increment of Al-Mg alloy proportionated to atomic fractional consistent of Mg is from Ref [229].

The study on SPD processed Al alloys in the literature [127,128,129,130,181, 182,184] and the modelling work in Chapter 5.2 and Ref [164] show that Al alloys with addition of Mg and Cu and containing a large fraction of fine nonshearable particles have a potential to achieve an improved grain refinement during SPD (see also Table 2.1). For instance, the grain size of Al-2024 (Al-4%Cu-1.5%Mg-0.4%Mn) after eight passes of ECAP can be refined to 0.3 μm [130], which is 30 times smaller than the channel size used in this work (10 μm). However, Al alloys with a large amount of Mg and Cu additions will loose their high thermal conductivity because a large amount of solutes in the Al phase will obstruct free conductive electrons movement (see section 2.2.2).

Fig. 9.1 shows the effect of Mg content on grain refinement of Al-Mg alloys after eight passes of ECAP, which is predicted using the model in section 5.2 (see also Ref [164]). The grain refinement after eight passes of ECAP is enhanced with increasing Mg content because the extra amount of dislocations (called 'chemically necessarily dislocations' in [164]) are generated during ECAP. However, the increasing Mg

content also decreases the thermal conductivity of Al-Mg alloys (see Fig. 9.1). The thermal conductivity of Al-Mg alloy with different Mg content at 25 ˚C shown in Fig. 9.1 is converted using their electrical conductivity by Eq. 2.1. The dependence of electrical resistivity of Al-Mg alloy on Mg content is adopted from Ref [229].

The above analysis indicates the increase of Mg content in Al alloys, which enhances the further grain refinement, will be detrimental to the thermal conductivity. A further experimental study on effect of Mg contents on grain refinement and thermal conductivity needs to be conducted to determine an optimal Mg content.

9.2 SPD process

In order to apply the present method in commercial production, the SPD technique used should be automatized. ECAP was used in the present work to produce UFG Al alloys. Compared with other processes to manufacture nanomicrostructured materials, ECAP was chosen due to its unique advantages that the samples processed by ECAP are relative large, an ECAP facility is relative easy to establish (provided a press is available) and the automation of producing UFG materials by ECAP is possible. In order to have an automatic production, some improved derivatives were developed to replace ECAP such as ECAP with a rotary die [230], ECAP with side extrusion [231], ECAP with multiple passes [232], equal channel angular rolling (ECAR) [233], continuous frictional angular extrusion [234] and dissimilar channel angular pressing (DCAP) [235]. Fig. 9.2 shows a schematic illustration of a continuous ECAP process, DCAP. However, the problems of ECAP and its derivatives are that the deformation occurring in processing is often not severe enough so that the capability of grain refinement is limited.

The HPT is more powerful in grain refinement than ECAP because a more severe strain can be created and strain can be generated without interruption. However, the size of HPT samples, although large enough for most MEMS applications, is much smaller than ECAP samples. There are no reports on automation of HPT but in principle this seems possible. In order to have a further grain refinement, it is worth performing HPT on Al alloys to produce UFG Al alloys. When automation of HPT becomes available, producing UFG Al alloys and applying in MEMS by HPT and embossing will be more attractive and inexpensive.

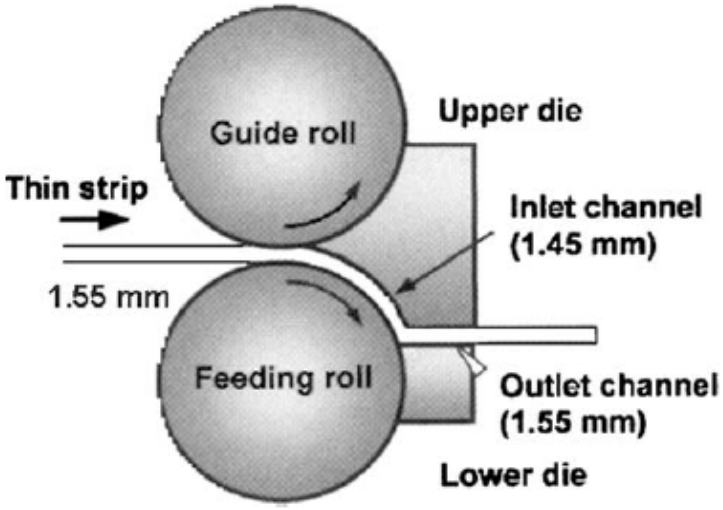

Fig. 9.2 The principle of the DCAP process for use in continuous production [235]

To reduce the cost, any process in which the commercially available equipments are used are attractive. Conventional heavy rolling can also produce Al foils with fine grain size. Moreover, if combined with above SPD techniques, the grain refinement can be further enhanced. The other SPD techniques such as accumulative roll-bonding (ARB), repetitive corrugation and straightening (RCS), cyclic extrusion twist extrusion (TE) and compression (CEC) (see Section 2.5.3-2.5.6) can be also easily adapted to the rolling or extruding equipments in a factory for industrial production of UFG Al alloys. Again, these techniques are less effective in grain refinement than HPT. If the application does not strictly require a maximum grain refinement, these SPD techniques together with the conventional heavy rolling may be suitable and can reduce the cost.

9.3 Potential of mass fabrication of MEMS components using UFG Al via embossing process

The application of UFG Al alloys processed SPD in MEMS depends on two things, i.e. performance of the MEMS components and cost of the whole process. The present study has shown the UFG Al can be embossed into MEMS components with sharp and smooth channels. The embossed UFG Al foils can be produced to micro heat exchangers through diffusion bonding and housing. The performance of the micro heat exchanger needs to be evaluated by checking pressure drop, leakage and heat transfer efficiency. The channels with sharp edges and smooth and flat top

surfaces provide a good condition for successful diffusion bonding. The small channel size and good bonding quality with high thermal conductivity of UFG Al should lead to highly efficient heat exchangers

The cost of the whole process using the current facility would be large because many subprocesses are involved such as ECAP, lithography, DRIE, embossing, bonding and housing. However, a process with a long list of procedure does not necessarily cause a high cost if automised mass fabrication can be achieved. Although fabrications of microelectronic products and MEMS devices involve many processes, they have been extensively used for personal computer, pressure sensors, gyroscopes, accelerometers used for air bag deployment. They are affordable for civilian use due to the automatization which reduces the cost. The processes in the current study such as demoulding and sample feeding are not automatic. This is because the current cold/hot embossing process was established at laboratory level and used to prove the possibility of fabrication MEMS components using UFG Al processed by ECAP. In addition, the equipments used in present cold/hot embossing process were designed and commissioned to fit the press available in the laboratory. The current process can be automatized for mass fabrication. For instance, the Jenoptik Hex-02 [53] and EVG750 [54] are commercially available hot embossing facilities for automised processing of polymers with micro scale features. Those embossing equipments can be adopted for UFG Al alloys provided the demoulding system can be improved to suit the UFG alloys.

9.4 Model development

Finally, it is relevant to note that in the course of the present work a number of models and model variants have been developed and tested that will be valuable beyond the more narrow topic studied in the present work. The grain refinement model in Ref [164] that was applied and tested in section 5.2 is also applicable to predict the grain size after other SPD processing, or large conventional rolling and extrusion. The SPD techniques have been presented for several decades and a number of physical models of grain refinement have been proposed. However, before the present model emerged there was still not a predictive model of grain refinement for quantitative prediction of grain size in a range of Al alloys with various compositions and after different strain of deformations. The modified strengthening

model in section 6.3 has shown validity in current dilute alloys (Al-1050, AlZr and AlZrSiFe). It is expected to be applicable to the prediction of strength of other alloys with high alloying element contents after a large strain of deformation when solid solution strengthening and precipitate strengthening are considered. The ISE model in section 7.2 employing SSD and GND predicts the nanoindentation hardness of Al, MgO, Ir and Cu measured by tips with different radii in a high accuracy. Moreover, following this ISE model, a model presented in section 8.3 predicts the distribution of nanoindentation hardness on the cross section of embossed Al foils and influence of the channel size on the embossing force. The later model is expected to valuable in microembossing processing of Al alloys and related processes with different shape of tools.

10 Conclusions

A novel process for the fabrication of a MEMS metallic component with features smaller than 10 μm and high thermal conductivity was investigated. In the first stage of processing, three ultra fine grained (UFG) Al-1050, AlZr and AlZrSiFe UFG aluminium alloys were produced by equal channel angular pressing (ECAP). The UFG Al alloys were then embossed at both room temperature and high temperature to fabricate components with a pattern of group of parallel channels. Conclusions are drawn as follows:

After 12 passes of ECAP, the grain size of Al-1050 alloys is decreased to 0.88μm with 84% of HAGB. The AlZr and the AlZrSiFe are refined to 1.0 μm with 90% of HAGB and 1.8μm with 77% of HAGB after eight passes of ECAP, respectively. The grain size predicted by a grain refinement model fits the measured grain size in a high accuracy with RMSE of 64 nm.

Texture evolution of three alloys during ECAP strongly depends on their initial condition. The texture of Al-1050 after one pass of ECAP as determined by EBSD fits both the Single Shear Model and the Two Plane Shear Model. The texture of Al-1050, AlZr and AlZrSiFe becomes weaker and more random with the increasing number of ECAP passes.

The microhardness on the cross section of the Al-1050 processed by one pass of ECAP is not homogenous. It is larger at the centre and decreases when approaching the edges (both the top edge and the bottom edge). The highest average microhardness, which appears at the centre, is 48 Hv. The average microhardness at the top edge and the bottom edge is 42 Hv and 39 Hv, respectively. The microstructure on the cross section is not homogenous either. The average grain sizes of the cross section increase from both the top edge and the bottom edge to the centre. The average grain size at the centre is 26 μm, which is larger than the grain size at the top edge and the bottom edge. After annealing at 350 ˚C for 0.5 h, the billet shows a more homogeneous distribution of microhardness and microstructure. The microhardness at the top edge, the centre and the bottom edge decreased to a similar value with slightly changed grain sizes.

The microhardness of UFG Al-1050, AlZr and AlZrSiFe produced by various passes of ECAP reduces with increasing annealing temperature. The relative high microhardness of UFG Al-1050, AlZr and AlZrSiFe can remain up to 250 ˚C, 350˚C and 350˚C, respectively.

A model was presented that captures the character of the hardness inhomogeneity on the cross section of UFG Al after one pass of ECAP and strengthening mechanism of UFG Al alloys produced by various passes of ECAP. The modelling results fit the experimental results well. The model shows that the contribution of dislocation density to the strength of Al1050 after one pass of ECAP is significantly higher than that from grain size.

The nanohardness of UFG Al-1050 measured by nanoindenter shows an indentation size effect. A model employing the concept of geometrically necessary dislocations was established to interpret the indentation size effect for an indenter with a tip worn to a rounded shape. The model successfully predicts the GND density increases with the increasing indentation depth at lower depth under the rounded conical tip. It accurately fits the experimental ISE data of a range of materials for indenter with worn tip.

Cold embossing of the UFG Al-1050 leads to a high failure rate of micro silicon dies. Hot embossing at 300 ˚C allows a reduced embossing force to be used, and this drastically reduces the failure rate. Hot embossing of the coarse-grained Al-1050 produces channels which are not smooth, but embossing of the UFG Al-1050 at 300 ˚C produces smooth channels and the pattern on the micro silicon mould is fully transferred to the foil surface. Embossing of ECAP processed UFG aluminium alloys has shown a good potential for application in microdevise fabrication.

The hardness distribution on the cross section of the embossed UFG Al-1050 was measured by nanoindentation. The nanoindentation hardness at the edge is larger than that at the centre of the cross section of the embossed UFG Al-1050 because of the GND introduced by embossing. A model employing the concept of geometrically necessary dislocation was established to interpret hardness distribution on the cross section and embossing force. The nanoindentation hardness on the cross section is accurately predicted by the current model with consideration of tip rounding effect,

plastic zone size, strengthening contribution of intrinsic stress and grain boundaries. Embossing force increases with the decreasing channel size because of the GND underneath the embossed surface that has been successfully predicted by the current model.

11 Future Work

Producing UFG aluminium is crucial to fabricate a MEMS component in a perfect shape by embossing because coarse-grained aluminium caused rounded channel edges and inhomogeneous deformation during embossing process. Studies of the mechanisms of grain refinement during severe plastic deformation (SPD) has found that the pressure torsion (HPT) is much more powerful than equal channel angular pressing (ECAP) in grain refinement [164]. Moreover, the aluminium alloys with Mg and/or Cu additions can be refined to nano-structured alloys with much smaller grain size than other aluminium alloys [164]. However, the strength of Al-Mg-Cu alloys (for instance, Al-2024) is much higher than commercial pure aluminium, which makes it hard to perform ECAP on Al-Mg alloys at room temperature. In addition, grain growth is unavoidable during hot ECAP, which is not desirable. Therefore, HPT seems a potential technique of producing nano-structured Al-Mg alloys because it provides a severe deformation for a high strength material at room temperature by hydrostatic pressure. Embossing of UFG Al-Mg-(Cu) alloys processed by HPT will be an interesting subject to study in the future.

To fabricate a cross flow micro heat exchanger, the UFG Al foils with a pattern of microchannels needs to be bonded. One way to bond the Al foil with micro features is diffusion bonding. However, there are a couple of things that need to be considered. Firstly, the oil and MoS_2 on surface of embossed Al foils used as lubricants during embossing needs to be removed properly without damaging the channels. Secondly, the oxide layer on top of the embossed surface should be also removed before diffusion bonding, and a vacuum oven will be needed.

The quality of diffusion bonding needs to be evaluated by observing the microstructure, checking pressure drop and measuring heat transfer efficiency. Finally, a proper housing process needs to developed to have a completed micro heat exchanger. Apart from the experimental work, a proper FE model needs to be build up to better understand the whole process.

A number of models and model variants have been developed in present thesis; some of them need further study and testing. In the modified strengthening model see (section 6.3), the mean free path caused by dislocations (l_d) was obtained by fitting. It

will be better if the value of l_d can be justified by microstructural investigation, e.g. TEM or EBSD. The average distance between dislocations with different Burgers vectors in a subgrain measured by TEM can be considered as the value of l_d. Alternatively, the area in a subgrain determined by EBSD can be considered as dislocation free area if the area is separated with the neighbouring areas in a misorientation angle of 1° or less. The average length/width of this area can be a measure of l_d . Additionally, the model predicts the inhomogeneity of microstructure and microhardness on the cross section of Al-1050 processed by one pass of ECAP. The inhomogeneity was attributed to the inhomogeneous strain during ECAP. How the inhomogeneous stain is specifically related to the inhomogeneous microstructure and microhardness is still not clear and needs to be further studied.

A linear superposition relation of GNDs and SSDs was used in the ISE model (see section 7.2) and the embossing model (see section 8.3) and the resulting model provides a fairly good prediction for single crystal materials and annealed metals. However, the density of SSDs is dramatically lower than GNDs in the present work, so further work would be needed to verify that this superposition holds for alloys with much higher SSD densities.

All of listed works are worth considering in the future.

Appendix A Drawings of Embossing Rig Components

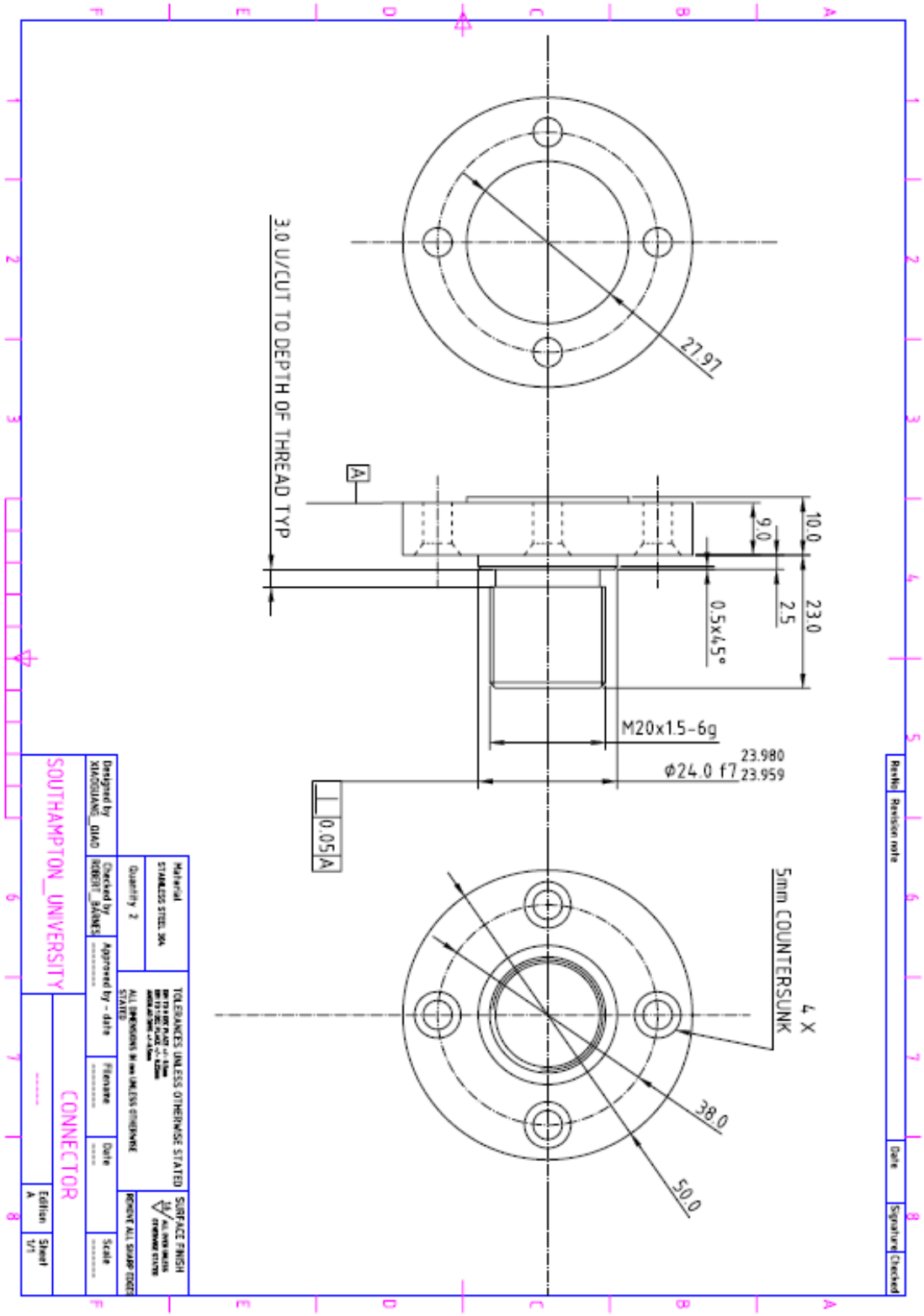

Fig. 0.1 Drawing of a connector for connecting rigs to Instron

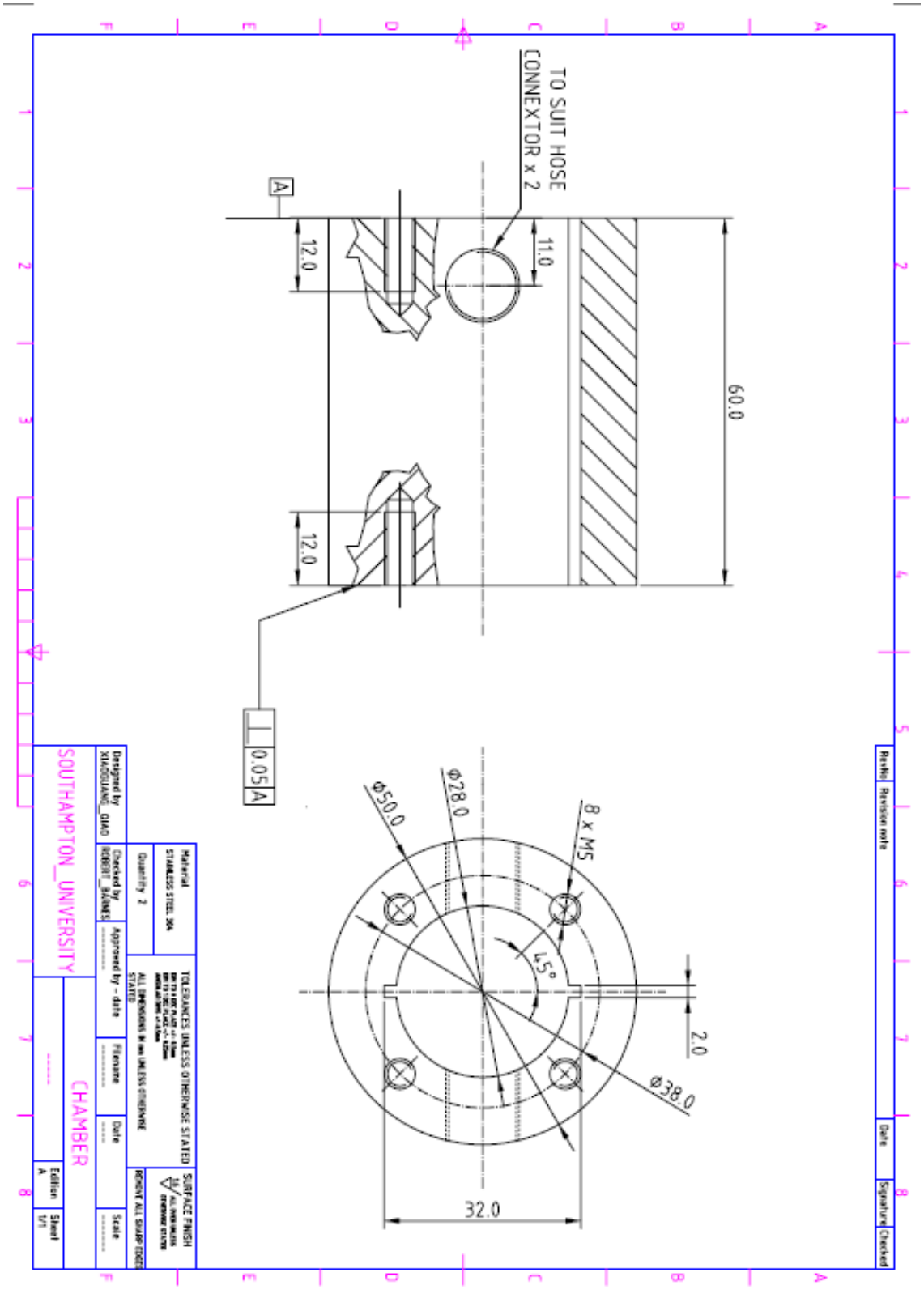

Fig. 0.2Drawing of a water chamber for cooling.

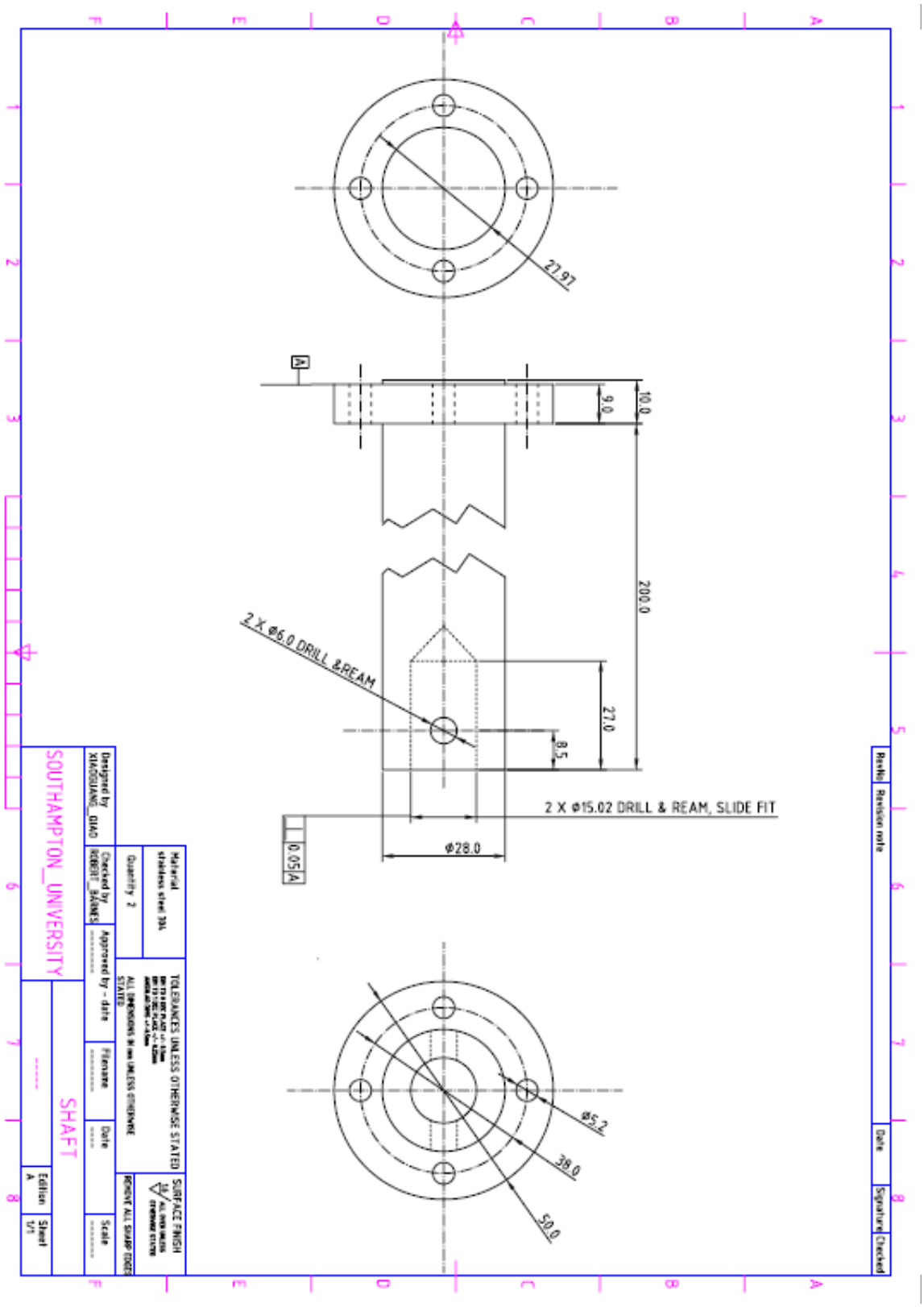

Fig. 0.3 Drawing of a shaft

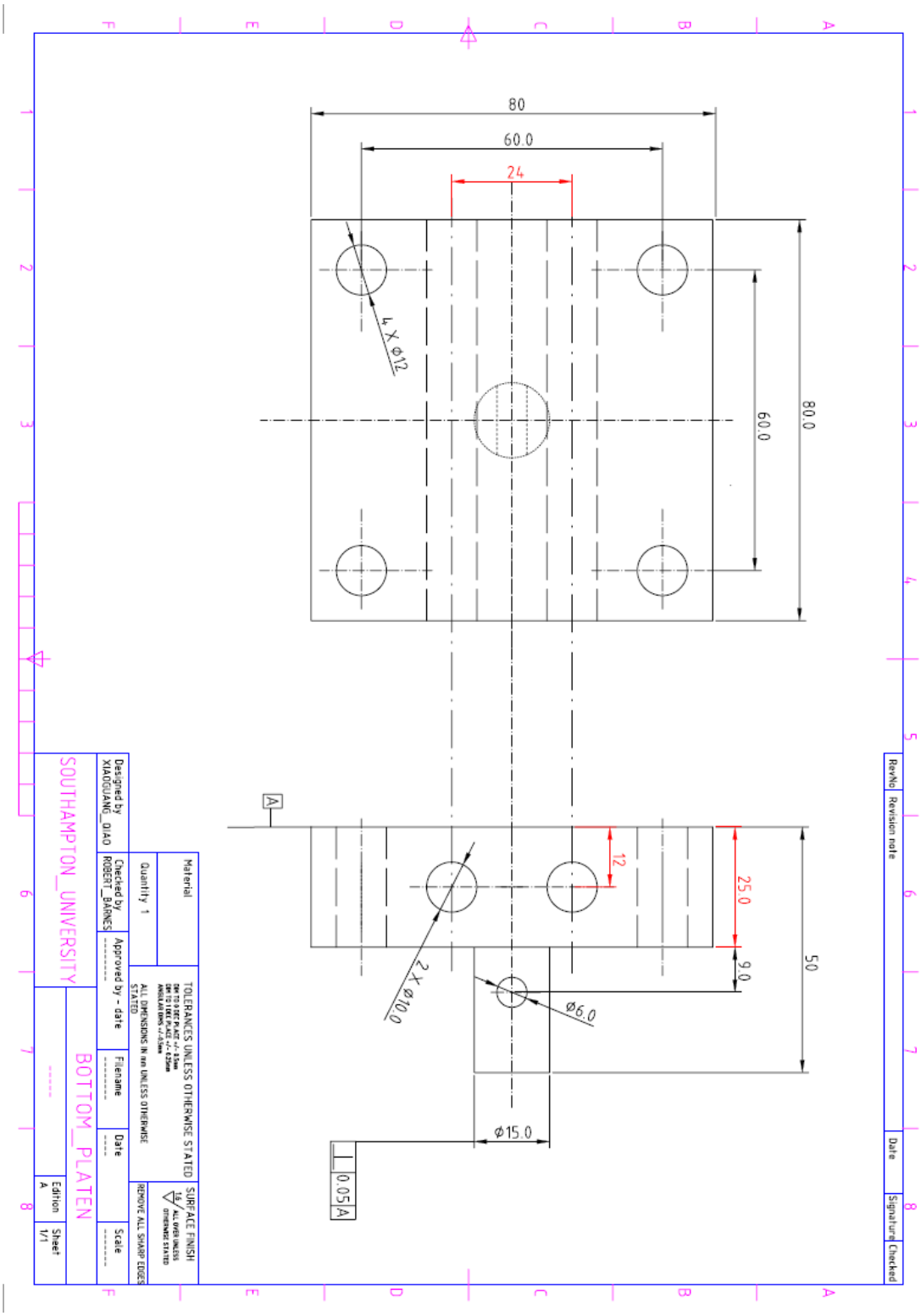

Fig. 0.4 Drawing of a platen with holes for guiding rods, heat elements.

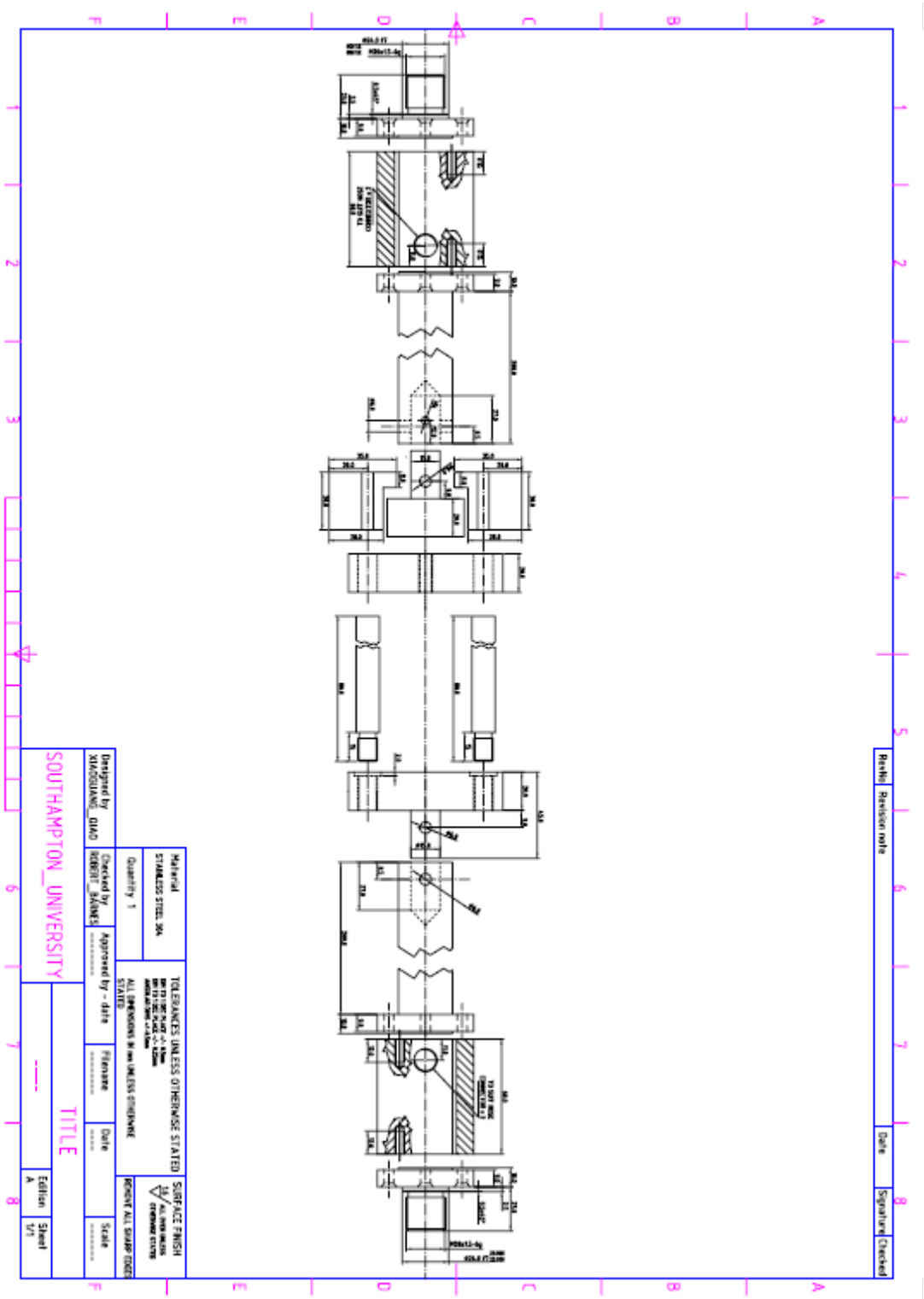

Fig. 0.5 Assembling drawing

Appendix B Topography of Micro Silicon Dies Measured by Confocal Laser System

The micro silicon die is a 14 mm long, 14 mm wide and 0.5 mm thick silicon wafer with a 10 mm long and 10 mm wide pattern etched in one side (see Fig.3.7 for type A). The pattern was designed to be a series of parallel channels with the same size for each wafer. The micro silicon die with different channel size have been fabricated by DRIE and their quality and conformity to the design been measured by confocal laser system and SEM.

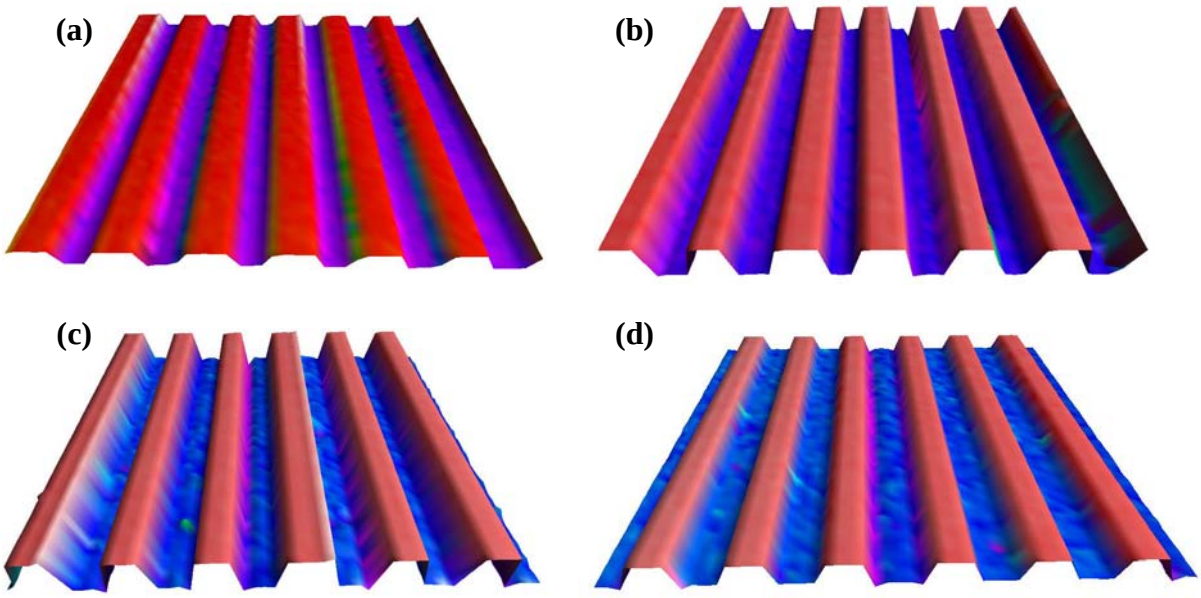

Fig. 0.1 Data from the confocal laser system showing the topography of the micro silicon die with different channel size: (a) 5 μm deep, 10 μm wide, (b) 10 μm deep, 10 μm wide, (c) 15 μm deep, 10 μm wide, (d) 15 μm deep, 25 μm deep.

Fig. 0.1 shows the topography obtained by the confocal laser system for the micro silicon dies with different channel sizes (Colour-depth presentation is set differently for each image. The channel depth of each channel is shown in Table 8.1). The grating width in Fig. 0.1 appears uneven in the same image; additionally, the edge on the top of channel and the sidewall of channel appear to not be smooth. However, these observations are artefacts due to the relatively large step size and the big spot size (2 μm, see Table 4.2) of the laser confocal system. For example, when the step size was set as 1.2 μm for measuring the channel with the size of 10 μm in depth and

10 μm in width, the width of the first channel could be measured as 9.6 μm (8 times step size) and the adjacent grating would then be measured as 10.8μm (9 times step size). Due to this artefact, width of the gratings would seem variable. The laser might also project on the edge of the grating so that a scattered reflected beam would be detected by the sensor then an irregular edge and unsmooth sidewall would be observed. However, the step size settings and the big spot size will not influence the measurement of the depth of a channel with width bigger than 3 μm.

References

1. R.Z. Valiev, R.K. Islamgaliev and I.V. Alexandrov, Bulk nanostructured materials from severe plastic deformation, Prog. Mater. Sci. 45 (2000) 103-189.
2. R.Z. Valiev, Y. Estrin, Z. Horita, T.G. Langdon, M.J. Zehetbauer and Y.T. Zhu, Producing bulk ultrafine-grained materials by severe plastic deformation, JOM 58 (2006) 33-39.
3. R.Z. Valiev, T.G. Langdon, Principles of equal-channel angular pressing as a processing tool for grain refinement, Prog.Mater. Sci. 51 (2006) 881–981.
4. A. Witvrouw, H.A.C. Tilmans and I. de Wolf, Materials issues in the processing, the operation and the reliability of MEMS, Microelectron. Eng. 76 (2004) 245–257.
5. Y.C. Tai and R.S. Muller, IC-processed electrostatic synchronous micromotors, Sens. Actuators 20 (1989) 49-55.
6. S.M. Spearing, Materials issues in microelectromechanical systems (MEMS). Acta Mater. 48 (2000) 179-196.
7. E. Arzt, Size effects in materials due to microstructural and dimensional constraints: a comparative review, Acta Mater. 46 (1998) 5611-5626.
8. D.B. Tuckerman and R.F. Pease. High-performance heat sinking for VLSI. IEEE Electron Device Lett., 2 (1981) 126-129.
9. P.X. Jiang, M.H. Fan, G.S. Si and Z.P. Ren, Thermal-hydraulic performance of small scale micro-channel and porous-media heat-exchangers, Int. J. Heat Mass Transfer 44 (2001) 1039-1051.
10. C. Vargel, M. Jacques and M.P. Schmidt, Corrosion of aluminium, Elsevier, 2004.
11. J.E. Hatch, Aluminium: properties and physical metallurgy, American Society of Metals, 1984.
12. L.F. Mondolfo, Metallography of aluminium alloys. John Wiley & Sons, New York 1943.
13. E. Nes, Precipitation of the metastable cubic Al3Zr-phase in subperitectic Al-Zr alloys. Acta Metall. Mater. 20 (1972) 499-506.
14. S.K. Das and L.A. Davis, High performance aerospace alloys via rapid solidification processing, Mater. Sci. Eng. 98 (1988) 1-12.
15. N. Ryum, The effect of fine disperse Al3Zr on the recrystallization of Aluminium. J. Inst. Metals. 94 (1966) 191-192.
16. H. Jones, Developments in aluminium alloys by solidification at higher cooling rates, Aluminium 54 (1978) 274-281
17. N. Ryum, Precipitation and recrystallization in an Al-0.5wt%Zr alloy, Acta Metall. Mater. 17 (1969) 269-278.

18. C.J. Sparks, E.D. Specht, G.E. Ice, P. Zschack and J. Schneibel, Bonding energies and long-range order in the trialuminides. Fall meeting of the Materials Research Society, Boston, USA, 1990, CONF-901105-92.

19. S. Srinivasan, P.B. Desch and R.B. Schwartz, Metastable phases in the Al3X(X = Ti, Zr, and Hf) intermetallic system, Scripta Metall. 25 (1991) 2513-2516.

20. K.E. Knipling, D.C. Dunand and D.N. Seidman, Nucleation and precipitation strengthening in dilute Al-Ti and Al-Zr alloys, Metall. Mater. Trans. A 38A (2007) 2552-2563.

21. K.E. Knipling, D.C. Dunand and D.N. Seidman, Precipitation evolution in Al-Zr and Al-Zr-Ti alloys during isothermal aging at 375-425˚C, Acta Mater. 56 (2008) 114-127.

22. K.E. Knipling, D.C. Dunand and D.N. Seidman, Precipitation evolution in Al-Zr and Al-Zr-Ti alloys during isothermal aging at 450-600˚C, Acta Mater. 56 (2008) 1182-1195.

23. X.D. Xu, Study on ageing and creep of Al-0.1Zr alloy, Mater. Sci. Eng. 432 (2006) 84-89.

24. E. Sahin and H. Jones, Extended solid solubility, grain refinement and age-hardening in Al-1 to 13wt%Zr rapidly quenched from the melt. Rapidly quenched metals III (1978) 138-145

25. S. Katsas, R. Dashwood, R. Grimes, M. Jackson, G. Todd and H. Henein, Dynamic recrystallization and superplasticity in pure aluminium with zirconium addition, Mater. Sci. Eng. A444 (2007) 291-297.

26. S.D. Park, B.G. Kim and H.W. Lee, Effects of deformation on electric conductivity in Al-Zr alloys, Mater. Sci. Forum 475-479 (2005) 1743-1746.

27. M. Gad-el-Hak, The MEMS Handbook. CRC, 2002.

28. M.J. Madou, Fundamentals of Microfabrication: the Science of Miniaturization, 2nd edition, CRC, 2002.

29. J.J. Allen, Micro electro mechanical systems design, Taylor & Francis Group, 2005.

30. C.S. Smith, Piezoresistive effect in germanium and silicon, Phys. Rev. 94 (1954), 42–49.

31. J.A. Hoerni, Method of manufacturing semiconductor devices, U.S. Patent 3025589, 1962.

32. J.S. Kilby, Miniaturized electronic circuits, U.S. Patent 3138743, 1959.

33. H.C. Nathanson, W.E. Newell, R.A. Wickstrom and J.R. Davis, The resonant gate transistor, IEEE Trans. Electron Devices, (1967) 117–133.

34. K.E. Petersen, Silicon as a mechanical material, Proc. IEEE, 70 (1982), 420–457.

35. I.Z. El-Abidine, M. Okoniewski and J.G. McRory, Tunable radio frequency MEMS inductors with thermal bimorph actuators, J. Micromech. Microeng. 15 (2005) 2063-2068.

36. A.T. Le, W.S. Cho, Y.S. Kim, J.B. Lee, C.O. Kim and H. Lee, A micro-LC-resonator fabricated by MEMS technique for high-frequency sensor applications, Sens. Actuators, A135 (2007) 547-551.

37. W. Ehrfeld, V. Hessel and H. Löwe. Microreactors: New Technology for Modern Chemistry. Wiley, 2000.

38. M. Gad-el-Hak, MEMS: Design and Fabrication: the MEMS Handbook. 2nd edition, CRC, 2006.

39. A.J.van Roosmalen, J.A.G. Baggerman and S.J. H. Brander, Dry etching for VLSI, Plenum Press, New York,1991.

40. D.M. Manos and D.L. Flamm, Plasma Etching, Academic Press, 1989.

41 . R.A. Powell, Dry Etching for Microelectronics, North-Holland Physics Publishing, 1984.

42. M.A. Blauw, Deep anisotropic dry etching of silicon microstructures by high-density plasmas, PhD Thesis, Delft University of Technology, Delft, NL, 2004.

43. F. Laermer, A. Schilp, Method of anisotropically etching silicon. German Pat. DE 4 241 045, 1994.

44. Y.J. Yang, W.C. Kuo and K.C. Fan, Single-run single-mask inductively-coupled-plasma reactive-ion-etching process for fabricating suspended high-aspect-ratio microstructures, Jpn. J. Appl. Phys. 45 (2006) 305–310.

45. C. Chang, Y.F. Wang, Y. Kanamori, J.J. Shih, Y. Kawai, C.K. Lee, K.C. Wu and M. Esashi, Etching submicrometer trenches by using the Bosch process and its application to the fabrication of antireflection structures, J. Micromech. Microeng. 15 (2005) 580–585.

46. C.H. Choi1 and C.J. Kim, Fabrication of a dense array of tall nanostructures over a large sample area with sidewall profile and tip sharpness control, Nanotechnology 17 (2006) 5326–5333.

47. E. W. Becker, W. Ehrfeld, D. Munchmeyer, H. Betz, A. Heuberger, S. Pongratz, W. Glashauser, H. J. Michel and V. R. Siemens, Production of separation nozzle systems for uranium enrichment by a combination of X-ray lithography and galvanoplastics. Naturwissenschaften 69 (1982) 520–23.

48. J. Hruby, LIGA technologies and applications, MRS bulletin (2001) 337-340.

49. W. Ehrfeld, V. Hessel, H. Löwe, Microreactors,new technology for modern chemistry, Wiley-VCH, 2000.

50. W. Ehrfeld and H. Lehr, Deep x-ray lithography for the production of three-dimensional microstructures from metals, polymers and ceramics. Radiat. Phys. Chem. 45 (1995) 349-365.

51. J. Hruby, Overview of LIGA Microfabrication. AIP Conf. Proc. 625(2002) 55-61.

52. A. Lebib, Y. Chen, J. Bourneix, F. Carcenac, E. Cambril, L. Couraud and H. Launois, Nanoimprint lithography for a large area pattern replication. Microelectron. Eng. 46 (1999) 319-322.

53. P. Datta and J. Goettert, Method for polymer hot embossing process development, Microsyst. Technol. 13(2007) 265-270.

54. P. Lindner, T. Glinsner and C. Schaefer, One micron precision optically aligned method for hot-embossing and nanoimprinting, Proc. IEEE Sensors, 2 (2002) 931-935.

55. A. Deodhar, P.S. Shiakolas and S. Belligundu, An AI based controller for temperature control for a hot embossing system, Proc. 13th Mediterranean Conf. Control Auto. Limassol, Cyprus, 6 (2005) 113-118.

56. D. Hardt, B. Ganesan, M. Dirckx, G. Shoji, K. Thaker and W. Qi, Process variability in micro-embossing, Innovation in Manufacturing Systems and Technology (IMST); 2004

57. T. Otto, A. Schubertb, J. Böhmb and T. Gessnera, Fabrication of Micro Optical Components by High Precision Embossing, Proc. SPIE, Micromachining and microfabrication 4179 (2000) 96–106.

58. F.K. Chen, T.B. Huang and S.G. Chen, Embossment formation in press forging of AZ31 magnesium-alloy sheets, Int. J. Adv. Manuf. Technol. 32 (2007) 272-279.

59. X.C. Shan, R. Maeda and Y. Murakoshi, Micro hot embossing for replication of microstructures, Jpn. J. Appl. Phys. 42(2003) 3859-3862.

60. M. Rode and B. Hillerich, Self-aligned positioning of microoptical components by precision prismatic grooves impressed into metals, J. Microelectromechanical Sys. 8 (1999) 58-64.

61. M. Worgull, M. Heckele and W.K. Schomburg, Large-scale hot embossing, Microsyst. Technol. 12 (2005) 110-115.

62. C.R. Friedrich and S.D. Kang, Micro heat exchangers fabricated by diamond machining, Preci. Eng. 16 (1994) 56-59.

63. K. Schubert, J. Brandner, M. Fichtner, G. Linder, U. Schygulla and A. Wenka, Microstructure devices for applications in thermal and chemical process engineering. Nanoscale Microscale Thermophys. Eng. 5 (2001) 17–39.

64. J.J. Brandner, E. Anurjew, L. Bohn, E. Hansjosten, T. Henning, U. Schygulla, A. Wenka and K. Schubert. Concepts and realization of microstructure heat exchangers for enhanced heat transfer Exp. Therm Fluid Sci. 30 (2006) 801-809.

65. W. Bier, W. Keller, G. Linder, D. Seidel and K. Schubert, Manufacturing and testing of compact micro heat exchangers with high volumetric heat transfer coefficients, ASME, Dynamic Systems and Control Division 19 (1990) 189-97.

66. J. Jiang, F. Mei, W.J. Meng, G.B. Sinclair and S. Park, Direct microscale imprinting of Al at room temperature with Si inserts, Microsyst. Technol. 14 (2008) 815–819.

67. J. Böhm, A. Schuber, T. Otto and T. Burkhardt, Micro-metalforming with silicon dies, Microsystem Tech. 7 (2001) 191-195

68. R. Neugebauer, A. Schubert, J. Böhm and T. Burkhardt, High Precision Embossing of Microparts, Proc. 6th Int. Conf. Tech. of Plast. (ICTP), Nürnberg, 9 (1999) 19-24.

69. M.S. Yeh, H.Y. Lin, H.T. Lin and C.B. Chang, Superplastic micro-forming with a fine grained Zn–22Al eutectoid alloy using hot embossing technology, J. Mater. Proc. Tech. 180 (2006) 17–22.

70. Y. Aaotome and A. Inoue, New amorphous alloys as micromaterials and the processing technologies, 13th Annu. Int. Conf. on MEMS, (2000) 288-293.

71. H. Justinger and G. Hirt, Estimation of grain size and grain orientation influence in microforming processes by Taylor factor considerations, J. Mater. Proc. Tech. 209 (2009) 2111-2121.

72. Y. Saotome, T. Zhang, and A. Inoue, Mat. Res. Soc. Symposium Proc 554 (1999) 385–390.

73. N.A. Stelmashenko, M.G. Walls, L.M. Brown, Yu.V. Milman, Microindentations on W and Mo oriented single crystals: An STM study, Acta Metall. Mater. 41 (1993) 2855-2865.

74. Q. Ma and D.R. Clarke, Size dependent hardness in silver single crystals, J. Mater. Res. 10 (1995) 853-863.

75. M. F. Ashby, The deformation of plastically non-homogeneous alloys. Phil. Mag. 21 (1970) 399-424.

76. N.A. Fleck, G.M. Muller, M.F. Ashby, J.W. Hutchinson, Strain gradient plasticity: Theory and experiment, Acta Metall. Mater. 42 (1994) 475-487.

77. I. Manika, J. Maniks, Size effects in micro- and nanoscale indentation, Acta Mater. 54 (2006) 2049-2056.

78. W.D. Nix, H. Gao, Indentation size effects in crystalline materials: A law for strain gradient plasticity, J. Mech. Phys. Solids, 46 (1998) 411-425.

79. J.G. Swadener, E.P. George, G.M. Pharr, The correlation of the indentation size effect measured with indenters of various shapes, J Mech Phys Solids 50 (2002) 681-694.

80. Y.Y. Lim, M.M. Chaudhri, The effect of the indenter load on the nanohardness of ductile metals: An experimental study on polycrystalline work-hardened and annealed oxygen-free copper, Philos Mag A 79 (1999) 2979-3000.

81. G. Feng, W.D. Nix, Indentation size effect in MgO, Scripta Mater. 51 (2004) 599-603.

82. A.A. Elmustafa, D.S. Stone, Nanoindentation and the indentation size effect: Kinetics of deformation and strain gradient plasticity, J Mech Phys Solids 51 (2003) 357-381.

83. D. Chicot, Hardness length-scale factor to model nano- and mico-indentation size effects, Mater. Sci. Eng. A 499 (2009) 454-461.

84. R.K. Abu Al-Rub, Prediction of micro and nanoindentation size effect from conical or pyramidal indentation, Mech. Mater. 39 (2007) 787-802.

85. Y. Huang, Z. Xue, H. Gao, W.D. Nix, and Z.C. Xia, A study of microindentation hardness tests by mechanism-based strain gradient plasticity, J. Mater. Res. 15 (2000) 1786-1796.

86. Y. Huang, S.Qu, K.C. Hwang, M. Li and H. Gao, A conventional theory of mechanism-based strain gradient plasticity, Int. J. Plast. 20 (2004) 753-782.

87. D.B. Tuckerman, Heat-transfer microstructures for integrated circuits, Ph.D Thesis, Stanford University, USA, 1984.

88. S. Kakaç and H. Liu, Heat Exchangers: Selection, Rating and Thermal Design, 2nd edition, CRC, 2002.

89. C. Harris, M. Despa, and K. Kelly. Design and fabrication of a cross flow micro heat exchanger, J. Microelectromechanical Sys. 9 (2000) 502-508.

90. S.W. Kang and S.C. Tseng. Analysis of effectiveness and pressure drop in micro cross-flow heat exchanger. App. Therm. Eng. 27 (2007) 877-885.

91. C.R. Friedrich and S.D. Kang. Micro heat exchangers fabricated by diamond machining, Preci. Eng. 16 (1994) 56-59.

92. C. Harris, K. Kelly, T. Wang, A. McCandless and S. Motakef. Fabrication, modeling, and testing of micro-cross-flow heat exchangers. J. Microelectromech. Syst. 11 (2002) 726-735.

93. J.Gruss, C.Bouzon and B.Thonon. Extruded Microchannel-Structured Heat Exchangers, Heat Transfer Eng. 26 (2005) 56–63.

94. W.Bier, W.Keller, G.Linder, D.Seidel and K.Schubert, Manufacturing and testing of compact micro heat exchangers with high volumetric heat transfer coefficients, Winter Annu. Meeting ASME. (1990) 189-197.

95. B. Alm, R. Knitter and J. Haußelt, Development of a ceramic micro heat exchanger-design, construction, and testing. Chem. Eng. Tech. 28 (2005) 1554–1560.

96. F.J. Humphreys, P.B. Prangnell, J.R. Bowen, A. Gholinia and C. Harris, Developing stable fine grain microstructures by large strain deformation, Phil. Trans. R. Soc. Lond. A 357 (1999) 1663-1681.

97. T.C. Lowe and R.Z. Valiev, The use of severe plastic deformation techniques in grain refinement, JOM, 56 (2004) 64-68.

98. A.P. Zhilyaev, G.V. Nurislamova, B.K. Kim, M.D. Baró, J.A. Szpunar and T.G. Langdon, Experimental parameters influencing grain refinement and microstructural evolution during high-pressure torsion, Acta Mater. 51 (2003) 753-765.

99. V.M. Segal, V.I. Reznikov, A. E. Drobyshevkij and V.I. Kopylov. Plastic metal working by simple shear. Metally 1 (1981) 115-123.

100. O.R. Valiahmetov, R.M. Galeyev and G.A. Salishchev. Mechanical properties of the titanium alloy VT8 with submicrocrystalline structure, Phys. Met. Metall. 70 (1990) 198-200.

101. Y. Saito, H. Utsunomiya, N. Tsuji and T. Sakai, Novel ultra-high straining process for bulk materials—development of the accumulative roll-bonding (ARB) process, Acta Mater. 47 (1999) 579-583.

102. M. Richert, H.P. Stüwe, M.J. Zehetbauer, J. Richert, R. Pippan, Ch. Motz and E. Schafler, Work hardening and microstructure of AlMg5 after severe plastic deformation by cyclic extrusion and compression, Mater. Sci. Eng. A 355 (2003) 180-185.

103. J.Y. Huang, Y.T. Zhu, H. Jiang and T.C. Lowe, Microstructures and dislocation configurations in nanostructured Cu processed by repetitive corrugation and straightening, Acta Mater. 49 (2001) 1497-1505.

104. V. Varyukhin, V. Tkatch, V. Maslov, Y. Beygelzimer, S. Synkov, V. Nosenko, S. Rassolov, A. Synkov, V. Krysov and V. Mashira. Consolidation of amorphous Al86Ni6Co2Gd6 melt spun ribbons by twist extrusion, Mater. Sci. Forum 503-504 (2006) 699-704.

105. R.Z. Valiev and I.V. Alexandrov, Development of severe plastic deformation techniques for the fabrication of bulk nanostructured materials, Ann.Chim.Sci.Mat. 27 (2002) 3-14.

106 C. Xu, Z. Horita, T.G. Langdon, The evolution of homogeneity in processing by high-pressure torsion, Acta Mater. 55 (2007) 203-212.

107. G. Sakai, Z. Horita, T.G. Langdon, Grain refinement and superplasticity in an aluminum alloy processed by high-pressure torsion, Mater. Sci. Eng. A393 (2005) 344-351.

108. R.Z. Valiev, R.S. Mishral, J. Grozal and A.K. Mukherjee, Processing of nanostructured nickel by severe plastic deformation consolidation of ball-milled powder, Scripta. Mater. 34 (1996) 1443-1448.

109. R.Z. Valiev, N.A. Krasilnikov and N.K. Tsenev, Plastic deformation of alloys with submicron-grained structure. Mater. Sci. Eng. A137 (1991) 35-40.

110 C. Xu, T.G. Langdon, Influence of a round corner die on flow homogeneity in ECA pressing, Scripta Mater. 48 (2003) 1-4.

111. V.M. Segal, K.T. Hartwig and R.E. Goforth, In situ composites processed by simple shear. Mater. Sci. Eng. A224 (1997) 107-115.

112. Y. Iwahashi, J.T. Wang, Z. Horita, M. Nemoto and T.G. Langdon. Principle of equal-channel angular pressing for the processing of ultra-fine grained materials, Scripta Mater 35(1996) 143-146.

113. P. B. Prangnell, C. Harris and S.M. Roberts, Finite element modelling of equal channel angular extrusion. Scripta Mater. 37 (1997) 983-989.

114. Y. Wu and I. Baker, An experimental study of equal channel angular extrusion. Scripta Mater. 37 (1997) 437-442.

115. R.E. Goforth, K.T. Hartwig and L.R. Cornwell, Severe plastic deformation of materials by equal channel angular extrusion (ECAE), in “Investigations and applications of severe plastic deformation” Edited by T.C. Lowe and R.Z. Valiev. Kluwer Academic Publishers, 2000.

116. T. Aida, K. Matsuki, Z. Horita and T.G. Langdon, Estimating the equivalent strain in equal-channel angular pressing, Scripta Mater. 44 (2001) 575-579

117. M. Furukawa, Y. Iwahashi, Z. Horita, M. Nemoto and T.G. Langdon, The shearing characteristics associated with equal-channel angular pressing. Mater. Sci. Eng. A 257 (1998) 328-332.

118. T.G. Langdon, M. Furukawa, M. Nemoto and Z. Horita, Using equal-channel angular pressing for refining grain size. JOM 52 (2000) 30-33.

119. M.A. Meyers, A. Mishra and D.J. Benson, Mechanical properties of nanocrystalline materials, Prog. Mater. Sci. 52 (2006) 427-556.

120. R.Z. Valiev, Y.V. Ivanisenko, E.F. Rauch and B. Baudelet, Structure and deformation behaviour of armco iron subjected to severe plastic deformation. Acta Mater. 44 (1996) 4705-4712.

121. Sh.R. Musalimov and R.Z Valiev. Dilatometric analysis of aluminium alloy with submicrometre grained structure. Scr Metall Mater 27 (1992)1685-1690

122. R.Z. Valiev, V.Yu. Gertsman and O.A. Kaibyshev, Grain boundary structure and properties under external influences, Physica Status Solidi (a) 97 (1986) 11-56.

123. Z. Horita, D.J. Smith, M. Furukawa, M. Nemoto, R.Z. Valiev and T.G. Langdon. Evolution of grain boundary structure in submicrometer-grained Al-Mg alloy. Mater. Charact., 37 (1996) 285-294.

124. C. Xu, M. Furukawa, Z. Horita, T.G. Langdon, The evolution of homogeneity and grain refinement during equal-channel angular pressing A model for grain refinement in ECAP, Mater. Sci. Eng. A 398 (2005) 66-76.

125. T.G. Langdon, The principles of grain refinement in equal-channel angular pressing, Mater. Sci. Eng. A 462 (2007) 3-11.

126. N.Q. Chinh, P. Szommer, T. Csanádi and T.G. Langdon, Flow processes at low temperatures in ultrafine-grained aluminium. Mater. Sci. Eng. A 434 (2006) 326-334

127. M. Furukawa, A. Utsunomiya, K. Matsubara, Z. Horita and T. G. Langdon, Influence of magnesium on grain refinement and ductility in a dilute Al–Sc alloy, Acta Mater. 49 (2001) 3829-3838.

128. S. Komura, Z. Horita, M. Furukawa, M. Nemoto and T.G. Langdon, An Evaluation of the Flow Behavior during High Strain Rate Superplasticity in an Al-Mg-Sc Alloy, Metall. Mater. Trans. A 32A (2001) 707-716

129. S. Lee, A. Utsunomiya, H. Akamatsu, K. Neishi, M. Furukawa, Z. Horita and T.G. Langdon. Influence of scandium and zirconium on grain stability and superplastic ductilities in ultrafine-grained Al–Mg alloys. Acta Mater. 50 (2002) 553-564

130. S. Lee, M. Furukawa, Z. Horita and T. G. Langdon. Developing a superplastic forming capability in a commercial aluminum alloy without scandium or zirconium additions, Mater. Sci. Eng. A342 (2003) 294-301

131. N. Gao, M.J. Starink, M. Furukawa, Z. Horita, C. Xu, and T.G. Langdon, Microstructural evolution in a spray-cast aluminum alloy during equal-channel angular pressing. Mate. Sci. Eng. A410-411 (2005) 303-307.

132. K. Oh-ishi, Z. Horita, D.J. Smith and T.G. Langdon, Grain boundary structure in Al-Mg and Al-Mg-Sc alloys after equal-channel angular pressing, J. Mater. Res. 16 (2001) 583-589.

133. W.Q. Cao, A. Godfrey, W. Liu and Q. Liu, EBSP study of the annealing behaviour of aluminium deformed by equal channel angular processing. Mater. Sci. Eng. A360 (2003) 420-425.

134. J. Wang Y. Iwahashi, Z. Horita, M. Furukawa, M. Nemoto, R.Z. Valiev and T.G. Langdon, An investigation of microstructrural stability in an Al-Mg alloy with submicrometer grain size, Acta Mater. 44 (1996) 2973-2982.

135. D.G. Morris and M.A. Munoz-Morris, Microstructure of severely deformed Al-3Mg and its evolution during annealing, Acta Mater. 50 (2002) 4047-4060.

136. J.L. Ning and D.M. Jiang, Influence of Zr addition on the microstructure evolution and thermal stability of Al-Mg-Mn alloy processed by ECAP at elevated temperature. Mater.Sci.Eng.A 452-453 (2007) 552-557.

137. H. Hasegawa, S. Komura, A. Utsunomiya, Z. Horita, M. Furukawa, M. Nemoto and T.G. Langdon, Thermal stability of ultrafine-grained aluminum in the presence of Mg and Zr additions. Mater. Sci. Eng. A265 (1999) 188-196.

138. Z.C. Wang and P.B. Prangnell, Microstructure refinement and mechanical properties of severely deformed Al-Mg-Li alloys, Mater. Sci Eng. A238 (2002) 87-97.

139. J. Mao, S.B. Kang and J.O. Park, Grain refinement, thermal stability and tensile properties of 2024 aluminium alloy after equal-channel angular pressing, J. Mater. Proc.Tech. 159 (2005) 314-320.

140. Z. Horita, T. Fujinami, M. Nemoto and T.G. Langdon, Equal-channel angular pressing of commercial aluminium alloys: grain refinement, thermal stability and tensile properties, Metall Mater Trans 31A (2000) 691-701.

141. R.Z. Valiev, I.V. Alexandrov, T.C. Lowe and Y.T. Zhu, Paradox of strength and ductility in metals processed by severe plastic deformation. J. Mater. Res. 17 (2002) 5-8.

142. R.Z. Valiev, Nanostructuring of metals by severe plastic deformation for advanced properties. Nature Mater 3 (2004) 511-516.

143. Y. Wang, M. Chen, F. Zhou and E. Ma, High tensile ductility in a nanostructured metal. Nature 419 (2002) 912-915.

144. M. Mabuchi, Y. Chino, H. Iwasaki, T. Aizawa and K. Higashi. The grain size and texture dependence of tensile properties in extruded Mg-9Al-1Zn. Mater. Trans. 42 (2001) 1182-1189

145. M. H.Yoo, Slip, twinning, and fracture in hexagonal close-packed metals. Metall. Trans, 12A (1981) 409-418.

146. P.G. Partridge, The crystallography and deformation modes of hexagonal closed-packed metals. Metall. Rev. (1967) 169-193

147. S. Ando, H. Tonda. Non-basal slip in magnesium-lithium alloy single crystals. Mater Trans 41 (2000) 1188-1191.

148. W.J. Kim, S.I. Hong, Y.S. Kim, S.H. Min, H.T. Jeong and J.D. Lee. Texture development and its effect on mechanical properties of an AZ61 Mg alloy fabricated by equal channel angular pressing. Acta Mater. 51 (2003) 3293–3307

149. J.W. Edington, K.N. Melton and C.P. Cutler, Superplasticity. Prog. Mater. Sci. 21 (1976) 61-170.

150. R.Z. Valiev, D.A. Salimonenko, N.K. Tsenev, P.B. Berbon and T.G. Langdon, Observations of high strain rate superplasticity in commercial aluminium alloys with ultrafine grain sizes. Scripta Mater 37 (1997) 1945- 1950

151. T.G. Langdon, A unified approach to grain boundary sliding in creep and superplasticity. Acta Metall. Mater. 42 (1994) 2437-2443.

152. R.C. Gifkins, Grain-boundary sliding and its accommodation during creep and superplasticity. Metall. Trans. A 7 (1976) 1225-32.

153 J.K. Mackenzie,Second paper on statistics associated with the random disorientation of cubes, Biometrika 45 (1958) 229-240

154. V.M. Segal, Equal channel angular extrusion: from macromechanics to structure formation, Mater. Sci. Eng. A271 (1999) 322-333.

155. L.S. Toth, Texture evolution in severe plastic deformation by equal channel angular extrusion, Adv. Eng. Mater.5 (2003) 308-316.

156. S. Li, I.J. Beyerlein, M.A.M.Bourke, Texture formation furing equal channel angular extrusion of fcc and bcc materials: comparison with simple shear. Mater.Sci.Eng. A 394 (2005) 66-77.

157. F. Montheillet, M. Cohen, J. J. Jonas, Axial stresses and texture development during the torsion testing of Al, Cu and α-Fe, Acta. Metall. 32 (1985) 2077-2089.

158. S.C. Wang, M.J. Starink, N. Gao, X.G. Qiao, C.Xu and T.G. Langdon, Texture evolution by shear on two planes during ECAP of a high-strength aluminium alloy, Acta Mater. 56 (2008) 3800-3809.

159. Y. Fukuda, K. Oh-ishi, M. Furukawa, Z. Horita and T.G. Langdon, the application of equal-channel angular pressing to an aluminium single crystal, Acta Mater. 52 (2004) 1387-1395.

160. W.Z. Han, Z.F. Zhang, S.D. Wu and S.X. Li, Influence of crystallographic orientations on deformation mechanism and grain refinement of Al single crystals subjectied to one-pass equal-channel angular pressing, Acta Mater. 55 (2007) 5589-5900.

161. F.J. Humphreys and M. Hatherly, Recrystallization and related annealing phenomena, Pergamon, 2nd edition, 2004.

162.C.P. Chang, P.L. Sun and P.W. Kao, Deformation induced grain boundaries in commercially pure aluminium, Acta Mater. 48 (2000) 3377-3385.

163. T.G. Langdon, M. Furukawa, M. Nemoto and Z. Horita, Using equal channel angular pressing for. refining grain size, JOM 52 (2000) 30-33.

164. M.J. Starink, X.G. Qiao and N. Gao, Predicting grain refinement by cold severe plastic deformation in alloys using volume averaged dislocation generation, Acta Mater. 57 (2009) 5796-5811.

165. U.F. Kocks, A statistical theory of flow stress and work-hardening, Phil. Mag. 13 (1966) 541-566.

166. H. Mecking, U.F. Kocks, Kinetics of flow and strain-hardening, Acta Metall Mater 29 (1981) 1865-1875.

167. U.F. Kocks, H. Mecking, Physics and phenomenology of strain hardening: the FCC case, Prog Mater Sci 48 (2003) 171-273.

168. Y. Estrin, H. Mecking, A unified phenomenological description of work hardening and creep based on one-parameter models Acta Metall Mater 32 (1984) 57-70.

169. A. Thorvaldsen, The intercept method--1. Evaluation of grain shape, Acta Mater. 45, (1997) 587-594.

170. M. Prell, C. Xu, T.G. Langdon, The evolution of homogeneity on longitudinal sections during processing by ECAP, Mater. Sci. Eng. A 480 (2008) 449–455.

171. ASM handbook. Vol. 2, Properties and selection: nonferrous alloys and special-purpose materials, tenth ed., ASM international. 1991.

172. M.J. Starink, A. Deschamps, S.C. Wang, The strength of friction stir welded and friction stir processed aluminium alloys, Scripta Mater. 58 (2008) 377-382.

173. M.J. Starink, S.C. Wang, A model for the yield strength of overaged Al-Zn-Mg-Cu alloys, Acta Mater.51 (2003) 5131-5150.

174. K. Marthinsen, E. Nes, A general model for metal plasticity, Mater. Sci. Eng. A 234–236 (1997) 1095-1098.

175. F. Hernández Olivares, J. Gil Sevillano, A quantitative assessment of forest-hardening in f.c.c. metals, Acta Metall. Mater. 35 (1987) 631-641.

176. E. Nes, T Pettersen and K. Marthinsen, On the mechanisms of work hardening and flow-stress saturation, Scripta Mater. 43 (2000) 55-62E.

177. M.F. Ashby, The deformation of plastically non-homogeneous alloys. Phil. Mag. 21 (1970) 399-424.

178. S.G. Chowdhury, A. Mondal, J. Gubicza, G. Krallics, A. Fodor, Evolution of microstructure and texture in an ultrafine-grained Al6082 alloy during severe plastic deformation, Mater. Sci. Eng. A 490 (2008) 335-342.

179. Y.H. Zhao, X.Z. Liao, Z. Jin, R.Z. Valiev, Y.T. Zhu, Microstructures and mechanical properties of ultrafine grained 7075 Al alloy processed by ECAP and their evolutions during annealing, Acta Mater 52 (2004) 4589-4599.

180 . M. Reihanian, R. Ebrahimi, M.M. Moshksar, D. Terada, N.Tsuji, Microstructure quantification and correlation with flow stress of ultrafine grained

commercially pure Al fabricated by equal channel angular pressing (ECAP), Mater Char 2008;59:1312-1323.

181. J. Gubicza, N.Q. Chinh, Gy. Krállics, I. Schiller, T. Ungár, Microstructure of ultrafine-grained fcc metals produced by severe plastic deformation, Curr. Appl. Phys. 6 (2006) 194-199.

182. J. Gubicza, N.Q. Chinh, Z. Horita, T.G. Langdon, Effect of Mg addition on microstructure and mechanical properties of aluminum, Mater. Sci. Eng. A 387-389 (2004)55-59.

183 . M.A. Munoz Morris, Gutierrez-Urrutia I, Morris DG. The effect of geometrically necessary dislocations on grain refinement during severe plastic deformation and subsequent annealing of Al–7% Si, Mater. Sci. Eng. A 493 (2008) 141-147.

184. S.C. Wang, Z. Zhu, M.J. Starink, Estimation of dislocation densities in cold rolled Al-Mg-Cu-Mn alloys by combination of yield strength data, EBSD and strength models, J. Microscopy 217 (2005) 174–178.

185 . J.R. Kissell and R.L. Ferry, Aluminium structures: a guide to their specifications and design, John Wiley&Sons, 2002.

186. G.Tempus, W.Calles and G.Scharf, Influence of extrusion process parameters and texture on mechanical properties of Al-Li extrusions, Mater. Sci. Tech. 7 (1991) 937-945.

187. M.F. Ashby and D.R.H. Jone, Engineering Materials 1, Pergamon Press, Oxford, 1980.

188 P. Hirsch and F. Humphreys, "Plastic Deformation of Two-Phase Alloys Containing Small Nondeformable Particles," in Physics of Strength and Plasticity Edited by A. S. Argon, MIT Press (1969) 189–216.

189. J.R. Kissell, R.L. Ferry, Aluminium structures: a guide to their specifications , design, second ed, John Wiley & Sons, New York, 2002.

190. B. Clausen, T. Lorentzen, T. Leffers, Self-consistent modelling of the plastic deformation of f.c.c. polycrystals and its implications for diffraction measurements of internal stresses, Acta Mater. 46 (1998) 3087-3098.

191. E.O. Hall, The deformation and ageing of mild steel: III. Discussion of results. Phys. Soc. Lond. 64 (1951) 747–753.

192. N.J. Petch, The cleavage strength of polycrystals. J. Iron Steel Inst. 174 (1953) 25–28.

193. A.W. Thompson, M.I. Baskes, W.F. Flanagan, The dependence of polycrystal work hardening on grain size. Acta Metall. Mater. 21 (1973) 1017–1028.

194. L.P. Evers, D.M. Parks, W.A.M. Brekelmans, M.G.D. Geers, Crystal plasticity model with enhanced hardening by geometrically necessary dislocation accumulation, J. Mech. Phys. Solids, 50 (2002) 2403-2424.

195. A. Acharya, J.L. Bassani, A. Beaudoin, Geometrically necessary dislocations, hardening, and a simple gradient theory of crystal plasticity, Scripta Mater. 48 (2003) 167-172.

196. J. Aldazabal, J. Gil Sevillano, Hall-Petch behaviour induced by plastic strain gradients, Mater. Sci. Eng. A365 (2004) 186-190.

197. L. P. Evers, W. A. M. Brekelmans, M. G. D. Geers, Non-local crystal plasticity model with intrinsic SSD and GND effects, J. Mech Phys Solids, 52 (2004) 2379-2401.

198. K.S. Cheong, E.P. Busso, A. Arsenlis, A study of microstructural length scale effects on the behaviour of FCC polycrystals using strain gradient concepts, Int J Plasticity, 21 (2005) 1797-1814.

199. W.A. Counts, M.V. Braginsky, C.C. Battaile, E.A. Holm, Predicting the Hall-Petch effect in fcc metals using non-local crystal plasticity, Int J Plasticity, 24, (2008) 1243-1263.

200 L. Ma, J. Zhou, R. Zhu, S. Li, Effects of strain gradient on the mechanical behaviors of nanocrystalline materials, Mater. Sci. Eng. A507 (2009) 42-49.

201. C. Polizzotto, Strain gradient plasticity, strengthening effects and plastic limit analysis, Int J Solids Structures, 47 (2010) 100-112.

202. Annual book of ASTM standards, E140-07. Vol 03.01, ASTM (2007).

203. J. Alkorta, J.M. Martı´nez-Esnaola, J. Gil Sevillano, Detailed assessment of indentation size-effect in recrystallized and highly deformed niobium, Acta Materi. 54 (2006) 3445–3452.

204. S. Qu, Y. Huang, W.D. Nix, H. Jiang,F. Zhang, K.C. Hwang, Indenter tip radius effect on the Nix–Gao relation in micro- and nanoindentation hardness experiments. J. Mater. Res. 19 (2004) 3423–3434.

205. Z. Xue, Y. Huang, K.C. Hwang, M. Li,. The influence of indenter tip radius on the micro-indentation hardness. ASME J. Eng. Mater. Technol. 124 (2002) 371–379.

206. Y. Huang, F. Zhang, K.C. Hwang, W.D. Nix, G.M. Pharr, G. Feng, A model of size effects in nano-indentation, J. Mech. Phys. Solids 54 (2006) 1668-1686.

207. K. Durst, B. Backes, M. Goken, Indentation size effect in metallic materials: Correcting for the size of the plastic zone, Scripta Mater. 52 (2005) 1093-1097.

208. K. Durst, B. Backes, O. Franke, M. Goken, Indentation size effect in metallic materials: Modeling strength from pop-in to macroscopic hardness using geometrically necessary dislocations, Acta Mater. 54 (2006) 2547-2555.

209. X. Qiu, Y. Huang, W.D. Nix, K.C. Hwang, H. Gao, Effect of intrinsic lattice resistance in strain gradient plasticity, Acta Mater. 49 (2001) 3949-3958.

210. E. Aifantis, On the microstructural origin of certain inelastic models,J Eng Mater Techn 106 (1984) 326-330.

211. N.A. Fleck, J.W. Hutchinson, Phenomenological theory for strain gradient effects in plasticity, J Mech Phys Solids 41 (1993) 1825-1857.

212. E. Aifantis, Physics of plastic deformation, Int J Plasticity 3 (1987) 211-247.

213. H. Gao, Y. Huang, W.D. Nix, J.W. Hutchinson, Mechanism-based strain gradient plasticity—I Theory J. Mech.Phys. Solids 47 (1999) 1239–1263.

214. Z. Zhu, M.J. Starink, Age hardening and softening in cold-rolled Al-Mg-Mn alloys with up to 0.4 wt% Cu, Mater. Sci. Eng. A 489 (2008) 138-149.

215. L. Qian, M. Li, Z. Zhou, H. Yang and X. Shi, Comparison of nano-indentation hardness to microhardness, Surf. Coat. Techol. 195 (2005) 264-271.

216. S. Qu, Y. Huang, G.M. Pharr, K.C. Hwang, The indentation size effect in the spherical indentation of iridium: A study via the conventional theory of mechanism-based strain gradient plasticity, Int. J. Plasticity 22 (2006) 1265-1286.

217. M. M. Chaudhri, Subsurface strain distribution around Vickers hardness indentations in annealed polycrystalline copper, Acta Mater. 46 (1998) 3047-3056.

218. K. Durst, B. Backes, M. Goken, Determination of plastic properties of poly crystalline metallic materials by nanoindentation - Experiments and finite element simulations, Mater. Res. Soc. Symp. Proc. 841 (2005) 311-316.

219. J. Alcala, O. Casals, J. Ocenasek, Micromechanics of pyramidal indentation in fcc metals: Single crystal plasticity finite element analysis, J. Mech. Phy. Solids 56 (2008) 3277-3303.

220. W.C. Oliver, G.M. Pharr, An improved technique for determining hardness and elastic modulus using load and displacement sensing indentation, J.Mater.Res.7 (1992) 1564–1583.

221. A. C. Fischer-Cripps, A review of analysis methods for sub-micron indentation testing, Vacuum, 58 (2000) 569-585.

222. J. Gong, H. Miao, Z. Peng, On the contact area for nanoindentation tests with Berkovich indenter: case study on soda-lime glass, Mater. Lett. 58, (2004) 1349-1353.

223. T. Sawa, K. Tanaka, Simplified method for analyzing nanoindentation data and evaluating performance of nanoindentation instruments, J. Mater. Res. 16 (2001) 3084-3096.

224. M. Martin, M. Troyon, Fundamental relations used in nanoindentation: Critical examination based on experimental measurements, J. Mater. Res. 17 (2002) 2227-2234.

225. E. Demir, Raabe D, Zaafarani N, Zaefferer S. Investigation of the indentation size effect through the measurement of the geometrically necessary dislocations beneath small indents of different depths using EBSD tomography, Acta Mater. 57 (2009) 559-569.

226. K.W. McElhaney, J.J. Vlassak and W.D. Nix, Determination of indenter tip geometry and indentation contact area for depth-sensing indentation experiments, J. Mater. Res. 13 (1998) 1300-1306

227. X.G. Qiao, M.J. Starink, N. Gao, Hardness inhomogeneity and local strengthening mechanisms of an Al1050 aluminium alloy after one pass of equal channel angular pressing, Mater. Sci.Eng. A 513-514, (2009) 52-58.

228. E.A. El-Danaf, M.S. Soliman, A.A. Almajid, M.M. El-Rayes, Enhancement of mechanical properties and grain size refinement of commercial purity aluminum 1050 processed by ECAP, Mater. Sci.Eng. A 458 (2007) 226-234.

229. A. Gaber, N. Afify, S.M. El-Halawany, A. Mossad, Studies on Al-Mg solid solutions using electrical resistivity and microhardness measurements, Eur. Phys. J. AP 7 (1999) 103-109.

230. Y. Nishida, H. Arima, J.C. Kim, T. Ando, Rotary-die equal-channel angular pressing of an Al – 7 mass% Si – 0.35 mass% Mg alloy, Scripta Mater, 45 (2001) 261-262.

231. A. Azushima, K. Aoki, Properties of ultrafine-grained steel by repeated shear deformation of side extrusion process, Mater. Sci. Eng. A337 (2002) 45-49.

232. K. Nakashima, Z. Horita, M. Nemoto, T.G. Langdon, Development of a multi-pass facility for equal-channel angular pressing to high total strains, Mater Sci Eng A281 (2000) 82-87.

233. C.Y. Nam, J.H. Han, Y.H. Chung, M.C. Shin, Effect of precipitates on microstructural evolution of 7050 Al alloy sheet during equal channel angular rolling, Mater Sci Eng A347 (2003) 253-257.

234. Y. Huang, P.B. Prangnell, Continuous frictional angular extrusion and its application in the production of ultrafine-grained sheet metals, Scripta Mater 56 (2007) 333-336.

235. J.Y. Suh, J.H. Han, K.H. Oh, J.C. Lee, Effect of deformation histories on texture evolution during equal- and dissimilar-channel angular pressing, Scripta Mater 49 (2003) 185-190.